Magnetization dynamics study on low-symmetry magnetic multi-layers

Aakanksha Sud

A dissertation submitted in partial fulfillment

of the requirements for the degree of

Doctor of Philosophy

of

University College London.

Department of Electronic and Electrical Engineering

University College London

November 17, 2021

I, Aakanksha Sud, confirm that the work presented in this thesis is my own. Where information has been derived from other sources, I confirm that this has been indicated in the work.

Abstract

In this thesis we study magnetization dynamics in different systems comprising of single-layer, multi-layer ferromagnetic and synthetic-antiferromagnetic (SyAF) thin films using techniques of ferromagnetic resonance (FMR) spectroscopy and spin transfer torque (STT) based FMR. In the first part, magnetic relaxation processes following the dynamical excitation of the spin systems are investigated using half-Heusler NiMnSb, a ferromagnet with the zinc-blende (inversion broken) crystal structure, as a prototype system. The experiments, performed at several different microwave frequencies and static magnetic field directions, enabled to observe a strong in-plane anisotropy of the linewidth. We attribute the linewidth anisotropy contribution to intrinsic Gilbert damping, extrinsic inhomogeneous broadening and two-magnon scattering process, supporting this by calculations of possible linewidth broadening mechanisms.

In the second part magnon-magnon coupling is studied in SyAFs and synthetic-ferrimagnets (SyFs). We demonstrate the control of coupling in SyAFs via intrinsic and extrinsic symmetry breaking (SB) in symmetrical and asymmetrical SyAF structures. In symmetrical SyAF there is an apparent mode crossing resulting from degeneracy of two non-interacting modes which is protected by a two-fold rotational symmetry. By tilting the external field we break this symmetry and an anti-crossing gap appears demonstrating the extrinsic SB. The coupling strength can be controlled by interlayer exchange field strength modification through growth and is demonstrated experimentally. We also study asymmetrical SyAF structures referred to as SyFs. An inherent SB exists in the SyF system which opens a gap even for an in-plane field condition. We generalize a theoretical model in the macro-spin limit

to describe the microwave absorption spectroscopy for the SB induced coupling in SyAFs and SyFs.

In the last part we use technique of STT-FMR to study dynamics in SyAF and multi-stack structures of Ni/Pt. Due to opposite polarization in two FM layers we observe change in parity of two spin wave modes in SyAF. Spin orbit torques are quantified in multi-stack structures of Ni/Pt and we show linewidth modulation with current in these multi-stack structures.

Acknowledgements

I would first like to offer my sincerest gratitude to my supervisor Prof. Hidekazu Kurebayashi for all his tremendous support and kind guidance throughout my PhD. He has been a great mentor and I feel extremely fortunate to spend my graduate career under him.

I want to express my sincere thanks to Prof Shigemi Mizukami for inviting me to Tohoku University and providing the fabrication and experimental facilities for carrying out the work outlined in Chapter 5 and 6. I would like to thank all my external collaborators at Tohoku-Iihama-san, Suzuki-san, Yuya who helped me in experiments during my stay at Tohoku. I am thankful to Kei for his crucial advise and help for the work carried out in Chapter 4 and 5.

I would like to thank Safe, Kazu, Kostas who guided me and trained me in the lab starting from the very first day of PhD. I also thank all my labmates for their helps in and outside the academics. Christoph for his assistance in experiments outlined in Chapter 5.

I thank the external collaborators, Dr Sukegawa and Dr Xiang for providing the NiMnSb samples. Dr Seki (Tohoku university) for growing the NiPt samples. Dr Anwar (Cambridge university) for his help in ion-milling. Prof Zubko for allowing me to use the annealing and ion-milling chamber and also giving the training for it. Evgenios for his help in milling. Kelvin for 3D printing. Vj and Lorella for their help in cleanroom training. Rohit for his help in repairing lock-in amplifier and designing the bias-tee holder.

Finally, I would like to thank my parents for their unconditional love, support and encouragement throughout my studies.

Impact Statement

The work presented in this thesis contributes to the fundamental understanding of spin dynamics in different magnetic multi-layer and low symmetry, broken inversion system and hence advances the research in the field of spintronics. In the case of NiMnSb (non-centrosymmetric ferromagnet), anisotropy in damping is realised and the different factors contributing to this anisotropic damping are studied. The control of damping is important for efficient magnetization reversal and a large value of intrinsic damping could speed up the writing process in memory devices. The results presented reveal the key mechanism to engineer the Gilbert damping and thus open a new pathway to develop novel functionality in spintronic devices.

The ability to reach strong coupling with many different excitations make magnons an ideal platform for examining solid-state coherent dynamics and exploitation of its unique functionality. The magnon-magnon coupling in synthetic antiferromagnets (SyAFs) is among the few reported works of strong coupling achievable at room temperature. The rotational symmetry breaking by application of external field at an angle allows the tuning of coupling strength. The in-situ tuning capabilities and engineerable properties makes them promising for future spintronic and high speed information processing applications. In asymmetrical structures with either dissimilarity in thickness or material of two ferromagnetic (FM) layers can induce magnon-magnon coupling without applying out-of-plane field, by breaking inherent two-fold symmetry. This has been shown experimentally in this thesis and we expect our result to enable device based SyAF spintronics with microwave control of Nèel vector. The parity control of spin wave excitations has been reported for first time in SyAF and it is demonstrated that by the use of lo-

cal spin torque excitations, the mode excitation symmetry of spin wave modes can be changed. The manipulation of spin-orbit torque (SOT) by electronic structure modification by growth has been shown in Ni/Pt multi-layers which elucidates the importance of growth on SOT efficiency and its effect on various magnetic parameters and thus can be useful for future spintronic and magnonic nano-devices.

Contents

List of Figures

[1] Measurements done by Dr. Seki

List of Tables

List of Abbreviations

FMR	Ferromagnetic Resonance
STT	Spin Transfer Torque
SOT	Spin Orbit Torque
VNA	Vector Network Analyser
CPW	Coplanar Waveguide
LLG	Landau-Lifshitz Gilbert
AMR	Anisotropic Magnetoresistance
SHA	Spin Hall Angle
vdW	van der Waals
SSW	Surface Spin Wave
BVSW	Backward Volume Spin Wave
FVSW	Forward Volume spin wave
PPSW	Perpendicular Standing Spin wave
SB	Symmetry Breaking
SyAF	Synthetic Antiferromagnet
SyF	Synthetic Ferrimagnet
SOC	Spin Orbit Coupling
RF	Radio Frequency

FM	Ferromagnet
FL	Field Like
DL	Damping Like
MAE	Magnetocrystalline Anisotropy Energy
GMR	Giant Magnetoresistance
SMR	Spin Hall Magnetoresistance
NM	Non-magnet
HM	Heavy Metal
FMI	Ferromagnetic Insulator
SHE	Spin Hall Effect
ISHE	Inverse Spin Hall Effect
CI	Current Induced

Chapter 1

Introduction

In the emerging field of 'Spintronics' (spin electronics) one seeks to exploit the spin degree of freedom of electrons which can also interact with their orbital moments. Controlling the injection, manipulation, transfer and detection of electron spins can derive new functionalities for electronics and photonics. For the next-generation electronic devices there has been a need to reduce power consumption and to increase the memory and processing capabilities. This has led to the discovery of new spintronic phenomena like spin-orbit torques [1], spin-Hall effect [2], spin transfer torque [3], spin Seebeck effect [4]. The integration of storage, processing, sensing and logic in a single device has the potential to complement and even outperform the semiconductor based electronics, offering advantages in terms of scaling, power consumption and processing speed.

The understanding of spin dynamics in nanomagnets requires a detailed knowledge of the precession of the magnetization vector, involving the conditions of dispersion, spin wave generation and various relaxation mechanisms after excitation. It involves various theoretical and experimental research areas (resonance, spin-torque, spin-injection, magnetic-reversal, non-linear dynamics) to interpret the different modes of magnetic damping. Controlling the Gilbert damping constant, α, in ferromagnetic materials is very crucial for future spintronic applications. It has been reported in earlier works [5, 6, 7, 8, 9] that in case of ferromagnetic materials, the strength of spin-orbit interaction affects both static and dynamic properties of magnetization. It can manipulate both crystalline magnetic anisotropy and

magnetization dynamics [10, 11]. Thus, one can expect that similar to magnetic crystalline anisotropy, damping parameter α governing the magnetization will also show a crystalline anisotropy. Recent theoretical works [12, 13] have suggested that α is magnetization orientation dependent and should be a 3×3 tensor in the phenomenological Gilbert equation. This prediction is based on the anisotropic electronic structure where the shape of the Fermi-surface depends on orientation of the magnetization direction due to spin-orbit interaction. Yet, α is often treated as scalar (isotropic) because the smearing of energy bands in the presence of electron scattering makes it experimentally difficult to observe the anisotropic damping in bulk materials.

According to the theoretical works [14, 15, 16, 17], α is related to the strength of spin-orbit interaction as $\alpha \sim \mathrm{n}(E_\mathrm{F})\ \xi^2\tau^{-1}$, where $\mathrm{n}(E_\mathrm{F})$ is the density of states at the Fermi level E_F, ξ is the strength of spin-orbit interaction and τ is the electron momentum scattering time. It has also been shown by Bruno [18] that the energy difference between the easy and hard direction of magnetization, ΔE, is related to the anisotropy of orbital angular momentum as $\Delta E \propto (\mu_\mathrm{L}^{\parallel} - \mu_\mathrm{L}^{\perp})$ where $\mu_\mathrm{L}^{\parallel}$ and $\mu_\mathrm{L}^{\perp}$ are the orbital moments parallel and perpendicular to the easy axis of magnetization respectively. Since the g-factor, g, measured in ferromagnetic resonance (FMR) is a measure of the orbital-to-spin magnetic moment ratio and since $\alpha \propto (g-2)^2$ [19], one could hope to identify anisotropic Gilbert-type (spin-orbit) damping in materials with large magnetic anisotropy. [20]. However, it should be noted that the identification of such an intrinsic anisotropic Gilbert damping may be impossible due to the presence of extrinsic contributions like two-magnon scattering which can also cause an angle dependent relaxation rate. Also, other mechanisms like inhomogeneous broadening and mosaicity broadening may hinder the determination of weak anisotropic Gilbert damping.

Another area of research which has shown tremendous stride recently is the utilization of magnetic excitations or magnons for novel quantum functionality. The capability of strong coupling and formation of hybrid dynamic systems with other excitations has facilitated the growth of hybrid magnonics enabling development of

various magnonic and spintronic technologies [21]. Spin waves can propagate and interfere, delivering phase information for coherent information processing. This makes magnons, which are the quanta of spin-waves, a forerunner to exploit and utilize new effects in magnon dynamics. Magnons are capable of a wide range of interactions for example they can couple with microwave or optical photons via magneto-optic Faraday effect [22], with phonons due to magnetoelastic coupling [23] and also other magnons [24]. Coherent manipulation of spin qubits has been possible due to interaction between magnons and spins such as nitrogen-vacancy centres in diamond. Layered antiferromagnets are exemplary materials showing magnon-magnon interactions. Both synthetic antiferromagnets (SyAF) and van der Waals (vdW) magnets show weak interlayer exchange interaction which enables acoustic and optical magnons. The interaction can be tuned through field orientation [24] and wave number [25]. This allows tuning of the magnon energy spectrum.

After the discovery of giant magnetoresistance (GMR) by Fert [26] and Grünberg [27], spintronics has gained wide importance as a sub-field of physics. In case of multi-layers with alternating ferromagnet and non-magnet layers, a giant change in resistance with applied field was observed, referred to as GMR, which depends on the magnetization of two adjacent ferromagnetic layers. The use of GMR to build the read head in hard disks has led to revolution in data storage and memories.

A promising way to write data in spin-valve is provided by spin-transfer phenomena. Spin transfer torque (STT) was first studied by Slonczewski [28] and Berger[29] in 1996. Magnetization of one layer is fixed (usually due to exchange bias) while the other is free to rotate. When current is passed through the fixed layer, it becomes spin polarized and transfers the angular momentum to the free layer and switches its magnetization either parallel or anti-parallel to fixed layer's magnetization. The data can be easily read through GMR, making this a useful technique for magnetic random-access memory (MRAM). Due to the compatibility of STT-MRAM with complementary metal-oxide semiconductor (CMOS) technology along with non-volatility, it has potential applications [30, 31, 32] in radio frequency identification, computers and so on. However, one of the disadvantages is high cur-

rent density which is very large for commercial standards and so new solutions need to be explored. In this thesis we report current-induced (CI) ferromagnetic resonance for two types of devices namely SyAF and Ni/Pt multi-stacks. The main purpose is to probe the magnetic properties of these materials and to measure the amplitude and symmetry of current-induced torques. All of the measurements in this thesis are carried out at room temperature. We utilise the technique of spin dynamics spectroscopy to investigate the magnetic relaxation in non-centrosymmetric ferromagnet (NiMnSb) and study the interaction of spin excitations of magnon modes in SyAF and synthetic ferrimagnets (SyFs).

Thesis Outline

A brief overview of background theory and physics topics related to the experimental chapters is given in Chapter 2. The experimental techniques used to obtain the experimental data is presented in Chapter 3.

In Chapter 4, we discuss the broadband-FMR measurement on series of NiMnSb samples of different thickness. Strong anisotropy in damping is observed. The various intrinsic and extrinsic contributions to FMR linewidth are separated. By performing complete frequency dependent and angular scans for the field applied in-plane and out-of-plane we are able to quantify the contributions of two-magnon, inhomogeneous and intrinsic Gilbert damping mechanisms which lead to broadening of the linewidth. The perpendicular standing spin wave (PSSW) mode is observed in thicker samples and exchange stiffness parameter is quantified from resonance field analysis of main mode and PSSW mode.

In Chapter 5, spin dynamics is studied in SyAF and SyF films. Strong magnon-magnon coupling is achieved in SyAF by breaking the orthogonal symmetry of two modes through tilt of magnetic moments. The effect of mutual spin pumping damping term, α_{sp}, is theoretically shown to have an effect on coupling strength indicating the coupling is being partially mediated by spin currents. The effect of inherent symmetry breaking on coupling strength is studied in SyF where the symmetry is broken due to the dissimilarity in thickness and the type of the two

ferromagnets (FM). A large coupling gap indicates stronger efficiency of inducing magnon-magnon coupling in asymmetrical structures. We also generalize a theoretical model in the macro spin limit by solving coupled equations of motion which complement experimental results.

In Chapter 6, the FMR driven by CI torques is studied in SyAF films. The mode excitation symmetry is changed between parallel and perpendicular pumping configuration due to anti-symmetric profile of the torques caused by opposite spin polarisation in the top and bottom Ta layers. The experimental results are supported with analytical expressions for the rectified voltages derived from our theoretical model and the magnetic parameters like spin Hall angle are obtained. Finally, the spin-orbit torques are studied in different Ni/Pt multi-layers grown on different substrates and with different stacking patterns. Through interface engineering and electronic structure modification by growth on Si/sapphire substrate the spin-orbit torque (SOT) efficiency for field-like (FL) and damping-like (DL) torques is changed and this is experimentally demonstrated. The spin Hall angle is calculated by DC current modulation of linewidth. Different anisotropy parameters are calculated from angular dependence and frequency dependence of resonance field which confirms the strain induced anisotropy in samples grown on sapphire. Moreover, large inhomogeneity is seen for epitaxially grown samples.

Chapter 2

Basic Background

In this chapter the background theory and the mathematics used in this thesis is presented. First the basic aspects of ferromagnetism are discussed. Then different magnetic energy terms in magnetic materials are described to understand the behaviour of magnetization along with different contributions to the magnetic anisotropy. The resonance equations which satisfy the resonance condition in the small angle limit of precessional motion are described in Sec. 2.4.3. The relaxation mechanism is explained in terms of different contributions to the ferromagnetic resonance linewidth. Finally in Sec. 2.8, current-induced spin transfer torques are discussed.

2.1 Ferromagnetism

Ferromagnetism is the phenomena in which specific solids present a spontaneous magnetization with parallel alignment of spins, even in the absence of an external magnetic field. The magnetic moments are coupled to each other due to exchange interactions leading to parallel alignment referred to as collective magnetism. For a ferromagnet in an applied magnetic field **B**, the appropriate Hamiltonian to solve is given by:

$$\hat{\mathcal{H}} = -\sum_{ij} \mathrm{J_{ij}} \mathbf{S_i} \cdot \mathbf{S_j} + g\mu_B \sum_j \mathbf{S_j} \cdot \mathbf{B} \tag{2.1}$$

where the exchange constant $\mathrm{J_{ij}}$ will be positive to ensure ferromagnetic alignment. The first term on right is the exchange energy and the second term refers to the

Zeeman energy. $S_{\mathrm{i}}, S_{\mathrm{j}}$ are the i^{th} and j^{th} spins respectively and $\mu_B = e\hbar/(2m_{\mathrm{e}})$ is the Bohr magneton (with elementary charge e, reduced Planck constant $\hbar$ and electron mass m_{e}) [33].

The ferromagnetic order appears only below a critical temperature known as the Curie temperature, which is characteristic for a given material, and the material attains a paramagnetic state above the Curie temperature [34].

In a magnetic solid of volume V consisting of a large number of atoms with magnetic moment $\boldsymbol{\mu}$, the magnetization or saturation magnetization $\mathbf{M}$ is given by:

$$\mathbf{M} = \frac{1}{V}\int_V \boldsymbol{\mu} dV \quad , \quad M_s = |\mathbf{M}| \tag{2.2}$$

$\mathbf{M}$ can be considered to be a smooth vector field which is continuous everywhere except at the edges of the magnetic solid. $\boldsymbol{\mu}$ is directly related to the total angular momentum $\mathbf{L}$ by:

$$\boldsymbol{\mu} = -g\frac{\mu_B}{\hbar}\mathbf{L} \tag{2.3}$$

where g is the Landé - factor.

Ferromagnetic order originates due to exchange interactions as described by the Hamiltonian in Eq. 2.1. These interactions are the short-range quantum mechanical exchange interaction following from the Pauli exclusion principle for fermions [35]. In addition, there is also a long-range (weak) interaction arising due to the dipolar field of each magnetic moment, which does not provide a decisive contribution to collective magnetism being too weak to account for the ordering in most magnetic materials, but it is the origin of shape anisotropy which is important for consideration when characterising magnetic materials.

Other kinds of magnetic ordering which are important to be highlighted in this thesis are antiferromagnetism and ferrimagnetism. If the exchange interaction is negative, $\mathrm{J_{ij}} < 0$, it is more favourable for the magnetic moments to align antiparallel to each other. This is called antiferromagnetism and it generally occurs in the system with two interpenetrating sub-lattices with magnetic moments pointing op-

posite to each other. The antiferromagnetic order disappears for temperatures above a critical temperature known as the Neèl temperature. When a strong magnetic field is applied to an antiferromagnet, depending upon the initial direction of sub-lattice magnetization with respect to applied external field, the magnetic moments start to rotate. For the applied field parallel to sub-lattice magnetization and greater than a critical field called spin-flop field H_{sf} [36], the two magnetic moments rotate in the direction perpendicular to the easy axis and snap into a different configuration called spin-flop transition (canted regime) as shown in Fig. 2.1 (d). However, if the anisotropy energy in the system is very large compared to the exchange energy, the net magnetization can jump directly from zero (when the sub-lattice moments are antiparallel along the easy axis) to saturated state (when the sub-lattice magnetic moments are aligned parallel along the easy axis). This is known as spin-flip transition.

Another class of materials are synthetic antiferromagnets (SyAFs) in which the two ferromagnets are coupled anti-parallel due to indirect exchange and are discussed later in this thesis.

When the two sub-lattices are not equivalent, the magnetization of two sub-lattices do not cancel out each other and the material will have a net magnetization [37]. The net magnetization can have a complicated temperature dependence and change sign at a temperature called the compensation temperature. Thus, the magnetic susceptibilities of ferrimagnets do not follow the Curie Weiss law [34].

2.2 Magnetic Interaction Energy

In a ferromagnet (FM), the spatial distribution of magnetization, *m(r,t)*, is given by the minimum of the free energy of the FM, *E*, that contains the contributions from different origins. The total energy, $E_{\mathrm{Tot}} = (\int_{\mathrm{FM}})\mathrm{dV}(\sum \varepsilon)$, is evaluated as an integral over the whole FM volume. It is given as the sum of the different local energies, namely exchange energy (E_{ex}), Zeeman energy (E_{Zeeman}), demagnetization energy (E_{demag}) and magnetocrystalline anisotropy energy, (E_{Anis}):

$$E_{\mathrm{Tot}} = E_{\mathrm{ex}} + E_{\mathrm{Zeeman}} + E_{\mathrm{demag}} + E_{\mathrm{Anis}} \tag{2.4}$$

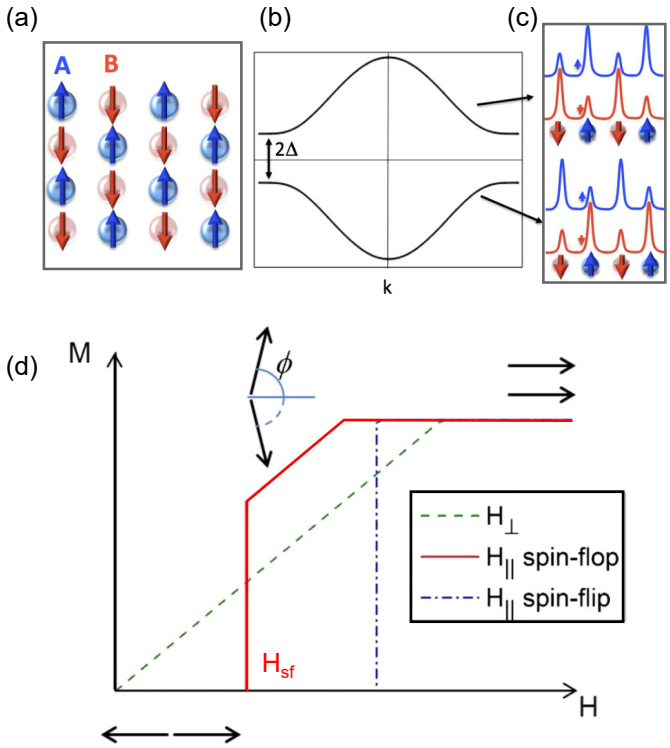

Figure 2.1: (a) Schematic representation of G-type of two-dimensional antiferromagnet with two sub-lattices referred to as A (blue arrows,pointing up) and B (red arrows, pointing down), (b) electronic band structure, and (c) spatial distribution of the corresponding density of states. (d) Magnetization manipulation by application of magnetic field in an antiferromagnet. The magnetic field rotates the two moments until saturation is achieved at the spin-flip field. Cases for field applied parallel and perpendicular to the easy axis are shown. Fig. adapted from [36].

2.2.1 Exchange Interaction

The fundamental energy contribution in a FM is the exchange interaction between electrons which enables ferromagnetic ordering. It is directly proportional to the overlap of spatial wave functions of the respective electrons and therefore is a short ranged interaction [38]. For electrons with spin **S** that are localized at lattice points, *i*, the exchange interaction can be expressed by the Heisenberg Hamiltonian form and is given by first term in Eq. 2.1 [39].

Based on energies of the singlet and the triplet states, the exchange constant can be defined as $J = (E_S - E_T)/2$ where $E_{(S,T)}$ are the energies for singlet and triplet states. Here, the singlet state refers to the quantum state with spin quantum number,

s =0 and with all electrons paired. The triplet state represents the quantum state with s =1, thus allowing values of spin components, m_s = -1, 0, 1. As mentioned earlier, depending upon the sign of J_{ij}, there can be parallel or anti-parallel alignment of neighbouring spins, resulting in ferromagnetic or antiferromagnetic order. The isotropic exchange energy as given by Eq. 2.1, results in random orientation of the magnetization with respect to the crystal axis.

The origin of exchange can be described based on the Heitler-London model of the hydrogen molecule [34]. The wave function for the joint state is given by the product of spatial and spin wave functions of single electron states. The overall wavefunction must be antisymmetric for the electrons to satisfy the Pauli Exclusion principle [40]. This means that for symmetric spatial state, the spin part must be antisymmetric singlet state ($S = 0$) or symmetric triplet state ($S = 1$) for antisymmetric spatial part. If two electrons are on the same atom, J_{ij} is usually positive which stabilises the triplet state with antisymmetric spatial state. This minimises the coulomb repulsion between the two electrons by keeping them at a distance which is consistent with Hund's rule.

The exchange mechanism described above is known as direct exchange since the interaction proceeds directly without the need for an intermediary. However another type of interaction known as indirect exchange interaction becomes important for many magnetic materials. Two of the important indirect exchange interactions in metals are the RKKY (Ruderman-Kittel-Kasuya-Yosida) [41, 42, 43, 44, 45, 46] interaction and antisymmetric exchange known as Dzyaloshinskii-Moriya (DMI) interaction [47]. The RKKY coupling is an indirect exchange interaction between two magnetic ions mediated by the conduction electrons. The conduction electrons are spin polarised by a localized magnetic moment which in turn couples to a neighbouring localised magnetic moment at a distance r away. The coupling is dependent on distance r and the coupling constant can be described as:

$$J_{\mathrm{RKKY}} \propto \frac{\cos(2k_{\mathrm{F}}r)}{r^3} \tag{2.5}$$

where k_{F} represents the radius of the Fermi surface. This interaction has oscillatory

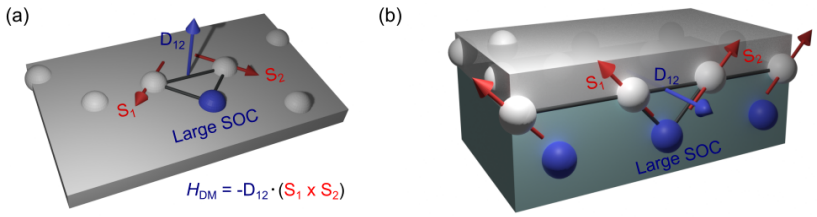

Figure 2.2: (a) Schematic representation of DMI generated by indirect exchange for (a) a triangle made of two atomic spins and an atom with strong spin-orbit coupling (SOC). (b) at the interface of a ferromagnetic metal (grey) and a metal with large SOC (blue). The DMI vector, D_{12}, is perpendicular to the plane of the triangle. Fig. adapted from [48].

dependence on the distance between the magnetic moments. The DMI is an indirect interaction acting between two spins $\mathbf{S_1}$ and $\mathbf{S_2}$ in the materials which exhibit spin-orbit coupling and lack inversion symmetry in the lattice or at the interface [48] as shown in Fig. 2.2. The interaction occurs between the excited state of one magnetic ion and the ground state of the other. The hamiltonian $\hat{\mathcal{H}}_{\mathrm{DM}}$ is given as :

$$\hat{\mathcal{H}}_{\mathrm{DM}} = \mathbf{D}_{12} \cdot \mathbf{S_1} \times \mathbf{S_2} \tag{2.6}$$

where, $\mathbf{D}_{12}$ is the DMI vector and vanishes when the inversion symmetry exists with respect to centre between two magnetic ions. When inversion symmetry is lacking in the material, the DMI interaction causes the two spins to be at right angles in a plane perpendicular to $\mathbf{D}_{12}$ and its effect is to cause the canting of the spins by small angles thus favouring chirality of the magnetic moments. Another type of indirect exchange occurs in ionic solids called the superexchange [49]. It is an indirect exchange interaction between non-neighbouring magnetic ions mediated by a non-magnetic ion placed between them.

2.2.2 Zeeman Energy

The Zeeman energy describes the energy splitting of a degenerate energy state by introducing an external field. This energy is described by the following equation:

$$E_{\mathrm{Zeeman}} = -\mu_0 \mathbf{M}.\mathbf{H}_{\mathrm{ext}} \tag{2.7}$$

where μ_0 is the vacuum permeability. The interaction between $\mathbf{M}$ in a magnetic system and any external magnetic field, $\mathbf{B}_{\text{ext}} = \mu_0 \cdot \mathbf{H}_{\text{ext}}$[1], exerts a torque on the magnetic moment which minimises the energy when aligned parallel to the applied field.

2.2.3 Demagnetization Energy

The second class of energy contribution is based on dipolar interactions between magnetic moments. In a FM, the magnetization at each point is subject to the field generated by the dipolar fields of the magnetic moments of the whole volume of FM. Magnetic poles appear on the surface of a uniformly magnetised sample giving rise to a demagnetising field, $\mu_0 H_{\text{d}}$. The corresponding energy is represented as [50]:

$$E_{\text{demag}} = -\frac{1}{2}\mu_0 \int_V \mathbf{M}(\mathbf{r}).\mathbf{H}_{\text{d}}(\mathbf{r}).d\mathbf{r} \tag{2.8}$$

In order to minimize the energy, the magnetization must lie in film plane. To pull the magnetization out-of-plane, a large energy has to be provided. The effect of demagnetizing field is therefore called the shape anisotropy. There are preferred directions for the magnetization which exist depending on the geometry of the FM, resulting in a low demagnetizing energy which are called easy axes/planes and directions with high demagnetizing energy, which are called hard axes/planes. For a thin film, considering only the shape anisotropy, the film plane is the easy plane and the normal to the plane is the hard axis. In a ferromagnetic ellipsoid, in which both the magnetization and the demagnetization field are homogeneous, the demagnetization field can be written in the following form [51]:

$$\mu_0 \mathbf{H}_{\text{d}} = -4\pi \bar{\bar{\mathbf{N}}} \mathbf{M} \tag{2.9}$$

where $\bar{\bar{\mathbf{N}}}$ is the demagnetising tensor of the second order and whose trace equals 1. This tensor is diagonal in the principal axes system of the ellipsoid and can be

[1] Throughout this thesis $\mathbf{H}_{\text{ext}}$ is given in Ampere per meter [A/m] and $\mathbf{B}_{\text{ext}}$ represents the external field and is given in Tesla [T], $\mathbf{B}_{\text{ext}} = \mu_0 \cdot \mathbf{H}_{\text{ext}}$

represented by 3×3 matrix as:

$$\bar{\bar{\mathbf{N}}} = \begin{bmatrix} N_{\mathrm{xx}} & 0 & 0 \\ 0 & N_{\mathrm{yy}} & 0 \\ 0 & 0 & N_{\mathrm{zz}} \end{bmatrix}, \qquad N_{xx} + N_{yy} + N_{zz} = 1. \tag{2.10}$$

where $N_{\mathrm{xx}}, N_{\mathrm{yy}}, N_{\mathrm{zz}}$ are called the demagnetizing factors.

2.2.4 Magnetocrystalline Anisotropy Energy

The magnetocrystalline anisotropy energy (MAE) is the difference in the free energy associated with the different directions of magnetization with respect to the crystallographic axes of the crystal. In the following, we briefly review the intrinsic contributions to the overall measured phenomenological magnetocrystalline anisotropy constants K_{i}. The spin-orbit coupling is the direct source of MAE. The spin-orbit coupling couples the electron spin to the orbital moment and consequently the energy of the system depends on the relative orientation between the magnetization (spin orientation) and crystal axis. If it is assumed in a solid that a crystal field forces the electron to move in a certain crystallographic plane, the electron spin will be aligned in a direction normal to this plane. In this way, a uniaxial anisotropy can arise regardless of the shape of the crystal. In a semi-classical picture, the spin-orbit interaction couples the spin and orbital angular momentum by [52]:

$$E_{\mathrm{SO}} = \xi(r)\mathbf{S}.\mathbf{L} \tag{2.11}$$

where $\xi(r)$ is the spin-orbit coupling (SOC) constant. The two common types of crystal anisotropy are cubic and uniaxial with the former sometimes referred to as biaxial anisotropy in thin films.

Cubic anisotropy

In a cubic system the cubic edges define the direction of easy axis of magnetization. The energy density associated with this, referred to as cubic anisotropy E_{C}, is described in terms of the direction cosines $(\alpha_{\mathrm{x}}, \alpha_{\mathrm{y}}, \alpha_{\mathrm{z}})$ of the magnetization vector with respect to the edges of the crystal cube. Due to the high symmetry of cubic

crystals, a low-order approximation of E_C is given as [53]:

$$E_C = K_{c1}(\alpha_x^2\alpha_y^2 + \alpha_y^2\alpha_z^2 + \alpha_x^2\alpha_z^2) + K_{c2}(\alpha_x^2\alpha_y^2\alpha_z^2) + ... \quad (2.12)$$

where K_{c1} and K_{c2} are the cubic anisotropy constants which are material specific and are determined experimentally. The strengths and signs of the anisotropy constants give information about the crystallographic direction for which the anisotropy energy is minimal.

Uniaxial anisotropy

The preference of magnetization in a ferromagnet to align in a single axis called the easy axis is described by the uniaxial anisotropy. The alignment of the magnetization along the easy axis minimizes the energy in the system. The uniaxial anisotropy energy density can be described by a power series [54]:

$$E_U = K_0 + K_{u1} + (\sin^2\theta) + K_{u2} + (\sin^4\theta) + K_{u3} + (\sin^6\theta) + ... \quad (2.13)$$

where θ is the angle between the magnetization direction and the anisotropy axis and $K_{u1}, K_{u2}, K_{u3}, ...$ are the anisotropy constants. In the above Eq. 2.13, the higher order terms ($\sin^4\theta, \sin^6\theta$,...) are very small and so we limit the case where the expansion is truncated after $\sin^2\theta$ term. In that case the sign of constant K_{u1} determines the anisotropic behaviour. When $K_{u1} > 0$, there can be two minima for anisotropy energy given as $\theta = 0$ and $\theta = \pi$. This describes an easy axis anisotropy. Conversely, when $K_{u1} < 0$ then the energy is minimised for $\theta = \pi/2$ and it represents the easy plane anisotropy. In comparison to the direct exchange interaction, the energy difference between magnetic easy and hard axis is very small and mostly ranges between μeV and meV (exchange interaction $\sim$ 0.01 - 0.1 eV) [55].

Magneto-elastic Anisotropy

Magneto-elastic anisotropy exists when stress is exerted on the magnetic system. This leads to the energy terms that depend both on the strain and the magnetization direction referred to as the magneto-elastic energy. This phenomenon is of particular importance in case of the epitaxial structures where considerable strain may

result either due to the epitaxial growth of the film on a substrate or in the adjacent layers having different lattice parameters. The inverse of this effect occurs when due to changing the direction of magnetization causes the deformation of the material. This is known as magnetostriction [56]. Generally, the magneto-elastic part of anisotropy for a cubic system can be written as:

$$E_{\mathrm{MEL}} = B_1(\alpha_{\mathrm{x}}^2\varepsilon_{11} + \alpha_{\mathrm{y}}^2\varepsilon_{22} + \alpha_{\mathrm{z}}^2\varepsilon_{33}) + 2B_2(\alpha_{\mathrm{x}}\alpha_{\mathrm{y}}\varepsilon_{12} + \alpha_{\mathrm{y}}\alpha_{\mathrm{z}}\varepsilon_{23} + \alpha_{\mathrm{z}}\alpha_{\mathrm{x}}\varepsilon_{31}) + ... \tag{2.14}$$

where B_1 and B_2 are the magneto-elastic coupling constants, $\varepsilon_{\mathrm{ij}}$ are the strain components and α_{i} the direction cosines given by:

$$\begin{aligned} \alpha_{\mathrm{x}} &= sin\theta cos\phi \\ \alpha_{\mathrm{y}} &= sin\theta sin\phi \\ \alpha_{\mathrm{z}} &= cos\theta \end{aligned} \tag{2.15}$$

2.3 Spin-dependent transport

Spin dependent transport in case of magnetic structures depends on how the spins and charge carriers interact with each other. A starting point to the application and physics of spin dependent transport came through the discovery of Giant Magnetoresistance [26] which constitutes one of the major areas of study in spintronics. Two main topics will be covered in this section. First is the anisotropic magnetoresistance (AMR) which occurs due to change in resistance caused by change in scattering of conduction electrons for different directions of magnetization. The second topic is the spin Hall Effect (SHE) which originates due to spin-orbit interaction leading to spin asymmetric scattering of conduction electrons in non-magnetic heavy metals thereby generating spin current due to spin Hall effect.

2.3.1 Anisotropic Magnetoresistance (AMR)

AMR was discovered in 1856 by Lord Kelvin. It can be described microscopically based on spin-orbit scattering of spin polarized conduction electrons which result in an anisotropic angular dependence of the current density $\overrightarrow{j}$ with respect to the

magnetization vector $\overrightarrow{M}$. The AMR signal is defined as below:

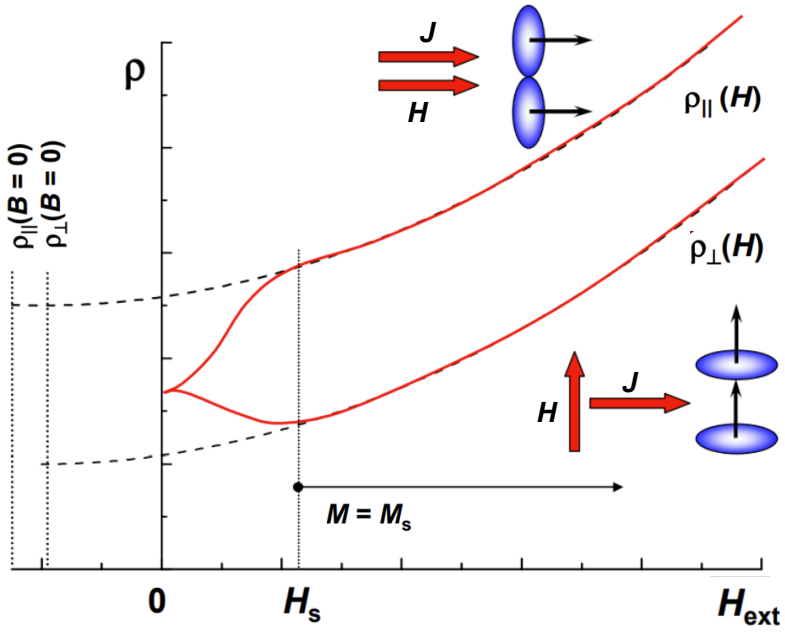

Figure 2.3: Resistivity plotted as a function of magnetic field for a ferromagnetic conductor. With increase of H_{ext}, the difference in resistivity between the cases of $\rho_{\parallel}$ and $\rho_{\perp}$ increases due to magnetic domain shifts within the ferromagnets. Fig. adapted from [57].

$$\frac{\Delta R}{R} = \frac{R(\overrightarrow{j} \parallel \overrightarrow{M}) - R(\overrightarrow{j} \perp \overrightarrow{M})}{R(\overrightarrow{j} \perp \overrightarrow{M})} \tag{2.16}$$

where ΔR is the resistance change. AMR is a small effect since the SOC is relatively weak compared to the exchange interaction. A resistance change $\Delta R/R$ of only a few percent is achieved in certain Ni-based alloys at best. For most transition metals $\Delta R/R$ is positive while in some materials like GaMnAs it is negative ($R_{\parallel} < R_{\perp}$) [58]. In case of $3d$ transition metals where the $3d$ band is not filled completely, both SOC and s-d scattering play a role in AMR. The sp electrons are responsible for conduction in these metals based on Mott's model [59]. When a magnetic field is applied the sp electrons get scattered into the d sub-bands increasing resistivity. The scattering cross section of charge distribution is dependent on the orientation of electron orbits which are in the plane of current for $\overrightarrow{j} \perp \overrightarrow{M}$ thus leading to small

resistance due to small scattering cross-section or perpendicular for $\overrightarrow{j} \| \overrightarrow{M}$ leading to high resistance state due to large scattering area [60]. The resistance change due to this phenomena can be expressed as :

$$R = R_{\perp} + (R_{\parallel} - R_{\perp}) \cos^2 \theta \tag{2.17}$$

where θ is the angle between $\overrightarrow{j}$ and $\overrightarrow{M}$.

2.3.2 Giant Magnetoresistance

Anisotropic magnetoresistance effect as described in previous section is small with the normalized value of $\Delta R/R$ equal to 1–6 % at room temperature for 3d-metals and alloys [61]. A revolution occurred in late 1980s with the discovery of giant magnetoresistance (GMR) in Fe/Cr/Fe multilayers [26]. The junction resistance was strongly dependent upon the orientation of the magnetization in two Fe layers (i.e parallel or antiparallel) as shown in Fig. 2.4 (a-b). This can also be explained based on the "two-current model" as shown in Fig. 2.4 (c-d). The current through

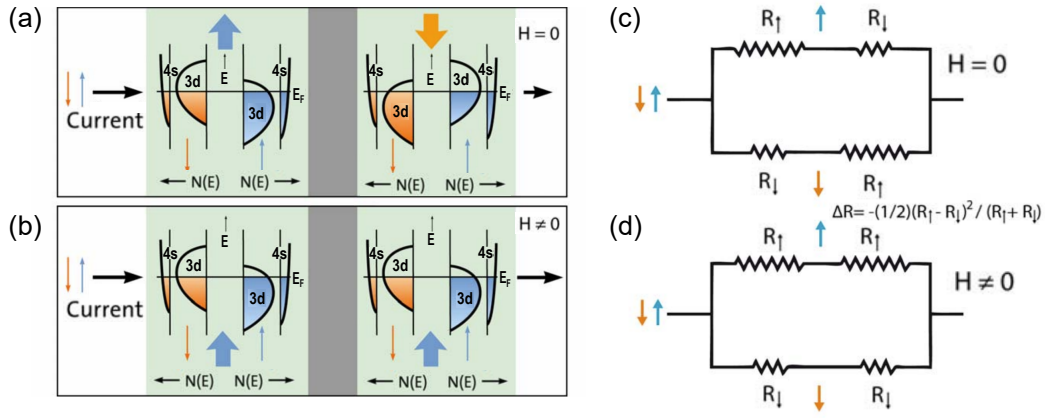

Figure 2.4: Schematics of electronic structure in a trilayer system composed of two ferromagnetic layers separated by a non magnetic spacer in between for (a) when the two layers have opposite magnetization and (b) when two layers have parallel magnetization. The corresponding two current model is shown on right for (c) anti-parallel and (d) parallel cases. The electrons experience a high resistance channel for anti-parallel case and low resistance for the parallel case. This shows clearly that the total resistance of two cases is different i.e there is a magnetoresistance effect. Fig. adapted from [57].

the ferromagnet is composed of spin-up current (for spins aligned parallel to M) and spin-down current (for spins aligned anti-parallel to M). Spin-flip scattering is considered to be negligible at the interface. The spin up and spin down particles have different density of states at the fermi level and so the resistance not only within each FM layer but also at the interface is different for the two as shown in Fig. 2.4 (a-b). The 3d density of states is larger for spin down sub-band for magnetization pointing up, resulting in higher scattering rate and higher resistivity for spin down electrons and vice versa for spin up electrons. In the anti-parallel case the electrons are alternatively $\uparrow$ and $\downarrow$ in each of the layers with respect to local magnetization and thus spin $\uparrow$ and $\downarrow$ channels are effectively mixed so the total resistance is $(R_\uparrow + R_\downarrow)/2$ and the larger the difference between $(R_\uparrow, R_\downarrow)$, larger is the negative magnetoresistance. For the parallel case , the resistance of spin up channel is $2R_\uparrow$ and for down channel is $2R_\downarrow$ thus giving total resistance as $2R\uparrow R\downarrow/(R_\uparrow + R_\downarrow)$ resulting in lower overall resistance compared to anti-parallel case.

2.3.3 Spin Hall Effect and Spin Hall magnetoresistance

SHE is a phenomena that results from spin-orbit interaction and links the orbital motion to spin direction acting as a spin dependent magnetic field. When an electric current flows through a material, it can give rise to a transverse spin current thus producing spin accumulation at opposite boundaries of the sample [62]. The direction of the spins at two boundaries is opposite to each other as shown in Fig. 2.5 (a). The reciprocal process is called the inverse spin Hall effect in which a transverse charge current is produced due to pure spin current [63] and is shown in Fig. 2.5 (b). The origin of SHE can be attributed to a number of spin-orbit mechanisms which can have different origins namely intrinsic or extrinsic, depend on the sample geometry, impurity band structure and also on carrier density without requirement of any external magnetic field or magnetic order. In the intrinsic SHE, the mechanism depends only on the electronic structure of the material with scattering playing a minor role. For an applied electric field in the x-direction, the electrons with momentum along $\pm y$ axis experience a torque causing their spins to tilt along the z-axis due to Rashba SOC. This generates a pure spin current in the y-axis [64].

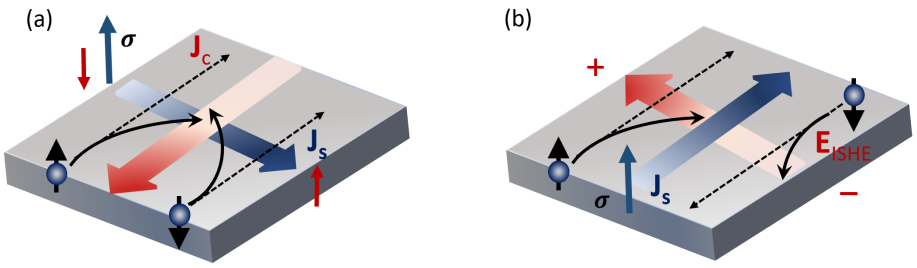

Figure 2.5: A schematic illustration of (a) direct spin-Hall effect and (b) inverse spin-Hall effect. Here, J_c, J_s, r and E_{ISHE} refer to the charge current, the spatial direction of a spin current, the spin-polarization vector of the spin current and electromotive force due to inverse spin Hall effect respectively. Fig. adapted from [63].

The extrinsic effects are due to skew-scattering and side-jump scattering. Skew-scattering is caused by the asymmetrical scattering of the electrons in presence of impurity due to spin-orbit interaction. This causes a conductivity perpendicular to the electron movement and depends on difference in SOC of impurity and conducting material [60]. In side-jump scattering a spin dependent displacement occurs due to SOC because of acceleration and deceleration of electrons [60]. The SHE is quantified by the spin Hall angle, θ_{SH} which is a measure of conversion efficiency between charge and spin currents and is given as:

$$\theta_{SH} = \frac{J_S}{J_c} \tag{2.18}$$

where, J_c and $(\hbar/2e)J_S$ are the charge and spin current densities respectively. The θ_{SH} is positive for (Pt, Au and Ag) and negative for (Ta, W, Mo). Thus its sign is material dependent.

Spin Hall magnetoresistance (SMR) has been observed in bilayer structures of YIG/Pt [66, 67, 68] and in some other bilayer systems [69, 70]. Spin currents flowing in the non-magnetic materials can give rise to SMR at the interface of ferromagnet/non-magnet (FM/NM). As mentioned in the previous section, due to SHE spin current are generated when a charge current flows through a magnetic conductor, giving rise to spin accumulation on opposite sides. Due to an imbalance in spin resolved electrochemical potential a diffusive current, J_s^{diff} is generated that

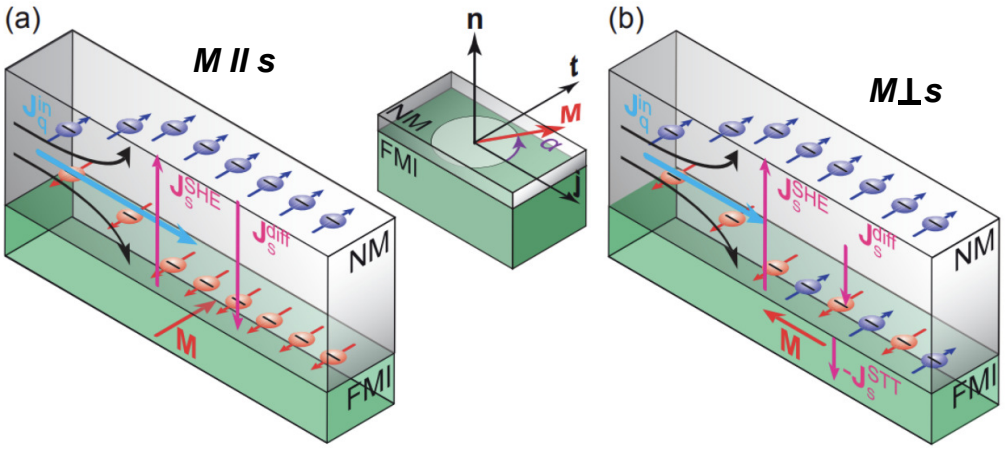

Figure 2.6: A schematic illustration of SMR in a non-magnet/ferromagnetic insulator (NM-FMI) interface. A charge current J_Q gives rise to spin current J_s^{SHE} due to SHE which is counteracted by a diffusive current J_s^{diff}. When the magnetization $M \| s$ no spin current can enter the FMI as shown in (a) but for $M \perp s$ a part of spin current, J_s^{STT}, can enter the ferromagnetic layer causing a reduction of J_s^{diff} and leading to a spin current remaining in the non magnetic layer which then increases the longitudinal resistivity. Fig. adapted from [65].

counteracts the initial spin current, J_s^{SHE} [65].

At equilibrium both currents are balanced as:

$$J_s^{diff} = -J_s^{SHE} \tag{2.19}$$

However, when a non magnetic layer is in contact with the FM layer, the spin accumulation at interface can enter the FM layer as pure spin current, J_s^{STT}, which decreases the J_s^{diff}. The spin absorption in FM layer occurs due to spin-transfer torque (STT) effect which is proportional to $M \times s$ and thus is dependent on the angle between M and spin polarisation, s. Two cases for $M \| s$ and $M \perp s$ can be considered as shown in Fig. 2.6 (a) and (b) respectively. For $M \| s$ STT vanishes and thus no spin current can enter the FM causing no change in resistance of the sample but for $M \perp s$ a part of spin current J_s^{STT} is absorbed by the ferromagnetic layer causing an unbalance between J_s^{SHE} and J_s^{diff} thus leading to a transverse spin current, with a finite diffusion length, remaining in the non-magnetic layer which then contributes to the longitudinal resistivity, ρ_{long} [71]. This change in resistivity

is angle dependent and is known as SMR given by [72]:

$$\rho_{\text{long}} = \rho_0 + \rho_1 \cdot (1 - m_{\text{t}}^2)$$
$$\rho_{\text{trans}} = \rho_1 m_{\text{j}}\text{t} + \rho_2 m_{\text{n}} \tag{2.20}$$

where, $m_{\text{t}}, m_{\text{n}}$ and m_{j} are the projections of magnetization on t, n, j respectively (the directions t, n, j are shown in Fig. 2.6) and ρ_{i} are the resistivity parameters.

2.4 Magnetization Dynamics

The magnetization dynamics is different from static phenomena based on the time scale on which the magnetic system is disturbed by an external stimulus and the timescale in which one observes its response. The dynamic processes occur on nanosecond timescale or faster compared to static phenomena which are usually in millisecond time range. The magnetization configuration in a magnetic system are resonantly disturbed from their equilibrium position by applying alternating magnetic fields at resonant frequency of the system compared to applying quasi static fields where the magnetization appears to be always in equilibrium since the dynamic processes happen in nanosecond regime. The underlying concepts and theoretical description of dynamic response are explained further.

2.4.1 Landau-Lifshitz and Gilbert Equation

The Landau-Lifshitz (LL) and Gilbert equation describes the dynamics of an isolated spin magnetic moment, $\boldsymbol{\mu}$, around an effective field, $\mu_0 \mathbf{H}_{\text{eff}}$ [73].

If $\mathbf{H}_{\text{ext}}$ acts on $\boldsymbol{\mu}$, the equilibrium state of the magnetic moment is affected. This results in a torque between the net external field and the magnetization. Classically, a magnetic moment in an effective field will be exposed to a torque given by:

$$\boldsymbol{\tau} = \boldsymbol{\mu} \times \mu_0 \mathbf{H}_{\text{eff}} \tag{2.21}$$

In this equation $\mu_0 \mathbf{H}_{\text{eff}}$ is the sum of all internal fields, some of which are discussed

above in the Eq. 2.4, as well as the static and dynamic external fields.

$$\mu_0 \mathbf{H}_{\text{eff}} = \mu_0(\mathbf{H}_{\text{ex}} + \mathbf{H}_{\text{anis}} + \mathbf{H}_{\text{demag}} + \mathbf{H}_{\text{ext}} + \mathbf{h}_{\text{rf}}(t) + ... \ ), \tag{2.22}$$

where $\mu_0 \mathbf{H}_{\text{ex}}$ and $\mu_0 \mathbf{H}_{\text{anis}}$ are the exchange field and the anisotropy field, and $\mu_0 \mathbf{H}_{\text{demag}}$ denotes the demagnetising field. Two important components are $\mu_0 \mathbf{H}_{\text{ext}}$ and the dynamic external field $\mu_0 \mathbf{h}_{\text{rf}}(t)$.
In terms of $\mathbf{L}$, we can express $\boldsymbol{\mu}$ by the Eq. 2.3. Due to the interaction of the magnetic moment with the magnetic field, a torque acts on the system and changes the angular momentum of the system (according to Newton's classical equation). Using the definition of the torque as $\boldsymbol{\tau} = d\mathbf{L}/dt$, Eq. 2.21 can be expressed as:

$$\frac{d\mathbf{L}}{dt} = -\frac{1}{\gamma}\frac{d\boldsymbol{\mu}}{dt} = \boldsymbol{\mu} \times \mathbf{H}_{\text{eff}} \tag{2.23}$$

Expressing the magnetization in terms of macroscopic approach as $\mathbf{M} = \boldsymbol{\mu}/V$, where V is the total volume, the Eq. 2.23 results in the LL equation [74]:

$$\frac{d\mathbf{M}}{dt} = -\gamma(\mathbf{M} \times \mathbf{H}_{\text{eff}}) \ , \tag{2.24}$$

which describes the precessional motion of $\mathbf{M}$ around $\mathbf{H}_{\text{eff}}$ (see Fig. 2.7 (a)).

The LL equation describes the motion of a magnetic moment without damping. For a system without damping the magnetization precesses with a constant angle between the direction of magnetization and the applied field. But in reality like many other physical systems, the precession is damped. By introducing damping, the magnetization spirals down and aligns with external field with a time dependence of $\boldsymbol{\tau}$=1/$\boldsymbol{\alpha}$, with α, the Gilbert damping constant. Various damping mechanisms are explained in further section.

In 1955, Gilbert [75] suggested a way to consider the damping for the equation of motion by adding a phenomenological viscous damping term to the LL equation, which has a vector component along the radial direction of the precession. This equation was referred to as the Landau-Lifshitz and Gilbert equation (LLG equa-

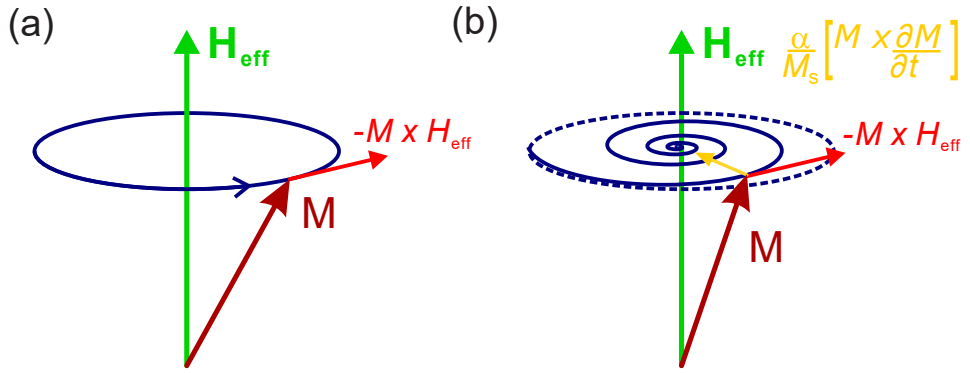

Figure 2.7: Schematic of magnetization dynamics. (**a**) The magnetization vector, **M** (brown) associated with total angular momentum, **L**, precesses counter-clockwise around the effective field $\mathbf{H}_{\text{eff}}$ (green) following the LL equation (i.e. no damping in the system, blue trace) described by Eq. 2.24. (**b**), On introducing damping, the magnetization follows a helical trajectory back to its equilibrium position, described in the LLG equation (Eq. 2.25) towards the direction of $\mathbf{H}_{\text{eff}}$.

tion) which consists of a precessional and a damping term expressed as:

$$\frac{d\mathbf{M}}{dt} = -\gamma(\mathbf{M} \times \mathbf{H}_{\text{eff}}) + \frac{\alpha}{M_S}(\mathbf{M} \times \frac{d\mathbf{M}}{dt}) \ , \tag{2.25}$$

where α is a material specific parameter of magnetic solids, which is a measure of the overall different viscous physical processes. The first term on the right-hand side of the above equation is the torque which describes the Larmor-precession of the magnetization in an elliptical orbit around $\mathbf{H}_{\text{eff}}$, while the second term is the Gilbert damping term which tilts **M** towards $\mathbf{H}_{\text{eff}}$ and produces gradual alignment of the two. As a result of the damping term, the motion of magnetization follows a helical trajectory as shown in Fig. 2.7 (b). The damping term is phenomenological which implies that the macroscopic origin of the magnetic damping is still not completely understood in detail and constitutes a very active area of research [76]. Possible relaxation mechanisms can be divided into intrinsic and extrinsic processes and are explained further.

2.4.2 Ferromagnetic Resonance

As introduced in the previous sections, a torque is exerted on the magnetization when subjected to an external magnetic field thereby causing a precessional mo-

tion of the magnetization. Several parameters affect the precessional frequency such as the shape of the ferromagnet, strength and direction of $\mathbf{H}_{\text{ext}}$ as well as $\mathbf{M}$. Application of microwave magnetic field at a frequency similar to the resonant frequency induces a precessional motion of the magnetization where all the magnetic moments oscillate in phase. This is the phenomenon of FMR, used to probe the magnetic properties of magnetic materials, where the ferromagnet shows a resonant absorption of the electromagnetic energy [77, 55].

FMR can be measured using two different techniques: the time-domain and the frequency-domain measurements. In case of time domain measurements, a rectangular pulse is applied to the saturated sample [2]. By measuring the precession of magnetization, the Larmour frequency can be obtained and the decay in time allows the determination of damping. In case of frequency-domain measurements, a fixed frequency is applied while sweeping the magnetic field. The absorption of the alternating signal is measured over the applied field allowing the effective resonance field to be measured. The linewidth of the absorption is a measure of the damping. Thus both the static and dynamic properties of a magnetic system can be obtained from the FMR spectra. From the resonance field in the spectra we can obtain information about the magnetic properties such as the *g*-factor, saturation magnetization and magnetic anisotropies in the system, and from the FMR linewidth, the magnetic inhomogeneity and the damping parameter for the magnetization precession can be obtained.

2.4.3 Resonance condition

The derivation for resonance condition is obtained by solving the complete FMR theory and considering the dynamical effects of exchange interactions and the conductivity along with the surface anisotropy. The coordinate system used for derivation is defined as in Fig. 2.8. For NiMnSb sample as discussed in details in Chapter. 4, it is sufficient to define the angle with respect to a crystal axis. The global coordinate system used is such that the axes (x, y, z) are aligned with the crystallo-

[2] "saturated" here describes the condition of all magnetic moments of a magnetic material being aligned parallel to the external magnetic field

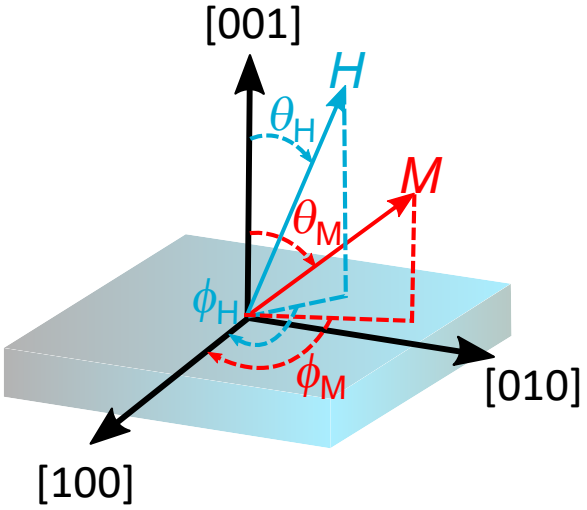

Figure 2.8: The coordinate system for a thin film which lies in the xy-plane and the magnetization **M** of the film points in the direction of vector $\vec{M}$. The applied DC magnetic field points in the direction of vector $\vec{H}$.

graphic axes [100], [010] and [001] respectively. The angles $\theta_{H/M}$ and $\phi_{H/M}$ are the polar and azimuthal angles of **H** and **M** with respect to the z- and x-axis, respectively. Using the macrospin model, the total magnetic moment can be considered as one large macrospin, **M**, which precesses around the local static field, **H**, at the Larmor frequency, $\omega_L = \gamma \mathbf{H}$. Here, we use the free energy approach developed by Smit-Beljars [78] in order to derive the resonance condition. The precession of total magnetic moment with free energy, **F**, occurs at the resonance frequency, $f=\omega/2\pi$, given by Smit-Beljars-Suhl equation [78, 79]:

$$\left(\frac{\omega}{\gamma}\right)^2 = \frac{1}{M_s \sin(\theta_M)}\left[\frac{\partial^2 F}{\partial \theta_M^2}\frac{\partial^2 F}{\partial \phi_M^2} - \left(\frac{\partial^2 F}{\partial \theta_M \partial \phi_M}\right)\right] \tag{2.26}$$

For the case of a thin film like NiMnSb under tetragonal distortion the free energy density, F, is given by [55]:

$$\begin{aligned} F = &-MH[\cos\theta_M \cos\theta_H + \sin\theta_M \sin\theta_H \cos(\phi_M - \phi_H)] - 2\pi M^2 \sin^2\theta_M \\ &- K_{2\perp}\cos^2\theta_M - \frac{1}{2}K_{4\perp}\cos^4\theta_M - \frac{1}{2}K_{4\parallel}\frac{1}{4}(3+\cos 4\phi_M)\sin^4\theta_M \\ &- K_{2\parallel}\sin^2\theta_M \sin^2\left(\phi_M - \frac{\pi}{4}\right) \end{aligned} \tag{2.27}$$

The first term in the equation above is the Zeeman energy, the second term is the demagnetization energy (shape anisotropy), $K_{2\perp}$ and $K_{4\perp}$ are the constants representing the out-of-plane uniaxial and cubic anisotropy, respectively, and the in-plane anisotropy constants are given by the in-plane uniaxial term, $K_{2\parallel}$ and an in-plane cubic term, $K_{4\parallel}$. The in-plane uniaxial anisotropy term reflects that the [110] and [1$\bar{1}$0] directions are not equivalent in NiMnSb [80].

The resonance condition for any different field orientation can be obtained from Eq. 2.26 by minimizing **F**, with respect to θ_M and ϕ_M [55]. Doing this for two geometries and using the coordinates defined above for ϕ_H=45° (**H** and **M** perpendicular to film plane), one finds:

$$\left(\frac{\omega}{\gamma}\right)^2 = \left[H_R\cos(\theta_H-\theta_M)+\left(-4\pi M+\frac{2K_{2\perp}}{M}+\frac{K_{4\perp}}{M}-\frac{K_{4\parallel}}{2M}\right)\cos 2\theta_M + \left(\frac{K_{4\perp}}{M}+\frac{K_{4\parallel}}{2M}\right)\cos 4\theta_M\right]\times\left[H_R\cos(\theta_H-\theta_M)+\left(-4\pi M+\frac{2K_{2\perp}}{M} + \frac{K_{4\parallel}}{M}\right)\cos^2\theta_M+\left(\frac{2K_{4\perp}}{M}\frac{K_{4\parallel}}{2M}\right)\cos 4\theta_M-\frac{2K_{4\parallel}}{M}-\frac{2K_{2\parallel}}{M}\right] \tag{2.28}$$

and for θ_M=θ_H=90°(**H** and **M** parallel to film plane) one obtains:

$$\left(\frac{\omega}{\gamma}\right)^2 = \left[H_R\cos(\phi_M-\phi_H)+\frac{2K_{4\parallel}}{M}\cos 4\phi_M-\frac{2K_{2\parallel}}{M}\cos\left(2\phi_M-\frac{\pi}{2}\right)\right] \times\left[H_R\cos(\phi_M-\phi_H)+4\pi M-\frac{2K_{2\perp}}{M}+\frac{K_{4\parallel}}{2M}(3+\cos 4\phi_M) + \frac{2K_{2\parallel}}{M}\sin^2\left(\phi_M-\frac{\pi}{4}\right)\right] \tag{2.29}$$

On resonance, the values for θ_M and ϕ_M can be determined by the condition $\partial F/\partial\theta_M = 0$ and $\partial F/\partial\phi_M = 0$; θ_M is then given by:

$$\sin(2\theta_M) = \frac{2H_R}{4\pi M_s - H_\perp}\sin(\theta_M-\theta_H) \tag{2.30}$$

where $H_\perp = 2K/M_s$ is the out-of-plane anisotropy field and ϕ_M can be obtained by solving:

$$H_R \sin(\phi_M - \phi_H) + (H_B/4)\sin 4\phi_M + (H_U/2)\cos 2\phi_M = 0 \qquad (2.31)$$

where, $H_U = 2K_{2\parallel}/M_s$ and $H_B = 2K_{4\parallel}/M_s$ are the in-plane anisotropy fields. The resonance condition for the in-plane and out-of-plane configurations can then be simplified by setting $\theta_M = \theta_H$ in Eq. 2.28 and $\phi_M = \phi_H$ and the following expressions come out for the two cases:

$$\omega = \gamma(H_R - 4\pi M_{eff}) \qquad out-of-plane \qquad (2.32)$$

$$\omega = \gamma\sqrt{H_R(H_R + 4\pi M_{eff})} \qquad in-plane \qquad (2.33)$$

where $M_{eff} = M_s - 2K_{2\perp}/M_s$. The measured linewidth, ΔH, from the resonance absorption peak in the FMR spectra consist of two contributions, extrinsic contribution and intrinsic contribution, where the intrinsic contribution is proportional to α [75] and different contributions are explained in following section.

2.5 Relaxation Mechanisms

The magnetic relaxation can be described by the LLG equation of motion as given in Eq. 2.25. In an FMR experiment, in the presence of uniform microwave field, all the spins rotate in phase (wave vector $\vec{k} = 0$) which is the condition for uniform precession. When the uniform mode decays, it dissipates energy into the lattice and also to other spin-wave ($\vec{k} \neq 0$) modes (thus conserving the energy within the spin system), which then ultimately decays by dissipating energy to the lattice. The energy dissipation to the lattice is direct and irreversible and described as viscous damping. Fig. 2.9 shows the different processes during magnetization relaxation dynamics. The viscous damping is represented by path (1) and path (2) shows a decay into non-uniform spin-waves ($\vec{k} \neq 0$), which then decay to the lattice via path (3). Path (2) is an intermediary path showing dissipation of uniform precession to the lattice through a reversible state.

This reversible state may include high energy magnons or Stoner excitation (more details shown in Fig. 2.12)

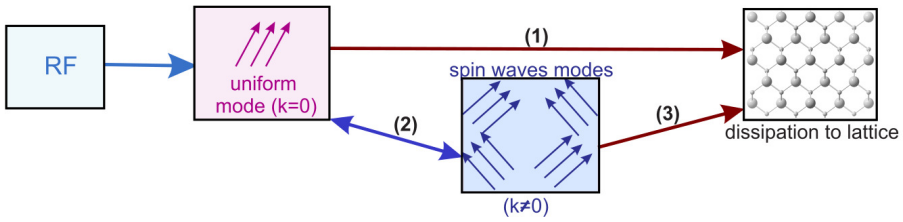

Figure 2.9: Schematic representation of different possible paths of the relaxation of precessional motion of magnetization. Fig. adapted from [81].

The above mentioned process can be explained by using the description given by Bloch-Bloembergen [82, 83, 81]:

$$\frac{1}{\gamma}\frac{d\vec{M}}{dt} = -\left[\vec{M}\times\vec{H}_{\text{eff}}\right] - \frac{M_{\text{x}}}{\gamma T_2}\hat{i} - \frac{M_{\text{y}}}{\gamma T_2}\hat{j} - \left[\frac{M_{\text{z}}-M_{\text{s}}}{\gamma T_1}\right]\hat{k}\ , \tag{2.34}$$

In Eq. 2.34, T_1 is the longitudinal relaxation rate which describes the direct dissipation to the lattice and T_2 is the transverse relaxation rate which represents the energy scattered into the transverse components of magnetization. Fig. 2.10 shows the two types of damping mechanisms. In case of damping following LLG equation (as shown in Fig. 2.10 (a)) , the length of $\vec{M}$ stays constant while it spirals around the magnetic field, but the z-component, M_z, increases. Whereas, in the case of damping following Bloch-Bloembergen mechanism the z-component stays constant for the case $T_1 \gg T_2$ due to the energy being scattered into the transverse component of magnetization (Fig. 2.10 (b)). The two different mechanisms which lead to the relaxation as shown in path (1) and (2) (Fig. 2.10) are described below.

2.5.1 Gilbert mechanism

Using Eq. 2.26, the intrinsic part of the FMR linewidth can be derived as [84]:

$$\begin{aligned}\Delta\omega &= \frac{\gamma\alpha}{M}\left[\frac{\partial^2 F}{\partial\theta_{\text{M}}^2} + \frac{1}{\sin^2\theta_{\text{M}}}\frac{\partial^2 F}{\partial\phi_{\text{M}}^2}\right];\\ \Delta H_{\text{HWHM}} &= \frac{dH}{d\omega}\Delta\omega\end{aligned} \tag{2.35}$$

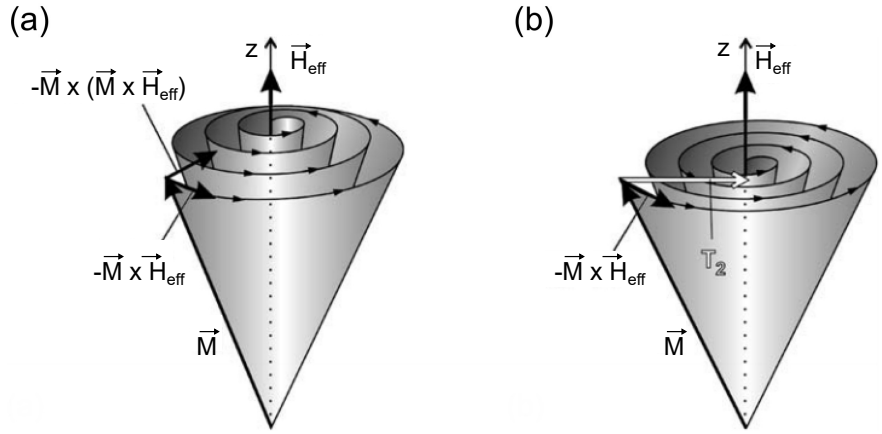

Figure 2.10: Schematic illustration of two damping mechanisms in ferromagnets (**a**) LLG and (**b**) Bloch-Bloembergen damping. Fig. adapted from [81].

Using the above Eq. 2.35 and assuming that magnetization is uniform across the sample, FMR linewidth can be expressed as [84]:

$$\Delta B_{\mathrm{HWHM}} \approx \frac{\alpha}{\gamma} \frac{\omega}{\cos\beta} \tag{2.36}$$

where β is angle between $\vec{M}$ and field, $\vec{B}$ and $\Delta \mathrm{B}_{\mathrm{HWHM}}$ is the half width at half maximum of the FMR absorption spectra expressed in Tesla. The origin of Gilbert damping can be explained in terms of spin dependent scattering. The section below describes the mechanism of spin-lattice dissipation in metallic ferromagnets originating from spin-orbit relaxation.

Spin-orbit relaxation

In 1967 Heinrich et al. [85] proposed a model for spin relaxation based on s-d exchange interaction. According to this model, two groups of electrons are considered, one that are mostly localized (denoted as d-electrons) and the second are itinerant electrons (here denoted as s-electrons). The interaction of the itinerant electrons and the localized d-spins can be obtained by integrating the s-d exchange energy density function. Due to s-d exchange interaction, the magnons and itinerant electrons are coherently scattered resulting in an electron-hole annihilation pair. It is then subsequently relaxed by spin-dependent scattering processes which transfer

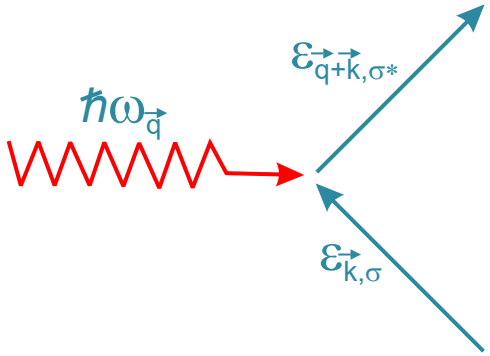

Figure 2.11: Schematic showing the spin flip scattering process. Here, $\vec{q}(\vec{k})$ denotes the magnon (electron) wave vector, σ and σ^* represent the spin-states.

angular momentum to lattice. Another model was proposed by Kambersky [86] who described that both ordinary and spin flip scattering processes dominate the Gilbert damping factor, α. These two processes depend on density of states and electron scattering time and affect the magnetization relaxation [86].

2.5.2 Two-magnon scattering mechanism

Apart from the Gilbert mechanism, another relaxation process that contributes to the damping is the two-magnon scattering. Path (2) as shown in Fig. 2.9 depicts the two-magnon scattering where the uniform mode is scattered to non-uniform mode ($\vec{k} \neq 0$) which then subsequently dissipates to the lattice. This is an extrinsic contribution to the damping and causes linewidth broadening of FMR spectra at resonance. Fig. 2.12, shows bulk spin wave-dispersion relation for different orientations of magnetic field. As the magnetic field orientation is changed from the perpendicular to parallel configuration with respect to the sample plane, a shift of band occurs. In perpendicular configuration no degenerate k spin states are available and the bottom of the spin-wave band at k = 0 coincides with the FMR frequency. When the magnetic field is applied in the sample plane referred to as parallel configuration, the band drops down and the the top of spin wave band at k = 0 equals the FMR frequency. This gives rise to an extended range of wave numbers degenerate with the uniform mode. The two magnon scattering mechanism has been described theoretically by Arias and Mills [87] based on linear response theory and experimentally

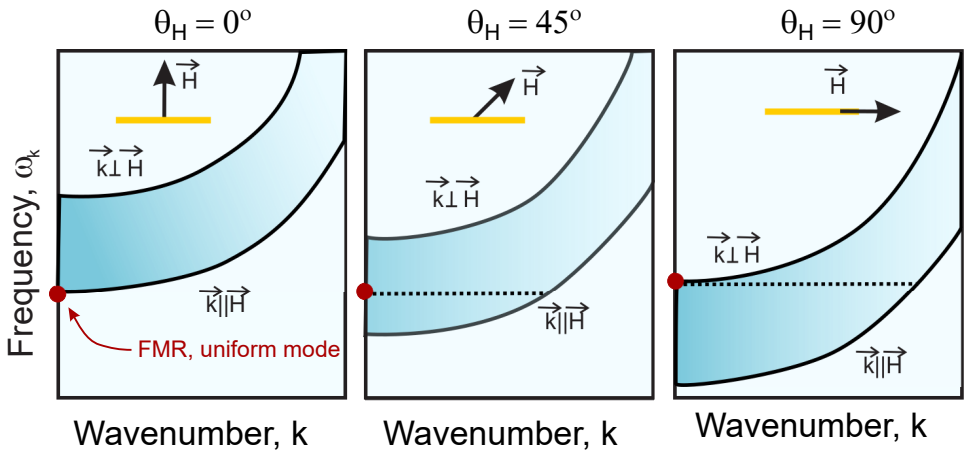

Figure 2.12: Schematic illustration of the spin-wave dispersion curve for different orientations of the applied magnetic field.

confirmed by several groups [88, 89]. When scattering centres are not isotropic in sample, an angle dependent two-magnon scattering can occur which switches off at a critical out-of-plane angle of magnetization. As shown in Fig. 2.12, when the magnetic field is applied obliquely with respect to the sample plane, finite wave vector modes are degenerate with the FMR mode for $|\theta_{eq}| > |\theta_c| = 45^{\circ}$. Thus the two-magnon scattering should operate for this regime. But when $|\theta_{eq}| < |\theta_c| = 45^{\circ}$, it should shut off since states degenerate to uniform mode are no longer available. It has been shown that the angle dependence of two magnon can be approximated by a step function and will be detailed in the following sections [87].

2.5.3 Ferromagnetic Resonance Linewidth Contributions

There are at least four contributions to the FMR linewidth [10]:

$$\Delta H(\omega, \psi_H) = \Delta H^{\text{Gilbert}}(\omega, \psi_H) + \Delta H^{\text{mosaic}}(\omega, \psi_H) + \Delta H^{\text{2mag}}(\omega, \psi_H) + \Delta H^{\text{inhom}} \tag{2.37}$$

where, ΔH denotes the peak-to-peak linewidth of the FMR signal. ψ_{H} denotes the two angles θ_H and ϕ_H, as defined in Fig. 2.8. The four different contributions to the FMR linewidth as given in Eq. 2.37 are described below:

The Gilbert contribution ($\Delta H^{\text{Gilbert}}$)

The phenomenological Gilbert damping parameter $\boldsymbol{\alpha}$ is used to describe damping in various magnetic systems. The Gilbert damping represents the intrinsic damping

and from Eq. 2.36 it follows that the FMR linewidth depends linearly on the microwave frequency [20]. By doing FMR measurements over a range of frequencies and plotting the FMR linewidth as a function of resonance frequency, $\boldsymbol{\alpha}$ can be extracted from the slope of the curve. However, the linear frequency dependence of FMR linewidth is valid only when magnetization and external field are parallel to each other. Otherwise the field-dragging contribution has to be included. When the FMR measurements are done by sweeping frequency, the linewidth is expressed in terms of frequency. The frequency swept linewidth can be converted to field-swept linewidth as:

$$\begin{aligned}\Delta H(\omega,\psi_{\mathrm{H}}) =& \gamma\frac{\partial H_{\mathrm{R}}(\omega,\psi_{\mathrm{H}}\equiv constant)}{\omega}.\Delta\left(\frac{\omega}{\gamma}\right)+ \\ & \gamma\frac{\partial H_{\mathrm{R}}(\omega\equiv constant,\psi_{\mathrm{H}})}{\psi_{\mathrm{H}}}.\frac{d\psi_{\mathrm{H}}}{d\omega}.\Delta\left(\frac{\omega}{\gamma}\right)\end{aligned} \tag{2.38}$$

where ψ_{H} denotes the two angles ϕ_{H} and θ_{H}. The second term in Eq. 2.38 represents the field-dragging contribution. It can be seen that the partial derivative gets large at angles for which $\mathbf{M}$ is dragged behind $\mathbf{B}=\mu_0\mathbf{H}$ due to magnetic anisotropy effects. $\mathbf{M}$ and $\mu_0\mathbf{H}$ are parallel along the hard and easy axes of magnetization which means that the dragging contribution vanishes for these angles. For this case the Gilbert damping contribution in Eq. 2.38 can be simplified as:

$$\Delta H^{\mathrm{Gilbert}}(\omega,\psi_{\mathrm{H}}\equiv\beta)\approx\frac{2}{\sqrt{3}}\frac{\alpha}{\gamma}\frac{\omega}{\cos\beta} \tag{2.39}$$

where β is the angle between $\mathbf{M}$ and external field, $\mu_0\mathbf{H}$. The factor of $\sqrt{3}$ accounts for the case when FMR lineshape is antisymmetric due to field modulation.

Mosaicity Broadening contribution ($\Delta H^{\mathbf{mosaic}}$)

The second term in Eq. 2.37 is called the mosaicity term and is caused by a small spread of sample parameters on a very large scale. This variation can be found in the internal fields, thickness or orientation of crystallites within the sample. Because of such variations the individual regions will have slightly different resonance fields and the overall signal will be superposition of these local FMR lines causing a broader linewidth. Such fluctuations of the directions of the anisotropy fields is

accounted by including the mosaicity contribution term given as [90]:

$$\Delta H^{\text{Gilbert}}(\omega, \psi_{\text{H}}) = \frac{\partial H_{\text{R}}(\omega, \psi_{\text{H}})}{\partial \phi_{\text{H}}} \Delta\phi_{\text{H}} + \frac{\partial H_{\text{R}}(\omega, \theta_{\text{H}})}{\partial \phi_{\text{H}}} \Delta\theta_{\text{H}} \tag{2.40}$$

where $\Delta\phi_{\text{H}}$ and $\Delta\theta_{\text{H}}$ represent the average spread of the direction of the easy and hard axes in the film plane and normal to film respectively. For measurements along easy and hard axes the partial derivatives are zero and so the mosaicity contribution vanishes.

Two-magnon scattering contribution (ΔH^{2mag})

As detailed in the previous section, the two magnon-scattering occurs when wave $k = 0$ magnons excited by FMR, scatters into degenerate states states of magnons having vectors $k \neq 0$. This process requires the presence of states degenerate to uniform mode and that there are scattering centres in the sample. If the long wavelength spin-waves are involved in the relaxation process, the defects of the order of several 100 nm rather than atomistic defects act as scattering centres.

The linewidth, ΔH^{2mag}, caused due to two magnon-scattering mechanism is a measure of the scattering rate of the uniform mode (k = 0) magnons into other spin-wave modes (k$\neq$ 0). For a homogeneously magnetised thin film, ΔH^{2mag} can be expressed as [10]:

$$\begin{aligned} \Delta H^{\text{2mag}}(\omega, \psi_{\text{H}}) \propto & \sum_{\langle x_i \rangle} \Gamma_{\langle x_i \rangle} f(\phi_{\text{H}} - \phi\langle x_i \rangle) \\ & \times \arcsin\left(\sqrt{\frac{\sqrt{\omega^2 + (\omega_0/2)^2} - \omega_0/2}{\sqrt{\omega^2 + (\omega_0/2)^2} + \omega_0/2}} \right) U(\theta_{\text{eq}} - \theta_{\text{c}}) \end{aligned} \tag{2.41}$$

with $\gamma\mu_0 M_{\text{eff}} = \gamma(\mu M_{\text{s}} - 2K_{2\perp}/M)$ and $\mu_0 M_{\text{eff}}$ being the effective magnetization that consists of saturation magnetization $\mu_0 M_{\text{s}}$ and the intrinsic out-of-plane anisotropy fields, $2K_{2\perp}/M$. $\mu_0 M_{\text{eff}}$ can be determined from the angle- dependent FMR resonance field. The factor, $\Gamma_{\langle x_i \rangle}$, denotes the strength of two-magnon scattering along the principle in-plane crystallographic direction $\langle x_i \rangle$. The $f(\phi_{\text{H}} - \phi\langle x_i \rangle)$ term shows that the two magnon contribution depends on the in-plane direction of μ_0H relative to the principal in-plane crystallographic directions $\langle x_i \rangle$ given by the angles $\phi_{\langle x_i \rangle}$.

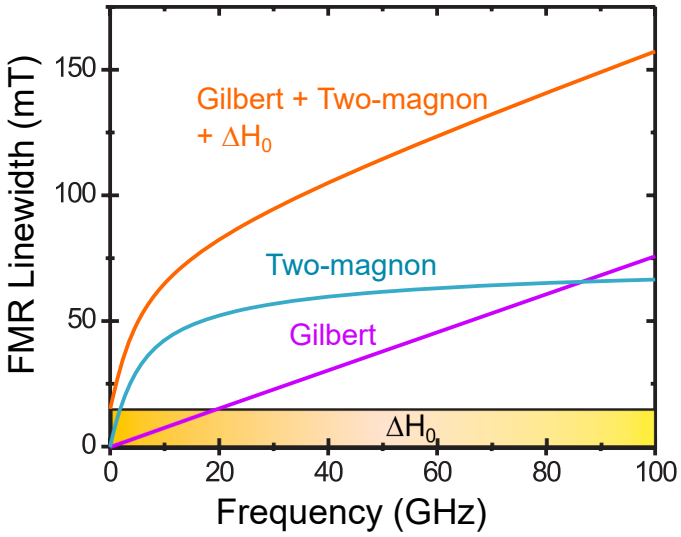

Figure 2.13: Schematic representation of the frequency dependence of the FMR linewidth for a thin film with in-plane magnetization showing different contributions. ΔH_0 represents frequency independent linewidth. Fig. adapted from [10].

For the case, when different contributions of two magnon- scattering along the principal crystallographic directions $\langle x_i \rangle$ occur, one has to sum up these contributions weighted by their angular dependence given by f. To describe the two-magnon process a step function is used given by $U(\theta_{eq} - \theta_c)$ as in Eq. 2.41. Its value is equal to 1 for $\theta_{eq} > \theta_c$ and zero for $\theta_{eq} < \theta_c$. This signifies the 'switching off' of the two-magnon scattering at a critical out-of-plane angle of magnetization. The different contributions to linewidth are shown schematically in Fig. 2.13.

2.6 Spin wave resonance

In previous sections FMR was described for uniform precession mode using LLG equation of motion for uniformly magnetized sample where all the magnetic moments are collinear and precess in-phase throughout the entire sample. However, in the presence of the dipole-dipole or exchange interaction, when the magnetic moments are excited locally, the precessional motion can propagate spatially like a wave known as the spin wave [91, 92]. The higher order resonance modes are excited because of the generation of spin waves which are shown in Fig. 2.14. Spin waves can be excited either by an inhomogeneous RF field or by non-uniformity of magnetic parameters across the thickness of the sample giving rise to lower sym-

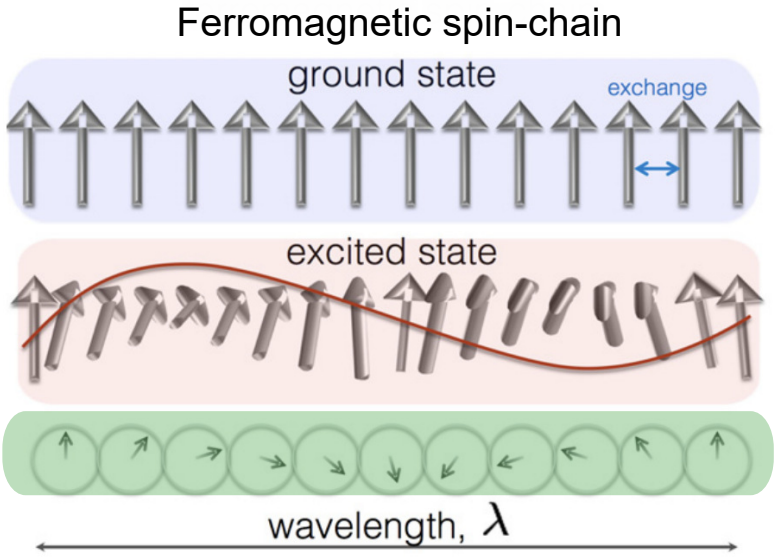

Figure 2.14: Ferromagnetic spin chain in ground state and excited state. The spin-flip is smeared over the whole system creating a spin wave with wavelength λ. Fig. adapted from [93].

.

metry of spins at surface compared to the bulk [91, 92]. The spin waves can be classified depending on the type of interactions which is dipole-dipole or exchange interaction. For the short wavelengths (for larger wavenumber k) the exchange interactions are dominant and the dispersion relation shows a quadratic behaviour, $\omega_{\mathrm{n,ex}} = \omega_{\mathrm{m}}\lambda_{\mathrm{ex}}k_{\mathrm{tot}}^2$ where $\omega_{\mathrm{n(m)}} = \gamma\mu_0 H(M)$ respectively. In contrast, the dipole interactions is dominant for long wavelength (smaller $k = 2\pi/\lambda < 10^6 m^{-1}$) [94]. The long wavelength spin waves are called the magnetostatic spin waves (MSWs).

2.6.1 Magnetostatic spin waves

The first observation of MSWs was done by White and Solt [95] in 1956 and theoretical explanation was given by Walker in 1958 [96] and Damon and Eshbach in 1962 [97]. Depending on direction of wavevector and static magnetization, the three types of MSWs can be obtained (shown in Fig. 2.15) as described below:

Magnetostatic Surface spin wave (MSSW)

This is also known as the Damon-Eshbach mode and corresponds to the geometry in which both the static magnetization and the wavevector (propagation direction)

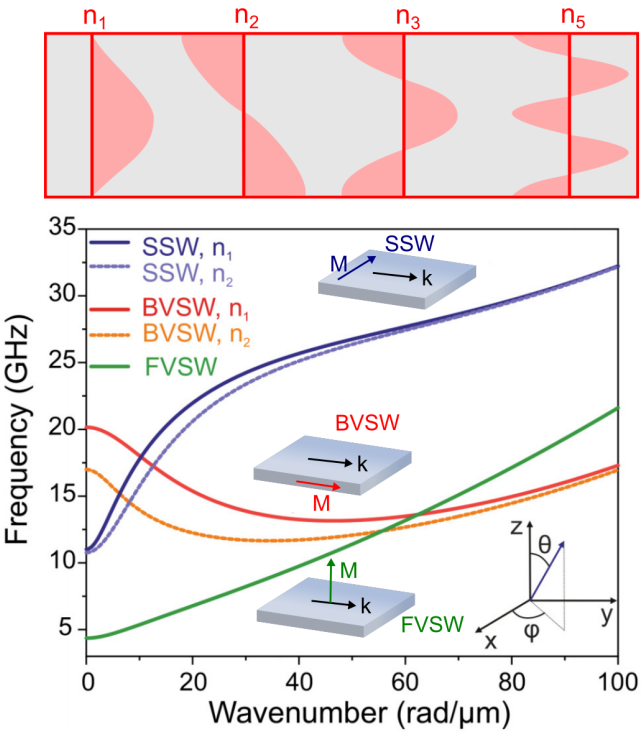

Figure 2.15: Dispersion relation for backward volume spin wave (BVSW), surface spin wave (SSW) and forward volume spin wave (FVSW) calculated for 100 mT external magnetic field in a CoFeB waveguide with thickness 30 nm. Two laterally confined modes are shown for BVSW and SSW. Different mode profiles for the modes are shown in the top panel. Fig. adapted from [99].

are in the sample plane and perpendicular to each other. On neglecting the in-plane anisotropy the dispersion relation for a film with thickness t_{film} is given as [98]:

$$\left(\frac{2\pi f}{\mu_0\gamma}\right)^2 = H_{\text{R}}\left(H_{\text{R}} + M_{\text{eff}}\right) + \frac{M_{\text{eff}}^2}{4}\left(1 - e^{-2\text{kt}_{\text{film}}}\right) \tag{2.42}$$

Magnetostatic Backward Volume spin wave (MBVSW)

This mode is observed when the static magnetization is parallel to the propagation direction and lie in the plane along the waveguide. For this mode the group velocity is negative and points in the opposite direction to the positive phase velocity. The mode is uniform over the entire sample volume and its dispersion relation is described as [100]:

$$\left(\frac{2\pi f}{\mu_0\gamma}\right)^2 = H_{\text{R}}\left[H_{\text{R}} + M_{\text{eff}}\left(\frac{1 - e^{-\text{kt}_{\text{fim}}}}{kt_{\text{film}}}\right)\right] \tag{2.43}$$

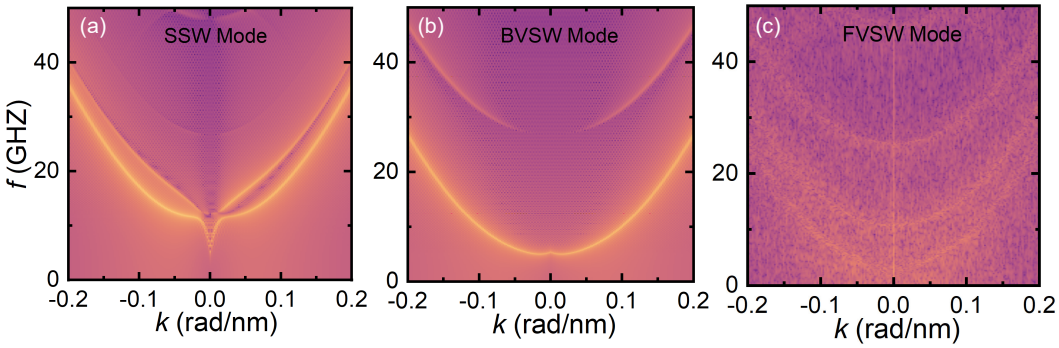

Figure 2.16: Micromagnetic simulations showing dispersion relation for (a) surface spin wave (SSW) (b) backward volume spin wave (BVSW) and (c) forward volume spin wave (FVSW) calculated for 40 mT external magnetic field in a NiMnSb waveguide with thickness 50 nm.

Magnetostatic forward volume spin waves (MFVSW)

MSFVW modes are observed when the static magnetization is perpendicular to the propagation direction as well as the waveguide plane. This mode is uniform throughout the sample volume and the group and phase velocity are parallel to each other. Its dispersion relation is given as [100]:

$$\left(\frac{2\pi f}{\mu_0 \gamma}\right)^2 = H_R \left[H_R + M_{eff}\left(1 - \frac{1 - e^{-kt_{film}}}{kt_{film}}\right)\right] \tag{2.44}$$

2.7 Perpendicular standing spin waves

In ferromagnetic films another spin wave mode which can be excited is the Perpendicular standing spin wave mode (PSSW) which has the wavevector perpendicular to the film plane. The wavevector for a film with thickness t_{film} can be given as $k_{PSSW} = n\pi/t_{film}$ where n is the order number. For the films with thickness in nanometer range, the wave vector is large and frequency is in the GHz regime. In order to excite the PSSW mode, a non-uniform excitation across the film thickness is required. Uniform magnetic fields can also excite PSSW mode when the magnetization of the film is pinned at both or one of the interfaces [101]. Thus unlike the MSWs, the PSSW mode is confined by boundary conditions between two surfaces. Thus only spin waves with specific wavelength can be excited. Fig. 2.17 shows

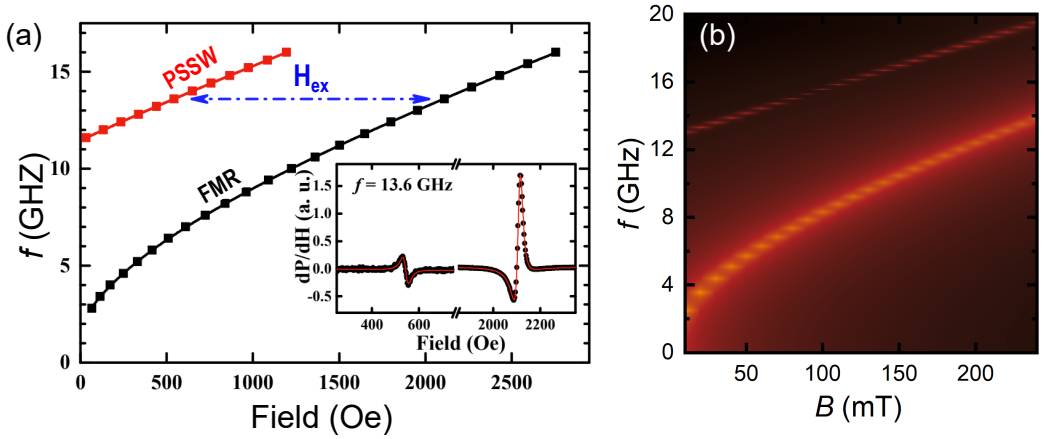

Figure 2.17: Resonance field vs frequency dependence for uniform FMR mode and PSSW mode in NiMnSb sample with thickness 38 nm. Fig adapted from [102]. Right panel shows the micromagnetic simulation for sample with thickness 40 nm and exchange stiffness constant of 8 pJ/m. Both the modes can be clearly seen.

the PSSW mode in NiMnSb sample. According to the Kittel model [103], odd spin wave (SW) modes are excited by a uniform RF field due to surface pinning caused by surface anisotropy interaction. In case of partial surface pinning both even and odd SW modes can be excited [104]. In the model given by Portis [105] a non-uniform volume magnetization in the absence of surface pinning can also can excite SW modes. Considering there is no surface pinning and the magnetization is in the sample plane, the dispersion relation for PSSW mode can be expressed as [98]:

$$\left(\frac{2\pi f}{\mu_0\gamma}\right)^2 = \left[H_R + \left(\frac{2A_{ex}}{\mu_0 M_s}\right)k^2_{PSSW}\right]\left[H_R + M_{eff} + \left(\frac{2A_{ex}}{\mu_0 M_s}\right)k^2_{PSSW}\right] \tag{2.45}$$

where A_{ex} is the exchange stiffness constant. It can seen from Eq. 2.42 and 2.45, the resonance frequency is higher as compared to uniform mode but is lower in MSBVW mode (see Eq. 2.43). For $k \to 0$, the dispersion relations of all threes spin wave modes converge to that of kittel formula for the uniform mode given in Eq. 2.33.

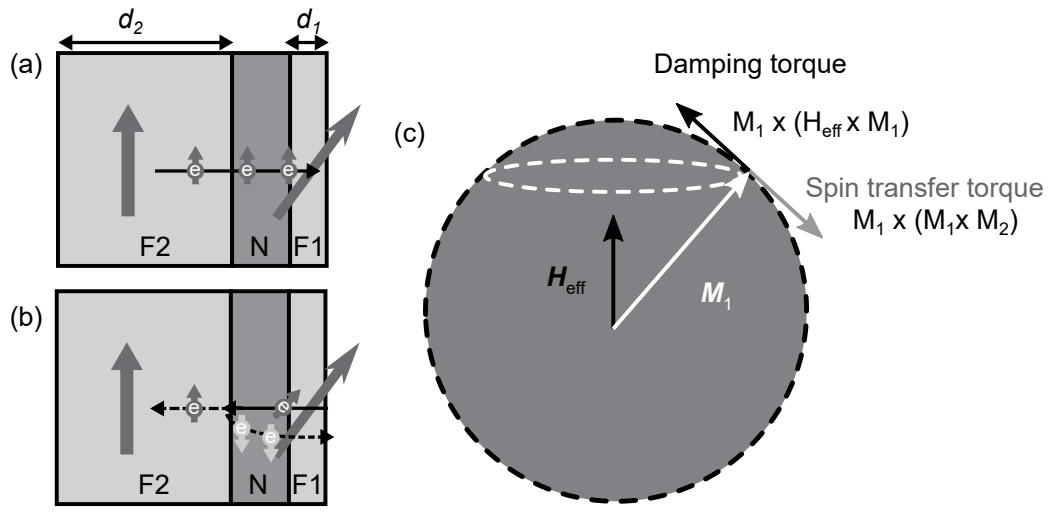

Figure 2.18: Flow of spin current in a trilayer structure consisting of Ferromagnet (F1)/non-magnet (N)/ferromagnet (F2) for (a) positive and (b) negative current. (c) Schematic representation of damping torque and spin transfer torque. Fig. adapted from [106].

2.8 Current-induced torques in ferromagnets

A charge current flowing through a FM/heavy metal bilayer system or in a FM with broken inversion symmetry can generate a torque and cause the precessional motion of the magnetization in FM. This electric-current induced spin torque in magnetic multilayers has been studied theoretically [28] as well as experimentally [2]. Considerable progress has been achieved recently and this effect has been explored for use in spin transfer torque induced magnetization switching [107], domain wall motion [108] as well as current induced linewidth modulation [2]. The innovation has opened up new paradigm for different different device applications like magnetic random access memories (MRAM), high frequency devices for telecommunications and most importantly the STT induced magnetization switching has offered an alternative to conventional field induced switching.

2.8.1 Spin-transfer torque (STT) and spin pumping

When a spin current flows through a ferromagnet, the spin angular momentum is transferred between the conduction electrons and the magnetization of ferromagnet and the overall spin angular momentum is conserved. This effect is known as spin-

transfer effect. This was predicted theoretically by Slonczewski [28] and Berger [29] in 1996 , and was first observed experimentally in a spin valve structure by Tsoi. et al. [109]. Fig. 2.18 shows a vertical spin valve device consisting of ferromagnet (F1)/ non-magnet (N)/ ferromagnet (F2) trilayer structure. We consider the magnetization of F1, $\mathbf{M}_1$ is initially tilted at an angle with respect to the magnetization of F2 which is $\mathbf{M}_2$. When a positive voltage is applied to the sample, the spins are injected from F2 to F1 and due to s-d exchange interaction, the spins get aligned to the direction of $\mathbf{M}_1$. In this process the electrons also exert a torque on $\mathbf{M}_1$ and cause it to rotate. The direction of the torque is given by $\mathbf{M}_1 \times (\mathbf{M}_1 \times \mathbf{M}_2)$. When the number of spins injected is very large , the torque from the spins overcomes the torque from $\mathbf{M}_1$ and thus cause it to tilt towards direction of $\mathbf{M}_2$ and thus direction of $\mathbf{M}_1$ becomes parallel to $\mathbf{M}_2$. In the case of voltage applied being negative, the electrons are injected from $\mathbf{M}_1$ into $\mathbf{M}_2$. The electrons which are antiparallel to $\mathbf{M}_2$ are reflected back at the interface and exert a torque on $\mathbf{M}_1$, rotating it antiparallel to $\mathbf{M}_2$.

Considering a single domain macrospin approximation, the LLG equation can be modified to include the contribution from spin transfer torque as shown in Eq. 2.46 [3].

$$\frac{\mathrm{d}\mathbf{M}}{\mathrm{dt}} = -\mu_0\gamma\mathbf{M}\times\mathbf{H}_{\mathrm{eff}} + \frac{\alpha}{\mathrm{M_s}}\mathbf{M}\times\frac{\mathrm{d}\mathbf{M}}{\mathrm{dt}} + \frac{\hbar\gamma J_c P g_{\mathrm{r}}^{\uparrow\downarrow}}{2eM_{\mathrm{s}}t_{\mathrm{FM}}}\mathbf{M}\times(\boldsymbol{s}\times\mathbf{M}) - \frac{\hbar\gamma J_c P g_{\mathrm{i}}^{\uparrow\downarrow}}{2eM_{\mathrm{s}}t_{\mathrm{FM}}}\mathbf{M}\times\boldsymbol{s} \tag{2.46}$$

Here, $g_{\mathrm{r(i)}}^{\uparrow\downarrow}$ is the real (imaginary) part of the interface spin mixing conductance; s is the unit vector of the spin polarization. e, P and t_{FM} are the electron charge, spin polarization factor and the thickness of the ferromagnetic layer respectively. The third term in Eq. 2.46 is the Slonczewski's anti-damping like term. The effect of this term is to modify the damping parameter. When the anti-damping torque is positive it dissipates the magnetization and suppresses the precessional motion and vice versa for negative torque. The last term in Eq. 2.46 is the field-like torque which acts as an additional magnetic field along s and is generally very small compared to

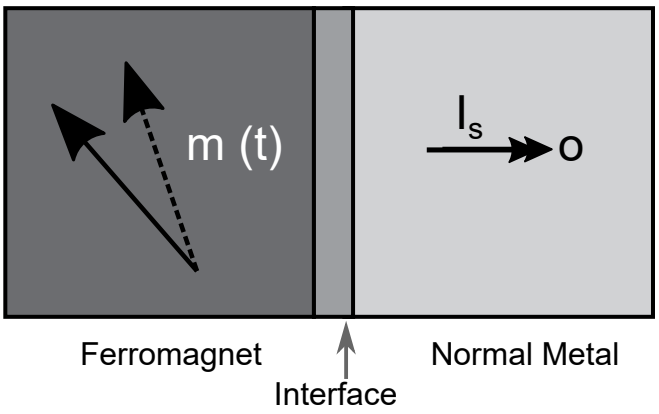

Figure 2.19: Spin pumping in a bilayer structure consisting of ferromagnet and a non-magnetic metal. The magnetization pumps a spin current, I_s, into the non-magnetic metal. Fig. adapted from [106].

anti-damping like term [110].

Spin-pumping

Spin pumping is the reciprocal effect of spin-transfer in which the currents are generated by magnetization dynamics. The first theoretical description of spin-pumping was given by Tserkovnyak et al. [111]. Both spin transfer and spin pumping show identical microscopic correlations according to Onsanger's reciprocity relations [112]. A schematic representation of spin pumping is shown in Fig. 2.19.

To conserve the angular momentum, spin current, I_s, is pumped out of the ferromagnet perpendicularly to **m**. Under these condition the pumped spin current can be expressed as:

$$\frac{e}{\hbar}\mathbf{I}_s = g_r^{\uparrow\downarrow}\mathbf{M}\times\frac{d\mathbf{M}}{dt} + g_i^{\uparrow\downarrow}\frac{d\mathbf{M}}{dt} \tag{2.47}$$

where the first term is similar to Gilbert damping term as in Eq. 2.46 implying that there is an enhancement of Gilbert damping given by:

$$\alpha_{\text{eff}}\ (t_{\text{FM}}) = \alpha_0 + \alpha_{\text{SP}} = \alpha_0 + \frac{\gamma\hbar}{4\pi M_s t_{\text{FM}}} g_{\text{eff}}^{\uparrow\downarrow} \tag{2.48}$$

where α_0, $g_{\text{reff}}^{\uparrow\downarrow}$ are the intrinsic Gilbert damping factor, and the effective real part of

the spin mixing conductance. The second term is the reciprocal term of the field-like torque and depends on the gyromagnetic ratio [111].

In this chapter, the basic background theory and concepts in magnetism have been explained, which are important for interpreting the results presented in the later chapters of the thesis. Different magnetic interactions and magnetization dynamics has been discussed along with the relaxation mechanisms which are important for the work done in chapters 4 and 5. The spin-transfer torques and the mechanism of generation has been discussed which is related to the work done in Chapter 6.

Chapter 3

Experimental Setup and techniques

In this chapter the experimental techniques used in this thesis are presented. It includes the coplanar waveguide (CPW) ferromagnetic resonance (FMR) technique used to study magnetization dynamics in Chapters 4, 5. The Spin transfer torque (STT)-FMR technique used in Chapter 6 is also described along with current induced (CI) STT-FMR.

3.1 Coplanar waveguide based FMR: Creation of Static and Dynamic fields

The technique of field modulated FMR is used for characterising ferromagnetic samples and to quantify various magnetic parameters. To perform such measurement, three basic components are needed:

- a static (controllable) magnetic field that can be rotated in the sample plane of the magnetic films.
- an RF (driving) field in the GHz range to excite the magnetization.
- a lock-in detection technique to improve signal to noise ratio requiring a modulating signal at a known frequency.

The experimental setup is illustrated in Fig. 3.1, where a coplanar waveguide is used that created microwave magnetic fields of variable frequencies. The detailed working is explained below:

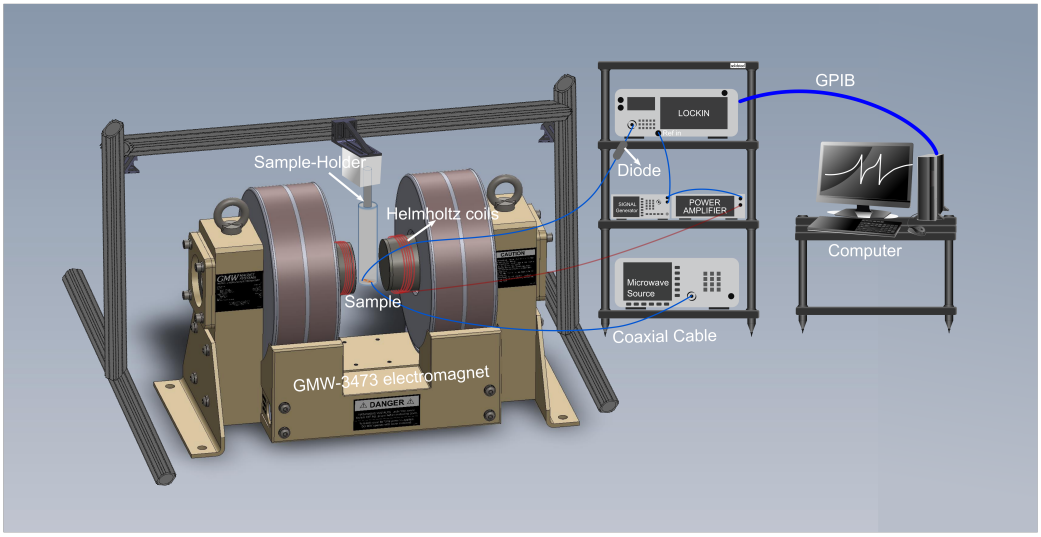

Figure 3.1: A schematic illustration of experimental setup for FMR experiments.

3.1.1 Experimental Realization

The measurement of FMR in ferromagnetic thin film gives access to the intrinsic magnetic energy landscape and the damping parameters of a given ferromagnetic (FM) layer. A typical measurement is performed by placing the ferromagnetic sample in a microwave magnetic field and measuring the power that is absorbed in the sample while sweeping the external field. The sample is placed on top of a CPW which is attached to a sample holder and brought into the gap of a controllable electromagnet.The microwave frequency and input power is fixed and the external field is swept through the FMR while the power reflected through the CPW is measured. As powermeter, a Schottky diode is used that act as a rectifier for the rf current such that the DC voltage is picked up when measuring with a low bandwidth device (lock-in amplifier). The absorption is thereby given by change in reflection of the coplanar waveguide that creates the driving field. The various parts are explained as below:

3.1.2 Static Field

In this thesis the measurements are performed with a fixed frequency f = (3-20) GHz and a variable external field $\mu_0 H_{\text{ext}}$. The required field range to reach the resonance fields for such frequencies lie between (0-900) mT for the used films. These

requirements are well fulfilled by electromagnets with a soft iron core. With such a magnet, fields upto 1.2 T can be created easily depending on geometry of magnet. The sample is mounted in the gap of the pole shoe in order to reach maximum and homogeneous field. The field is set by controlling the current through the coil using a controllable power supply that can be set by computer. The field at the position of the sample is measured by Hall probe. The field is rotated in the sample plane by rotating the magnet assembly using motor control keeping the sample position fixed.

3.1.3 Creation of the Driving Field

The precession of the magnetization is driven by a small, oscillating magnetic field in the microwave range of frequencies. In the presented work this field is created by the use of a coplanar waveguide.

Coplanar waveguides: The advantage of CPWs is that they can be designed for a wide bandwidth in frequency and allow for the creation of fields up to the order of 1 mT with relatively low output power (< 500 mW) delivered by standard microwave generators. In addition its design is flexible and can be adjusted to suit experimental needs. A sketch of basic geometry of a CPW is shown in Fig. 3.2. The CPW consists of three current carrying lines separated by a gap. The inner signal line carries a current. The outer lines (ground lines) carry half of this current in opposite direction thereby closing the circuit. The current that flow through the lines creates an Oersted field. The FM layer is placed on top of signal line. In our measurements the width of signal line is $\sim$ 0.5 mm and the ground lines are connected to ground plate as shown in Fig. 3.3 and see Appendix. H for details. The impedance of the CPW is an important factor for consideration when using it for FMR experiments, and it can be matched to 50 Ω by carefully controlling the parameters shown in Fig. 3.2, where the easiest parameters to vary are the signal line width (s) and the distance from the ground plane to signal line (w) [113]. The CPWs used for the experiments done in this thesis were fabricated in the UCL workshop using Roger's RT-Duroid 500 board. The CPW is connected to a microwave source which can transmit frequency of upto 20 GHz.

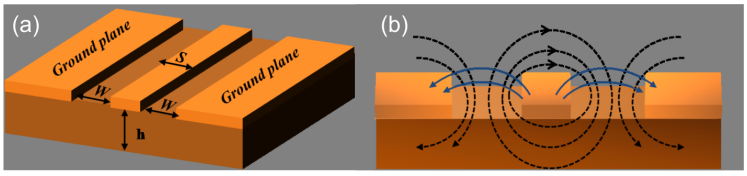

Figure 3.2: (a) Geometry of the coplanar transmission waveguide, where the central signal line of width, s, is separated by air gaps of width, w, from the ground planes. The relation between s, w and h (thickness of dielectric substrate) determines the impedance of the waveguide. The signal line is used to carry a high frequency signal. The current flow creates an Oersted field which is used to excite magnetization dynamics. (b) shows the rf field distribution around the conductors of the coplanar transmission line: dashed lines show the magnetic field force lines, and the solid lines show the electric field force lines.

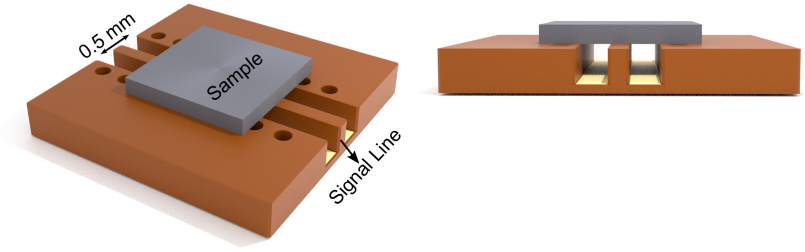

Figure 3.3: A schematic illustration of sample mounted on CPW. The sample is placed face down (ferromagnetic layer in contact with signal line). The right panel shows the side view.

3.1.4 Modulating field

In order to improve the signal to noise ratio (SNR) a lock-in detection technique is employed which requires modulating the signal at known frequency. This modulation is provided by an additional set of Helmholtz coils powered by an AC source which in turn produces a small modulation (H_{ac}) to the much larger (H_{DC}). Therefore, with this modified measurement scheme one actually measures the derivative of the transmitted/reflected power(dP/dH_{DC}),schematically shown in Fig. 3.4. This absorption is then generally fitted with symmetric and anti-symmetric Lorentzian function. The fitting formula used to extract the parameters is given in Eq. 3.1. By analysing these absorption peaks, the resonance position H_{res} and the linewidth ΔH can be determined and from these measurements it is possible to obtain the dynamic properties for a given magnetic sample.

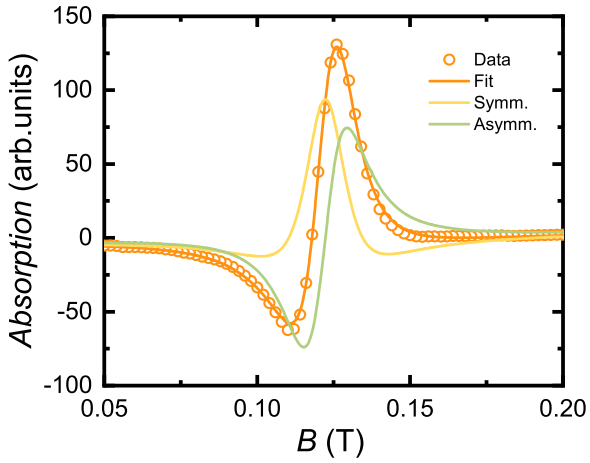

Figure 3.4: A schematic illustration of the absorption FMR signal

$$\frac{dP}{dH_{\mathrm{DC}}} = -V_{\mathrm{sym}}h_{\mathrm{ac}}\frac{2(H-H_{\mathrm{res}})\Delta H^2}{((H-H_{\mathrm{res}})^2+\Delta H^2)^2} - V_{\mathrm{asym}}h_{\mathrm{ac}}\frac{\Delta H((H-H_{\mathrm{res}})^2-\Delta H^2)}{((H-H_{\mathrm{res}})^2+\Delta H^2)^2} \tag{3.1}$$

Here, V_{symm} and V_{asym} denote the symmetric and antisymmetric Lorentzian components.

The advantage of the broadband FMR setup is the possibility of obtaining a full field vs. frequency map of the resonances, not being limited to a single frequency as compared to a cavity-based FMR setup, since by measuring the FMR linewidth as a function of frequency, one can extract both Gilbert damping factor, α, which characterises the frequency dependent contribution to the damping, as well as the inhomogeneous frequency independent contribution to the linewidth. Thus, using the broadband FMR the resonance conditions can be more fully explored and exploited by extracting the Gilbert damping parameter from a series of field-resolved FMR traces taken in a range of frequencies.

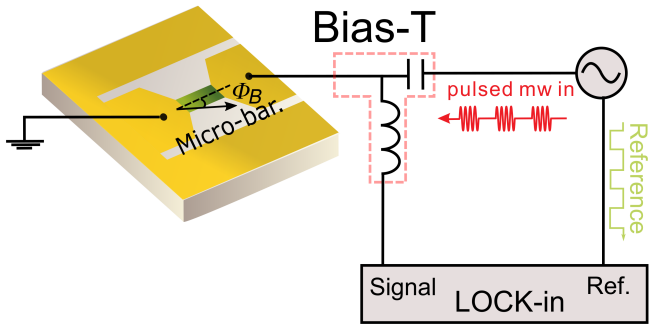

Figure 3.5: A schematic diagram for CI-FMR measurement. The circuit inside the red dashed line is the bias-tee.

3.2 Current Induced Ferromagnetic Resonance (CI-FMR)

Unlike the conventional CPW-FMR as described above which is driven by external microwave magnetic field generated by waveguide, the magnetization dynamics in CI-FMR is driven by effective magnetic field generated by passing the microwave charge current through the sample bars. The nature of this effective magnetic field has been discussed in details in Chapter 2. By using CI-FMR we can quantify the current induced torques and characterise the ferromagnetic samples [114].

The schematic of experimental setup is shown in Fig. 3.5. The device (micro-bar) is wire bonded between the open-circuit coplanar waveguide and a low frequency connection (not shown here) which provides a microwave ground. The sample is placed in an external magnetic field produced from the electromagnet to align the magnetization. Due to large impedance mismatch (the sample has nominal resistance in few $\sim k\Omega$ whereas the microwave transmission line and the waveguide has the charactersitic impedance of 50 Ω), the signal reaching the sample is a fraction of the incident signal. The microwave current is supplied to the sample using an Anritsu MG3692C signal generator. The microwave current is pulse modulated to allow the lock-in detection to improve the signal to noise ratio. Inside the ferromagnet, the oscillating current induced torques cause the magnetization, $\boldsymbol{M}$ to precess, which causes time varying change in the resistance. This when combined with microwave current inside the device, produces a measurable DC voltage due

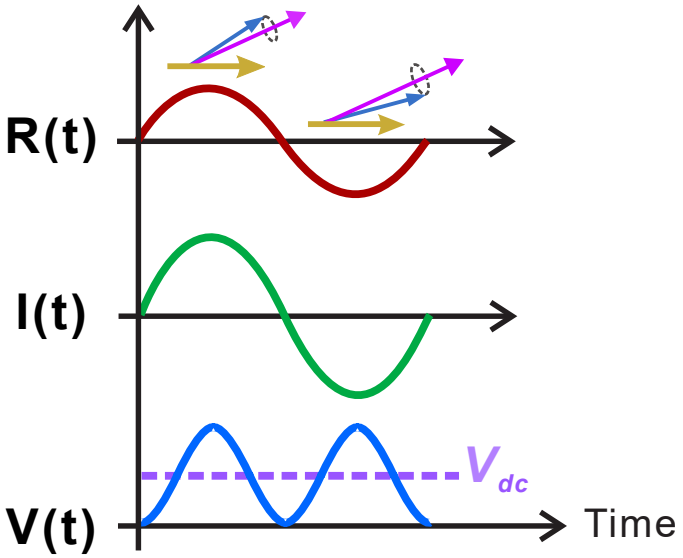

Figure 3.6: Illustration of frequency mixing effect. The magnetization precession causes a time-dependent change in device resistance which combines with the oscillating ac current inside the device, $I\cos(\omega t)$, giving rise to an ac voltage component varying at double frequency and a DC voltage component known as photovoltage.

to frequency mixing effect [115, 116] as shown in Fig. 3.6.

The mechanism of generation of DC voltage can be either due to spin rectification, which exploits the anisotropic magnetoresistance (AMR) or spin Hall magnetoresistance (SMR) effect in ferromagnetic samples, or it can be due to spin pumping in case of ferromagnet/hevy metal bilayer films.

Spin rectification – As mentioned in Sec. 2.8.1, a spin-polarized current reciprocally interacts with the magnetization in a ferromagnet through direct transfer of spin angular momentum. The time dependent change in resistance due to AMR when mixed with applied current ($I_{\mathrm{MW}} = I_0\cos(\omega t)$) generates a DC voltage which can be expressed as:

$$V(t) = I_0\cos(\omega t)\cdot \mathrm{R}(t) \tag{3.2}$$

and the time varying sample resistance is given by:

$$R(\mathrm{t}) = R_\perp + \Delta R\cos^2\left[\theta + \theta_\mathrm{c}\cos(\omega t)\right] \tag{3.3}$$

where θ_c is the cone angle of magnetization precession. Under the small-angle approximation ($\theta_c << 1$), we can expand Eq. 3.3 using Taylor's series to the first order in θ_c and putting it into Eq. 3.2 gives the voltage as:

$$V(t) \approx I_0 \cos(\omega t) \left[R_\perp + \Delta R \cos^2\theta - \Delta R \cdot \theta_c \sin(2\theta) \cos(\omega t) \right] \tag{3.4}$$

By simplifying the above expression we obtain the time independent component of voltage which is measured in the experiment:

$$V_{SR} = -\frac{1}{2} I_0 \Delta R \theta_c \sin(2\theta) \tag{3.5}$$

As mentioned in Appendix. F, the rectified DC voltage is obtained by solving the Landau-Lifshitz and Gilbert (LLG) equation and it is expressed as sum of symmetric and antisymmetric Lorentzian components given as:

$$V_{SR} = V_{sym-SR} \frac{\Delta H^2}{(H_{ext} - H_{res})^2 + \Delta H^2} + V_{asy\text{-}SR} \frac{(H_{ext} - H_{res})\Delta H}{(H_{ext} - H_{res})^2 + \Delta H^2} \tag{3.6}$$

$$\tag{3.7}$$

where,

$$V_{sym-SR} = \frac{I_0 \Delta R}{2} \frac{\omega}{\mu_0 \gamma \Delta H (2H_{res} + H_1 + H_2)} h_z \sin 2\theta = \frac{I_0 \Delta R}{2} A_{sym} h_z \sin 2\theta \tag{3.8}$$

$$\begin{aligned} V_{asy-SR} &= \frac{I_0 \Delta R}{2} \frac{(H_{res} + H_1)}{\Delta H (2H_{res} + H_1 + H_2)} \left(-h_x \sin\theta + h_y \cos\theta \right) \sin 2\theta \\ &= \frac{I_0 \Delta R}{2} A_{asy} \left(-h_x \sin\theta + h_y \cos\theta \right) \end{aligned} \tag{3.9}$$

where the terms H_1 and H_2 represent the anisotropy in the sample and ΔR is the AMR coefficient. The terms h_x, h_y, h_z refer to the components of effective driving field $\mu_0 \mathbf{h}_{eff} = \mu_0 \left(h_x, h_y, h_z \right) e^{j\omega t}$. Complete expression for different anisotropy terms is given in Appendix. F.

Spin pumping – In case of ferromagnet/heavy-metal bilayer systems another component that contributes to DC voltage is due to spin pumping [1]. The lineshape

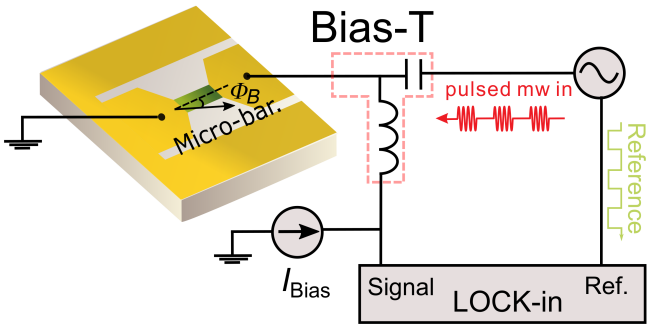

Figure 3.7: A schematic diagram for DC bias controlled CI-FMR measurement. The circuit inside the red dashed line is the bias-tee.

for spin pumping signal is purely symmetric since it is independent of the phase between magnetization precession and applied charge current. As given in [117], the DC voltage generated due to spin pumping can be expressed as:

$$V_{\mathrm{sym-SP}} = R_0 w_{\mathrm{HM}} \frac{2e}{\hbar} \theta_{\mathrm{SH}} \lambda_{\mathrm{HM}} \eta \tanh\left(\frac{t_{\mathrm{HM}}}{2\lambda_{\mathrm{HM}}}\right) j_{\mathrm{s}}^{0} \sin\theta \tag{3.10}$$

where, $w_{\mathrm{HM}}, t_{\mathrm{HM}}, \theta_{\mathrm{SH}}$ and λ_{HM} are the width of the bar, thickness of heavy metal (HM), spin Hall angle and spin diffusion length of the HM respectively; e is the elementary charge and $\hbar$ is the reduced Planck constant. η is a correction factor for the ellipticity of the magnetization precession and j_{s}^{0} is the spin-current density at the interface given by [63]:

$$j_s^0 = \frac{\hbar g_{\mathrm{eff}}^{\uparrow\downarrow} \gamma^2 (\mu_0 h_{\mathrm{eff}})^2 \left[\mu_0 M_{\mathrm{eff}} \gamma + \sqrt{(\mu_0 M_{\mathrm{eff}} \gamma)^2 + 16(\pi f)^2}\right]}{8\pi\alpha_{\mathrm{eff}}^2 \left[(\mu_0 M_{\mathrm{eff}} \gamma)^2 + 16(\pi f)^2\right]} \tag{3.11}$$

where $g_{\mathrm{eff}}^{\uparrow\downarrow}, h_{\mathrm{eff}}, \gamma_{\mathrm{eff}}$ and M_{eff} are the spin mixing conductance, current induced effective field, gyromagnetic ratio and effective magnetization respectively.

3.3 Linewidth Modulation by DC current bias

Magnetization precession can be modulated electrically due to the spin Hall effect (SHE). When a DC bias current (I_{DC}) is applied, depending on the relative orientation of I_{DC} with respect to magnetization, can cause an increase or decrease of

effective magnetic damping (α) and hence ΔH [118]:

$$\begin{aligned}\Delta &= \frac{2\pi f}{\gamma}\left(\alpha + \frac{\sin\theta}{(H_{\text{ext}} + 2\pi M_{\text{eff}})\,\mu_0 M_S t_{\text{FM}}}\frac{\hbar J_S}{2e}\right) \\ &= \frac{2\pi f}{\gamma}\left(\alpha + \frac{\sin\theta}{(H_{\text{ext}} + 2\pi M_{\text{eff}})\,\mu_0 M_S t_{\text{FM}}}\frac{\hbar\theta_{\text{SHE}} J_C}{2e}\right)\end{aligned} \tag{3.12}$$

where J_{S} is the spin current density. α is extracted from the frequency dependence of linewidth. Fig. 3.7 shows the schematic of the circuit used for the measurement. As compared to the circuit of CI-FMR shown in Fig. 3.5, an additional DC current source is introduced. Keithley K2400 acts as DC current source. By applying different DC bias currents, the CI-FMR measurement is done and linewidth is extracted by fitting. Since the microwave current is modulated at lock-in frequency of 12 Hz it causes oscillation of sample resistance at same frequency by certain amount (ΔR_{MW}) due to joule heating. Because of this oscillating resistance the DC bias current, I_{Bias} causes an oscillating voltage proportional to $I_{\text{Bias}}\Delta R_{\text{MW}}$ which appears as additional background voltage in lock-in detected signal. By fitting the linewidth dependence as a function of I_{Bias}, spin Hall angle can be estimated using Eq. 3.12.

Chapter 4

Relaxation of magnetization dynamics in non-centrosymmetric ferromagnet NiMnSb

4.1 Introduction

Magnetic relaxation processes are of considerable importance for thorough understanding of spin dynamics in ferromagnetic systems. The energy relaxation rate is quantified using the phenomenological Gilbert damping parameter [73]. Inspite of numerous reports in this avenue starting from as early as fifties [119, 120, 121], a generalized conceptual knowledge is still rather fragmented which is most likely because of the damping in the system being sample dependent. Although we often describe damping in terms of intrinsic and extrinsic properties, a possible caveat is that there always exists some ambiguity regarding how these two can be distinguished accurately. When we talk about intrinsic properties, the most inherent contribution to system damping is often described in terms of spin-orbit interaction and itinerant electrons. Although there do exist other intrinsic contributions from eddy-current and phonon drag, they play negligible role for ultrathin films. The microscopic description of intrinsic damping based on s-d exchange interaction was explained in the model given by Heinrich, Fraitová and Kamberský [122]. Apart from this many other models [123, 124, 125, 126, 127] highlight the underlying physics of

magnetic relaxation and damping in ferromagnets but most of them portray the idea that the leading mechanism governing intrinsic damping can be attributed to spin-orbit interaction. Control of damping is indeed important for realization of efficient magnetization reversal for memory applications. A large value of intrinsic damping suppresses the precessional motion of the magnetization of soft magnetic underlayer and write pole in Perpendicular Magnetic recording (PMR) devices. This leads to reduction of transition-jitter caused by head field fluctuations [128]. Thus control of damping is important for PMR devices in order to speed up the writing process. However, the presence of structural distortions, inhomogenities and defects referred to as extrinsic contributions can often mask the intrinsic contributions leading to uncertainity in calculated damping values. Thus, separation of contribution to linewidth from these effects is essential to clarify the origin of damping. This becomes more important for materials with low intrinsic damping. In the framework of Landau-Lifshitz and Gilbert (LLG) equation the intrinsic damping term is described by the constant α and the ferromagnetic resonance (FMR) linewidth, ΔH, scales linearly with resonance frequency. On extrapolating the curve for frequency dependence of ΔH, the extrinsic contributions can be inferred as the zero frequency offset, ΔH_0, which must be absent in case of no inhomogeneities pertaining to negligible extrinsic contribution. In case of lattice strained structures the spin dynamics is strongly affected by the presence of self-assembled network of misfit dislocations which tend to increase the damping by a process described as two-magnon scattering [129, 130, 131, 132, 133, 134] when degenerate modes with wave vector ($k \neq 0$) are available for relaxation. The two-magnon scattering component can be anisotropic and cause channelling of scattered magnons pertaining to its dependence on k [134]. The effect of two-magnon is more pronounced when inhomogeneous field is much smaller than the interaction field [135, 136]. In this case the FMR lineshape is Lorentzian which deviates from standard form and can resemble Gaussian peak shape for larger inhomogeneities [135]. For long wavelength (small k), we cannot treat the extrinsic contribution to linewidth to be coming only from two-magnon scattering. In the case of large sample inhomogeneities, the standard

two-magnon picture fails to explain the broadening in linewidth due to the spatial variation of internal fields [137, 138] and varying crystallite orientation. The resultant FMR signal is then attributed to the superposition of local resonances. This can often result in non-zero ΔH_0 offset. In order to interpret the extrinsic contribution we should obtain ΔH in the vicinity of film normal when the two-magnon is switched off [139, 140, 89, 141]. The presence of non-zero offset in film normal condition could imply the dominance of large scale inhomogeneities on linewidth broadening.

In this chapter, microwave induced magnetization dynamics is investigated in a broad band ferromagentic resonance type experiment revealing the contribution of extrinsic and intrinsic relaxation terms in half-Heusler NiMnSb, a ferromagnet with zinc-blende crystal structure. As pointed out by Barýakhtar and coworkers [142, 143, 144, 145] the "form of relaxation terms is influenced by the crystal symmetry", hence the phenomenological damping term should be a tensor instead of an isotropic scalar constant. This is explored in this studies. Moreover, it had been also pointed out by Kamberský [86] that two processes, ordinary and spin-flip scattering dominate the Gilbert damping factor G (G = $\alpha\gamma M_s$) and they depend on the density of states at the Fermi-level, $D(E_F)$ and electron scattering time, τ. They are given as:

$$G_{\text{spin-flip}} = \left(\frac{\gamma\hbar}{2}\right)^2 D(E_F)(g-2)^2/\tau, \tag{4.1}$$

$$G_{ordinary} = \left(\frac{\gamma\hbar}{2}\right)^2 D(E_F)\lambda_{SO}^2(g-2)^2/\tau, \tag{4.2}$$

where λ_{SO} is the strength of spin orbit interaction and g is the Landé g-factor. The magnetic anisotropy energy density is related to the anisotropy of orbital angular momentum [18] and also the g-factor measured in FMR is a measure of the orbital to spin magnetic moment ratio[146]. Thus, from Eq. 4.2, since damping depends on g-factor, the materials with large magnetic anisotropy should show large anisotropy in damping [20]. By performing various angle and frequency dependent scans, different anisotropy components and damping parameter are quantified

which shows anisotropy in damping for thinner films. Apart from all these theoretical works many experimental studies [20, 147, 148, 149, 150, 151, 90] also claim existence of anisotropic damping. However, convincing experimental evidence for the anisotropic damping in bulk ferromagnets is still lacking. Moreover, the anisotropy of damping may average out for the continuous rotation of magnetization trajectory around a fixed static FMR bias field [152]. This is because the phonon reservoir smears out the electron bands at high temperature [14, 12] due to dominant interband transitions explained by bubbling Fermi-surface model [153, 154] thus making the experimental detection of anisotropic damping difficult. Gilbert damping which is determined by the electrons at the Fermi surface [155, 16] becomes anisotropic due to anisotropic electronic structure due to spin-orbit interaction during magnetization precession. This is however true in low temperature regime dictated by breathing fermi surface model determined by intra-band electron scattering. Apart from this, contribution to damping from structural and chemical disorder [156] may further hinder the observation of anisotropic damping due to inter-band scattering. Thus making overall detection of anisotropic damping in bulk ferromagnets difficult. By rigourous analysis of linewidth, the presence of anisotropic Gilbert damping is confirmed in the samples which diasppears as the thickness is increased.

The FMR linewidth leads to precise determination of the magnetic relaxation parameters of these samples. The various contributions to the FMR linewidth due to Gilbert damping and other relaxation terms in NiMnSb are distinguished and analysed quantitatively. A general model is presented to explain both the angular and frequency dependencies of the FMR linewidth yielding unique set of relaxation parameters. In general, the contributions to linewidth from two different channels: (i) Contribution due to Gilbert type relaxation and (ii) non-Gilbert type (extrinsic) contribution, are separated. These contributions have been discussed in details in Chapter 2.

The idea to choose NiMnSb for this study is to explore the interplay between the crystal structure and magnetism. The non-centrosymmetric crystal, NiMnSb is

of particular importance. In the case of NiMnSb with zinc-blende structure there exists a bulk inversion asymmetry (BIA) which results in Dresselhaus spin-orbit coupling whereas the structural inversion asymmetry (SIA), due to deformation or an asymmetric electric potential, results in the Rashba type spin-orbit coupling field [157]. Hence, this study helps to understand the spin-orbit interaction of a crystalline ferromagnetic structure. The cubic half-Heusler lattice of NiMnSb, shares $\bar{4}$3m point-group symmetry. Under a tetragonal distortion the symmetry of these crystals reduce to $\bar{4}$2m point group. Here, the importance of symmetry breaking on magnetic damping is addressed. This work is different from recent study of anisotropic damping in ultrathin Fe film on GaAs [90] where the origin of anisotropic damping is mediated by the anisotropic density of states at the interface following from the effect of interfacial spin orbit coupling on electronic structure. Finally, the tuning of anisotropy in damping is demonstrated through variation in thickness of film. This work will provide new insight into understanding the mechanism of magnetic relaxation.

4.2 NiMnSb Sample

NiMnSb belongs to the family of Heusler alloys [158]. Heusler alloys can be classified as full-Heusler with chemical formula X_2YZ and half-Heusler with formula XYZ, which crystallize in $L2_1$ and $C1_b$ crsytal structure respectively as shown in Fig 4.1. (Here, X and Y are transition metals and Z is a non-magnetic element [159]). NiMnSb crystallizes in non-centrosymmetric (lack of inversion asymmetry) half-Heusler cubic structure $C1_b$. The interest in this material started when Groot *et al*. [160] calculated its band structure and predicted it to be half-metallic. Since then a lot of research has been done for this material [161, 162, 163, 164, 165, 166]. This composition is a very interesting material for application in spintronics devices due to its high spin polarization [167, 168], high Curie temperature and small value of Gilbert damping [169, 170]. The hybridization states of elements X and Y form a very large bandgap for $C1_b$ configuration which is desirable for enhancing the performance of magnetoresistive devices. In a ferromagnet with nearly half-metallic

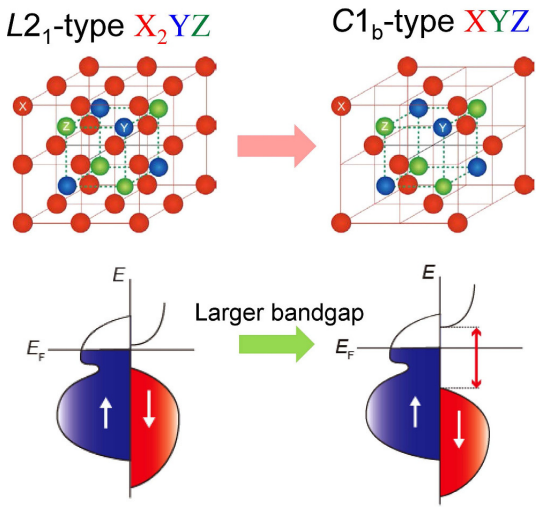

Figure 4.1: Schematic of the crystalline cell structures with atom occupancy (top panel) and electronic band structure (bottom panel) near the Fermi level for $L2_1$-type full-Heusler (left) and $C1_b$-type (right) half-Heusler alloys. Fig. adapted from [175] .

band structure, the isotropic interband term is suppressed [13] and the damping can be dominated by the anisotropic contribution. Recent works have claimed the observation of anisotropic damping in half-metallic Heusler alloy [171, 147]. In NiMnSb the minority spin band is semiconducting with a gap at fermi-level, E_F. Such materials can be considered as hybrid between metal and semi-conductors. Recently this material has been found to be promising candidate for observing spin-orbit torques at room temperature [172]. The anisotropy of NiMnSb is found to be sensitive to its lattice constant which can be controlled by either varying Mn concentration [173] or by inducing external strains [174]. A variation in the composition of NiMnSb can result in both the change in strength and direction of anisotropy. Also, it has been reported that there is a dependence of anisotropy on thickness [170], hence the anisotropy can be tuned by varying thickness and stoichiometry when grown in thin films, thus opening the way to engineer material with desired magnetic properties.

The cubic half-Heusler lattice of NiMnSb as shown in Fig. 4.2, shares $\bar{4}3m$ point-group symmetry. Due to the presence of global inversion asymmetry, a net spin polarization with a non-zero integral value over the unit cell is obtained. In this study the NiMnSb films were grown on GaAs substrate which resulted in tetragonal distortion due to strain caused by substrate-lattice mismatch. This causes a lowering

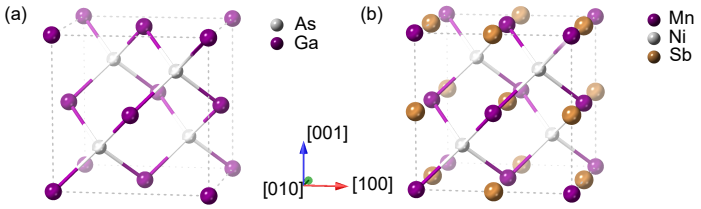

Figure 4.2: (a) Crystal unit cell of GaAs, where the inversion partners are occupied by different atomic species, hence making the unit cell globally non-centrosymmetric, and results in non-zero net spin polarization. (b) Crystal unit cell of NiMnSb, symmetry is analogous to that of GaAs i.e zinc-blende structure [176].

.

of symmetry to $\bar{4}$2m. The current induced spin polarization for $\bar{4}$2m has Dresselhaus symmetry with respect to applied current direction [176, 177, 114, 178]. The resulting symmetry lowering caused by associated strain fields influences the magnetic properties [169, 90].

4.3 Sample Growth and Film Characterization

The samples were grown by Dr. Sukegawa (NIMS, Japan) and Dr. Xiang (NIMS, Japan). Preparation of thin film of NiMnSb was carried out in a magnetron co-sputtering system with a base pressure of 1×10^{-7} Pa. Semi-insulating GaAs(001) wafers were used as substrate for the growth of the film. The GaAs substrates were cleaned using 35% hydrochloric acid (HCl) aqueous solution at room temperature for 9 min before being annealed at 400°C for 30 min in order to desorb the contaminants. The annealing was done in sputtering chamber and was monitored using reflection high energy Electron Diffraction (RHEED) [179] until a well ordered 4×6 reconstruction appeared. The NiMnSb film was grown by co-deposition of Ni, Mn and Sb targets at 250° C and Ar gas pressure of 0.4 Pa. Ni was deposited by RF sputtering whereas Mn and Sb were deposited by DC sputtering after calibrating the deposition rate for each element. The NiMnSb deposition rate was set to 0.12 nm/s. Annealing was done for sample thickness 20-100 nm post deposition at 400° C within the sputtering chamber while 15 nm thick sample was not

Table 4.1: Overview of NiMnSb films investigated in this study. The blanks in the table for 15 nm sample indicate that XRD measurements were not done for the samples and so the lattice constant parameters were not extracted. NA for 15 nm sample stands for not annealed.

Sample Thickness (nm)	Lattice Constant (c) (Å)	Lattice Constant (a) (Å)	c / a	(c-a) / a (%)	Uniaxial easy axis	Lattice Mismatch (%)	M_s (kA/m)	Annealing Temp.(° C)
15	-	-	-	-	[1$\bar{1}$0]	-	446±1	NA
20	5.921±0.002	5.937±0.002	0.9973±0.0006	-0.2694±0.0006	[1$\bar{1}$0]	4.891±0.002	532±5	400
50	5.921±0.001	5.928±0.001	0.9988±0.0003	-0.1212±0.0003	[1$\bar{1}$0]	4.873±0.001	545±2	400
100	5.924±0.002	5.933±0.004	0.9984±0.0009	-0.155±0.001	[1$\bar{1}$0]	4.782±0.002	583±2	400

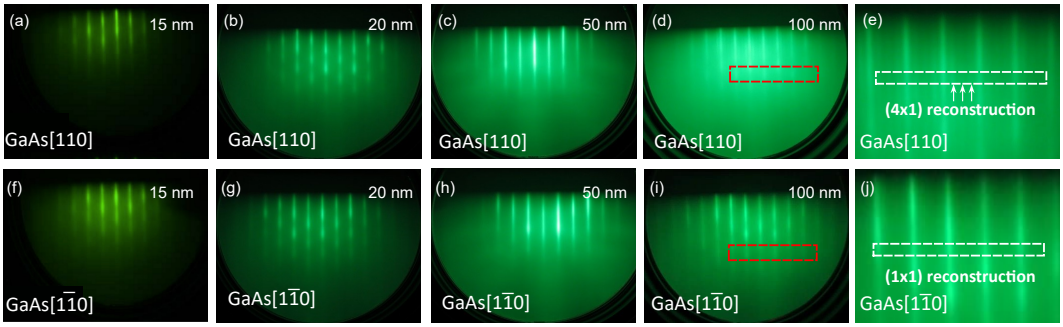

Figure 4.3: RHEED image of the NiMnSb film for (a) 15 nm (b) 20 nm (c) 50 nm and (d) 100 nm film thickness measured with incident electron beam along [110] and [1$\bar{1}$0] directions. The real inplane periodicity is given by the outer streaks. The streaks between the middle streak and the outer streak are caused by 4 × 1 reconstruction for incident beam along [110] direction. The RHEED streak reconstruction vanishes for incident beam along [1$\bar{1}$0] direction.

annealed[1]. Finally, a 3 nm thick capping layer of MgO was deposited on films using RF-sputtering at room temperature for protection against oxidation. Inductively coupled plasma analysis of a 100 nm-thick reference film deposited on a thermally oxidized Si substrate at room temperature allowed the measurement of film composition to be $Ni_{31.1}Mn_{33}Sb_{35.9}$. Monitoring of the growth process and surface structure analysis was done in-situ using RHEED.[2]

The RHEED pattern for different thickness of grown film are shown in Fig. 4.3. The RHEED patterns show straight streaks, corresponding to a 4×1 reconstruction when the electron beam was oriented along [110] direction and 1×1 reconstruction when the electron beam was oriented along [1$\bar{1}$0] direction as shown in Fig. 4.3. From the RHEED patterns one can conclude that the two directions [110] and [1$\bar{1}$0]

[1]The 15 nm sample was from a different batch. The growth conditions were maintained similar to the deposition of 20-100 nm thickness but after the growth of 15 nm sample, no post-deposition annealing was done.

[2]RHEED measurements done by Dr. Sukegawa

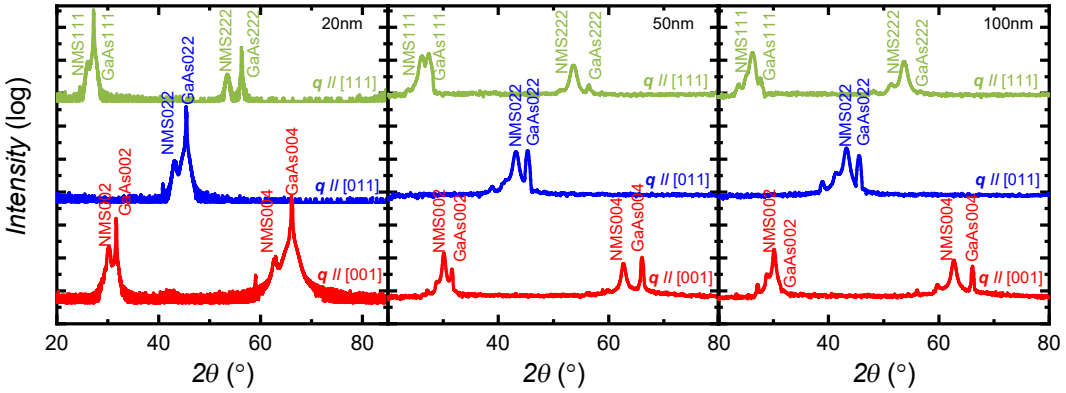

Figure 4.4: Out-of-plane and XRD profiles obtained from 20 nm, 50 nm and 100 nm thick NiMnSb crystalline films deposited on GaAs (001) substrate. The profiles along various scattering vectors q of GaAs are shown.

are not equivalent pertaining to anisotropy in the system.

The characterization of crystal growth properties of the grown films was done by X-ray diffractometry (XRD)[3] using Cu-Kα radiation (λ = 0.154 nm). Out of plane XRD results for samples with thickness 20-100 nm are shown in Fig. 4.4. XRD measurements were not performed for 15 nm thick sample. The XRD traces confirm that the NiMnSb film is grown epitaxially on the GaAs substrate with cube on cube orientation relationship of GaAs(001) || NiMnSb(001) which is consistent with earlier reported works [173]. Moreover, formation of single $C1_b$ is confirmed from the absence of any secondary phases in the profile. The lattice constants were calculated using both out-of-plane ($q \parallel 00h$) and in-plane peaks ($q \parallel hl0$)[4].The calculations were done by Dr. Sukegawa. The lattice constants for different thickness of NiMnSb were calculated using least square method from the peak positions and using Bragg's law. Table. 4.1 shows the lattice constants for all different film thickness along with the easy axis for inplane magnetization. In Fig. 4.4, scans along $q \parallel [011]$ and $q \parallel [111]$ are also shown. This was done to obtain the lattice spacings for oblique directions in addition to the information about secondary phases. These scans were done at a tilt angle of 54.7° and 45° from (001) plane for $q \parallel [111]$ and $q \parallel [011]$ respectively. Also it can be seen that no secondary phases are present. Due to the presence of lattice mismatch, there is an elongation or compression of

[3]XRD measurements done by Dr. Sukegawa
[4]The in-plane data is not shown in this thesis

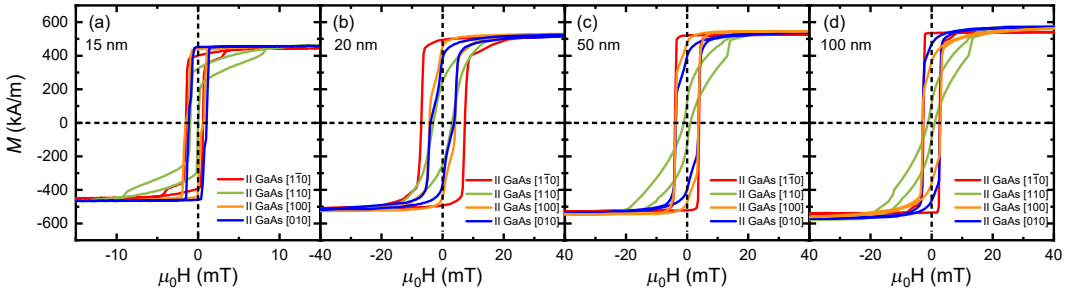

Figure 4.5: Hysteresis loops for in-plane applied field along GaAs [1$\bar{1}$0], [110], [100] and [010] for (a) 15 nm (b) 20 nm (c) 50 nm and (d) 100 nm. The hard axis is [110] for all the samples as shown in the figure.

the out of plane lattice constant c, resulting in tetragonal distortion. From the data of oblique scans it is seen that the lattice spacings are tuned by existence of tetragonal distortion along the film perpendicular direction. The bulk value for lattice constant is 0.593 nm and 0.5653 nm for NiMnSb [180] and GaAs [181] respectively. Comparison of results to bulk value indicate that the sign of distortion generated by growth is opposite to the lattice mismatch of their bulk constants. The lattice mismatch (%) is given in Table. 4.1. In the samples a growth induced strain can develop due to the lattice mismatch of the substrate and NiMnSb epilayer. This strain caused deformation of the lattice. In our samples it was observed that the strain-induced tetragonal distortion (c-a/a) of films decreases from 0.27 % to 0.15 % as the thickness is increased. Although within the given uncertainities we could not see any change in strain with thickness but the presence of structural defects can also cause strain fields and affect the magnetic properties and reduce the crystal symmetry [170]. Moreover, the interfacial regions can be pseudomorphically strained [170]. The strength of this strain is difficult to be quantified by using only XRD measurements. Apart from this, the presence of misfit dislocations are speculated near the GaAS/NiMnSb interface which also influences the lattice relaxation. To be noted here is that in spite of $\sim$ 5% lattice mismatch, an epitaxial growth was maintained which is visible from the RHEED and XRD data. By tuning the growth conditions an epitaxial growth can be possible in large lattice mismatch systems[182] and for different thickness of NiMnSb samples used in this study, an epitaxial growth was observed.

The magnetic hysteresis loops[5] were measured using a vibrating sample magnetometer (VSM) at room temperature. Fig. 4.5 shows the magnetization curves obtained when applying field H along [1$\bar{1}$0], [110], [100] and [010] in GaAs. These data demonstrate that the hard axis corresponds to [110]. Furthermore, the shape of hysteresis loops measured in different crystallographic directions indicate the presence of both uniaxial and cubic magnetic anisotropies. Table. 4.1 summarizes the estimated saturation magnetization values for different thicknesses of the film. The bulk value of saturation magnetization for NiMnSb is 741 kA/m which is about 1.3 times larger than the extracted saturation magnetization (M_s) in the grown films. This deviation from the bulk value was also reported in earlier works [183] and the reason can be attributed to the saturation magnetization being sensitive to the growth conditions and stoichiometry [184]. This can indicate that there is a presence of significant amount of structural disorder in the grown films. Apart from this, other causes for reduction can be attributed to smaller concentration of Ni and Mn atoms with respect to Sb atoms, existence of dead layers at the interfaces or the residual antisite defects in the $C1_b$ lattice. All the above factors can be attributed to be responsible for the lower value of saturation magnetization as compared to the bulk value. In order to maintain high crystallinity and minimum roughness the growth temperature was set at 250° C followed by post-annealing for 20-100 nm thick samples. It can be seen that for annealed samples the M_s value is larger which indicates an improved atomic ordering. The coercive field for the samples is 15 Oe, 71 Oe, 39 Oe and 26 Oe for 15 nm, 20 nm, 50 nm and 100 nm respectively. The increase in coercive field for annealed samples is not yet clear but a full square easy axis hysteresis loop for annealed sample indicate of improved crystalline structure and chemical order [185] while for 15 nm sample the easy axis show poor squareness. There is also a variation in anisotropy for annealed samples.

[5]VSM measurements provided by Dr. Sukegawa

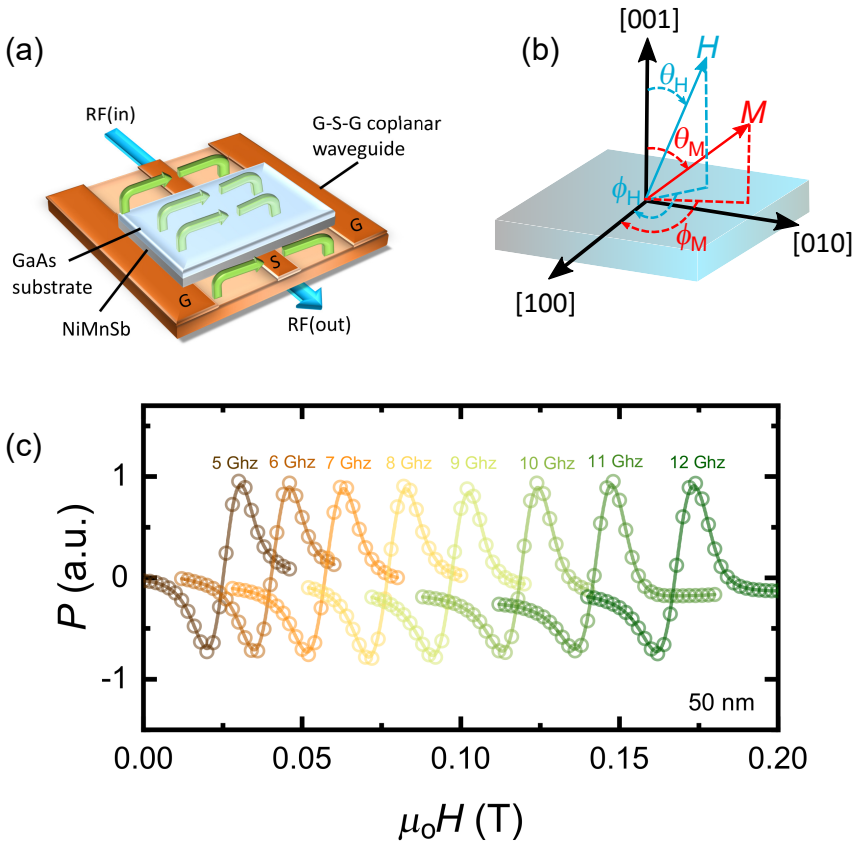

Figure 4.6: Typical absorption spectra induced by ferromagnetic resonance in NiMnSb. a) Schematic of the ferromagnetic resonance excitation in sample. Microwaves pass through the transmission line which at an appropriate magnetic field can resonantly excite the sample. The decrease in RF energy due to absorption on resonance is converted to a DC Voltage by a diode. b) Crystal orientation of NiMnSb and definition of the angles of magnetization, ϕ_M, and external magnetic field, ϕ_H, with respect to [100] direction. c) Typical absorption spectra for several selected frequencies measured at ϕ_H=-45° and room temperature. Each spectrum can be fitted by combination of symmetric and antisymmetric lorentzian function, from which the FMR resonance field, H_{res} and the linewidth, Δ H are obtained.

4.4 Resonance measurements

Ferromagnetic resonance is a key technique to determine the magnetic properties of ferromagnets. Having the capability of full angle dependent measurements of the ferromagnetic resonance in-plane as well as out-of plane offers the possibility to determine the in-plane and out-of plane anisotropy constant, the saturation magnetization, the Gilbert damping factor and the g-factor of the examined samples. The FMR experiments were carried out with the magnetic moment in the plane of the film (in-plane configuration) and out-of-plane of the film (out-of-plane configuration) using the experimental set up described in Chapter 3. The external field was modulated with an amplitude of few Oersteds at 12 Hz and a phase sensitive detection was used to increase the signal-to-noise ratio. With this modified measurement scheme, the derivative of the transmitted/reflected power, (dP/dH_{dc}), is measured. Fig. 4.6 shows the typical absorption spectra for 50 nm thick fim. This absorption is then fitted with symmetric and anti-symmetric Lorentzian functions. The fitting formula used to extract the parameters is given in Eq. 3.1. By analysing these absorption peaks, the resonance position and the linewidth are determined and dynamic properties for a given magnetic sample are obtained. The results of extensive frequency dependence as well as angle dependent measurements of the FMR linewidth are presented in the following sections. The advantage of the broadband FMR setup as compared to cavity based FMR has been discussed in Chapter 3.

4.5 Angular dependence of resonance field and linewidth

4.5.1 Magnetic field anisotropy

The angular dependence of FMR resonance fields is shown in Fig. 4.7 (e-h) for different thickness of NiMnSb at microwave frequency, f = 5 GHz. The data is fitted using resonance condition:

$$\left(\frac{\omega}{\gamma}\right)^2 = \mu_0^2 H_1 H_2 \tag{4.3}$$

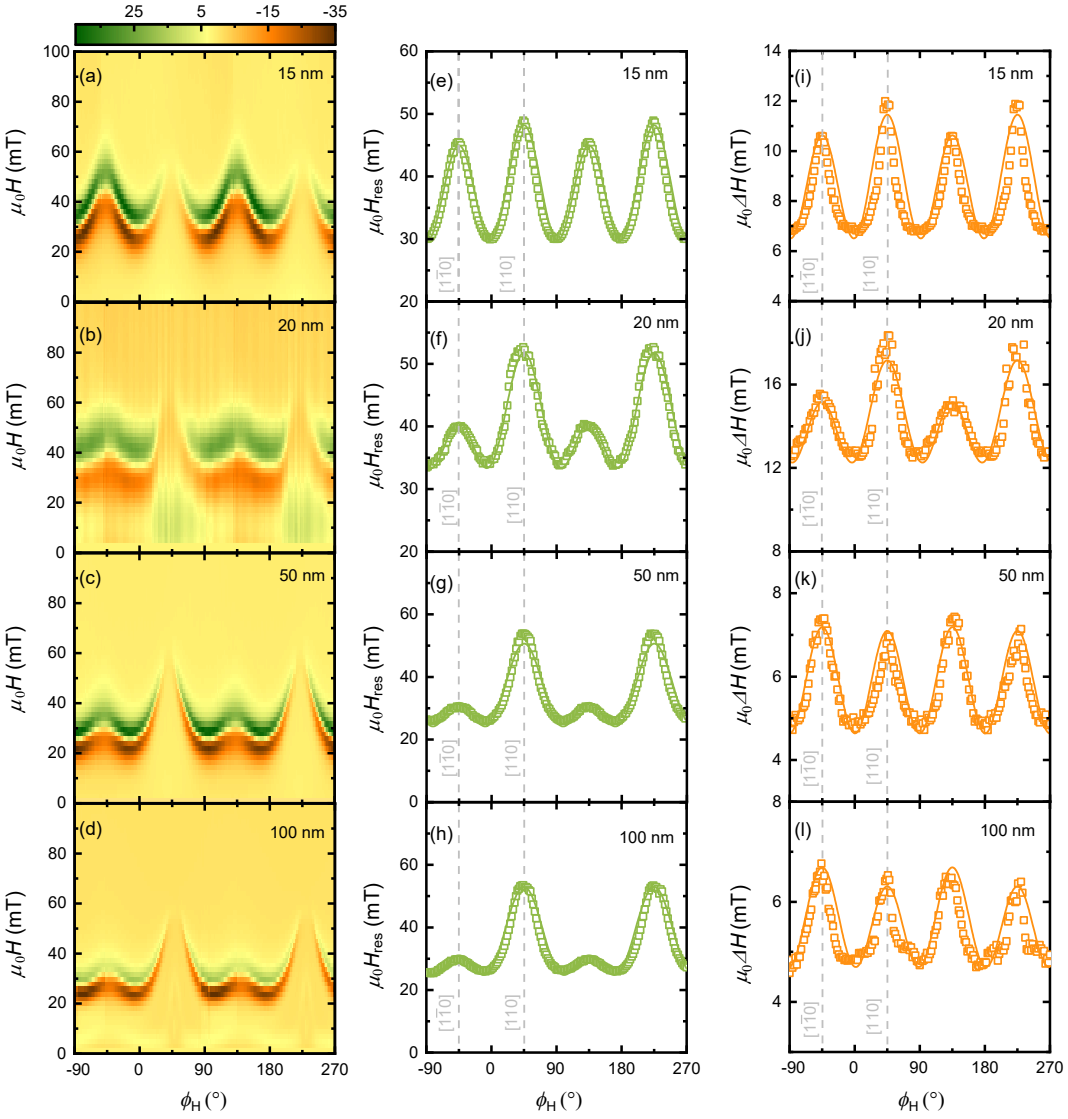

Figure 4.7: (a-d) Microwave absorption from an in-plane rotational scan of external magnetic field as a function of applied magnetic field and angle measured at 5 GHz for different sample thickness (a) 15 nm (b) 20 nm (c) 50 nm and (d) 100 nm. (e-h) In-plane angular dependence of FMR resonance field H_{res} obtained from fitting FMR scans for different set of samples measured at 5 GHz. (i-j) Corresponding linewidth, ΔH as a function of in-plane rotational angle for different sample thicknesses. The solid lines represent the fitting.

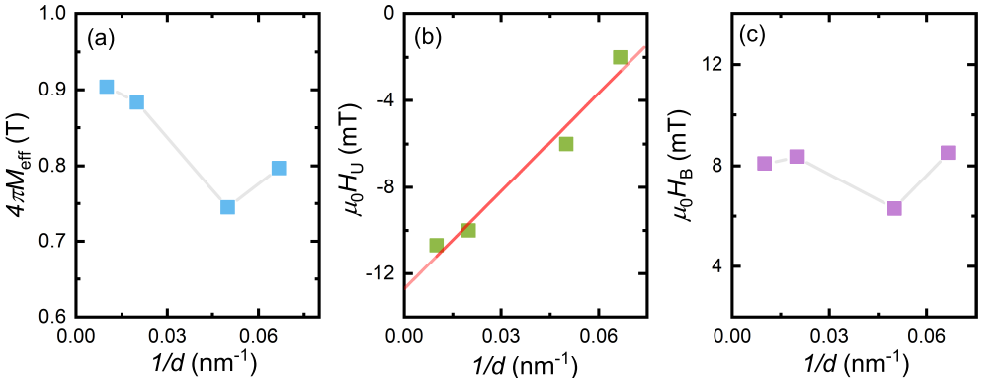

Figure 4.8: The inverse thickness (d^{-1}) dependence of (a) Effective saturation magnetization $4\pi M_{\text{eff}}$ (b) Uniaxial in-plane magnetic anisotropy field, $\mu_0 H_{\text{U}}$ and (c) Biaxial in-plane magnetic anisotropy field, $\mu_0 H_{\text{B}}$. Note - The error bars are smaller than the marker on the plots.

$$H_1 = H\cos(\phi_{\text{M}} - \phi_{\text{H}}) + 4\pi M_{\text{eff}} + \frac{H_{\text{B}}(3+\cos 4\phi_{\text{M}})}{4} - H_{\text{U}}\sin^2(\phi_{\text{M}} - \frac{\pi}{4})$$
$$H_2 = H\cos(\phi_{\text{M}} - \phi_{\text{H}}) + H_{\text{B}}\cos(4\phi_{\text{M}}) - H_{\text{U}}\sin(2\phi_{\text{M}}) \quad (4.4)$$

where ω is the angular frequency, γ is the gyromagnetic ratio, H_{B} and H_{U} are the in-plane biaxial and uniaxial anisotropy constants. By fitting the ϕ_{H} dependence of H_{res}, one can obtain the magnitude of different in-plane anisotropy constants given by $H_{\text{B}}, H_{\text{U}}$ as summarised in Table. 4.3 (shown on page 121). The magnitude of M_{eff} and anisotropy constants increase as thickness increases due to increase of magnetization. The slight deviation occurs for 15 nm sample which is not annealed post-deposition. One can see from Fig. 4.7 that the magnetic hard axis is along [110]. It is seen that both uniaxial and bi-axial (crystalline) anisotropies are present in our epitaxial NiMnSb films for all film thickness. The results are comparable with previous works [170, 173]. Although our films are grown on GaAs and a direct comparison with the films grown on InP is not possible. However, it is found that our results match fairly well with the results of [173] for similar Mn concentration. From the 1/d (thickness) dependence of uniaxial anisotropy H_{U}, a linear dependence was seen which showed a decrease in magnitude with decreasing thickness. This can indicate that interfacial effects do not play a role in modifying H_{U}. Furthermore, the asymptotic value of $H_{\text{U}}(d \to \infty)$ = -12 mT is obtained. Due to anisotropic strain relaxation of in-plane tetragonal strain this anisotropy can exist for thicker films

[170]. From [186, 187] it was found that in Fe/GaAs there is anisotropic strain relaxation along [110] and [1$\bar{1}$0] orientation due to misfit dislocation. However, in our case the lattice constants of two axes (a and b) are same and hence such argument is not true. Thus, further study needs to be done to understand the microscopic origin of the uniaxial anisotropy in these films which can cause symmetry lowering in bulk and thus allowing uniaxial anisotropy to exist. The close agreement between $M_{\rm s}$ value measured by VSM and $M_{\rm eff}$ extracted from FMR analysis further confirm the negligible in-plane lattice strain in our films and hence there is no sizable surface anisotropy arising in both MgO/NiMnSb and NiMnSb/GaAs interfaces. The inplane four-fold anisotropy component $H_{\rm B}$ non-monotonically increases with increases in film thickness for annealed samples. This component exists because of the lattice symmetry which can be expected to give rise to a magnetic anisotropy with the same symmetry, corresponding to the observed four-fold anisotropy component. Also to be noted is that in case of annealed samples $H_{\rm U}$ is larger for 20 nm i.e for sample with lowest vertical lattice constant and the value decreases for increasing vertical lattice constant. A further observation which can provide more insight into uniaxial anisotropy behavior can come from RHEED used for in-situ growth monitoring. Th 4 $\times$1 reconstruction pattern for [110] and 1 $\times$1 reconstruction pattern for [1$\bar{1}$0] direction further confirms the uniaxial anisotropy existence for the films.

4.5.2 FMR linewidth anisotropy

It can be seen from Fig. 4.7 that there is strong oscillation in ΔH for different $\phi_{\rm H}$. As mentioned in Chapter 2 earlier, the in-plane angular and frequency dependence of ΔH can be expressed as:

$$\begin{aligned}\Delta H &= \Delta H_{\rm inhom} + \frac{2\pi\alpha f}{\gamma\mu_0\Phi} + \left|\frac{\partial H_{res}(\omega,\psi_{\rm H})}{\partial\phi_{\rm H}}\Delta\phi_{\rm H}\right| \\ &\quad + \sum_i \frac{\Gamma_{\rm i}^0 f_i(\phi_{\rm H})}{\mu_0\gamma\Phi}\sin^{-1}\left(\sqrt{\frac{\sqrt{\omega^2+(\omega_0/2)^2}-\omega_0/2}{\sqrt{\omega^2+(\omega_0/2)^2}+\omega_0/2}}\right) \\ \Phi &= (d\omega^2/dH)/(\mu_o^2\gamma^2(W_{\rm x}+W_{\rm y})),\end{aligned} \tag{4.5}$$

where the first term is due to the inhomogeneity of the sample. The second is the phenomenological Gilbert damping term with α as the dimensionless coefficient, which is intrinsic in magnetic materials, and depends on frequency. When $\phi_H \neq \phi_M$, a correction factor Φ due to field dragging effect plays a role in linewidth broadening, here W_x and W_y are the stiffness fields. A spatial variation of magnetic anisotropy over a sample causes mosaicity broadening represented by the third term. Detailed explanation has already been given in Chapter 2. The last term represents two-magnon scattering.

From Fig. 4.7 (i-l), it can be found that the magnitude of ΔH around [110] is significantly larger than that along [1$\bar{1}$0] for 15 nm and 20 nm sample. However, it is almost the same for both [1$\bar{1}$0] and [110] directions for thicker samples (50 nm and 100 nm) which is distinctive compared to 15 nm and 20nm results. The smaller value of ΔH around [1$\bar{1}$0] is a first indication of an anisotropic damping for the thinner samples and non-existence of anisotropy in damping in thicker samples. This also shows that the linewidth depends strongly on magnetization orientation. To understand that the anisotropy in linewidth is coming from intrinsic contribution alone or not required more detailed analysis for which other contributions have to be carefully analysed. It has been reported by Kurebayashi et al. [88] that anisotropy in linewidth for ultrathin Fe layer on GaAs can be attributed to two-magnon scattering while in a similar system measured by L.Chen et al. [90] the anisotropic Gilbert damping is indicated responsible for anisotropic linewidth. Hence, all contributions were analysed to understand the anisotropic linewidth behaviour. Within the expression of Eq. (4.5), the field dragging, mosaicity and two-magnon scattering contributions depend on ϕ_H. ϕ_M was numerically calculated from the energy-density relation using Eq. 2.31 and the results are shown in Fig. 4.9.

Based on these values, the line-shape of field dragging versus ϕ_H was calculated as shown in Fig. 4.9 (e-h) and it showed a distorted four-fold symmetry that does not fit with the ΔH measured experimentally. Likewise, the calculated line-shape of the mosaicity contribution (Fig. 4.9 (i-l)) showed another distorted four-fold symmetry. Therefore, the only possibility to explain the in-plane ΔH oscillation

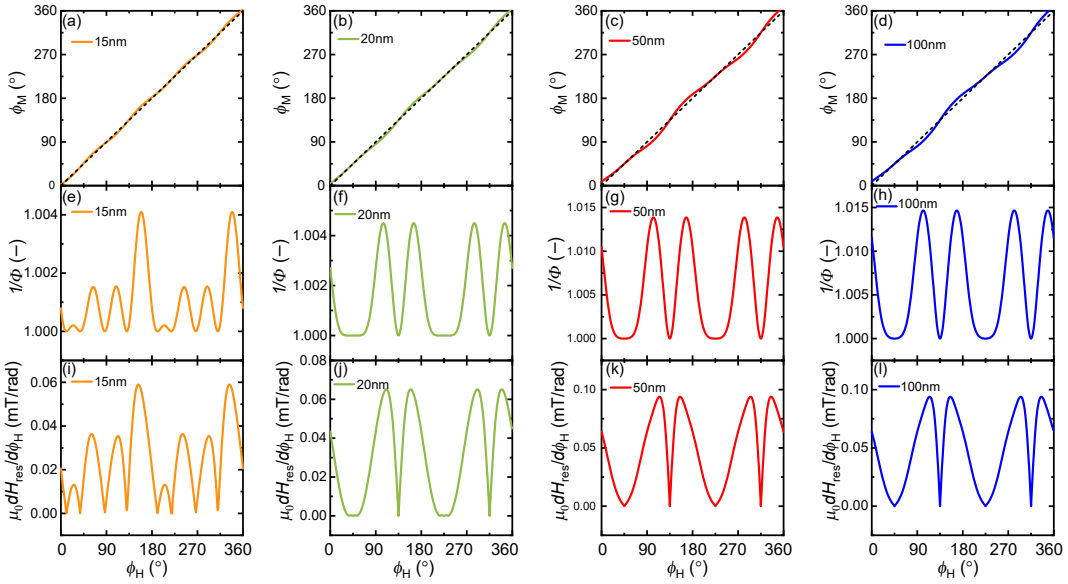

Figure 4.9: (a-d) Equilibrium magnetization angle, ϕ_M, as a function of measured magnetic field angle, ϕ_H, for different samples calculated from Eq. 2.31. The external magnetic field is varied as a function of ϕ_H and the resonant frequency is kept fixed at 5 GHz. The dashed line represents ϕ_M=ϕ_H. (e-h) 1/Φ and (i-l) $dH_{res}/d\phi_H$ calculated from ϕ_M and other FMR fit parameters for different samples.

is either due to intrinsic Gilbert damping or extrinsic inhomogeneous broadening and two-magnon. For this FMR linewidth is extracted for various static field angles ($0^\circ - 360^\circ$) and frequencies in the range (5-12 GHz). In order to quatify the two-magnon scattering component, out-of-plane angular dependence is done starting at in-plane magnetic easy or hard axis.

4.6 Two-Magnon Scattering

As discussed earlier in Chapter 2, the two-magnon scattering is suppressed for normal configurations. For investigating the presence of two-magnon scattering, out-of-plane spectra and frequency dependence of ΔH is examined. If two magnon component is present then linewidth shows a non-linear (convex) behaviour as a function of frequency for the magnetic moment in the sample plane which is different from the linear form of Gilbert contribution ($\Delta H^{\text{Gilbert}}$) as shown in Fig. 2.13. Fig. 4.10 shows the out-of-plane spectra obtained at 5 GHz for 15 nm sample. For all samples the linewidth at $\theta_H = 0^\circ$ was significantly lower compared to $\theta_H = 90^\circ$.

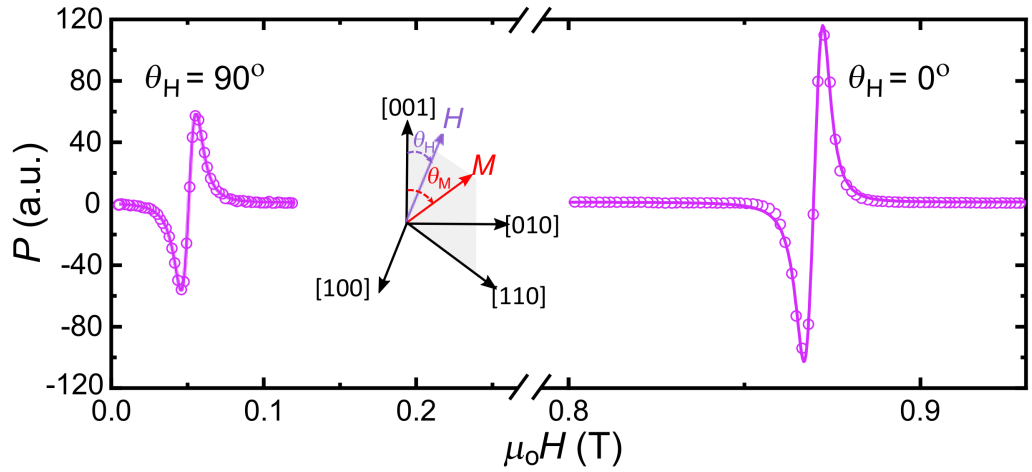

Figure 4.10: Standard full film FMR measurements for out-of-plane rotation. Typical FMR spectra at $\theta_H = 0^\circ$ and 90° for NiMnSb (15 nm). The inset shows the out-of-plane angles of magnetic-field, θ_H, and magnetization θ_M. Here, [001] denotes the out-of-plane (z-direction) and [100], [010] denote x and y-directions respectively.

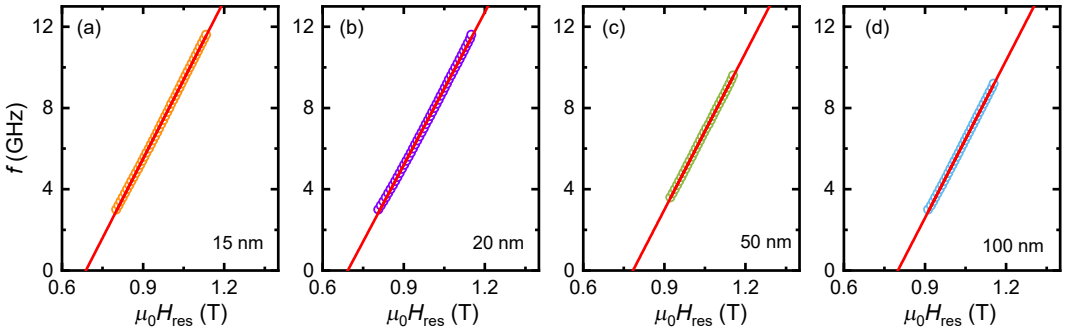

Figure 4.11: Resonance field, H_{res} as a function of frequency for out-of-plane magnetic field direction. The solid lines are the fit curves obtained using Eq. 2.32.

This meant that two-magnon is operative for all samples. The results for frequency dependence in out-of-plane configuration are presented in the following section.

4.6.1 Out-of-plane linewidth frequency dependence

The out-of-plane frequency dependence for resonance field (H_{res}) and linewidth (ΔH) are shown in Fig. 4.11 and Fig. 4.12 From the dependence of ΔH on frequency for different samples as shown in Fig. 4.12, the value of α and ΔH_0 were obtained and summarised in Table. 4.2. The value of α is similar to earlier reported values [188, 173, 189]. The source of large inhomogeneous broadening [190] as evident from the large intercept can be due to surface irregularities. From the AFM

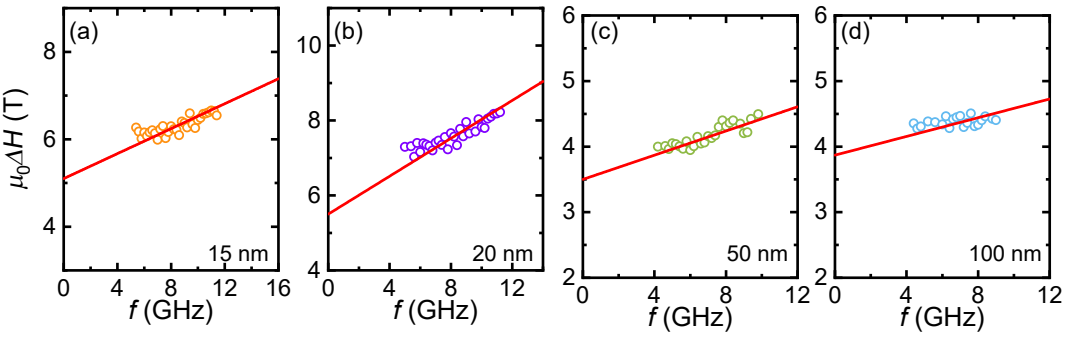

Figure 4.12: Linewidth as a function of frequency for field applied perpendicular to the film plane for which two-magnon is inactive. The solid lines are the linear fitting curves. The value of Gilbert damping parameter, α, is obtained from the slope and the intercept corresponds to the inhomogeneous broadening contribution ΔH_0

Table 4.2: Summary of the magnetic properties extracted from the dependence of resonance field and linewidth on applied frquency for the field perpendicular-to-plane ($\perp$), out-of-plane configuration, along with Gilbert α and inhomogeneous broadening contribution. Note - The uncertainty values reported here are the standard error of the fitting parameters obtained from curve fitting.

Sample Thickness (nm)	$4\pi M_{\text{eff}}^{\perp}$ (T)	$\gamma^{\perp}$ GHz/T	α_{001} ($\times 10^{-3}$)	$\mu_0\Delta H_0$ (mT)	g-factor	$\mu_0 M_s$ (T)
15	0.688 ± 0.002	25.9 ± 1.3	4.1 ± 0.3	5.1 ± 0.1	1.789 ± 0.008	0.561 ± 0.002
20	0.692 ± 0.002	25.2 ± 1.1	7.2 ± 0.4	5.5 ± 0.1	1.741 ± 0.007	0.668 ± 0.006
50	0.783 ± 0.003	25.6 ± 1.1	2.6 ± 0.3	3.5 ± 0.1	1.768 ± 0.007	0.684 ± 0.002
100	0.799 ± 0.003	25.8 ± 1.3	2.3 ± 0.3	3.9 ± 0.1	1.782 ± 0.008	0.732 ± 0.002

measurements (not shown here), the mean average roughness obtained was ~ 0.2 nm for all samples except 20 nm thickness for which it was 0.31 nm signifying substantial amount of surface irregularities. However, this is not always the case as has been noticed in recent studies in Heusler alloys[191]. Inspite of films being crystalline and smooth the origin of large zero-offset as evident from their results was unclear. Apart from this, large inhomogeneities in our samples can be predicted from the FWHM of rocking curve which gives the value $\sim 2.2^{\circ}$ for 20 nm and $\sim 1.5^{\circ}$ for other samples which hint that defects like mosaicity and curvature create disruptions in the perfect parallelism of the atomic planes. Although there is no direct evidence as to the origin of large inhomogeneities [137] from sample structure characterisation so the FMR technique was used to further delve into its origin. The value of g-factor is also summarised in Table. 4.2. It is seen that the value is lower compared to the free electron value of 2.1. This is because in addition

to spin-orbit interaction, the interaction between free electrons/holes with localized moments can also modify the g-factor and be responsible for lower g-factor. It is called s-d or sp-f hybridization [192]. However, whilst this might provide the route to an explanation, the reasons for the low values found here are not completely understood. Also it can be seen that values of M_s are different from M_{eff}. This is because of the presence of out of plane anisotropy as explained in chapter 2.

4.6.2 Out-of-plane linewidth angular dependence

The two-magnon contribution due to interfacial scattering is negligible in our samples due to large thickness of films. For detailed investigation of bulk two-magnon contribution, an out-of-plane scan is done. As mentioned above, two-magnon component can be obtained by analysing the linewidth in vicinity of film normal and comparing it to in-plane case. Decrease in linewidth for perpendicular configuration hints at two-magnon scattering being operative in all the measured films. However, since other inhomogeneous contributions also exist, there is a need to estimate and compare all contributions. For out-of-plane measurements starting at the in-plane magnetic easy or hard axis, the linewidth expression is given by:

$$\begin{aligned}\Delta H &= \Delta H_{\text{inhom}} + \frac{2\pi\alpha f}{\gamma\mu_0\Phi} + \left|\frac{\partial H_{\text{res}}}{\partial\theta_{\text{H}}}\Delta\theta_{\text{H}}\right| \\ &\quad + \sum_i \frac{\Gamma_{\text{i}}^{\text{out}} f_i(\phi_{\text{H}})}{\mu_0\gamma\Phi}\sin^{-1}\left(\sqrt{\frac{\sqrt{\omega^2+(\omega_0/2)^2}-\omega_0/2}{\sqrt{\omega^2+(\omega_0/2)^2}+\omega_0/2}}\right) \\ \Gamma_{\text{i}}^{\text{out}} &= \Gamma_{\text{i}}^{0}\Phi A(\theta-\pi/4)\frac{dH_{\text{res}}(\theta_{\text{H}})}{d\omega(d\theta_{\text{H}})}\Big/\frac{dH_{\text{res}}(\theta_{\text{H}}=0)}{d\omega(d\theta_{\text{H}}=0)}\end{aligned} \tag{4.6}$$

As already explained in Chapter 2, a step function is used to express the two magnon scattering. The equation is similar to in-plane case but two magnon strength $\Gamma_{\text{i}}^{\text{out}}$ is θ_{H} dependent. Fig. 4.13 show the out-of-plane measurements of H_{res}, ΔH and two-magnon linewidth $\Delta H_{2\text{mag}}$. The experimentally measured H_{res} is fitted by a curve produced with magnetic parameters obtained in the in-plane angular dependence measurements as outlined in Sec. 4.5.1, from which θ_{M} is calculated as shown in inset of Fig. 4.13 (a). With these reliable parameters and Eq. 4.6, simultaneous fits were carried out for the out-of-plane angular and frequency dependent

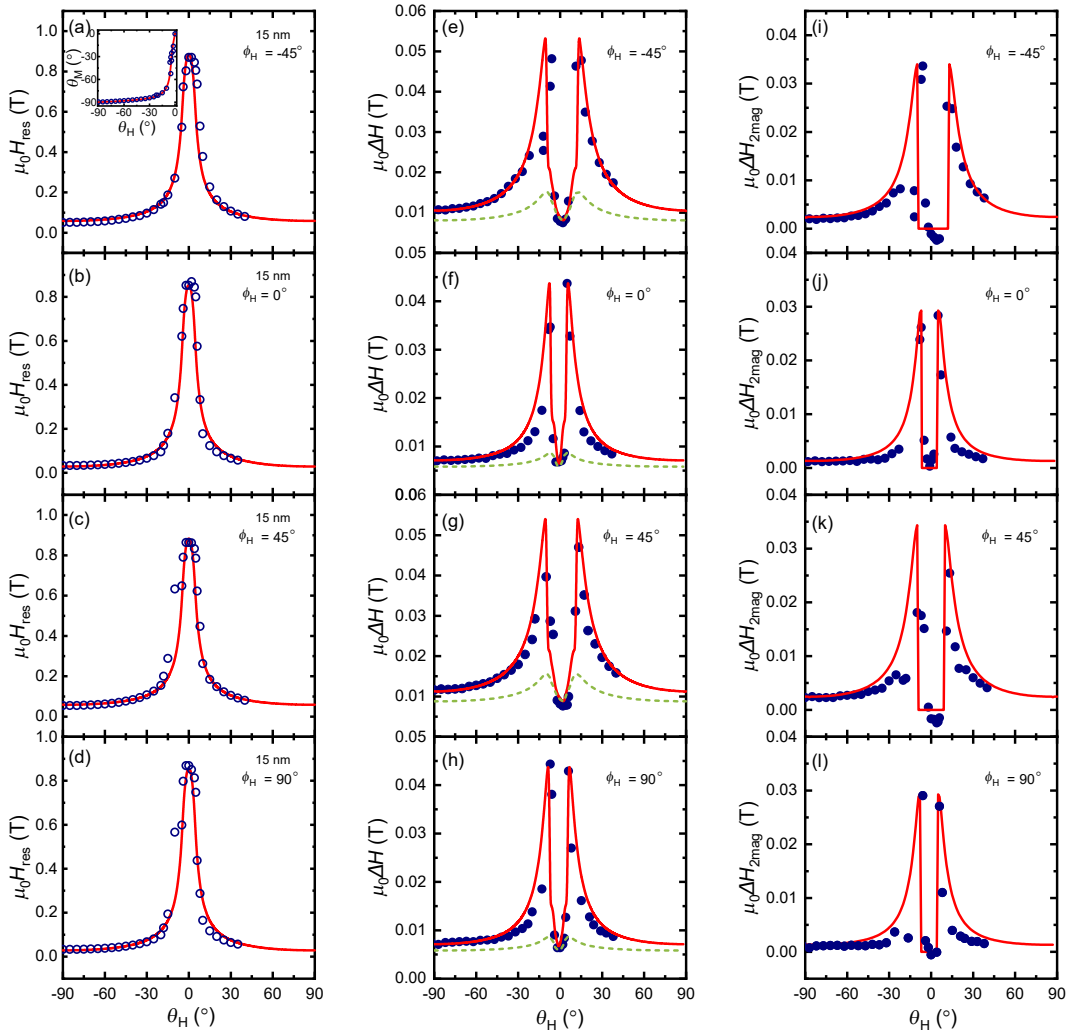

Figure 4.13: (a-d) The resonance field H_{res} and inset (a) the equilbrium angle θ_M as a function of out-of-plane angle θ_H starting from different in-plane angles for the sample with thickness 15 nm. The experimental data is measured at 5 GHz. All the curves shown are result of numerical fits. (e-h) Linewidth ΔH as a function of out-of-plane angle starting from different in-plane angles as in (a-d). (i-l) Two-magnon linewidth components extracted by differentiating measured ΔH from other components as given in Eq. 4.6. The curve is calculated by using the last term in Eq. 4.6.

component of ΔH data as shown in Fig. 4.13 (e-h)[6] which yield the fit parameters as summarised in Table. 4.3, where $\Gamma_{\rm i} f_i(\phi_{\rm H})$ represents the two-magnon scattering strength for $\phi_{\rm H}$. Since, inhomogeneous contributions, two-magnon and intrinsic Gilbert α contributions can all be anisotropc, the data was fitted using two-fold and four-fold components for α (Gilbert damping), $\Gamma_{\rm i}^{out} f_i$ (two-magnon scattering efficiency) and $\Delta H_{\rm inhom}$ (inhomogeneous-broadening) as shown in Eq. 4.7:

$$\alpha(\Gamma_{\rm i}^{\rm out} f_{\rm i}, \Delta H_{\rm inhom}) = a + b \cdot \cos 2(\phi - \frac{\pi}{4}) + c \cdot \cos 4(\phi - \frac{\pi}{4}) \tag{4.7}$$

where, ϕ is the starting in-plane angle. The resultant fit curves are shown in Fig. 4.13 (e-h). A good agreement is seen in experimental data and theory for all cases starting from different in-plane angles.

We then proceed to extract the linewidth originating from the two-magnon scattering by the experimental data and the fitting results, namely using: $\Delta H_{\rm 2mag} = \Delta H - \Delta H_{\rm inhom} - \frac{2\pi\alpha f}{\mu_0 \gamma \Phi} - \left| \frac{\partial H_{\rm res}}{\partial \theta_{\rm H}} \Delta\theta_{\rm H} \right|$. The value obtained for $\Delta H_{\rm 2mag}$ is plotted in Fig. 4.13 (i-l) together with the curve obtained using the last term in Eq. 4.6. All the data is well matched with the curve calculated. However, even using two-magnon term the single isotropic α could not fit the data for hard axis frequency dependence as shown in Fig. 4.18 which shows the anisotropy in Gilbert damping. Furthermore, from fitting, the parameter of two-magnon scattering strength ($\Gamma_{\rm i} f_{\rm i}$) is found to be very small $\sim$ 2 GHz as compared to other works [88]. The low value of two-magnon scattering strength shows that the defect induced spin-wave scattering is not prominent in the sample. Two-magnon scattering can occur if scattering centres in form of defects are present. If they are present as point lattice defects or dislocation lines along the main crystallographic directions, then scattering intensity should reflect the symmetry of lattice. Moreover, the absence of convex dependence when external field is along easy and hard axis (shown in Fig. 4.18) which is typical for systems without two-magnon scattering further confirms the contribution from two-magnon to be small for our samples.

Similar procedure as explained above was followed for fitting the angular de-

[6]Frequency dependence fits shown in later sections

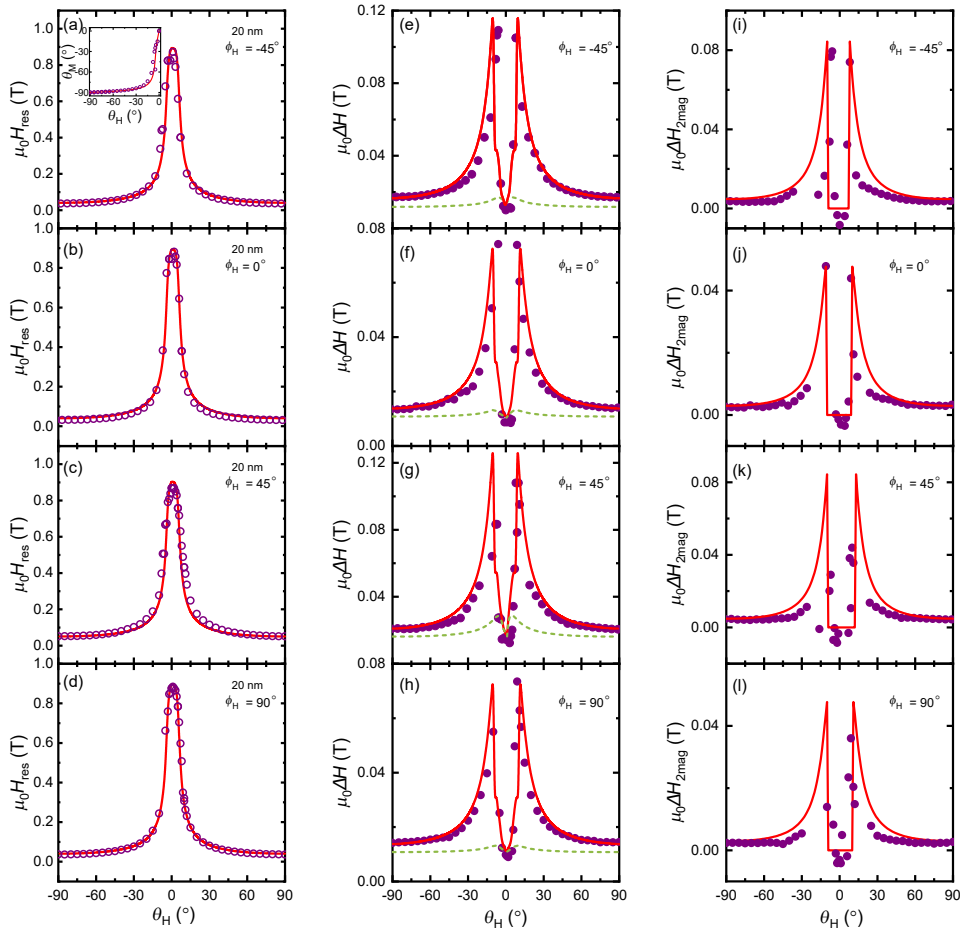

Figure 4.14: (a-d) The resonance field H_{res} and inset (a) the equilbrium angle θ_M as a function of out-of-plane angle θ_H starting from different in-plane angles for the sample with thickness 20 nm. The experimental data is measured at 5 GHz. All the curves shown are result of numerical fits. (e-h) Linewidth ΔH as a function of out-of-plane angle starting from different in-plane angles as in (a-d). (i-l) Two-magnon linewidth components extracted by differentiating measured ΔH from other components as given in Eq. 4.6. The curve is calculated by using the last term in Eq. 4.6.

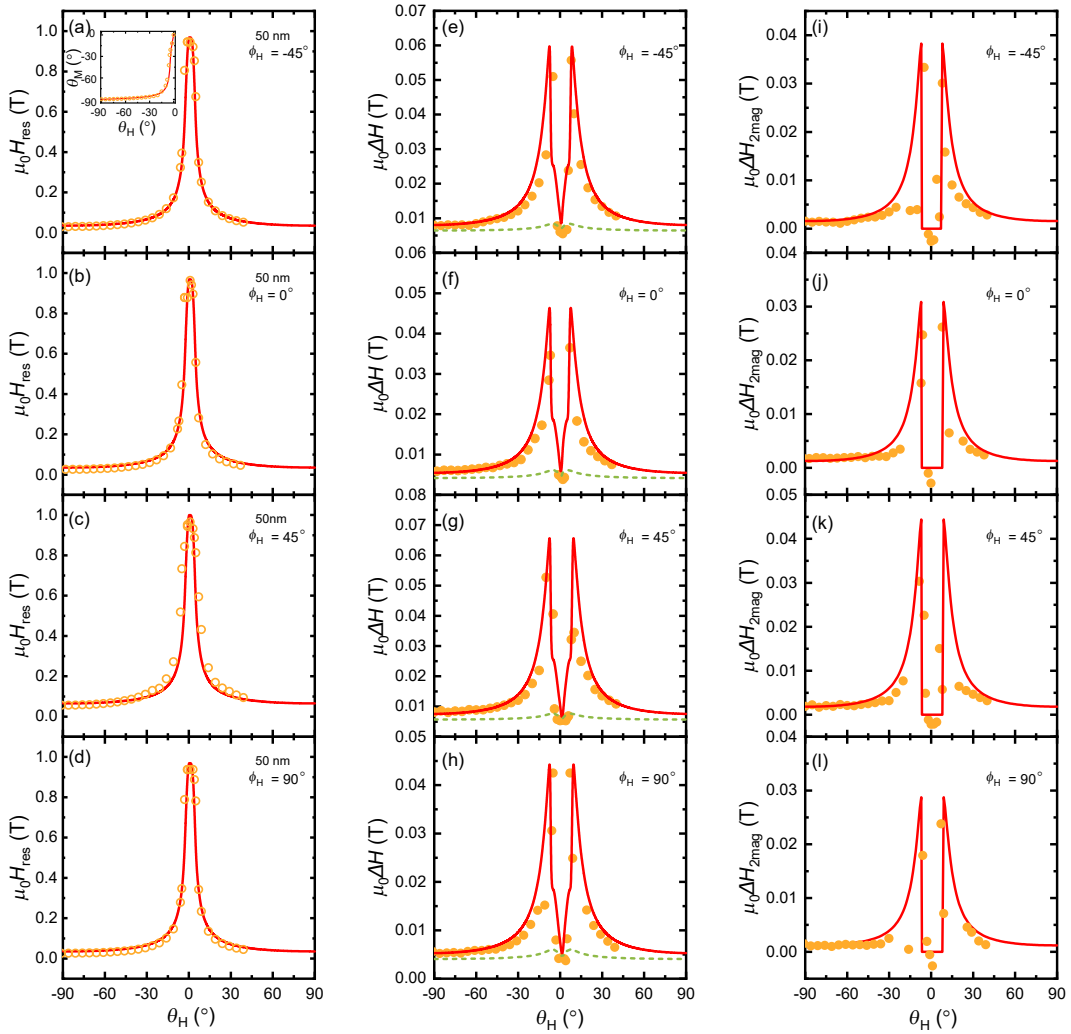

Figure 4.15: (a-d) The resonance field H_{res} and inset (a) the equilbrium angle θ_{M} as a function of out-of-plane angle θ_{H} starting from different in-plane angles for the sample with thickness 50 nm. The experimental data is measured at 5 GHz. All the curves shown are result of numerical fits. (e-h) Linewidth ΔH as a function of out-of-plane angle starting from different in-plane angles as in (a-d). (i-l) Two-magnon linewidth components extracted by differentiating measured ΔH from other components as given in Eq. 4.6. The curve is calculated by using the last term in Eq. 4.6.

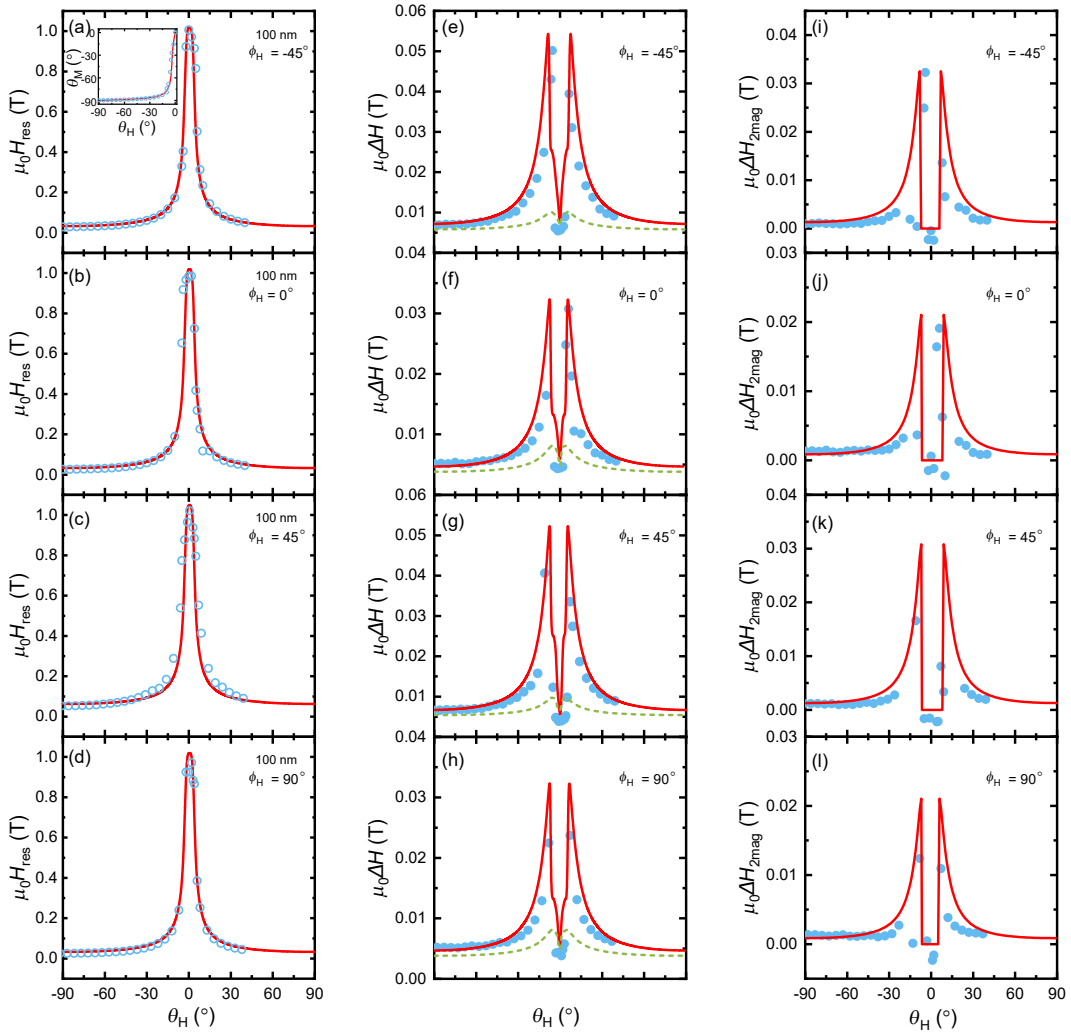

Figure 4.16: (a-d) The resonance field H_{res} and inset (a) the equilbrium angle θ_M as a function of out-of-plane angle θ_H starting from different in-plane angles for the sample with thickness 100 nm. The experimental data is measured at 5 GHz. All the curves shown are result of numerical fits. (e-h) Linewidth ΔH as a function of out-of-plane angle starting from different in-plane angles as in (a-d). (i-l) Two-magnon linewidth components extracted by differentiating measured ΔH from other components as given in Eq. 4.6. The curve is calculated by using the last term in Eq. 4.6.

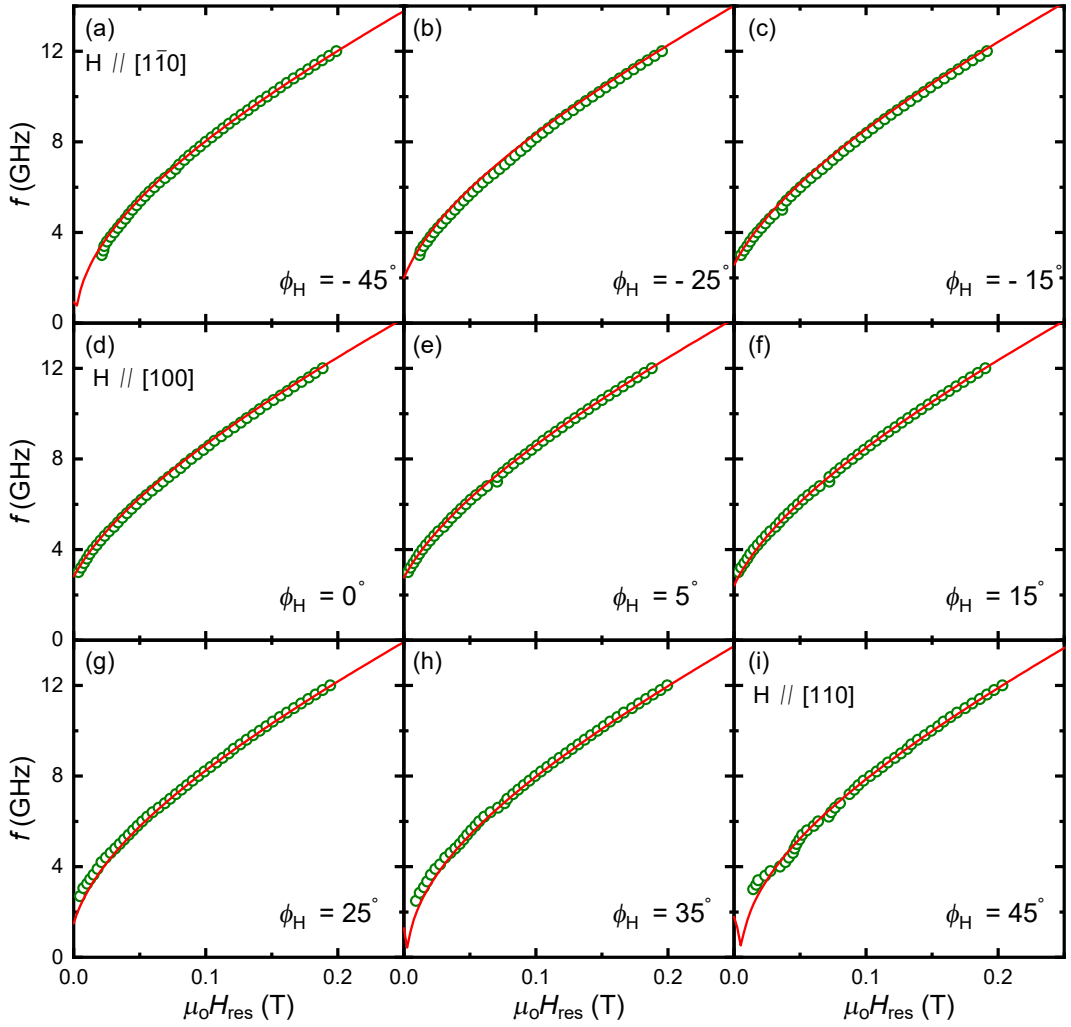

Figure 4.17: Resonance field as a function of frequency for 15 nm sample for different in-plane magnetic field angles between [1$\bar{1}$0] and [110] directions. The solid lines are fit obtained using resonance condition given in Eq. 4.4.

pendence of ΔH for other thickness i.e 20 nm, 50 nm and 100nm as shown in Fig. 4.14, Fig. 4.15, Fig. 4.16. For the thicker films (50 nm and 100 nm) the data could be fitted with single α value for all cases starting from different in-plane angles. Thus, we can say that the α changes from isotropic to anisotropic as the thickness is decreased.

4.7 In-plane frequency dependence of linewidth

Analysing the dependence of ΔH on frequency f is a generalized method for extracting magnitude of phenomenological Gilbert damping paraneter, α accurately. Fig. 4.18 shows the frequency dependence of linewidth, ΔH, along different mag-

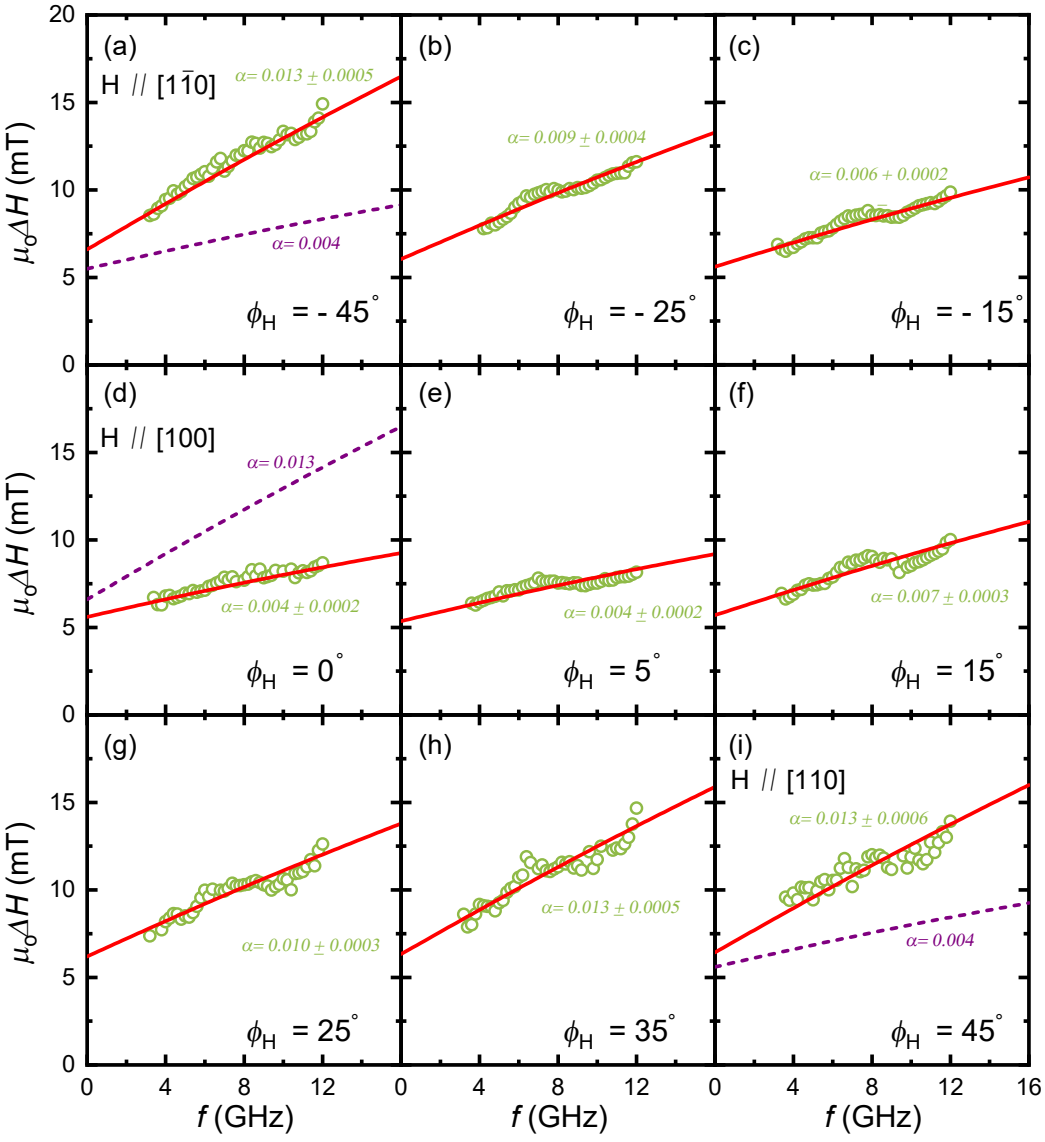

Figure 4.18: (a-j) Dependence of the linewidth, ΔH, on microwave frequency, f, with H along different magnetic field angles between [1$\bar{1}$0] ($\phi_H = -45^\circ$) and [110] ($\phi_H = 45^\circ$) orientations. For different directions the frequency linewidth data shows different slope. The solid red lines are the fitting curves using Eq. 4.5. These results show that damping anisotropy emerges for 15 nm and the damping value gradually increases from[100] to [110]. The dashed lines are calculated using $\alpha = 0.013$ and $\alpha = 0.004$ for [110] and [100] respectively.

netic field orientations for sample with thickness 15 nm. The measuremente were performed for the fields at which the sample is fully saturated. For all directions, ΔH dependence with f show distinctively different slopes indicating the existence of anisotropic damping. Due to small effect of field dragging the value of ϕ_M deviates from ϕ_H for directions other than $[1\bar{1}0]$ and [110]. The frequency dependency of ΔH can be well reproduced considering intrinsic Gilbert damping, inhomogeneous broadening and two-magnon contribution for easy and hard axes where effect of mosaicity broadening and field dragging disappears. The two-magnon component is extracted from out-of-plane angular dependence as explained in previous section. The best fit to data shown in Fig. 4.18 (a-i) (red solid lines) suggest that the magnitude of α gradually increases from [100] to [110] direction. The value of α obtained is comparable to previous works [173]. From the resonance field vs frequency dependence the value of saturation magnetization can be found and the results are summarised in Table. 4.3. The extrinsic contributions to linewidth such as inhomogeneity and two magnon scattering can broaden the linewidth and can cause non linear frequency dependence [193]. However, for all angles a significant linear dependence is seen indicating that two-magnon component is small as has also been obtained from out-of-plane angular dependence.

In Fig. 4.19 to Fig. 4.24 frequency dependence of resonance field and linewidth, ΔH is shown for sample 20 nm - 100 nm. The fit curves were obtained following similar procedure as above. In case of 20 nm, anisotropic damping is prevalent similar to 15 nm but for thicker films, 50 nm and 100 nm, for all directions ΔH shows same slope indicating isotropic damping. The best fit curve shows that linewidth as a function of frequency can be fit by single α value for all angles in thicker samples. Thus, it can be said that α changes from isotropic to anisotropic as the thickness of sample is decreased below a critical thickness. Furthermore α increases as thickness decreases. The mechanisms which can be responsible for the above mentioned change of anisotropic behavior with thickness can be the change in sensing of spin-orbit interaction when thickness is increased. It has been noted that the point group symmetry of NiMnSb is $\bar{4}$3m. The symmetry of these crystals

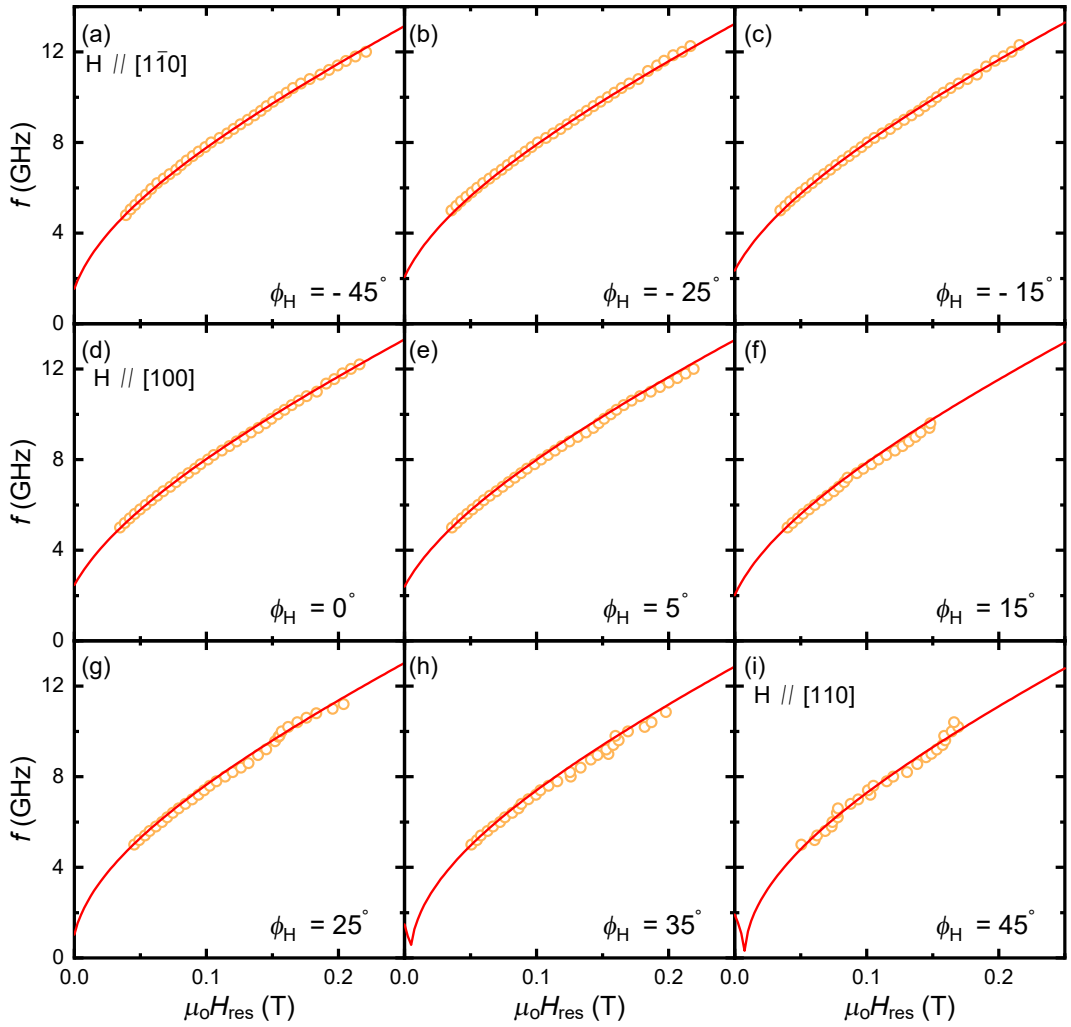

Figure 4.19: Resonance field as a function of frequency for 20 nm sample for different in-plane magnetic field angles between [1$\bar{1}$0] and [110] directions. The solid lines are fit obtained using resonance condition given in Eq. 4.4.

reduces to point group $\bar{4}$2m under a tetragonal distortion, corresponding, for example, to the lattice-matching growth strain [176] which corresponds to Dresselhaus symmetry. The points groups $\bar{4}$2m and $\bar{4}$3m belong to the non-centrosymmetric crystal classes of tetragonal and cubic systems, respectively [194]. Thus, as the thickness is increased, the strength of strain decreases which decreases the Dresselhaus spin-orbit coupling field and thus the symmetry of damping changes. Since the Gilbert damping and its anisotropy are determined by the electronic properties as mentioned in Chapter 2, monitoring the electronic structure should provide a deeper understanding of the experimental observations.

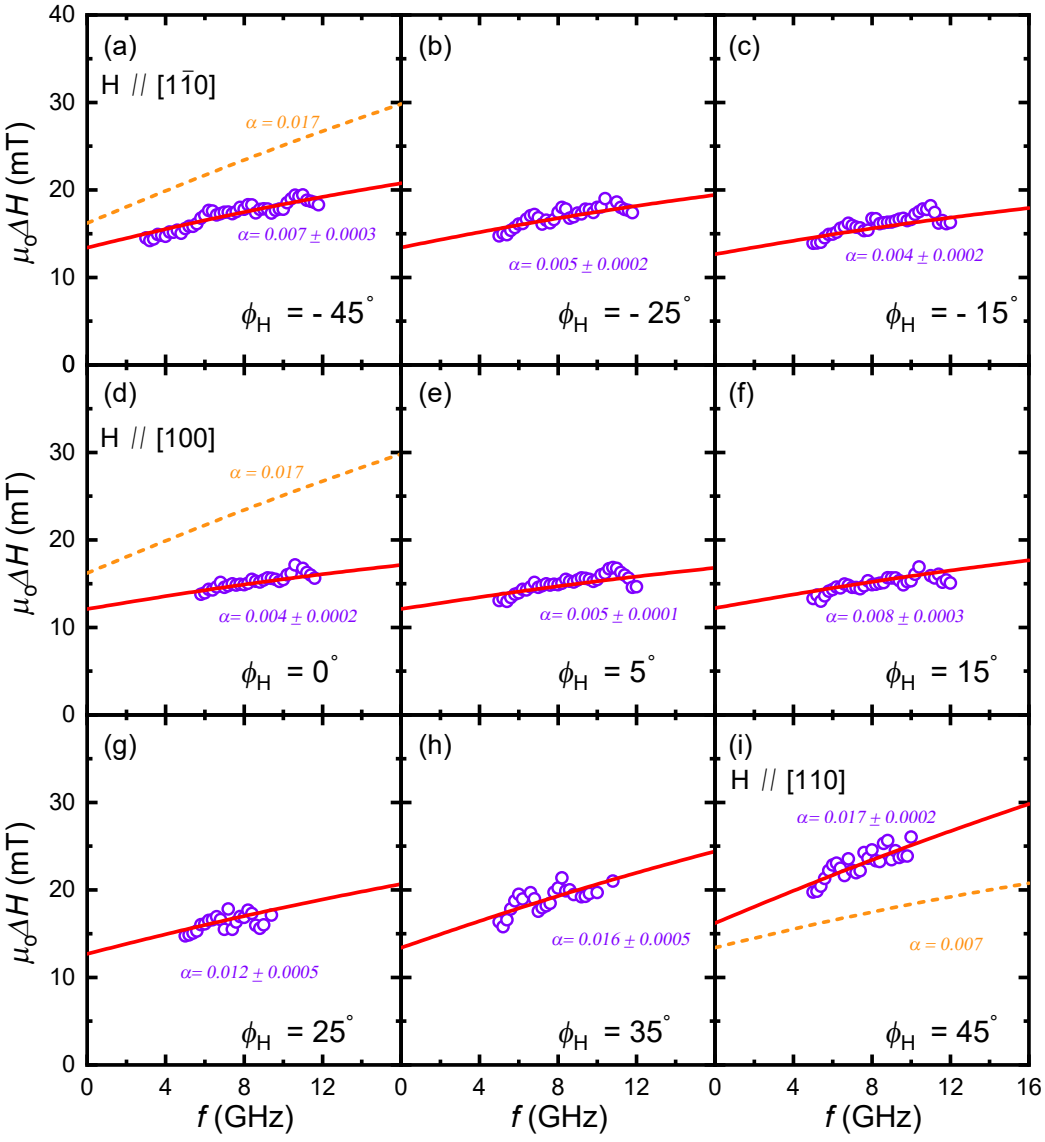

Figure 4.20: (a-j) Dependence of the linewidth, ΔH, on microwave frequency, f, with H along different magnetic field angles between [1$\bar{1}$0] ($\phi_H = -45^\circ$) and [110] ($\phi_H = 45^\circ$) orientations. For different directions the frequency linewidth data shows different slope. The solid red lines are the fitting curves using Eq. 4.5. These results show that damping anisotropy emerges for 20 nm and the damping value gradually increases from[1$\bar{1}$0] to [110]. The dashed lines are calculated using $\alpha = 0.017$ and $\alpha = 0.007$ for [110] and [1$\bar{1}$0] respectively.

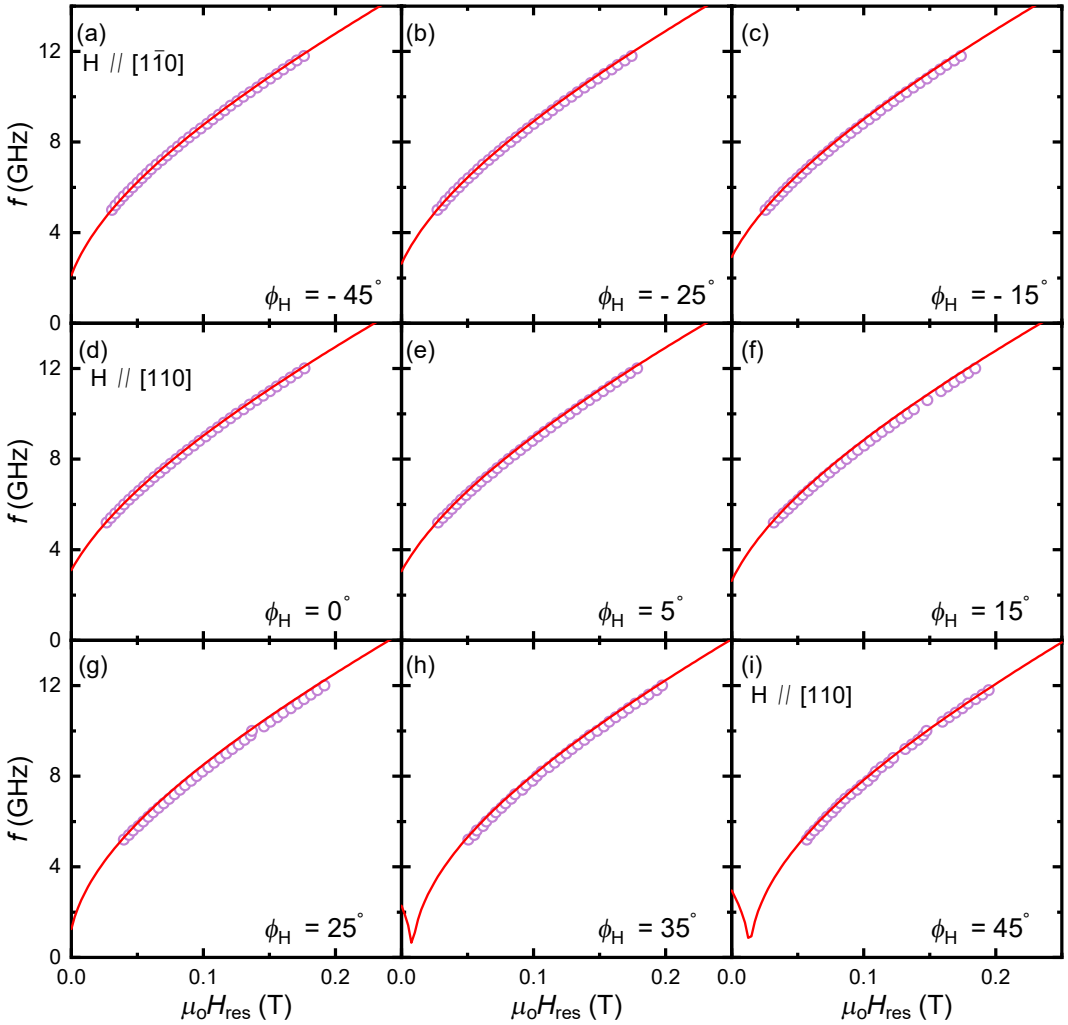

Figure 4.21: Resonance field as a function of frequency for 50 nm sample for different in-plane magnetic field angles between [1$\bar{1}$0] and [110] directions. The solid lines are fit obtained using resonance condition given in Eq. 4.4.

Table 4.3: Summary of the magnetic properties extracted from the dependence of resonance field and linewidth on applied frequency and angle for the field in-plane ($\|$) configuration, along with Gilbert α and two-magnon efficiency contribution. Note - The uncertainty values reported here are the standard error of the fitting parameters obtained from curve fitting.

Sample	$\mu_0 M_{eff}$ (T)	$\mu_0 H_2$ (mT)	$\mu_0 H_4$ (mT)	$\gamma/2\pi$ (GHz/T)	$\alpha_{[1\bar{1}0]}$	$\alpha_{[110]}$	$\sum_i \Gamma_i f_i$ ([1$\bar{1}$0])	$\sum_i \Gamma_i f_i$ ([110])
15 nm	0.797 ± 0.002	-2.02 ± 0.01	8.47 ± 0.03	26.9 ± 1.3	0.0133 ± 0.0005	0.0132 ± 0.0006	1.68 ± 0.01	1.71 ± 0.01
20 nm	0.745 ± 0.004	-6.03 ± 0.01	6.32 ± 0.02	26.1 ± 1.3	0.0069 ± 0.0003	0.0172 ± 0.0002	3.18 ± 0.02	3.63 ± 0.02
50 nm	0.883 ± 0.005	-10.31 ± 0.03	8.33 ± 0.03	26.9 ± 1.4	0.0022 ± 0.0001	0.0022 ± 0.0001	1.41 ± 0.01	1.51 ± 0.01
100 nm	0.904 ± 0.005	-10.73 ± 0.03	8.14 ± 0.03	26.5 ± 1.3	0.0055 ± 0.0002	0.0055 ± 0.0002	1.22 ± 0.01	1.12 ± 0.01

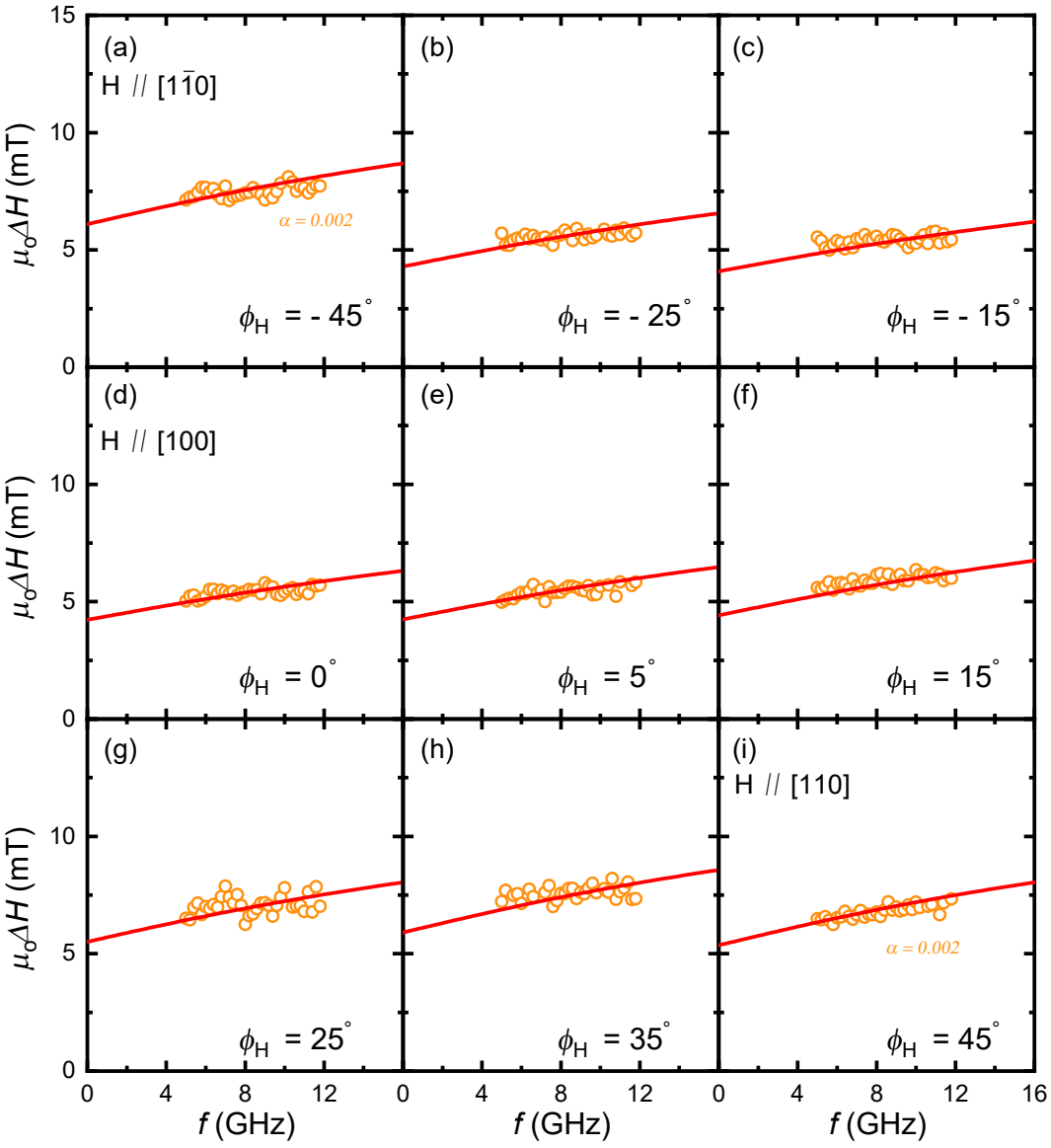

Figure 4.22: (a-j) Dependence of the linewidth, ΔH, on microwave frequency, f, with H along different magnetic field angles between [1$\bar{1}$0] ($\phi_H = -45^\circ$) and [110] ($\phi_H = 45^\circ$) orientations. The solid red lines are the fitting curves using Eq. 4.5. The data for all angles could be fitted with same α showing isotropic damping for 50 nm. The solid lines lines are calculated using α = 0.002 for all directions.

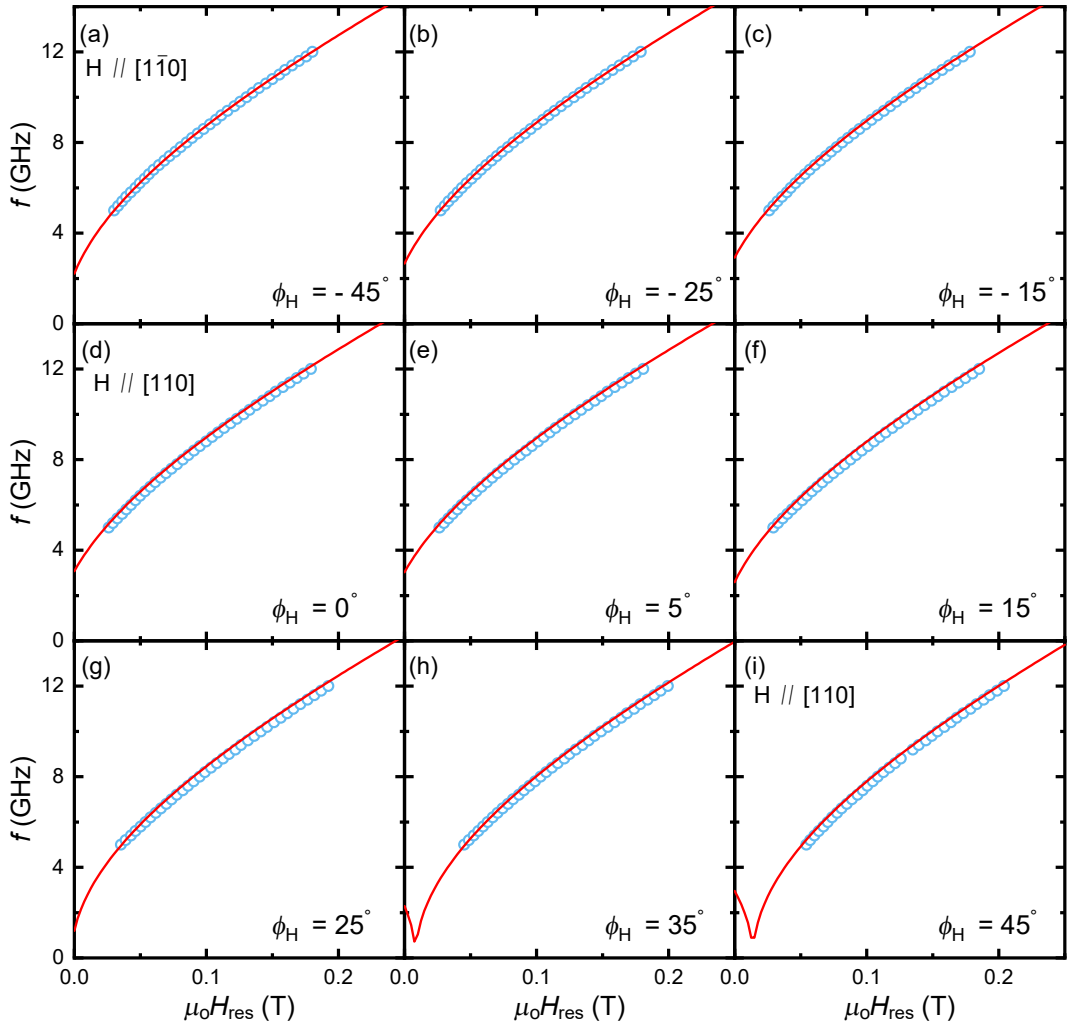

Figure 4.23: Resonance field as a function of frequency for 100 nm sample for different in-plane magnetic field angles between [1$\bar{1}$0] and [110] directions. The solid lines are fit obtained using resonance condition given in Eq. 4.4.

4.8 Anisotropy of Gilbert damping and inhomogeneous broadening

The plot of the Gilbert damping parameter, α, obtained from fitting of linewidth-frequency dependence as in Fig. 4.26 showed the D_{2d} like point group symmetry (see Appendix. B) for 20 nm which coincides with symmetry of crystalline anisotropic magnetoresistance results from previous works [172, 195]. This follows from the symmetry of spin-orbit fields as already shown in Eq. (4.2) that the Gilbert damping depends on strength of spin-orbit interaction. Also, as shown in the recent works [90] the observed anisotropic damping for the ultrathin Fe layers on

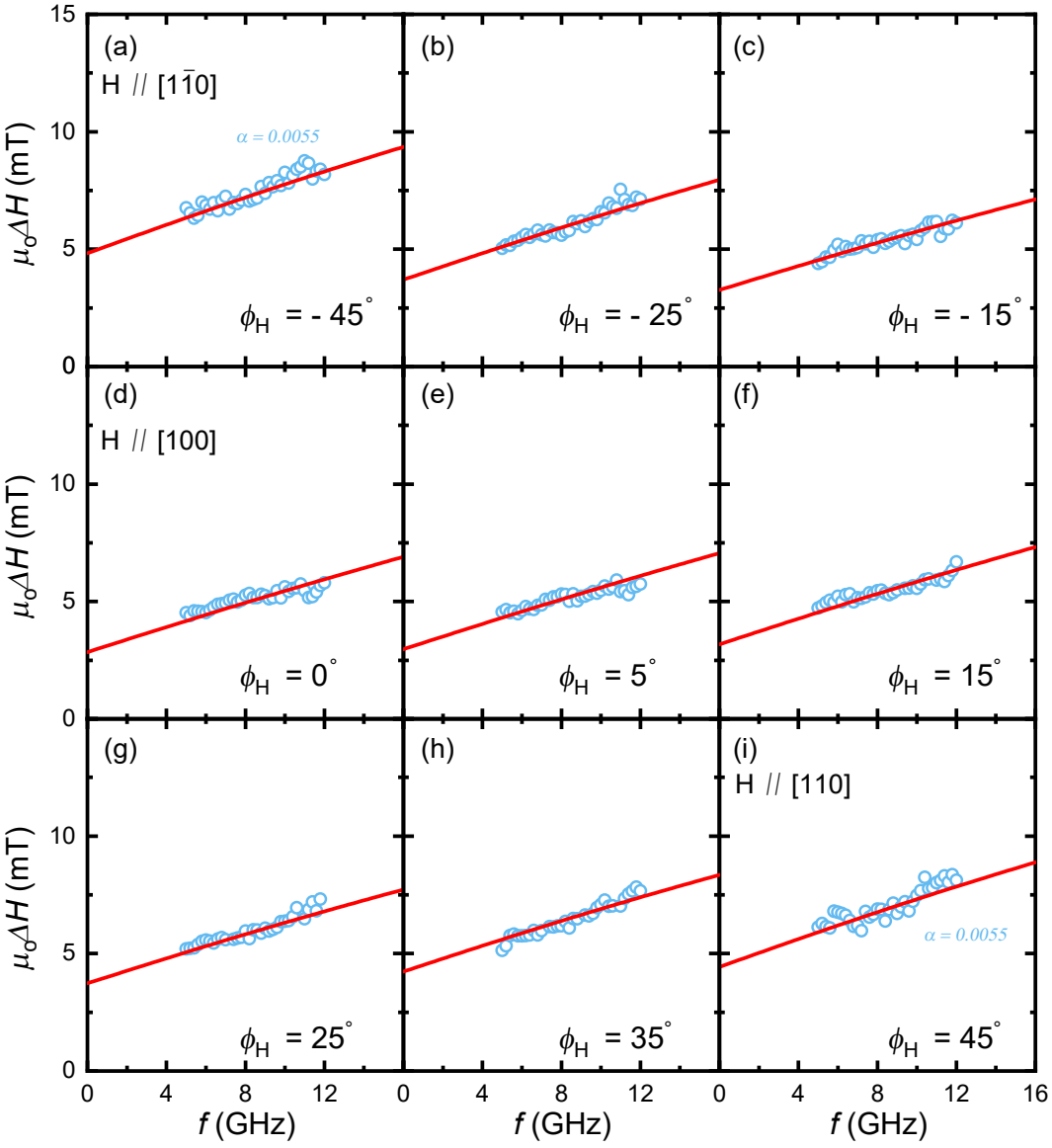

Figure 4.24: (a-j) Dependence of the linewidth, ΔH, on microwave frequency, f, with H along different magnetic field angles between [1$\bar{1}$0] ($\phi_H = -45^\circ$) and [110] ($\phi_H = 45^\circ$) orientations. The solid red lines are the fitting curves using Eq. 4.5. The data for all angles could be fitted with same α showing isotropic damping for 100 nm. The solid lines lines are calculated using α = 0.005 for all directions.

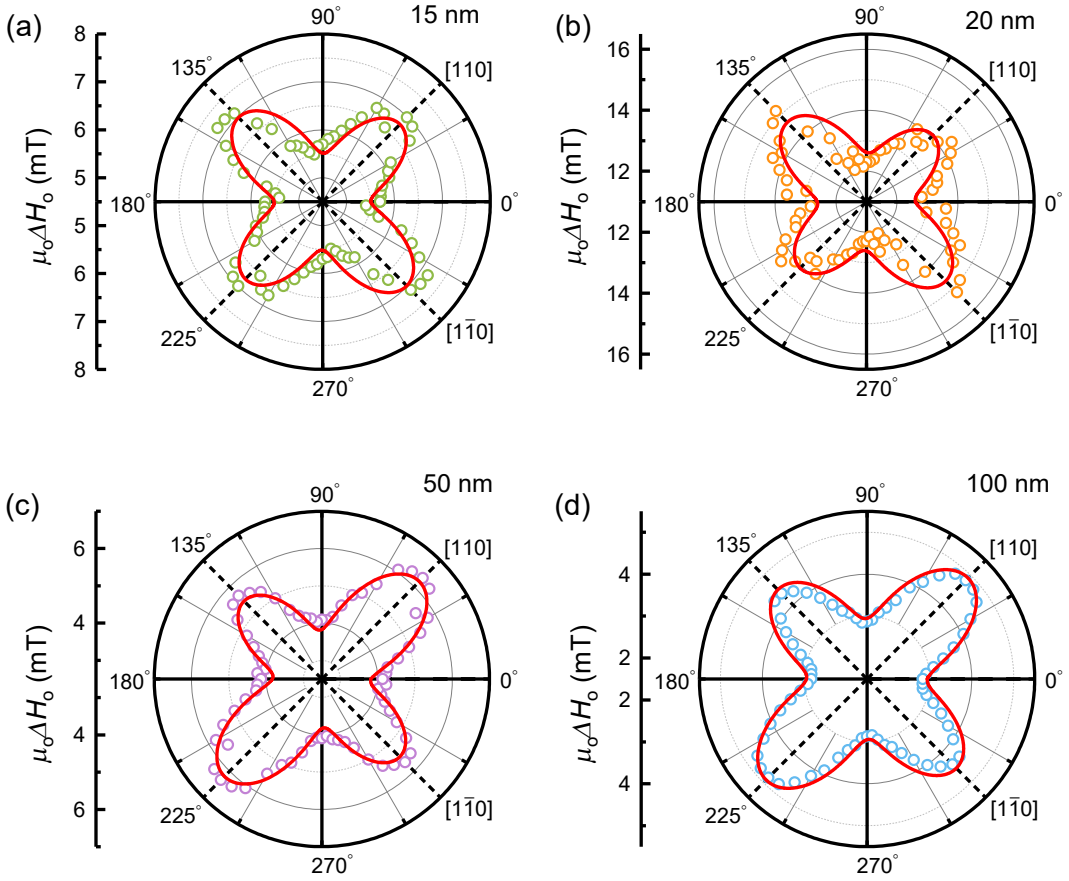

Figure 4.25: Magnetic-field angle dependence of inhomogeneous broadening parameter, ΔH_{inhom}, for different samples. ΔH_{inhom} shows anisotropic behaviour for all samples with a dominant four-fold symmetry.

GaAs comes from the interfacial spin-orbit coupling which modifies the electronic structure on varying the magnetization orientation. In our sample the observed anisotropy of Gilbert damping can be attributed to Dresselhaus spin-orbit coupling arising due to Bulk Inversion Asymmetric nature of crystal structure [172] under tetragonal distortion. For 15 nm however, the symmetry is four-fold represented by C_{4v} point group. This is the sample which is not annealed. This hints that annealing modifies the electronic structure causing variation in SOT efficiency [196] and also symmetry of fields resulting in change in symmetry of damping tensor. It was also found that along with the given anisotropic value of α, the inhomogeneous broadening ΔH_{inhom} as shown in Fig. 4.25 and two-magnon term $\Delta H_{2\text{mag}}$ also showed a distorted four-fold symmetry. This shows that the inhomogeneities are reflected from bulk lattice symmetry. Thus, using the given values of α and ΔH_{inhom} and

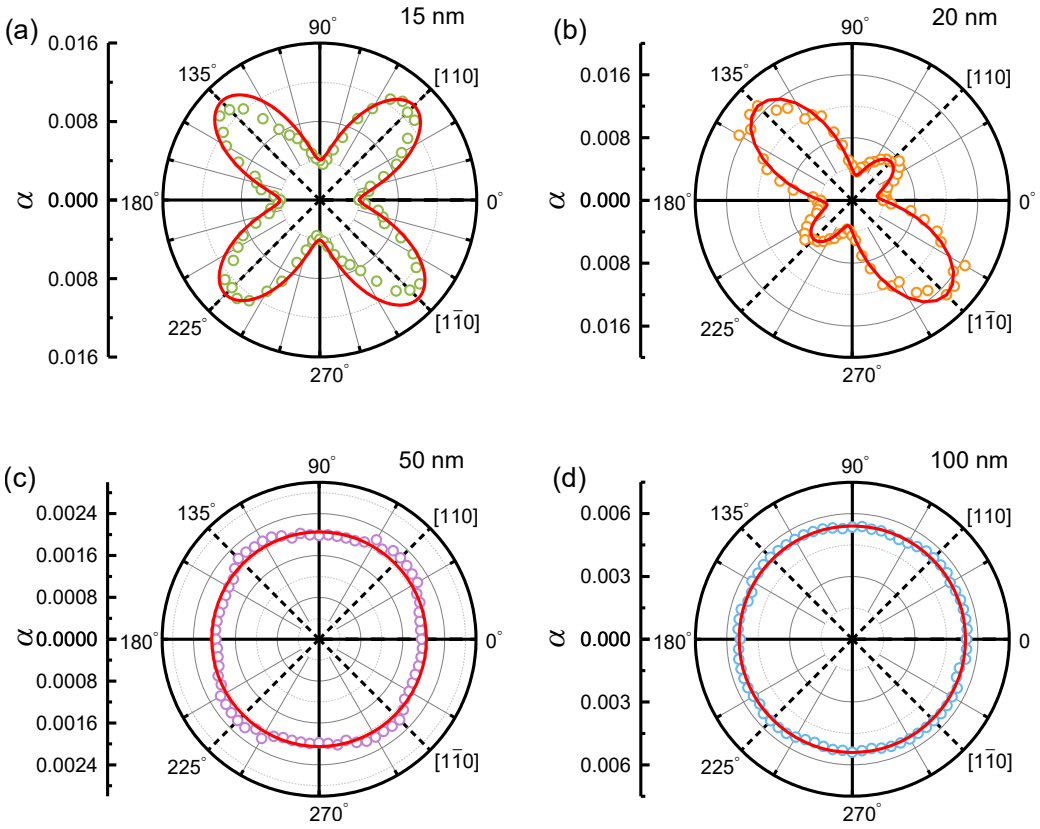

Figure 4.26: Magnetic-field angle dependence of intrinsic damping parameter, α, for different samples. α shows anisotropic behaviour for 15 nm and 20 nm with a dominant four-fold symmetry for 15 nm and two-fold symmetry for 20 nm and is isotropic for thicker samples.

$\Delta H_{2\text{mag}}$ we can explain the given anisotropy in linewidth. To be noted is that for thicker samples the behavior for α becomes isotropic as explained earlier.

In a microscopic picture, we can say that the shape of fermi surface depends on the orientation of the magnetization due to SOC. Hence, the anisotropy in damping can be attributed to the angle dependence of $D(E_F)$. The diminishing anisotropy in thicker samples can be explained by the modification of the Fermi surface and thus $D(E_\text{F})$ by interfacial strain relaxation. In particular, anisotropy in linewidth can be attributed to inhomogeneous broadening and two-magnon contribution for 50 nm and 100 nm samples and to combined effect of Gilbert damping, inhomogeneous broadening and two-magnon for 15 nm and 20 nm sample in which the anisotropy in the spin-orbit interaction responsible for crystalline magnetic anisotropy leads to anisotropy of α with similar symmetry [12].

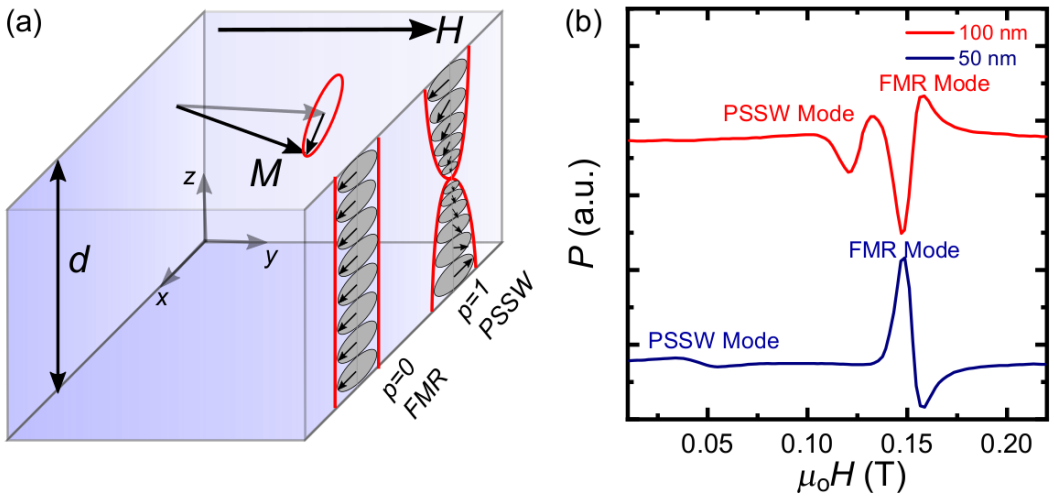

Figure 4.27: (a) Schematic representation of FMR and PSSW modes in magnetic film. Here d refers to the thickness of the film. (b) Resonance curves for $f = 10.8$ GHz for 50 nm and 100 nm thickness. The PSSW mode is seen on the left and FMR mode is seen on the right. Exchange stiffness constant increases with film thickness leading to shift of PSSW mode to right in thicker films.

Further discussion that needs to be done is that although all the samples exhibited the uniaxial anisotropy, the anisotropy in Gilbert damping is apparent only for thin samples, this excludes a direct link between effective field and anisotropic damping. It can be said that damping is a transport quantity (dominated by dynamical electrons near Fermi surface) and magnetic anisotropy is a static quantity as determined by second order perturbation theory that contains contributions not only from states at fermi level but all occupied states. Thus magnetic anisotropy depends on contribution from all filled bands but damping depends only on states at fermi level and so both of them need not be linked directly. Because of this, it is impossible to predict anisotropy quantitatively from microscopic calculation.

We can further say that considering the electronic contributions to damping from bulk and interface, the decrease in α value with thickness as evident from experimental results as well shows that appearance of anisotropic damping is not abrupt. The mechanism which can be responsible for this behavior can be attributed to electronic band effect dominating the damping near the interface which diminishes as we go away from interface. Thus we can say that the response at interface is stronger than bulk.

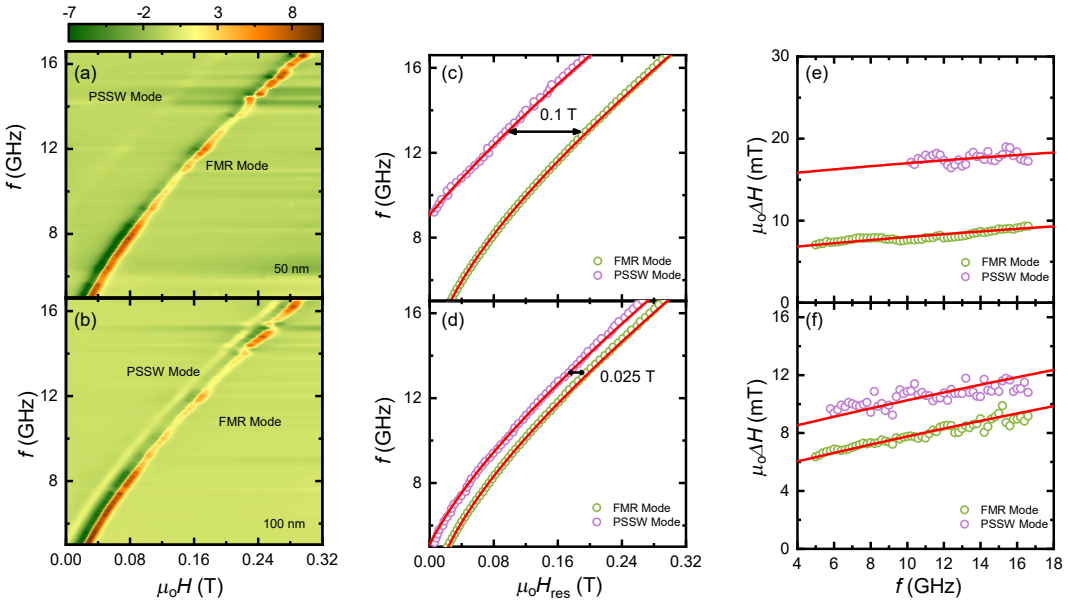

Figure 4.28: 2D colorplot of FMR absoprtion measured from scan of resonace frequency f as a function of applied magnetic field for (a) 50 nm and (b) 100 nm film thickness. (c-d) Resonance frequency f as a function of resonance field for the uniform (FMR) mode and PSSW mode for magnetic field applied at ϕ_H = -45° for 50 nm and 100 nm. The solid lines are the fitting curves. (e-f) Linewidth as a function of frequency for FMR and PSSW mode extracted by fitting the resonance spectra for (e) 50 nm and (f) 100 nm.

4.9 Exchange spin wave resonance in NiMnSb

In addition to the zero wave vector uniform FMR mode described in previous sections where all of the spins precess in phase through the film thickness, additional higher order spin wave modes can be excited in thin film samples. One such higher order mode is called perpendicular standing spin wave (PSSW) mode, schematically shown in Fig. 4.27. The PSSW mode was excited and readily measured in relatively thick films of NiMnSb (50 nm and 100 nm). For thinner films (15-20 nm) no PSSW mode is detected due to the higher frequency which surpassed the available bandwidth (2-20 GHz). The PSSW mode has a nonzero wave vector pointing out of the film plane and its amplitude and phase is dependent on the film thickness [98, 105]. Due to non-uniform strength of microwave field across the film thickness, the PSSW mode was excited efficiently as can be seen in Fig. 4.27 (b).

To explore the characteristics of the PSSW mode, frequency dependent measurements were done with magnetic field in the film plane as shown in Fig. 4.28

(a-d). Both FMR and PSSW mode can be fitted independently since they are well separated by exchange field, H_{ex}. It can be seen that similar to uniform FMR mode, the resonance of PSSW mode can be described by using modified resonance condition (Eq. 4.4) with the term H in H_1, H_2 being replaced by $H + H_{ex}$. The modified equation for $\phi_M = \phi_H$ is given as:

$$\left(\frac{\omega}{\gamma}\right)^2 = \mu_0^2 H_1 H_2 \tag{4.8}$$

$$\begin{aligned} H_1 &= H + H_{ex} + 4\pi M_{eff} + \frac{H_B(3+\cos 4\phi_M)}{4} - H_U \sin^2(\phi_M - \frac{\pi}{4}) \\ H_2 &= H + H_{ex} + H_B \cos(4\phi_M) - H_U \sin(2\phi_M) \end{aligned} \tag{4.9}$$

Here, H_{ex} represents the exchange field given as:

$$H_{ex} = \frac{2A}{\mu_0 M_s}\left(\frac{n\pi}{d}\right)^2 \tag{4.10}$$

where the parameters A, n, d represents exchange stiffness, order of PSSW mode and film thickness respectively. The offset in magnetic field between uniform and FMR mode as shown in Fig. 4.28 (c-d) represents H_{ex}. Using the values of $\mu_0 M_s$ as 0.684T and 0.733 T for 50 nm and 100 nm respectively and $n = 1$ (first PSSW mode), the value of exchange stiffness was calculated as 6.9 pJ/m for 50 nm and 6.82 pJ/m for 100 nm sample which is similar to earlier reported works [102]. We further look into the damping of PSSW mode by fitting the frequency dependence of linewidth as shown in Fig. 4.28 (e-f). Both FMR and PSSW mode can be fitted by similar value of damping given by α = 0.002 for 50 nm and α = 0.005 for 100 nm however, the extrinsic contribution coming from inhomogeneous broadening is larger for PSSW mode for both the samples. Since PSSW mode is confined by boundary conditions between two surfaces as shown in Fig. 4.28, implying that surface inhomogeneity have profound effect for PSSW mode.

We further look into the PSSW mode by performing the angular dependence at fixed frequency. Fig. 4.29 (a-b) shows the contour maps of the measurements for the sample 50 nm and 100 nm at f = 10.8 GHz and 8 GHz respectively. The

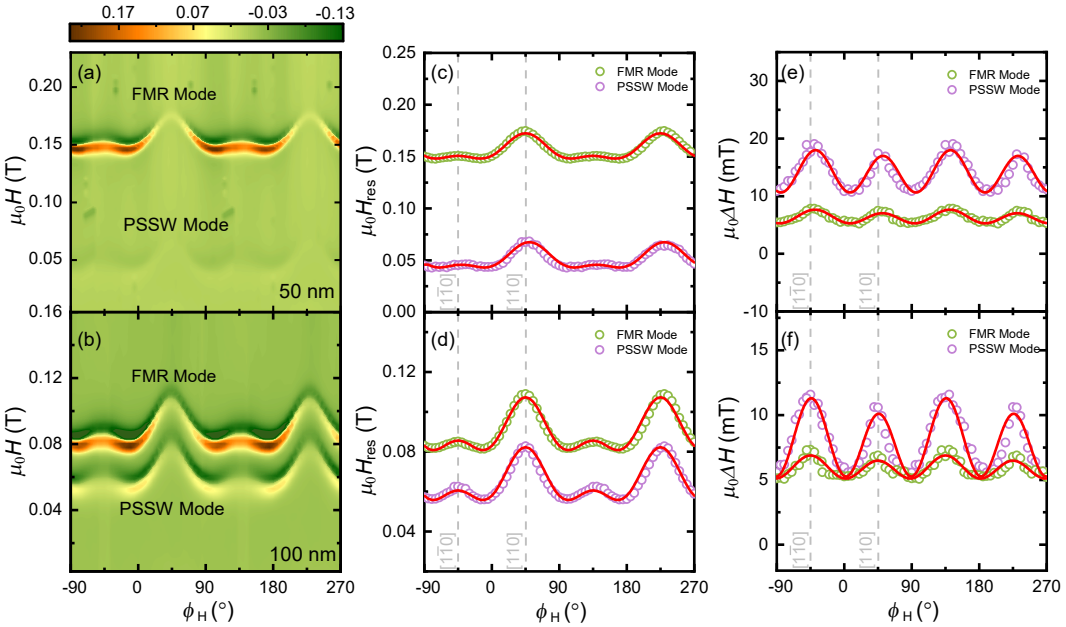

Figure 4.29: (a-b) 2D plot of the resonance absorption measured from an in-plane rotational scan of external magnetic field as a function of applied magnetic field and angle at f =10.8 GHz for 50 nm and f = 8GHz for 100 nm. (c-d) In-plane angular dependence of FMR resonance field H_{res} obtained from fitting FMR and PSSW scans for different set of samples. (i-j) Corresponding Linewidth, ΔH as a function of in-plane rotational angle for different sample thicknesses.

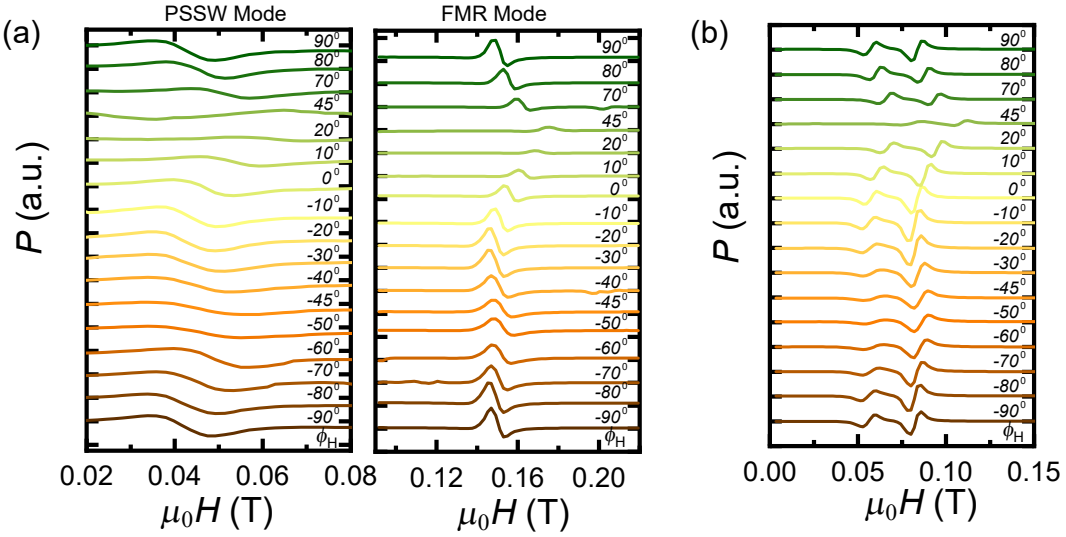

Figure 4.30: Resonance Spectra for FMR and PSSW modes obtained from rotational scan of the in-plane applied magnetic field at f =10.8 GHz for (a) 50 nm and (b) f = 8GHz for 100 nm.

resonance spectra obtained from the angular dependence are shown in Fig. 4.30. Resonance field as a function of magnetic field angle, ϕ_H obtained from fitting the spectra is plotted in Fig. 4.29 (c-d). It can be seen that both uniaxial and bi-axial anisotropies are present in magnetic field angle dependence of PSSW mode similar to uniform FMR mode and the two resonance modes are well separated by a uniform gap equivalent to H_{ex} field. The resonance at higher magnetic field is the uniform FMR mode, while the one at lower field can be attributed to the first PSSW mode [197]. Corresponding angular dependence of linewidth for the two modes is shown in Fig. 4.29 (e-f). The two resonance modes share similar anisotropy in linewidth as apparent from Fig. 4.29. This anisotropy in PSSW mode can be attributed to a similar reasoning as for FMR mode.

4.10 Conclusion

To summarise, in this study the crystalline anisotropy of the intrinsic Gilbert damping has been demonstrated for NiMnSb film on GaAs substrate. The extrinsic contributions to the FMR linewidth from two-magnon and inhomogeneous broadening were separated from the intrinsic damping effect by doing in-plane and out-of-plane rotational measurements and quantifying the parameters separately. A two-fold and four-fold symmetry in α was clearly observed for 20 nm sample and 15 nm sample respectively with the value of α along the easy axis being smaller then along hard axis. This interesting characteristic should be considered when building spintronic devices for future use. Where previously it has been considered that damping is isotropic our work provides a strong evidence of anisotropic nature of magnetization relaxation.

Moreover, the dependence of anisotropic damping on thickness has also been studied. The diminishing anisotropy with increasing thickness can be used for future tuning of anisotropic damping. The isotropic behavior seen in thicker film (50 nm and 100 nm) can be attributed to the decrease in strength of interfacial strain in these samples with increasing thickness, which should decrease the Dresselhaus spin-orbit coupling field. Also considering electronic contributions from bulk and

interface, the decrease in anisotropy with thickness shows that response at interface is stronger than the bulk.

Additionally, the PSSW mode was observed in thicker films and the exchange stiffness constant was determined. Both FMR and PSSW mode show similar anisotropy in magnetic field and linewidth.

In addition to the the works summarized above, there are still several things that can be done in future. First is investigating the effect of temperature on linewidth and damping anisotropy. Temperature dependence measurement can give a deeper understanding on the mechanism behind damping anisotropy. Apart from this it is desirable to understand the effect of stoichiometry on damping anisotropy i.e effect of changing stoichiometry from Ni-rich to Mn-rich sample. It has been shown in earlier works [197] that composition affects the magnetodynamic properties and it will be worthwhile to check the effect on relaxation parameters as well. Finally, in a broader picture, other members of half-Heusler alloy family like IrMnSb, CoTiSb can be studied which will offer more flexibility and tunability for future control of damping and subsequent device buildup.

Chapter 5

Tunable magnon-magnon coupling in synthetic antiferromagnets

5.1 Introduction

Generating new spin-wave states can be an enabling role for developing future spintronic/magnonic devices [198]. While individual spin-wave modes can be tailored by changing material parameters of host magnets, a novel approach of creating new spin-wave states is to couple two modes coherently by tuning them into resonance, where physical parameters of the coupled modes can also be modified. Although the coupling phenomena could be phenomenologically explained by a classical coupled-oscillator picture in general, microscopic descriptions of this type of hybridisation are rich, offering novel functionalities of state control and energy/information transfer. For example, strong coupling of light-matter interaction is envisaged to offer fast and protected quantum information processing [199, 200, 201]. Within this expanding research domain, strong coupling between microwave photons and collective spins in magnetically-ordered systems has been extensively studied in recent years [202, 203, 204, 205].

Magnon-magnon coupling has an advantage over the light-matter interaction, in terms of coupling strength. The coupling strength of light-matter interactions is sometimes significantly reduced by a lack of spatial mode overlapping of the two, and so scientists have made considerable efforts to achieve large coupling

strength by designing optimum geometries for efficient mode-volume overlapping [206, 207]. On the other hand, magnon-magnon interaction does not suffer from this since two modes normally reside within the same host media, providing mode overlapping of 100% or close to. While magnon-magnon coupling has been studied in single magnets [208, 209, 210, 211] and magnetic bi-layers [212, 213, 214], magnon-magnon interaction in highly tunable material systems could offer unexplored parameter spaces on which to tailor the coupling phenomena. Synthetic antiferromagnets (SyAFs) as a host for magnon-magnon coupling have attracted prodigious interest due to the controllable exchange coupling in the GHz regime[215] making them a test bed for various magnonic applications. Moreover, the ease of fabrication and miniaturization allowing them to be integrated into microwave circuits have allowed the realization of broad device concepts for use in coherent information processing [216] and microwave electronics [217].

In this chapter, the study of magnon-magnon coupling is reported in SyAFs using microwave spectroscopy at room temperature. Two distinct spin-wave modes arising from interlayer exchange coupling between two magnetic layers are clearly observed and are hybridised at degeneracy points. A full phenomenological model is provided for the mode coupling, magnetic relaxation and coupling strength as a function of different material parameters for SyAF modes. Aided by these derived relationships, it is demonstrated that the interlayer exchange field strength, which can be controlled by sample growth, allows the engineering of the coupling strength. Along with this the tunability of coupling strength by out-of-plane-tilt angle is demonstrated experimentally. It is further numerically shown that the spin-current mediated damping plays a role in influencing the coupling strength. Our demonstration and full details of the magnon-magnon coupling phenomena in SyAFs will act as a springboard for further research along this avenue [215].

Further, the magnon-magnon coupling phenomena is explored in asymmetrical SyAF, referred to as as synthetic ferrimagnets (SyFs) where the presence of structural asymmetry either due to imbalance in layer thickness of two ferromagnets or the dissimilar ferromagnets breaks the degeneracy of two modes as in symmetri-

cal SyAFs. This symmetry breaking facilitates the mode coupling significantly and both experimentally and quantitatively the mode coupling phenomena is described in SyFs.

5.2 Synthetic-Antiferrromagnet sample

A SyAF is a multi-layer structure consisting of two ferromagnetic (FM) thin films coupled antiferromagnetically through a non-magnetic spacer (NM) [215, 24]. Stacking a number of FM bilayers with antiferromagnetic coupling forms a superlattice as shown in Fig. 5.1. Weak interlayer coupling in these materials comes mainly from oscillatory Ruderman-Kittel-Kasuya-Yosida (RKKY) coupling [218, 219, 220] which is the magnetic analogue of Friedel-like oscillations caused by adjacent ferromagnetic layer in the spin density of non-magnetic spacer. For thick spacer layers the interlayer exchange coupling is suppressed. Varying the thickness of spacer allows the tuning of interaction from ferromagnetic (parallel alignment) to anti-ferromagnetic (anti-parallel alignment). As compared to the crystal antiferromagnets where the spins are atomistically coupled, the dynamics in SyAF can be described by macrospin model of two coupled spins. This is because in case of crystal antiferromagents the phase coherence extends over a distance larger than the length scale of antiferromagnetic order causing macrospin model to break down. Moreover, the interlayer exchange coupling in SyAF is much weaker as compared to direct or superexchange coupling in crystal antiferromagnets. This lowers the energy scale in SyAF down to GHz regime allowing conventional techniques to be employed for studying the dynamics.

5.2.1 Magnon modes

Low-energy spin-wave modes in SyAFs in their canted regime are acoustic and optical modes [221, 222, 223] where two coupled moments precess in-phase (acoustic) and out-of-phase (optical) as shown in Fig. 5.2(a). These modes have been studied and discussed already around 1990s, e.g. by Grunberg et al. using Brilloin light scattering [224] and Zhang et al. by microwave cavity experiments [225]. The acoustic (optical) mode is excited by perpendicular (parallel) configuration

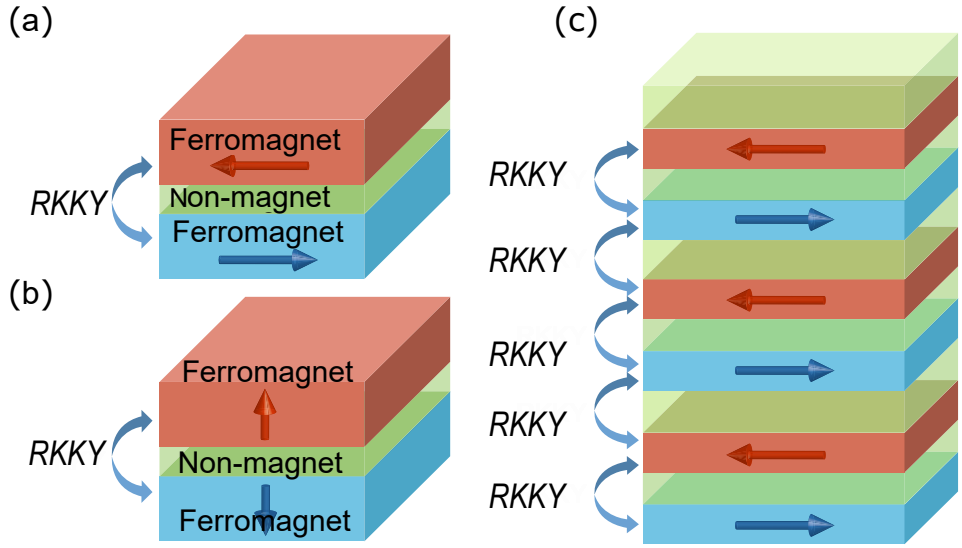

Figure 5.1: Schematic of synthetic-antiferromagnetic bilayers with (a) in-plane magnetization, (b) out-of-plane magnetization. (c) Super lattice structure. The arrows depict the direction of magnetization. RKKY coupling and dipolar fields add (a) or subtract (b) depending on direction of magnetization. Fig. adapted from Ref. [215]. (Note - Sample geometry as in (a) has been used for this study.)

between microwave and applied magnetic fields. There are a number of reports in which these two modes in different SyAFs have been studied in great detail [226, 227, 228, 229, 230]. For example, mutual spin pumping within the coupled moments has been proposed [231, 232, 233] and experimentally demonstrated [234, 235, 236, 237]. Both optical and acoustic mode frequencies as a function of the middle layer that influences the interlayer exchange coupling strength have been studied and reported earlier [238, 237]. Since the resonant frequency of two modes shows different magnetic field dependence (as discussed more later), we can find the degeneracy point of the two modes by tuning experimental conditions. When the two moments are canted within the plane, the motion of the optical and acoustic modes can be decoupled [211], meaning that the two modes are not allowed to hybridise. This restriction can be lifted when we tilt the moments towards the out-of-plane direction and we will be able to hybridise them (see Fig. 5.2(b) for schematic understanding). The strength of hybridisation is defined by g_c which represents a rate of energy transfer between the two modes. When this rate is fast, compared to mode dissipation rates of individual modes, we expect well-defined coupled modes

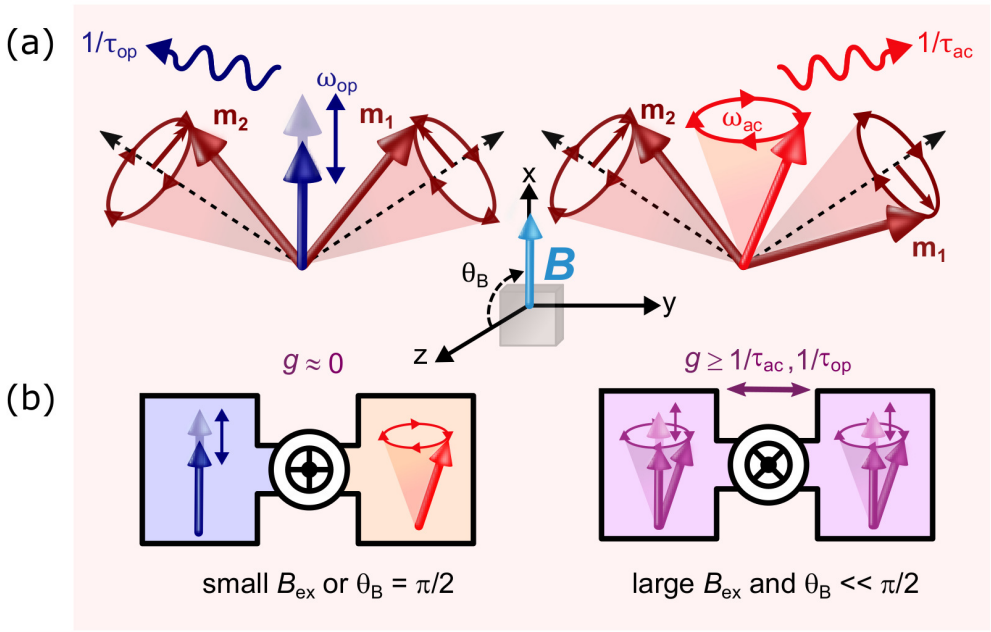

Figure 5.2: (a) Schematic of acoustic and optical modes in SyAFs. Two moments (m_1 and m_2) are coupled antiferromagnetically and canted at equilibrium. Under microwave irradiation, they precess in-phase (acoustic mode) and out-of-phase (optical mode) at different angular frequencies ω_{ac} and ω_{op}, respectively. θ_B is defined as in the figure, where the z axis is the film growth direction. $\theta_B = 90^{\circ}$ corresponds to the field applied in the sample plane. (b) Schematics of the magnon-magnon coupling phenomena with the optical and acoustic modes. When the exchange field (B_{ex}) is small or two moments are within the film plane, the coupling strength (g) is zero, so the two modes do not couple. The coupling strength can be valved by tuning B_{ex} and θ_B and achieve strong magnon-magnon hybridisation, as shown on the right panel.

before the excited states are relaxed. Control of the coupling strength *in-situ* and *ex-situ* will be potentially useful to a scheme of reconfigurable energy and information transfer using coherent coupling.

5.2.2 Sample growth and characterization by vibrating sample magnetometer

The SyAF stacked films used in this study[1] were prepared by magnetron co-sputtering at a base pressure of 1×10^{-7} Pa. The films were grown on a Si oxide substrate with the stacking pattern of Ta(3 nm)/CoFeB(3 nm)/Ru(t nm)/CoFeB(3

[1] Samples grown by Dr Kamimaki

nm)/Ta(3 nm) where Ru thickness was varied to tune the interlayer exchange coupling [228]. Two set of samples were prepared with Ru thickness as $t = 0.5$ nm and $t = 0.6$ nm. In order to characterise the static magnetic properties, Vibrating sample magnetometer (VSM) was used. Figure 5.3 shows magnetometery characterisation of two samples used in the present study.

The following free energy expression which includes of linear and quadratic exchange coupling contributions [239, 240, 237] was used to describe static magnetization direction in a synthetic antiferromagnet (SyAF):

$$F = \sum_{j=1}^{2} \left[M_s \boldsymbol{B} \cdot \boldsymbol{m_j} + \frac{1}{2} M_s B_s \left(\boldsymbol{m_j} \cdot \boldsymbol{z} \right)^2 \right] + \frac{2J_{ex1}}{d} \boldsymbol{m_1} \cdot \boldsymbol{m_2} + \frac{2J_{ex2}}{d} \left(\boldsymbol{m_1} \cdot \boldsymbol{m_2} \right)^2 \quad (5.1)$$

Here, M_s, $\boldsymbol{B}$, $\boldsymbol{m}_{1(2)}$, B_s, $J_{ex1(2)}$ are the saturation magnetization, external magnetic field vector, the unit vector of individual moments in a SyAF, demagnetisation field, the linear and quadratic antiferromagnetic interlayer exchange coupling constants, respectively; d is the thickness of two ferromagnetic layers which are identical in the present case. In the above Eq. 5.1, zero temperature model was used. For temperatures greater than 0 K, the effect of thermal magnetisation processes may reduce the coercivity [241] but its effect on calculation of B_s, $J_{ex1(2)}$ is less pronounced

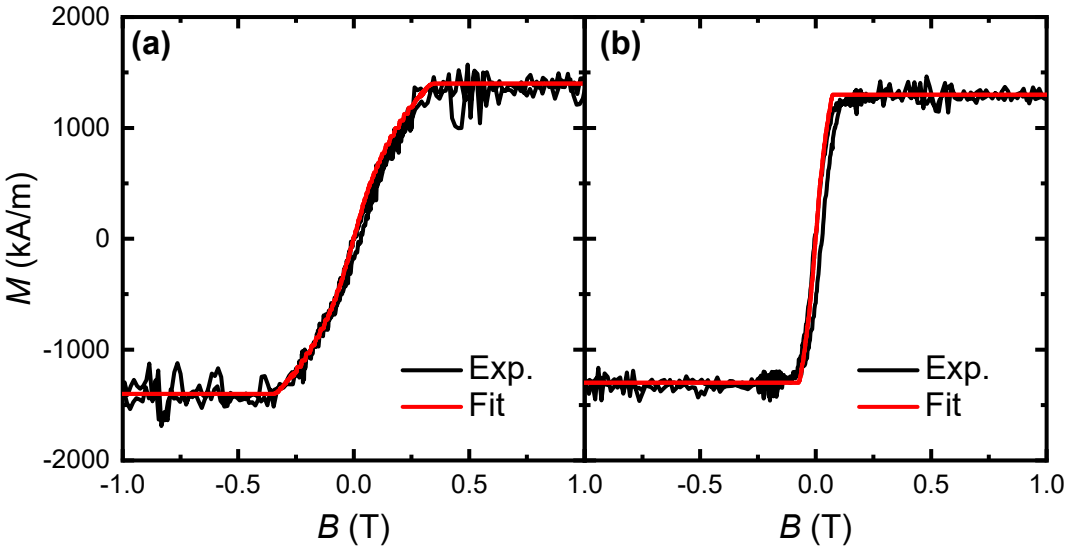

Figure 5.3: (a-b) Magnetization curve of the CoFeB (3 nm)/Ru (t nm)/CoFeB (3 nm) measured by vibrating sample magnetometer for (a) t = 0.5 and (b) t = 0.6. The black (red) curve is the experimental (calculation) results.

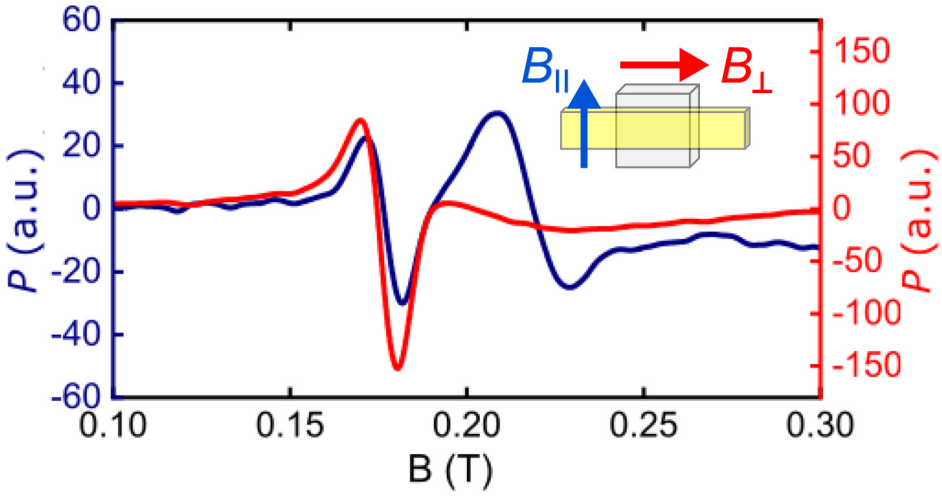

Figure 5.4: Microwave absorption spectrum for $\theta_B = 90^\circ$, measured at 13.4 GHz. Two magnetic field directions ($B_\parallel$ and $B_\perp$) are defined as per the inset. Here, $\theta_B = 90^\circ$ corresponds to the field applied in the sample plane.

[242] and is thus neglected for the given study. The red lines in the Figure 5.3 are calculated by using $M(B) = M_s \cos\phi(B)$ [237, 240, 222] where $\phi(B)$ is the angle between the applied magnetic field direction and equilibrium direction of individual moments which is obtained for all field values by minimizing Eq. 5.1 reiteratively until good matching to experimental data was achieved. The red curves in Figure 5.3 were generated by the linear and quadratic exchange fields of 140 (30) $\pm$ 1.2 (0.6) mT and 7 (2) $\pm$ 0.1 (0.03) mT for the 0.5 (0.6) nm Ru thickness sample, together with M_s= 1400 (1300) kA/m for the 0.5 (0.6) nm Ru sample. The effective magnetic field acting on both moments can be given by differentiating the exchange coupling terms (F_{ex}) in Eq. 5.1 with respect to $\boldsymbol{m}_{1(2)}$:

$$B_{ex,1(2)} = -\frac{1}{2M_s}\frac{\partial F_{ex}}{\partial m_{1(2)}} = -\frac{J_{ex1}}{d}\boldsymbol{m}_{2(1)} - \frac{2J_{ex2}}{d}(\boldsymbol{m_1}\cdot\boldsymbol{m_2})\boldsymbol{m}_{2(1)} \tag{5.2}$$

$\boldsymbol{m}_1 \cdot \boldsymbol{m}_2$ is a scalar value defined by the relative angle between $\boldsymbol{m}_1$ and $\boldsymbol{m}_2$. The second-order exchange coupling term was incorporated within B_{ex} for analysis in this study.

5.3 Spin Dynamics Characterisation

The sample chips were placed on a coplanar waveguide (CPW) board to perform broadband spin dynamics characterisation (as explained in Chapter 3). For each measurement, the frequency was kept fixed while sweeping a dc external magnetic field with an ac modulation component at 12 Hz. Figure 5.4 shows typical measurement curves for two field directions ($B_{\parallel}$ and $B_{\perp}$) defined by the figure inset. Systematic experiments were carried out for a wide range of frequency (5-20 GHz) as well as field angle to study mode hybridisation and linewidth evolution of SyAFs. Figure 5.5 shows a number of individual scans for microwave absorption experiments.

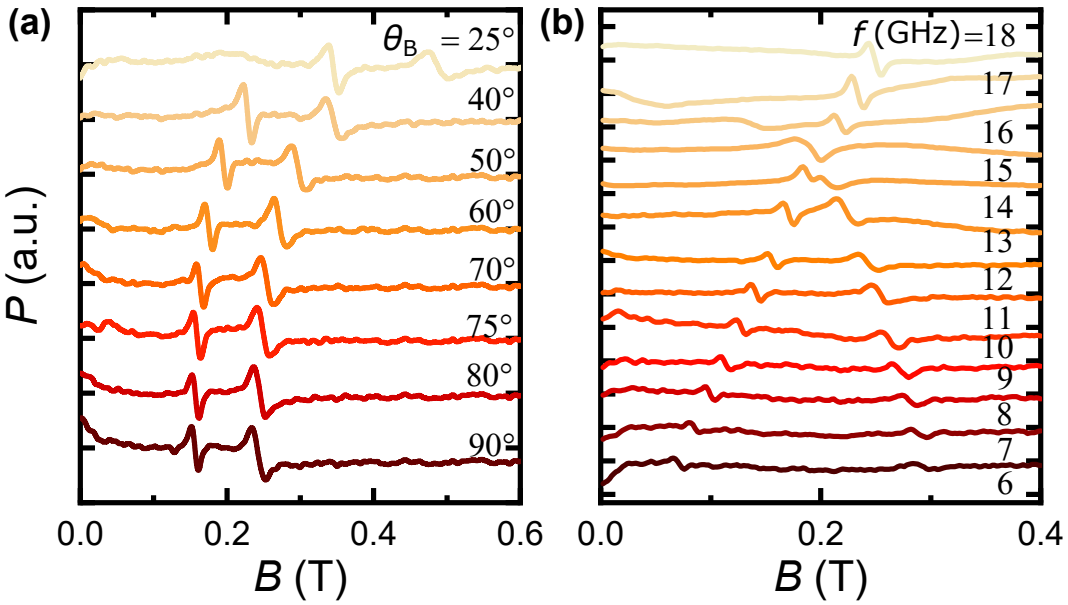

Figure 5.5: Individual field scans taken by measuring Ru 0.5 nm sample for (a) different θ_B and excitation frequency of 12 GHz, and (b) for different frequencies and $\theta_B = 90^\circ$.

The peak position and linewidth were extracted using derivative Lorentzian functions [243] (See Chapter 3). Figures 5.6 (a)-(b) show two-dimensional color plots of microwave absorption as a function of microwave frequency and magnetic field. Two modes can be clearly identified in Fig. 5.6 (a) for the $B_{\parallel}$ condition whereas only one in Fig. 5.6 (b) for $B_{\perp}$. This is because for $B_{\parallel}$, both modes can be excited since microwave rf fields have components of both parallel and perpendicular to $B_{\parallel}$ due to their spatial distribution above the waveguide. For $B_{\perp}$ measure-

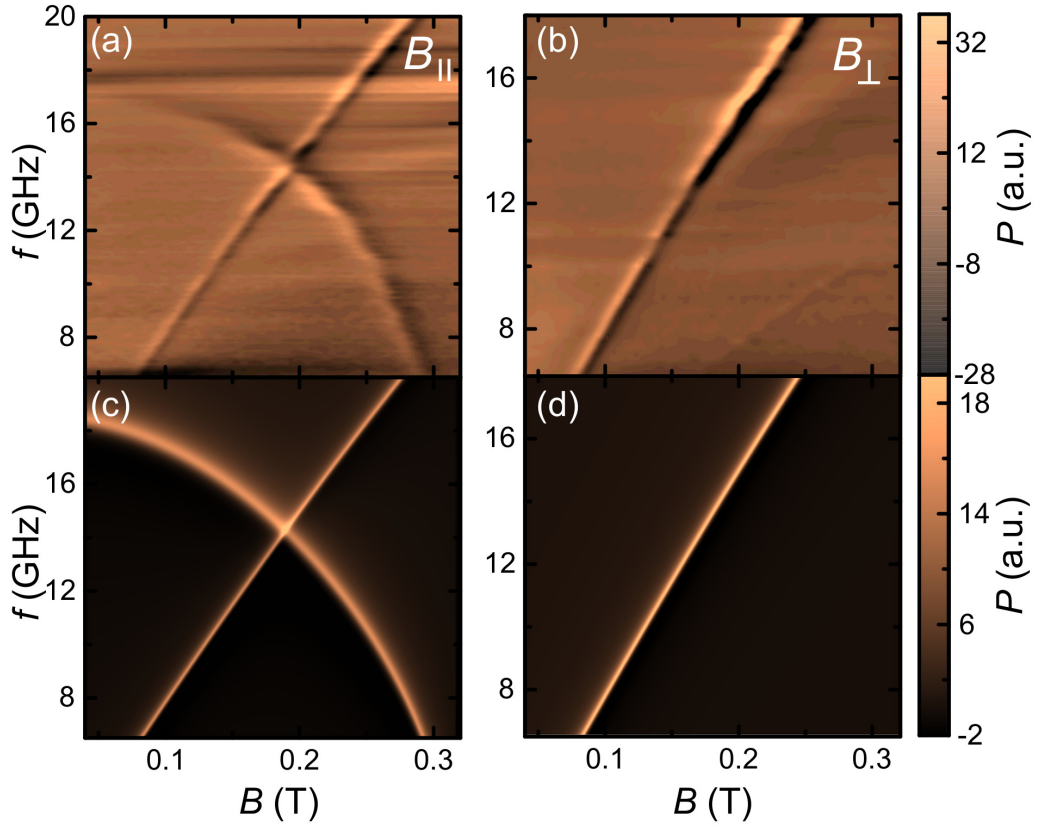

Figure 5.6: Microwave transmission spectrum as a function of frequency and applied field for two configurations of applied magnetic fields (a) $B_{||}$ and (b) $B_{\perp}$ for $\theta_B = 90^{\circ}$. (c)-(d) Theoretical results for the same experimental conditions as Fig. (a) and (b) respectively.

ments, the microwave magnetic field only possesses components perpendicular to $B_{\perp}$, hence only exciting the acoustic mode. In order to analyse these results quantitatively, coupled Landau-Lifshtitz-Gilbert (LLG) equation was solved with small angle approximation [244, 245, 211, 246] (see Appendix D) and the resonance condition of the two modes is obtained as:

$$\omega_{ac} = \gamma B_0 \sqrt{\left(1 + \frac{B_s}{2B_{ex}}\right)}, \tag{5.3}$$

$$\omega_{op} = \gamma \sqrt{2B_{ex}B_s \left(1 - \left(\frac{B_0}{2B_{ex}}\right)^2\right)}, \tag{5.4}$$

Here, B_{ex}, B_s, B_0 and γ are the exchange field, the demagnetisation magnetiza-

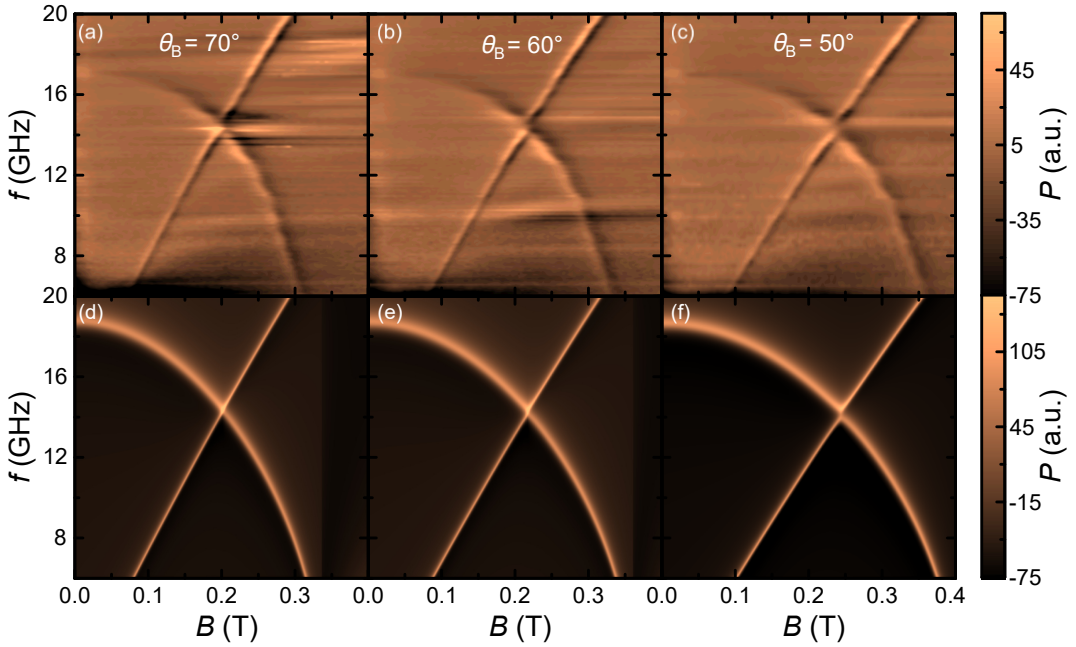

Figure 5.7: (a-c) Microwave transmission as a function of frequency and applied field for different θ_B. The avoided crossing starts to appear as θ_B is decreased and the frequency gap increases. (d)-(f) Simulation results for the same experimental condition as (a)-(c), respectively.

tion, the resonance field and the gyromagnetic ratio, respectively. From the best fit results the value for B_{ex}, B_s and $\gamma/2\pi$ was found to be 0.14 T, 1.5 T and 29 GHz/T respectively. Resonance frequencies predicted by Eqs. 5.3 and 5.4 can reproduce experimental results very well as shown in Figs. 5.6 (c) and (d), strongly supporting that the coupled SyAF modes were experimentally observed and studied. Since the frequency of the two modes show different magnetic field dependencies, it is possible to study mode coupling of the two by tuning the mode frequencies. In Fig. 5.6 (a) , a clear crossing of the two modes at $B_0 \approx 0.2$ T is observed. This "crossing" means that the two modes are not able to hybridise due to mode symmetry [211]. The mode crossing without apparent interaction indicates a degeneracy at the crossing point which is protected by symmetry when the applied field lies in the sample plane.

5.4 Magnon-magnon mode coupling

The mode symmetry can be broken by tilting the moment towards the out-of-plane direction. By breaking this symmetry, magnon-magnon coupling with large tun-

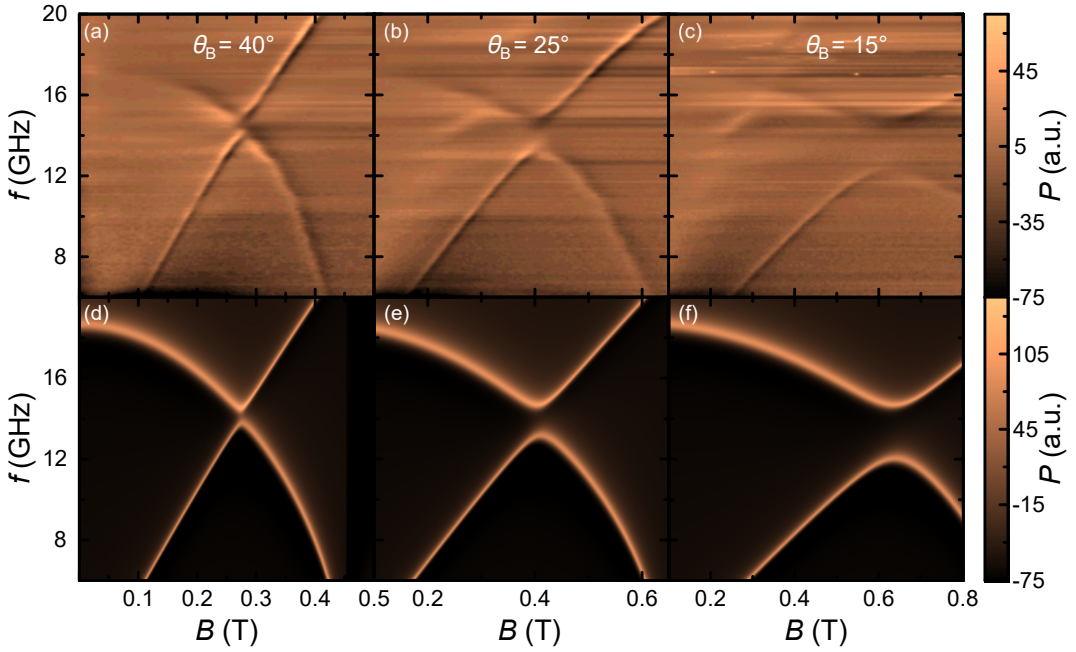

Figure 5.8: (a-c) Microwave transmission as a function of frequency and applied field for different θ_B. The avoided crossing starts to appear and the frequency gap increases as θ_B is decreased. Large coupling gap can be seen at low angles. (d)-(f) Simulation results for the same experimental condition as (a)-(c), respectively.

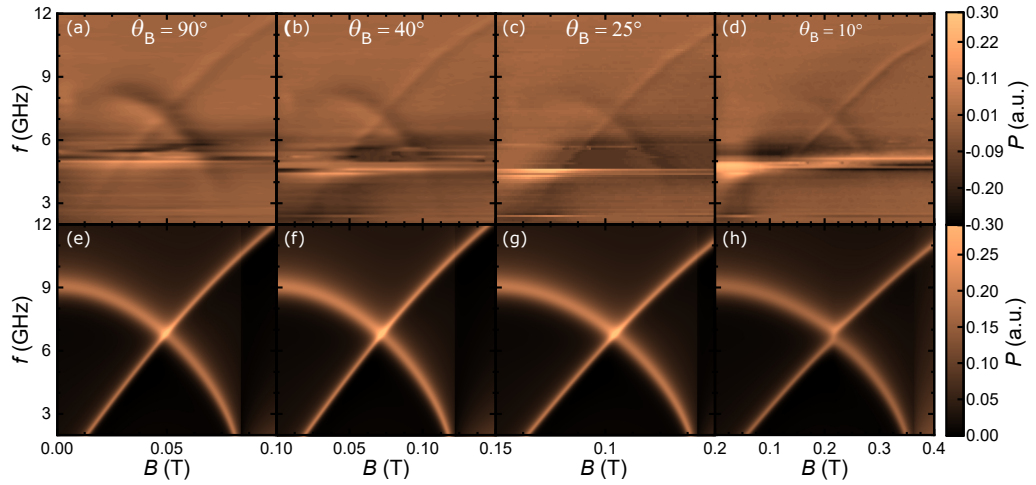

Figure 5.9: Microwave transmission as a function of frequency and applied field, for the sample with the Ru thickness of 0.6 nm for different θ_B. Small gap opening corresponds to the weak exchange coupling of the sample. Figures (e-h) plot simulation results for the same experimental conditions as Fig. (a-d).

able gaps can be induced between the two resonant modes. In principle, breaking this symmetry causes hybridization of the two thus generating an anti-crossing gap. Therefore similar experiments as outlined above were repeated for $\theta_B \neq 90^\circ$ as shown in Figs. 5.7 and Figs. 5.8 (a-c). The two modes start to show an avoided

crossing as θ_B is decreased and is more prominent below 50° as seen in Figs. 5.8 (a-c), indicating mode hybridisation which can be quantitatively discussed by using the coupling strength $g_c/2\pi$, the half of the minimum frequency gap.

To quantify the effect of exchange coupling on mode hybridisation and coupling gap, measurements were performed for the sample with the Ru thickness of 0.6 nm with weaker exchange coupling strength. The same analysis procedure and plots have been carried out for experimental data and shown in Figs. 5.9. In Figs. 5.9, it was noticed that there exist magnetic-field independent background signals around 5 GHz which is considered as transmission losses unrelated to magnetization dynamics. Nevertheless, it is highlighted that the gap opening is much weaker than those measured for the sample with the Ru thickness of 0.5 nm. This is attributed to the size of exchange coupling, which has been independently quantified by VSM as explained above.

5.4.1 Coupling Strength

As mentioned above the coupling strength $g_c/2\pi$ is determined as half of the minimal frequency spacing. It is the parameter which quantifies the strength of interaction between two magnon modes. Depending upon value of $g_c/2\pi$ in comparison to losses in the system we can describe different regimes of coupling which are weak, strong, ultrastrong and deepstrong coupling [247, 248]. When the coupling strength is smaller than losses in the system it is said to be a weak coupling regime. In case of the strong coupling regime, the coupling strength is increased to the point such that the rate of coherent exchange of energy between two magnon modes is higher than their decay rates.

Fig. 5.10 shows the θ_B dependence of $g_c/2\pi$ where $g_c/2\pi$ grows with the out-of-plane component, with the highest value exceeding 1 GHz. The fit curves are calculated by solving coupled LLG equation as described below. It can be further seen that for sample with Ru thickness 0.6 nm, the exchange coupling strength is very weak.

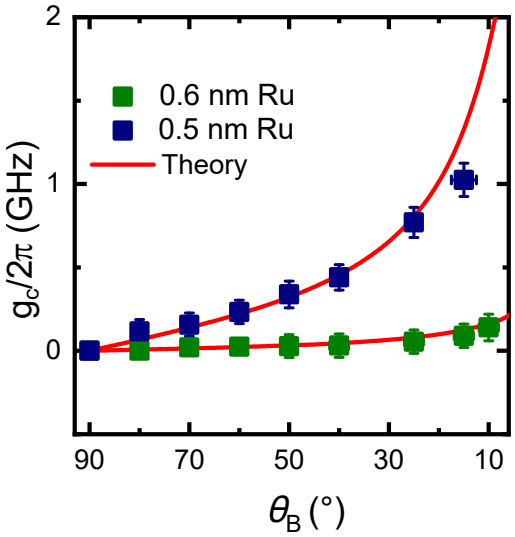

Figure 5.10: The coupling strength $g_c/2\pi$ as a function of θ_B. The results from two samples with the Ru thickness of 0.5 nm and 0.6 nm are plotted. The 0.5 nm sample shows sizable $g_c/2\pi$, compared to much smaller $g_c/2\pi$ for 0.6 nm. The red curves are produced by Eq. 5.6 given below.

5.5 Quantitative Description of magnon magnon coupling

The magnon-magnon coupling phenomena is described in SyAFs by a 2×2 matrix eigenvalue problem derived from the coupled LLG equations with mutual spin pumping terms [233] (see Appendix D):

$$\begin{bmatrix} \omega^2 - \omega_{op}^2 + i(\nu_{o1} + \nu_{o2})\omega & (i\omega - \nu_{o1}\gamma B_s)\,\eta m_{z0} \\ (-i\omega + \nu_{a2}\gamma B_s)\,\eta m_{z0} & \omega^2 - \omega_{ac}^2 + i(\nu_{a1} + \nu_{a2})\omega \end{bmatrix} \tag{5.5}$$

Here, $\eta = 2B_{ex}/B_s$, $m_{z0} = B_0\cos\theta_B/(B_s + 2B_{ex})$, $\nu_{o1} = (\alpha_0 + \alpha_{sp})(1 - m_{z0}^2) - \alpha_{sp}\{1 - m_{z0}^2 - (B_0^2\sin^2\theta_B/4B_{ex}^2)\}(m_{z0}^2/m^2)$, $\nu_{o2} = \alpha_0\eta(1 - B_0^2\sin^2\theta_B/4B_{ex}^2)$, $\nu_{a1} = \alpha_0\eta(m_{z0}^2 + B_0^2\sin^2\theta_B/4B_{ex}^2)$ and $\nu_{a2} = \alpha_0(\eta + 1)(1 - m_{z0}^2)$, respectively, with α_0 and α_{sp} being the standard Gilbert damping constant and one arising from mutual spin pumping between the two magnetic layers. The real part of the eigenvalues gives the resonance frequencies and the imaginary part represents the loss rates of the two modes. The eigenvalue problem was numerically solved with parameters described above and it was found that the coupled equations can model our experi-

mental observation well for each experimental set, such as Figs. 5.7 (d-f), Figs. 5.8 (d-f) and Figs. 5.9 (e)-(h) reproducing corresponding experimental results. The 2×2 matrix was simplified by neglecting the damping terms to calculate the eigenvalues and an analytical expression for the coupling strength was found as below (see Appendix D):

$$g_{\mathrm{c}}=\frac{\gamma B_{\mathrm{ex}}B_0}{2B_{\mathrm{s}}+4B_{\mathrm{ex}}}\cos\theta_{\mathrm{B}}. \tag{5.6}$$

This correctly captures the experimental observation as $g_{\mathrm{c}}/2\pi$ grows with decreasing θ_{B}. The red curve in Fig. 5.10 is calculated by this equation and there is quantitative agreement between experiments and theory, despite marginal deviation at small θ_{B}. Eq. 5.6 suggests that the coupling strength can be tuned by B_{ex} which is validated by results of measurement on SyAF sample having the Ru thickness of 0.6 nm (green points in Fig. 5.10). For this sample, it was found that B_{ex} is decreased to 30 mT due to a weaker interlayer coupling and accordingly, as expected, there was a significant decrease of $g_{\mathrm{c}}/2\pi$ as summarised in Fig. 5.10. These results show the tunability of the mode coupling strength in SyAFs by both thin-film growth engineering (*ex-situ*) as well as out-of-plane tilt angle (*in-situ*).

5.6 Magnetization relaxation of magnon modes

Next the relaxation of the SyAF modes is discussed. Figure 5.11 (a-f) represent plots of the half width at half maximum (HWHM) linewidth (ΔB) extracted for individual sweeps for both modes. ΔB of the acoustic mode increases with increasing magnetic field, with a characteristic anomaly around the field where the two modes hybridise. ΔB of the optical mode however shows a different magnetic field dependence as it decreases with increasing magnetic field. This is primarily due to the relationship of the magnetic-field-domain linewidth and frequency-domain linewidth as given by:

$$\Delta B_{\mathrm{op(ac)}}=\left|\frac{d\omega_{\mathrm{op(ac)}}}{dB}\right|^{-1}\frac{1}{\tau_{\mathrm{op(ac)}}}. \tag{5.7}$$

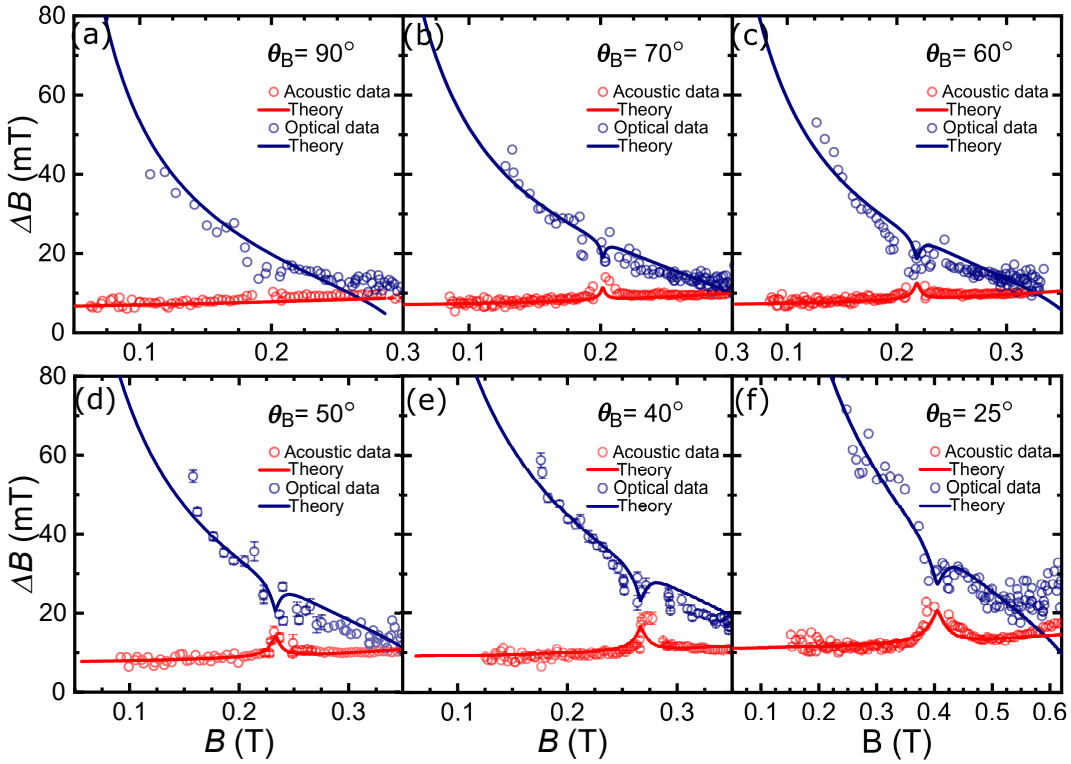

Figure 5.11: (a-f) HWHM linewidth as a function of magnetic field for θ_B of (a) 90° (b) 70° (c) 60° (d) 50° (e) 40° and (f) 25° for sample with Ru thickness 0.5 nm. Solid lines represent results from the theoretical model discussed in Appendix D.

When the resonance field is low, $|d\omega_{\rm op}/dB|$ becomes small, which can extrinsically enhance the observed ΔB in the experiments.

In order to extract material-specific parameters such as α_0 from the data, the eigenvalue problem was solved and the imaginary part was compared with experimental results. It was found that the linewidth calculated from the imaginary part models excellently for the experiments as shown in Figs. 5.11 (a-f) for fields below the saturation field. The theoretical model is valid only in the canted regime and for high fields above saturation field it fails to match the experimental results because at high field the forced ferromagnetic regime is operative. Extracted α_0 and $\alpha_{\rm sp}$ for different $\theta_{\rm B}$ are plotted in Fig. 5.12 (a). This confirms that there is a sizable spin pumping component for every angle measured, in consistence with previous reports [233, 236, 228, 249]. The Ru thickness is much shorter than its spin diffusion length of 14 nm [250]. As a result, when two ferromagnets are precessing in-phase, according to spin pumping theory [111], spin currents flowing out of the

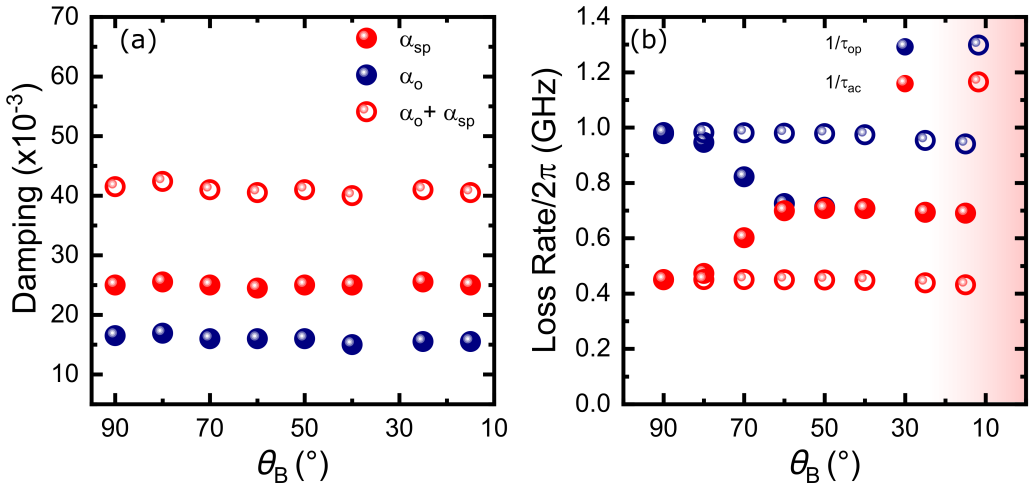

Figure 5.12: (a) Extracted values of damping parameters from HWHM fittings for sample with Ru thickness 0.5 nm (b) Calculated loss rates of each mode at the crossing point as well as those of the hybridised modes.

two are cancelled out hence developing zero time-dependent spin accumulation in the Ru layer. However, when two moments precess out of phase, the emitted spin currents no longer cancel out, leading to the spin-accumulation which induces an additional damping mechanism for the optical mode. In the experiments, it was observed that both α_0 and α_{sp} are independent of θ_B, which can be understood that the Gilbert damping components are a material parameter, independent of experimental conditions. It is to be noted here that the canted angle has been already taken into account in the expressions.

An interesting observation is that the experimentally deduced ΔB for both modes also show "attraction" around the avoided crossing points. This demonstrates that magnetic relaxation can be modified by mode coupling phenomena. In the crossing regime, two modes are no longer pure acoustic or optical and therefore it is not possible to use the ac spin pumping picture associated with the phase difference between two moments. Rather, a simple phenomenological picture of hybridised energy losses would be a better one. When two modes with different loss rates start to couple coherently, their loss rates also start to merge together [251]. This is because the energy transfer mixes the two loss rates since the high (low)-loss mode becomes the low(high)-loss mode as a function of time. This feature was

observed in the experiments. This loss rate hybridisation is reproduced by using numerical simulations from the eigenvalue problem as shown in Figs. 5.11 (a-f). This linewidth averaging is similar to ones discussed in spin-photon coupling systems [252, 22] as well as magnon-magnon coupling at YIG/NiFe interfaces [214]. To quantify the loss rates for both modes Eq. 5.7 was used. First of all, the loss rate of individual modes was estimated at the avoided crossing point (open circles in Fig. 5.12 (b)), by extrapolating from the values outside the coupling regime. Both show a very weak angular dependence, which can be understood that the damping (Fig. 5.12 (a)) has no angular dependence with a subtle change of the mode-crossing frequency when θ_B is decreased. By contrast, loss rates for the hybridised modes (solid circles in Fig. 5.12 (b)), estimated by our eigenvalue problem, exhibit clear attraction as the coupling strength is increased by changing θ_B. After $\theta_B = 60^\circ$, the loss rates of the two modes coalesce into a single number which is exactly the average of the two rates $1/\tau_{mix}$=(1/2)($1/\tau_{ac}$+$1/\tau_{op}$) where $1/\tau_{mix}$ is the loss rate of the hybridised states. Furthermore, through the course of our simulation study, it was found that α_{sp} can have an effect on g, suggesting that the magnon-magnon coupling is partially mediated by spin currents. It was observed that for large α_{sp} the coupling between the two modes can be completely suppressed (see Sec. 5.7). This highlights that the damping-mediated coupling control cannot be achieved by simply changing α_0 in our system, something specific for the magnetic relaxation via spin pumping to the coupling and the energy exchange. Although it is not possible to control α_{sp} in our experiments, it could act as an extra parameter to define the magnon-magnon coupling strength in SyAFs. Finally, it was seen that the highest $g_c/2\pi$ achieved (1.0 GHz) outnumbers the loss rates of the individual modes, indicating that this magnon-magnon coupling starts to enter the strong coupling regime in our experiments. Although these experiments are just at the onset of the strong coupling regime, it suggests the potential improvements and control of the coupling strength against the individual loss rates. Eq. 5.6 can be simplified as $g_c/2\pi \propto B_{ex}/B_s$, suggesting that a sample with a higher B_{ex} as well as a smaller B_s shows a large coupling strength. Achieving similar coupling with low-damping

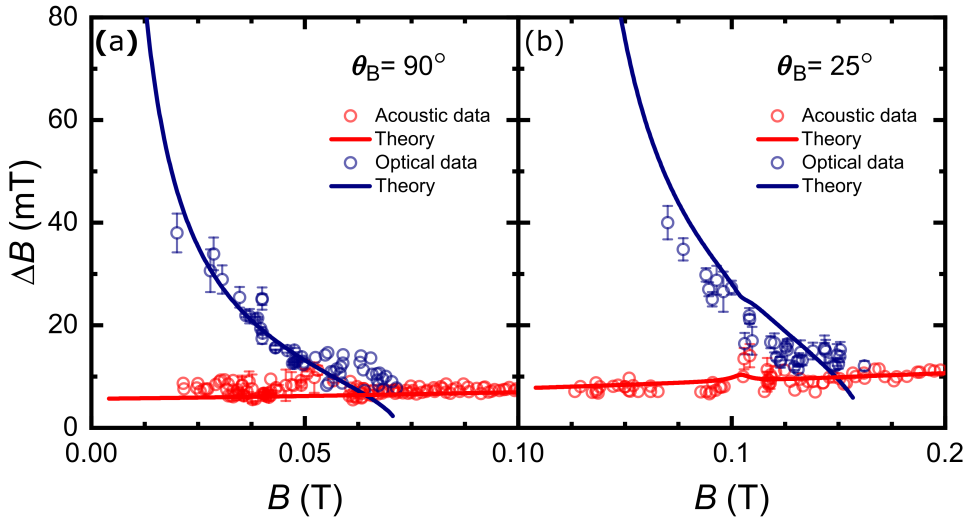

Figure 5.13: (a-f) HWHM linewidth as a function of magnetic field for θ_B of (a) 90° (b) 25° for sample with Ru thickness 0.6 nm. Solid lines represent results from the theoretical model discussed in Appendix D.

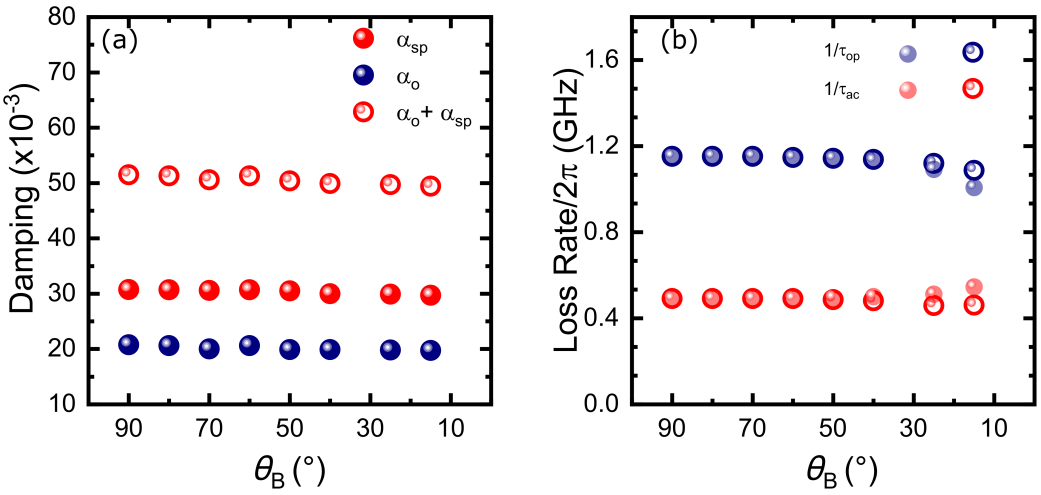

Figure 5.14: (a) Extracted values of damping parameters from HWHM fittings for sample with Ru thickness 0.6 nm (b) Calculated loss rates of each mode at the crossing point as well as those of the hybridised modes.

materials could be another plausible path.

Figs. 5.13 shows the linewidth plots for the sample with the Ru thickness of 0.6 nm. The same analysis procedure as dicussed above was carried out for this sample as well and the loss rate hybridization is reproduced using numerical simulations. The angular dependence for damping and loss rate is shown in Figs. 5.14 (a) and (b) respectively. It can be seen that very weak angular dependence is seen for

loss rate of individual modes both for regions near the crossing regime and outside the crossing regime which is apparent from the weaker coupling strength for this sample.

5.7 Impact of the Mutual Spin Pumping Damping on the Coupling

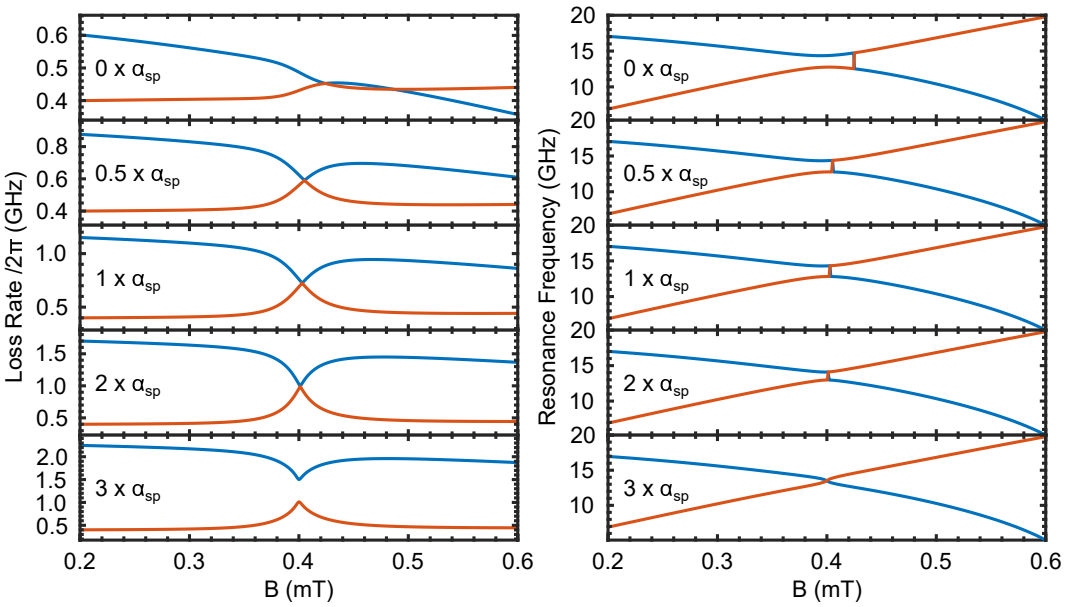

Figure 5.15: Simulated loss rate (left panel) and resonance frequency (right panel) of the acoustic (red) and optic (blue) modes as a function of applied magnetic field at an angle of $\theta_B = 27°$ for different multiples of the mutual spin pumping damping $\alpha_{sp} = 0.0255$. These are produced by solving Eq. D.20 (see Appendix D) with other parameters of $B_S = 1.583$ T, $B_{ex,1} = 0.14$ T, $B_{ex,2} = 0.0065$ T, $\gamma/2\pi = 29$ GHz/T and $\alpha_0 = 0.0155$.

The theory model allows to explore parameter regimes beyond experimental conditions. In an effort to understand the coupling of the two magnetic resonance modes in a SyAF, the dependence of the damping parameters on the coupling strength were investigated qualitatively. Especially, the effect of the damping arising from the mutual spin pumping between the two ferromagnets was studied. This is because of the derived matrix form in Eq. D.24 (see Appendix D) in which α_{sp} exists in the off-diagonal term, strongly suggesting that this parameter can contribute

to the coupling of optical and acoustic modes. Figure 5.15[2] shows the simulated loss rate and resonance frequency of the acoustic and optic modes as a function of the magnetic field B for $\theta_B = 27°$. Here, $\theta_B = 27°$ was chosen for simulations because this corresponded to the experimental data measured at $\theta_B = 25°$. The plots show the results of the full eigenvalue problem defined in Eq. D.20 (see Appendix D) for several values of α_{sp}. For zero α_{sp}, the loss rate of the acoustic and optic mode cross at a lower magnetic field than the point of minimal frequency separation between the resonance frequencies of the two modes. With increasing α_{sp}, the crossing of the loss rates shifts higher in magnetic field until it appears at the same field as the minimal frequency separation of the resonance frequencies. For the highest α_{sp} the loss rate no longer cross and are separated. The dispersion of the resonance frequencies remains mostly unchanged for $\alpha_{sp} = 0$ and $\alpha_{sp} = 0.0255$. It was observed that for higher α_{sp}, the coupling strength reduces and eventually goes to zero for the highest α_{sp} we plot. From the change of the coupling strength with α_{sp}, it can be concluded that the coupling is partially mediated by spin currents. This change in the coupling behaviour can only be achieved by changing α_{sp}. In contrast, a change of the Gilbert damping α_0 has no influence on the coupling strength and only affects the loss rate of the modes. Our theory model suggests that the coupling between the acoustic and optic modes of a synthetic antiferromagnet is not fully described by a classical coupled harmonic oscillator model.

In summary, the magnon-magnon coupling in SyAF CoFeB/Ru/CoFeB multilayers is shown experimentally. Clear magnon-magnon hybridisation has been observed when the optical and acoustic modes are tuned into resonance. The magnon-magnon coupling strength has been controlled by bringing the moments into the out-of-plane direction, which breaks the orthogonality of the two modes. In addition, the interlayer exchange coupling is found to tune the coupling strength. The loss rate of two modes exhibits an averaging effect upon hybridisation. Our eigenvalue problem approach serves to provide the analytical expression of the coupling strength as well as numerical explanations/predictions of the experimental data. It can be envisaged

[2]The simulations in Sec 5.7 were done by Dr. Zollitsch and the Fig. 5.15 was provided by him.

that results in the present study will be transferable to other weakly-coupled antiferromagnetic systems since the phenomenological descriptions of their spin-wave modes should be identical to the model developed.

5.8 Hybridisation and mode coupling in Synthetic Ferrimagnets

Recent developments in hybrid magnonics have invigorated prodigious interest in intriguing phenomena of coherent magnonic interactions between different physical systems [253, 254, 255, 256, 257]. Tunability and flexibity provided by magnons in coupling to various dynamic systems have made them great contenders for various quantum sensing and information processing applications [21, 258]. The intuitive description of interaction in various hybrid systems is essentially dependent on g_c which determines the rate of energy transfer. In a broader picture a larger coupling strength is essential for efficient and faster device operation. Strong coupling strength in sub-GHz regime has been reported for interaction of magnon with microwave photon [259, 260]. However, using microwaves for coherent control at nanoscale becomes challenging owing to Dicke's scaling law [261], i.e $g_c \propto \sqrt{N}$, where N is number of spins, implying weak couplings in nanomagnets [262, 263, 264]. This problem is circumvented for magnon-magnon coupling due to smaller length scale and lower losses in a magnonic cavity [265].

A large magnon-magnon coupling strength reaching strong coupling regime has been reported in single magnets [210], metal-insulator hybrid structures [265] and more recently in weak exchange coupled van der waal magnets(vdW) [266] and SyAF [24]. Recent reports have also shown tunability of coupling strength in vdW magnets [266] and synthetic antiferromagnets which is achieved by growth as in SyAF, or rotational symmetry breaking caused by tilting external field [24, 211] or by dynamic dipolar interaction in case of non-uniform precession [25]. Apart from this coupling control in multi-layered systems has been demonstrated computationally [267, 268]. The general difficulty in device fabrication, atmospheric sensitivity and low curie temperatures [266] render the vDW materials less appealing

and so SyAFs are highly sought after materials for coupling strength engineering. In most existing works, the tunability of coupling has been reported only for symmetrical SyAF structure where the two FM sublayers have the same thickness (t) and magnetization (M) [24, 25, 211]. By modifying either t or M forms a structure with unbalanced antiparallel moments known as SyF. In SyF an inherent symmetry breaking between two sub-layers causes hybridization of two magnon modes and an anti-crossing gap is visible for in-plane applied fields. This is in contrast to symmetric SyAF where the mode coupling is protected by two-fold rotational symmetry [24] and an extrinsic symmetry breaking is necessary to couple the magnon modes. Thus, SyF offer another approach for tuning the magnon-magnon interaction beyond the use of external-field mediated symmetry breaking. In this study the mode coupling in SyFs is investigated. The effect of asymmetry achieved by varying thickness as well as material of two sub-layers, on the strength of interaction is described. A large frequency gap reminiscent of mode hybridisation is clearly seen and the gap increases when two sub-layers are made from two different FM materials signifying stronger coupling. The interaction between ferromagnetic and anti-ferromagnetic resonance modes is systematically examined as a function of resonance frequencies and different magnetic field strength directions. A macrospin model is provided to describe the mode coupling which accurately reproduced the experimental observations. Further the coupling strength is calculated numerically and it is demonstrated how to engineer it by inter-layer exchange field tunability through growth. The results and demonstration of coupling phenomena in SyFs will facilitate the research on physics of strong coupling between different magnonic excitations and their coherent manipulation and engineering for device applications [215]. Fig. 5.16 shows the schematic for the coupling phenomena in a SyF structure.

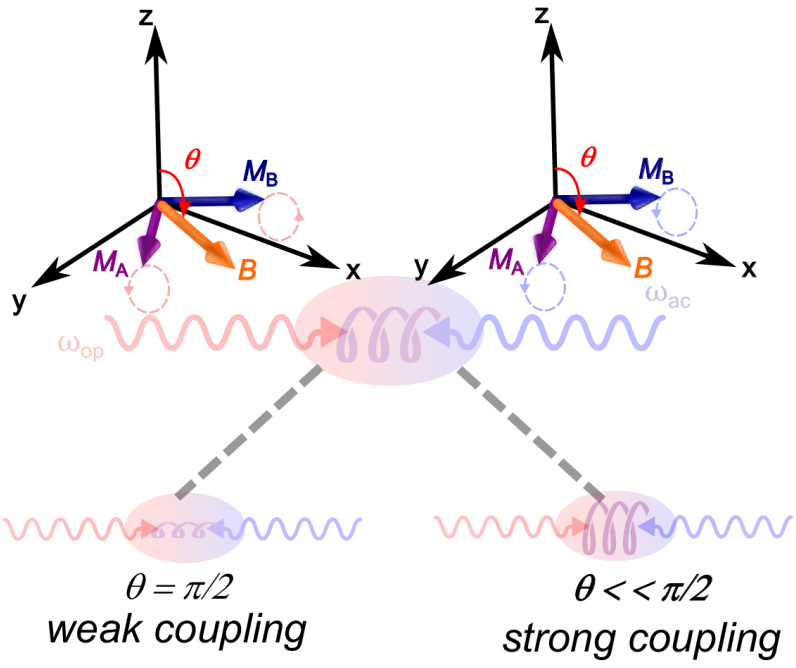

Figure 5.16: Schematics of magnon-magnon coupling phenomena in Synthetic Ferrimagnet. Two moments are coupled antiferromagnetically and at certain magnetic field they enter into spin-flop regime. θ is defined as shown in the figure where z is the growth direction of the film. The asymmetry in structure breaks the rotation symmetry of magnetization and cause the coupling. When the two moments are in the film plane coupling is weak and can be tuned by varying θ.

5.9 Sample growth and magnetometry characterisation

The samples were grown using the technique of magnetron co-sputtering[3] in an ultrahigh-vacuum compatible sputtering chamber with the base pressure of 1×10^{-7} Pa. The SiO_2 substrate was used and 5 different samples were prepared. The stacking pattern was Ta(5)/FM_1(d_A)/Ru/FM_2(d_B)/Ta(5) where the numbers in bracket are thickness in nm. The $FM_{1(2)}$ refer to the ferromagnet and $d_{A(B)}$ are the thickness of the two ferromagnets and are summarised in Table. 5.1.

In order to characterise the static magnetic properties, VSM was used. Figure 5.17 shows normalized hysteresis loops for the samples used in the present study. Three distinct regions based on magnetization direction of two layers are

[3]Samples grown by Dr. Suzuki

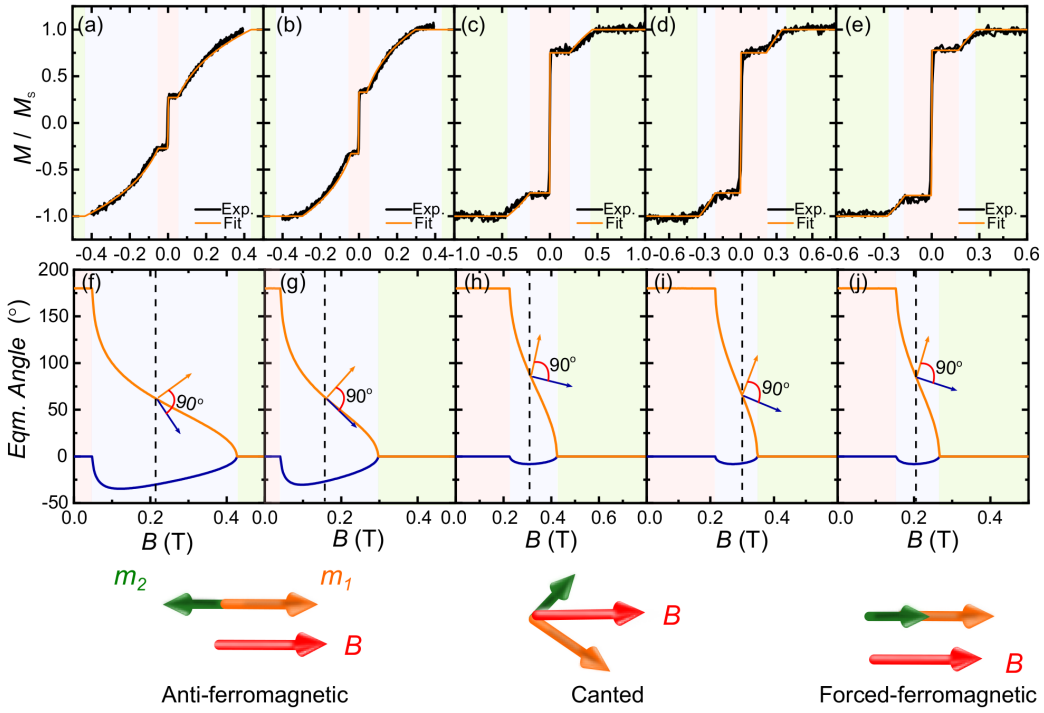

Figure 5.17: (a-e) Normalized M-H loops for different set of samples (a) Ta/NiFe(5)/Ru(0.4)/NiFe(3)/Ta (b) Ta/NiFe(3)/Ru(0.4)/NiFe(5)/Ta (c) Ta/NiFe(1.5)/Ru(0.45)/CoFeB(3)/Ta (d) Ta/NiFe(1.5)/Ru(0.5)/CoFeB(3)/Ta and (e) Ta/NiFe(1.5)/Ru(0.55)/CoFeB(3)/Ta. The field is applied along the in-plane easy axis. The solid lines are fit obtained by calculating magnetization corresponding to equilibrium angles of magnetization for two FM layers shown in (f-j) obtained by minimization of free energy equation.

shown in different colours. In the antiferromagnetically coupled regime (shown in pink) there is an anti-parallel alignment of spins in the two layers. As the field is increased , the magnetization direction for the two layers enter into the spin-flop (canted) regime where the two moments tilt from the equilibrium position. Finally at higher field values the magnetic moments are aligned with each other in the saturation (forced ferromagnetic) regime as indicated by green colour.

The free energy density expression, given in Eq. 5.8 which includes of bilinear and biquadratic exchange coupling contributions [239, 24, 240, 237] was used to

describe static magnetization direction.

$$w = \mu_{\mathrm{A}} \left\{ -M_{\mathrm{A}} \boldsymbol{H} \cdot \boldsymbol{n}_{\mathrm{A}} + \frac{M_{\mathrm{A}}^2}{2} (n_{\mathrm{A}}^{\mathrm{z}})^2 \right\} + \mu_{\mathrm{B}} \left\{ -M_{\mathrm{B}} \boldsymbol{H} \cdot \boldsymbol{n}_{\mathrm{B}} + \frac{M_{\mathrm{B}}^2}{2} (n_{\mathrm{B}}^{\mathrm{z}})^2 \right\} + \rho_{\mathrm{E}} \boldsymbol{n}_{\mathrm{A}} \cdot \boldsymbol{n}_{\mathrm{B}} + \rho_{\mathrm{Q}} \left(\boldsymbol{n}_{\mathrm{A}} \cdot \boldsymbol{n}_{\mathrm{B}} \right)^2 \tag{5.8}$$

Here, $\mu_{\mathrm{A(B)}} = \mu_0 \frac{v_{\mathrm{A(B)}}}{v}$, w, $\boldsymbol{H}$, $M_{\mathrm{A(B)}}$, $v_{\mathrm{A(B)}}$, $\rho_{\mathrm{E(Q)}} = \frac{\Lambda_{\mathrm{E(Q)}}}{v}$, $v = \sqrt{v_{\mathrm{A}} \cdot v_{\mathrm{B}}}$ are the magnetic permeability for the two layers, magnetic free energy density, applied external magnetic field, magnetizations for the respective layers, the spatial volumes occupied by $M_{\mathrm{A,B}}$, bilinear and biquadratic exchange constant expressed in units of energy density and reference volume respectively. $\boldsymbol{n}_{\mathrm{A,B}}$ represent the unit vector of magnetization given by $\boldsymbol{n}_{\mathrm{A,B}} = \boldsymbol{M}_{\mathrm{A,B}} / M_{\mathrm{A,B}} = |\boldsymbol{M}_{\mathrm{A,B}}|$. The film normal was taken parallel to the $\hat{\boldsymbol{z}}$. For obtaining the ground state, the energy density to be minimised is considered for the case when $\boldsymbol{n}_{\mathrm{A,B}}$ are in the plane. This can be expressed as Eq. 5.9 which is minimised reiteratively to obtain the values for $\cos\phi_{\mathrm{A,B}}$, the angles between the applied magnetic field direction and equilibrium direction of individual moments, for each field value which are shown in the bottom panel of Fig. 5.17.

$$w = -\mu_{\mathrm{A}} M_{\mathrm{A}} \boldsymbol{H} \cos\phi_{\mathrm{A}} - \mu_{\mathrm{B}} M_{\mathrm{B}} \boldsymbol{H} \cos\phi_{\mathrm{B}} + \rho_{\mathrm{E}} \cos\left(\phi_{\mathrm{A}} - \phi_{\mathrm{B}}\right) + \rho_{\mathrm{Q}} \cos^2\left(\phi_{\mathrm{A}} - \phi_{\mathrm{B}}\right). \tag{5.9}$$

The orange curves in the Fig. 5.17 are the magnetization calculated for each field value as:

$$\frac{M(H)}{M_{\mathrm{s}}} = \frac{M_{\mathrm{A}}}{M_{\mathrm{A}} \cdot d_{\mathrm{A}} + M_{\mathrm{B}} \cdot d_{\mathrm{B}}} d_{\mathrm{A}} \cos\phi_{\mathrm{A}} + \frac{M_{\mathrm{B}}}{M_{\mathrm{A}} \cdot d_{\mathrm{A}} + M_{\mathrm{B}} \cdot d_{\mathrm{B}}} d_{\mathrm{B}} \cos\phi_{\mathrm{B}}. \tag{5.10}$$

where, M_{s} is the total saturation magnetization for the sample and $d_{\mathrm{A,B}}$ are the thickness for the two layers. The bilinear and biquadratic exchange constants used to generate the curves are summarised in the Table 5.1.

Table 5.1: Summary of the VSM magnetometry parameters used to obtain the magnetization curves shown in Fig. 5.17 according to Eqs. 5.9 and 5.10. The left column represent the sample geometry where ".." represents the SiO_2 substrate and the FM near to the substrate is the second FM layer referred to as B. $\rho_{E(Q)}$ are the bilinear and biquadratic coupling constants respectively and $\boldsymbol{M}_{A(B)}, d_{A(B)}$ are the magnetization and thickness for the two ferromagnetic layers (NiFe/CoFeB).

Sample geometry	$\mu_0 M_A$ (T)	$\mu_0 M_B$ (T)	$\frac{\rho_E}{\sqrt{M_A \cdot M_B}}$ (T)	$\frac{\rho_Q}{\sqrt{M_A \cdot M_B}}$ ((T)	d_A (nm)	d_B (nm)
Ta/NiFe/Ru(0.4)/NiFe/Ta/..	0.951 ± 0.004	0.909 ± 0.004	0.145 ± 0.001	0.0310 ± 0.0001	5.03 ± 0.03	3.02 ± 0.02
Ta/NiFe/Ru(0.4)/NiFe/Ta/..	0.951 ± 0.004	0.909 ± 0.004	0.1005 ± 0.0005	0.0211 ± 0.0001	3.02 ± 0.02	5.03 ± 0.03
Ta/CoFeB/Ru(0.55)/NiFe/Ta/..	1.428 ± 0.006	0.413 ± 0.001	0.0781 ± 0.0004	0.0052 ± 0.0002	3.02 ± 0.02	1.51 ± 0.01
Ta/CoFeB/Ru(0.5)/NiFe/Ta/..	1.428 ± 0.006	0.413 ± 0.001	0.1055 ± 0.0005	0.0052 ± 0.0002	3.02 ± 0.02	1.51 ± 0.01
Ta/CoFeB/Ru(0.45)/NiFe/Ta/..	1.428 ± 0.006	0.413 ± 0.001	0.1215 ± 0.0005	0.0105 ± 0.0005	3.02 ± 0.02	1.51 ± 0.01

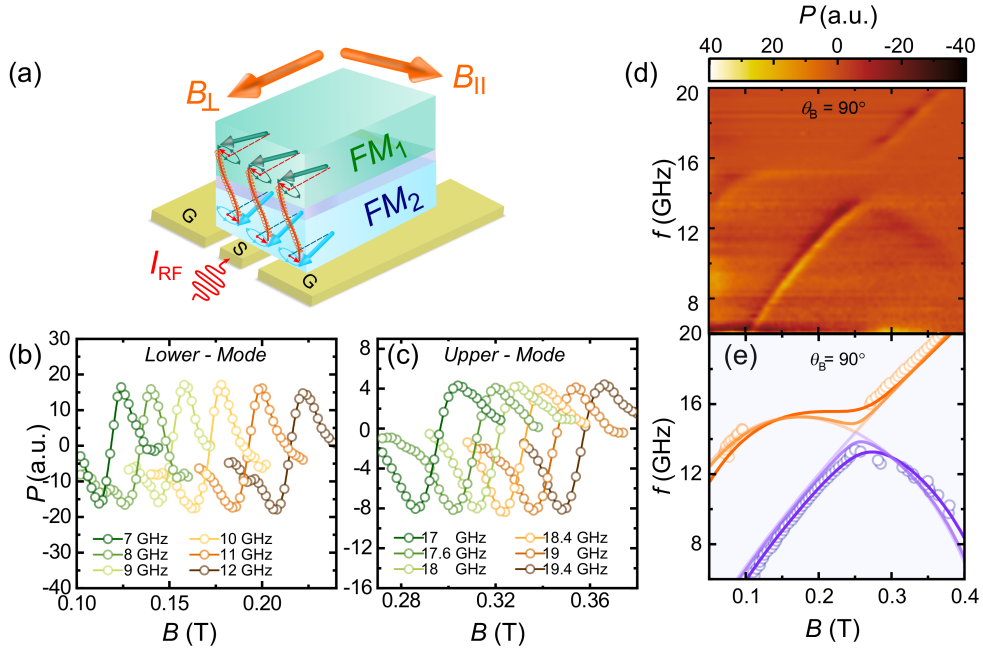

Figure 5.18: (a) Sketch of measurement geometry. FMR spectra are obtained by placing the sample on a CPW. A microwave current is injected into the CPW signal line that produces a nearly uniform excitation field. On resonance absorption is measured as shown in (b) for the upper (High frequency) and (c) lower (low frequency) modes.(d) Microwave transmission as a function of frequency and applied field for NiFe(5)/Ru(0.4)/NiFe(3) at in-plane direction for θ=90° and applied field direction ($B_{||}$) as defined in (a). The avoided crossing appears as shown for the sample. (e) Fitting results for data as in(d). The solid lines are fit curves obtained from macrospin model.

5.10 Spin Dynamics Characterisation

To study the dynamic properties, the FMR measurements were done by placing the sample on a CPW board similar to Sec.5.3 and is shown in Fig. 5.18. The mea-

surements were performed by sweeping the dc external field with an ac modulation component at 12 Hz while the frequency was kept constant. The lock-in amplifier was used to detect the transmission. The asymmetry in the samples results in inherent two-fold rotational symmetry breaking in contrast to the symmetrical case. Since the two modes are coupled as evident from the gap in Fig. 5.18 (d), they have interchangeable mode character and so they are referred as upper (high frequency) and lower (low frequency) modes. Next section is focused on the samples where the asymmetry is caused by different thickness of the two ferromagnetic layers.

5.11 Asymmetric NiFe/Ru/NiFe samples

The resonance curves for lower and higher frequency modes measured at $\theta = 90^{\circ}$ and $B_{\parallel}$ configuration for the sample NiFe(5)/Ru(0.4)/NiFe(3) is shown in Fig.5.18 (b-c). Both modes can be clearly seen in the color plot Fig.5.18 (d) and a clear anti-crossing gap is observed around $B = 0.25$ T in the canted regime. By fitting the measurement results using the derivative of lorentzian function using Eq. 3.1 the resonance position was obtained as shown in Fig.5.18 (e). To obtain the solid lines, the macrospin approach is used and the coupled equation of motions are solved which can be written in the matrix form. The evolution of the two modes is then captured by solving the four-by-four matrix eigen value problem:

$$\begin{vmatrix} -\omega - \xi_{\mathrm{A}} & -\eta_{\mathrm{A}} & -\zeta_1 & -\zeta_2 \\ -\overline{\eta_{\mathrm{A}}} & \omega - \xi_{\mathrm{A}} & -\overline{\zeta_2} & -\overline{\zeta_1} \\ -\overline{\zeta_1} & -\zeta_2 & -\omega - \xi_{\mathrm{B}} & -\eta_{\mathrm{B}} \\ -\overline{\zeta_2} & -\zeta_1 & -\overline{\eta_{\mathrm{B}}} & -\omega - \xi_{\mathrm{B}} \end{vmatrix} = 0, \tag{5.11}$$

where $\xi_{\mathrm{A,B}}$ represents the bare acoustic and optical mode frequency as in synthetic antiferromagnetic case when the asymmetry parameter given by r is 0. The complete expression for $\xi_{\mathrm{A,B}}$ is given as:

$$\xi_{\mathrm{A}} = \omega_{\mathrm{A}}^{+} - r^{-1}\left(n^{00}\omega_{\mathrm{E}} + \left\{2\left(n^{00}\right)^2 - |\boldsymbol{e}_{\mathrm{A}} \cdot \boldsymbol{n}_{\mathrm{B}}^{0}|^2\right\}\omega_{\mathrm{Q}}\right), \tag{5.12}$$

$$\xi_{\mathrm{B}} = \omega_{\mathrm{B}}^{+} - r\left(n^{00}\omega_{\mathrm{E}} + \left\{2\left(n^{00}\right)^2 - |\boldsymbol{e}_{B} \cdot \boldsymbol{n}_{\mathrm{A}}^{0}|^2\right\}\omega_{\mathrm{Q}}\right), \tag{5.13}$$

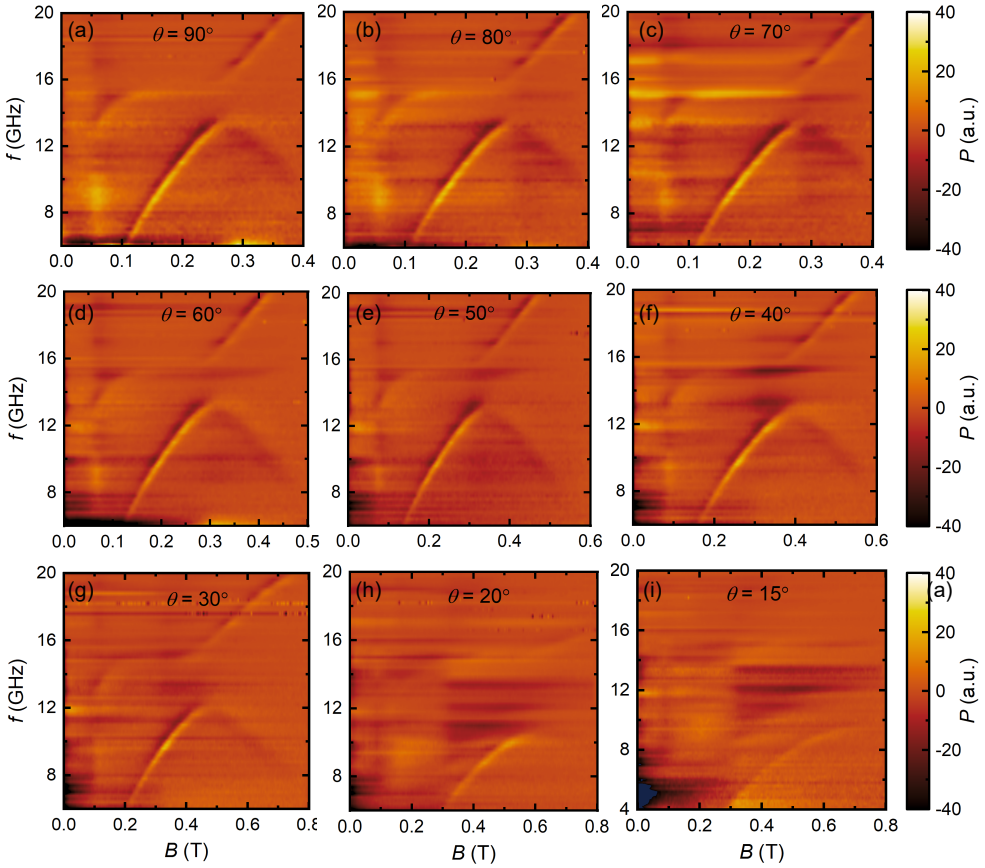

Figure 5.19: Microwave transmission as a function of frequency and applied field for different θ for NiFe(5)/Ru(0.4)/NiFe(3) sample. The coupling gap starts to increase as θ is decreased.

Here, $\omega^{\pm}_{\mathrm{A,B}} = \left(\omega^{\theta}_{\mathrm{A,B}} \pm \omega^{\phi}_{\mathrm{A,B}}\right)/2$ with $\omega^{\theta}_{\mathrm{A,B}} = |\gamma_{\mathrm{A,B}}| B^{\theta}_{\mathrm{A,B}}, \omega^{\phi}_{\mathrm{A,B}} = |\gamma_{\mathrm{A,B}}| B^{\phi}_{\mathrm{A,B}}$ representing the resultant frequency at given fields and $\boldsymbol{e}_{\mathrm{A,B}}, n^{00}$ are the chirality vectors and directional cosines respectively. See Appendix E for more details. The remaining terms in Eq. 5.11 are expressed as below.

$$\eta_A = \omega_A^- + r^{-1}\left(\boldsymbol{e}_A \cdot \boldsymbol{n}_B^0\right)^2 \omega_Q, \tag{5.14}$$

$$\eta_B = \omega_B^- + r^{-1}\left(\boldsymbol{e}_B \cdot \boldsymbol{n}_A^0\right)^2 \omega_Q, \tag{5.15}$$

$$\zeta_1 = \frac{\left(\omega_E + 2n^{00}\omega_Q\right)\boldsymbol{e}_A \cdot \overline{\boldsymbol{e}_B} + 2\omega_Q\left(\boldsymbol{e}_A \cdot \boldsymbol{n}_B^0\right)\left(\overline{\boldsymbol{e}_B} \cdot \boldsymbol{n}_A^0\right)}{2}, \tag{5.16}$$

$$\zeta_2 = \frac{\left(\omega_E + 2n^{00}\omega_Q\right)\boldsymbol{e}_A \cdot \boldsymbol{e}_B + 2\omega_Q\left(\boldsymbol{e}_A \cdot \boldsymbol{n}_B^0\right)\left(\boldsymbol{e}_B \cdot \boldsymbol{n}_A^0\right)}{2}, \tag{5.17}$$

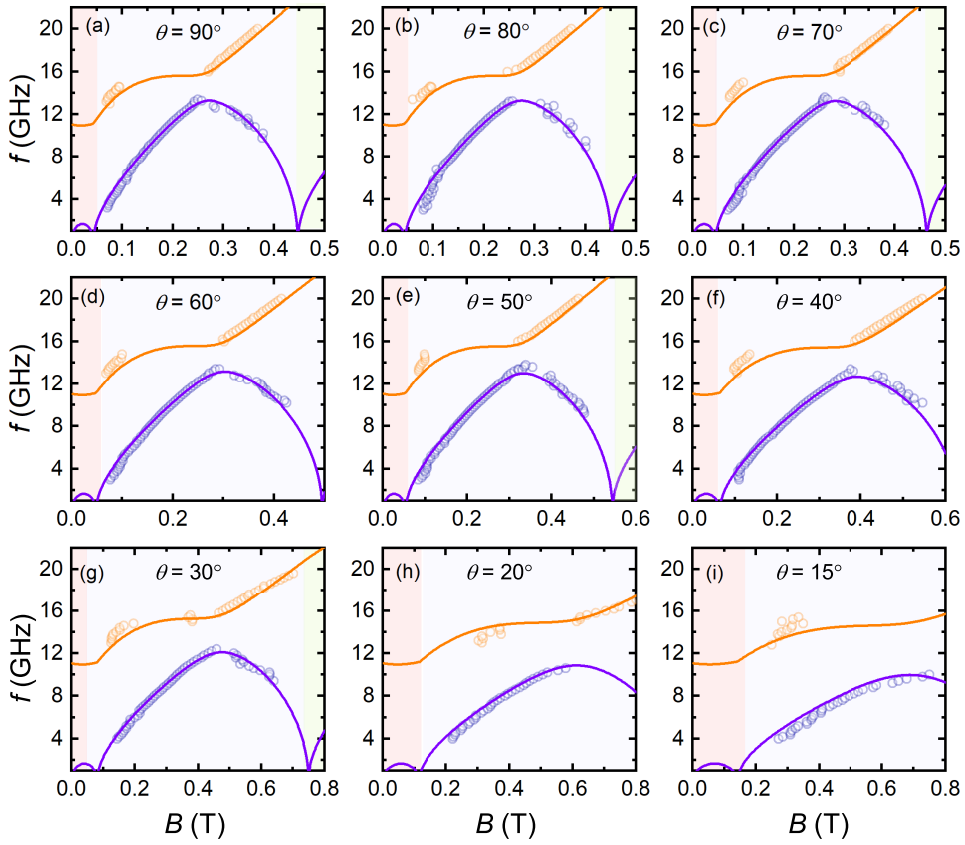

Figure 5.20: Fitting results for data of NiFe(5)/Ru(0.4)/NiFe(3) sample shown in Fig. 5.19 for different θ values. The coupling gap, increases as θ is decreased. The solid lines are fit curves obtained from macrospin model. The colors red, blue and green correspond to anti-ferromagnetic, canted and forced -ferromagnetic regions respectively.

The material parameters obtained from the VSM measurements as summarised in Table. 5.1 are used to obtain the resonance frequencies by solving the eigen value problem and the results are shown as solid lines in Fig. 5.18 (e). The results from the theoretical model matches the experimental data nicely and a coupling gap $\approx$ 1.8 GHz is seen. This is in contrast to the symmetric sample when the two layers are of same thickness and the gap is closed for the in-plane applied field. To show this, simulations were done for the case with both NiFe layers as same thickness of 5 nm and the crossing of two modes was observed. As the asymmetry was introduced by changing the layer thickness we could see the gap opening since the two layers are subjected to different exchange field strength. The results are summarised in Fig. 5.18(e).

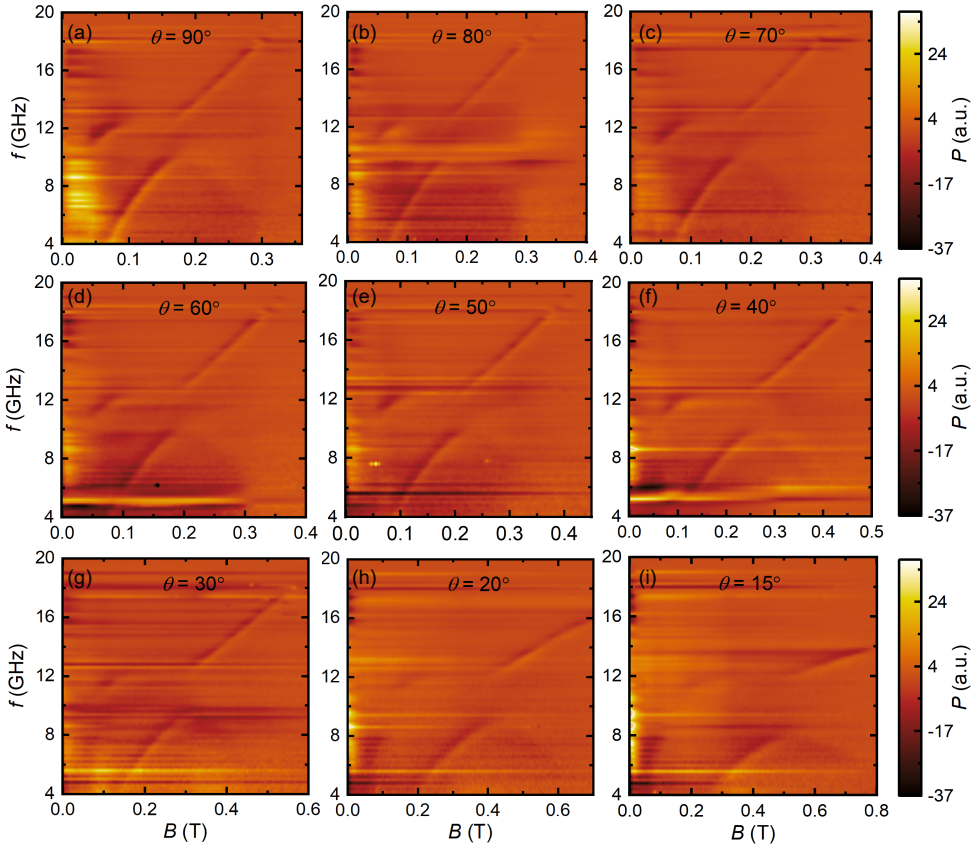

Figure 5.21: Microwave transmission as a function of frequency and applied field for different θ for NiFe(3)/Ru(0.4)/NiFe(5) sample. The coupling gap starts to increase as θ is decreased.

Further increase of the coupling gap and thus coupling strength (half of the coupling gap) was done by tilting the moments toward the out-of-plane direction as shown in Fig. 5.19. When the angle θ is decreased from 90°, it was observed that the gap size starts to increase, similar to those reported in synthetic anti-ferromagnets case in Sec. 5.4. Fig. 5.20 shows the results from the macrospin model.

The theoretical model reproduces the experimental result nicely for all the angles as evident from Fig. 5.20. The maximum coupling gap is quantified from the well-fit calculation results and is greater than the one obtained for symmetrical case with identical ferromagnet thickness [24]. This signifies stronger coupling achievable in asymmetrical case compared to symmetrical SyAF. Similar measurement and analysis was repeated for NiFe(3)/Ru(0.4)/NiFe(5) sample and the results are summarised in Fig. 5.21, 5.22.

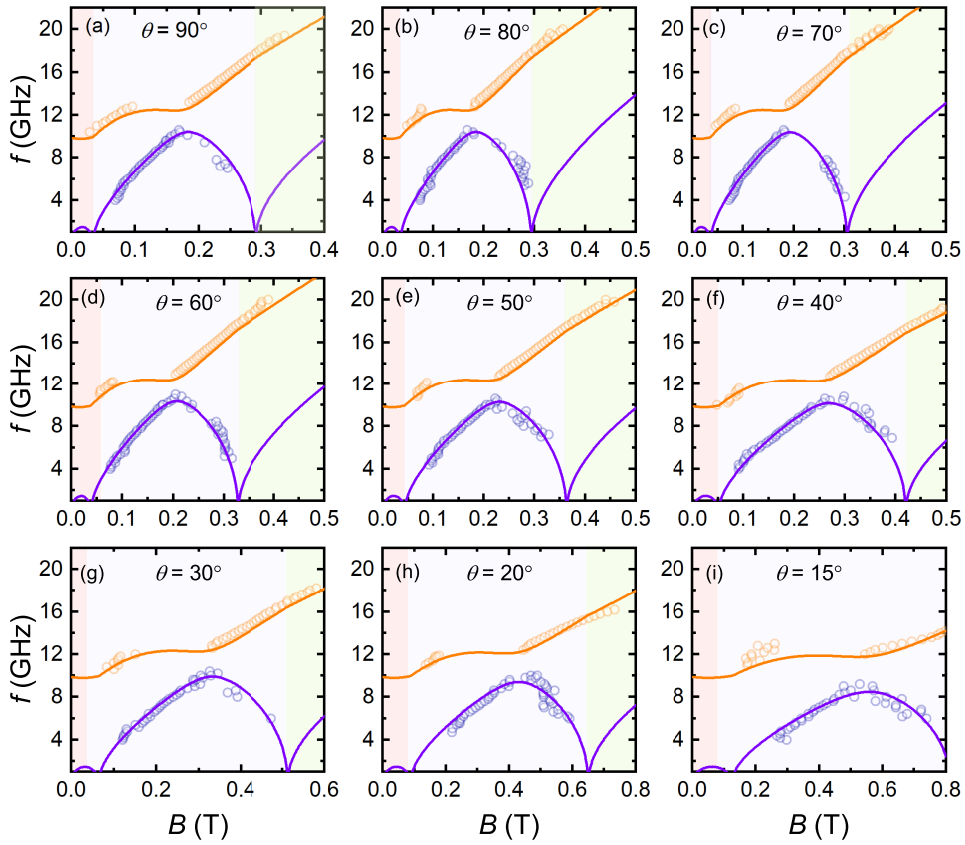

Figure 5.22: Fitting results for data of NiFe(3)/Ru(0.4)/NiFe(5) sample shown in Fig. 5.21 for different θ values. The coupling gap, increases as θ is decreased. The solid lines are fit curves obtained from macrospin model. The colors red, blue and green correspond to anti-ferromagnetic, canted and forced-ferromagnetic regions respectively.

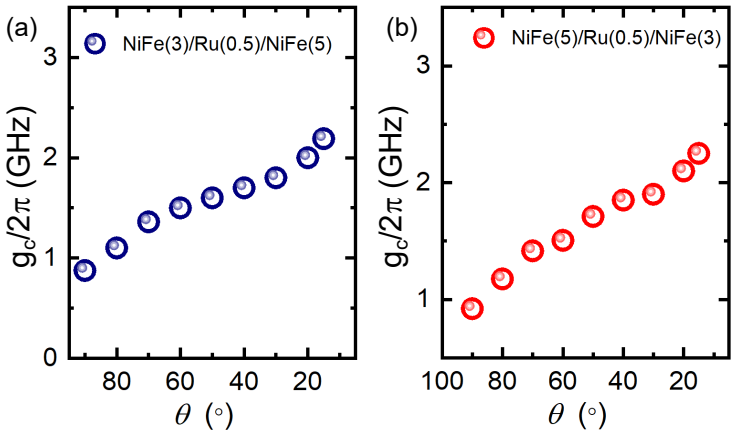

Figure 5.23: The coupling strength $g_c/2\pi$ as a function of θ. The results from two samples (a) NiFe(3)/Ru(0.4)/NiFe(5) and (b) NiFe(5)/Ru(0.4)/NiFe(3) are plotted. Both samples show similar $g_c/2\pi$ and maximum strength achieved is large compared to symmetrical SyAF case [24].

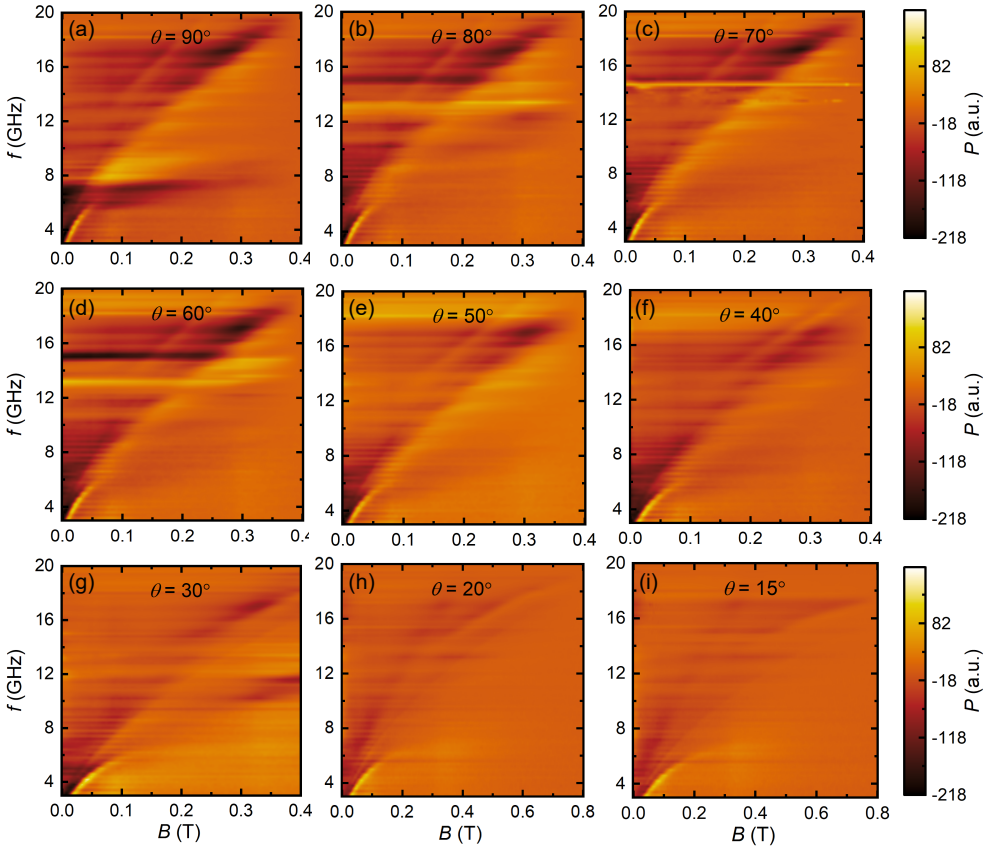

Figure 5.24: Microwave transmission as a function of frequency and applied field for different θ for CoFeB(3)/Ru(0.45)/NiFe(1.5) sample. The numbers in brackets correspond to the thickness in nm. Two modes are visible for the antiferromagnetic regime. (Note- fitting results shown in Fig. 5.27)

The coupling strength, $g_c/2\pi$, calculated as half of the coupling gap for both the samples is plotted in Fig. 5.23. Both samples show similar values of $g_c/2\pi$ as evident from similar exchange field strength. The results signify the effect of asymmetry on $g_c/2\pi$ and provide a means for tuning $g_c/2\pi$ both intrinsically (layer-thickness variation) and increasing the strength by modifying the tilt angle of the two moments (extrinsic symmetry breaking). Also it signifies greater efficiency in inducing magnon-magnon coupling in asymmetrical SyFs. From Fig. 5.23 it can be visualised that coupling strength (or coupling gap) shows an increase as θ is decreased toward out-of-plane direction. Moreover, by designing the layer thickness ratio of two layers we can tune the gap to achieve larger coupling values.

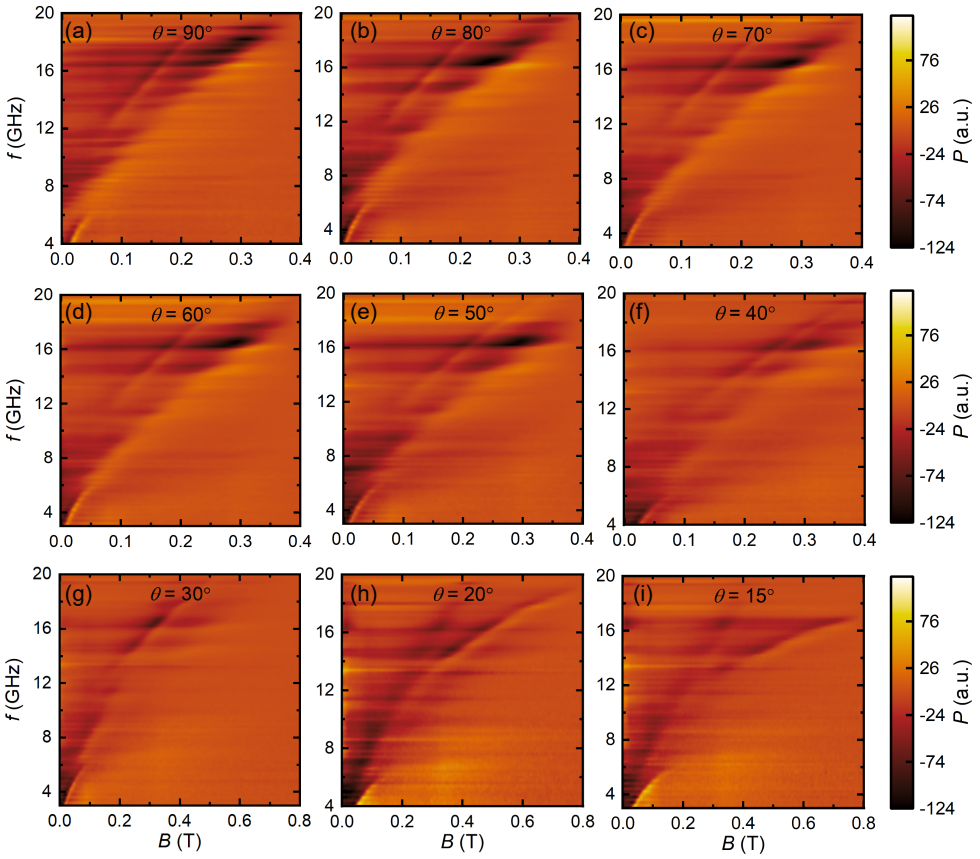

Figure 5.25: Microwave transmission as a function of frequency and applied field for different θ for CoFeB(3)/Ru(0.5)/NiFe(1.5) sample. The numbers in brackets correspond to the thickness in nm. Two modes are visible for the antiferromagnetic regime. (Note- fitting results shown in Fig. 5.28)

5.12 Asymmetrical CoFeB/Ru/NiFe samples

Another way to introduce the asymmetry is by using two different FM layers. In the previous section we focussed on two FM of same material but different thickness ($d_A \neq d_B$). This section shows the effect of the change in exchange field strength caused by dissimilar FM as well as Ru thickness on the coupling. Three different samples were studied with different Ru thickness, d_{Ru} = 0.45 nm, 0.5 nm and 0.55 nm. All the samples had the FM_1 as CoFeB with thickness 3 nm and FM_2 as NiFe with thickness 1.5 nm. The exchange field strength and other material parameters obtained from VSM data are summarised in Table. 5.1. It can be seen that as the Ru thickness layer is increased the exchange field strength value decreases signifying weaker interlayer coupling for thicker Ru samples. Fig. 5.24, 5.25 and 5.26

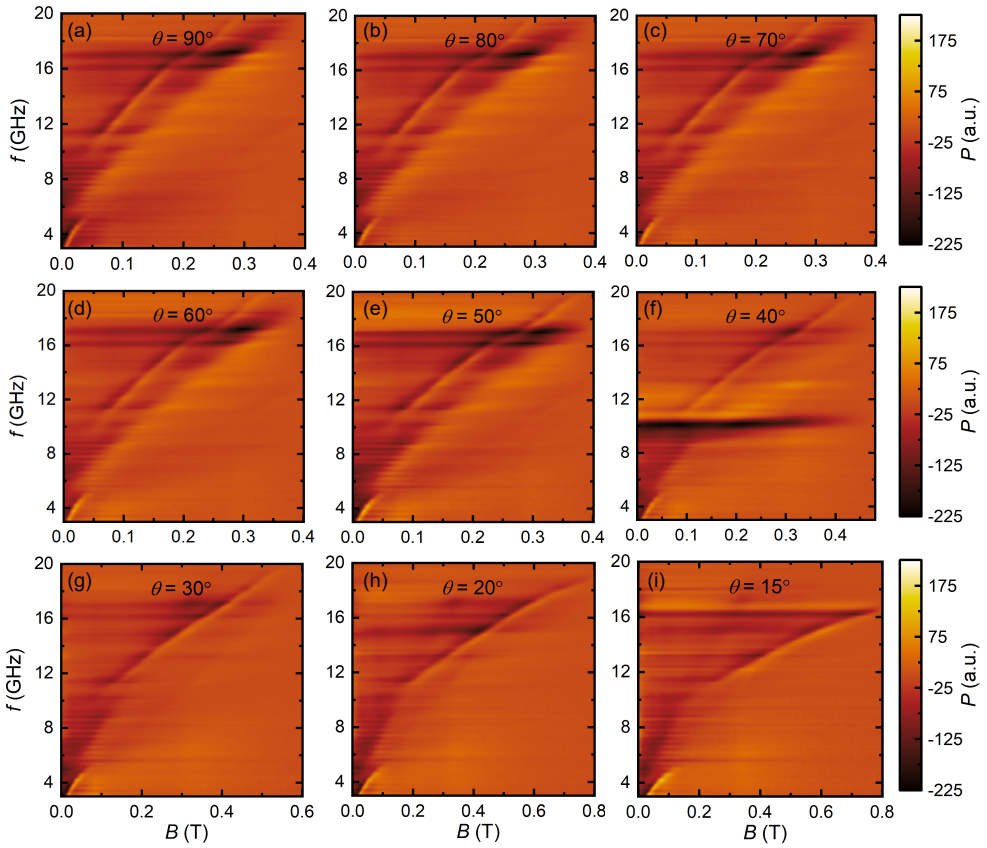

Figure 5.26: Microwave transmission as a function of frequency and applied field for different θ for CoFeB(3)/Ru(0.55)/NiFe(1.5) sample. The numbers in brackets correspond to the thickness in nm. Two modes are visible for the anti-ferromagnetic regime. (Note- fitting results shown in Fig. 5.29)

shows the colorplot for samples with Ru thickness 0.45 nm, 0.5 nm and 0.55 nm in respectively for $B_\perp$ case. For the case of applied field in-plane $\theta = 90^\circ$, for the sample with Ru thickness = 0.45 nm a coupling gap of 6.84 GHz is achieved in the anti-ferromagnetic regime which decreases to 6.3 GHz and 5.6 GHz for Ru thickness 0.5 nm and 0.55 nm respectively. Compared to the previous case when two FM were of same material it can be seen that the anti-ferromagnetic region is larger for these samples which means that a larger field is required to cant the two momemts and bring these samples into spin-flop regime. Moreover, it is to be noted that in the colorplot we donot see both modes in canted regime since the measurement is for $B_\perp$ case where due to geometry only one mode is excited. (See Sec. 5.3. Because of lower SNR ratio the colorplot is shown only for the transverse geometry).

A full angular dependence was carried out for all the three samples by tilting

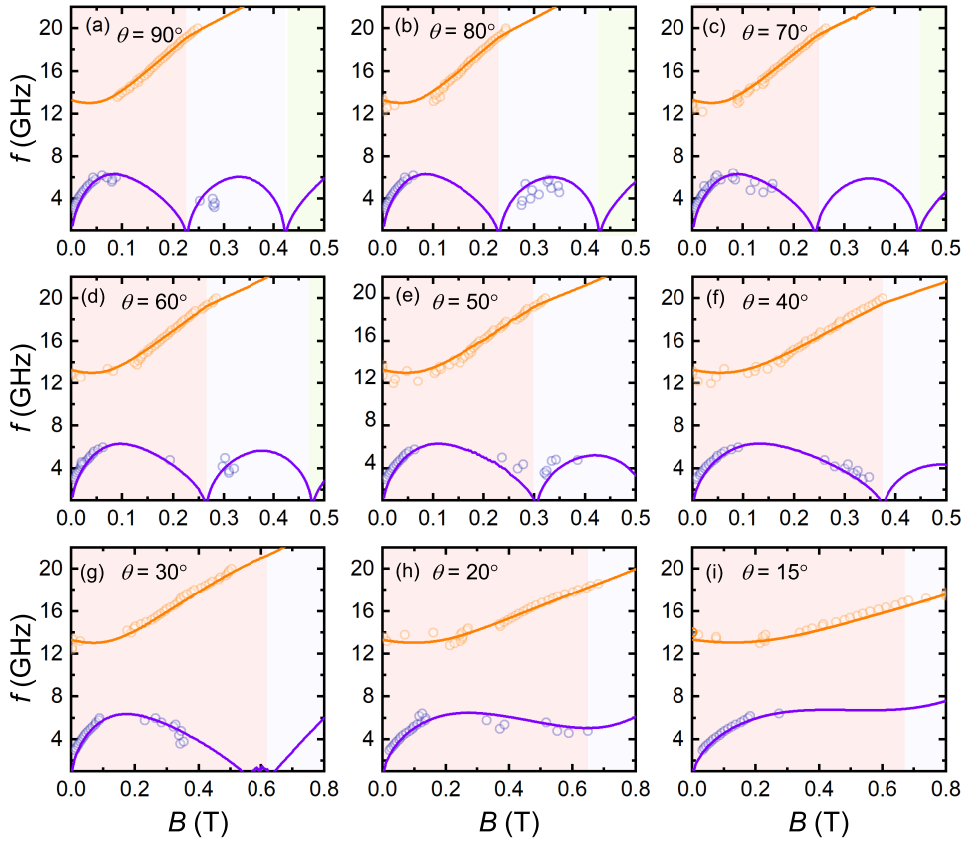

Figure 5.27: Fitting results for data of CoFeB(3)/Ru(0.45)/NiFe(1.5) sample shown in Fig. 5.24 for different θ values. The coupling gap varies as θ is decreased. The solid lines are fit curves obtained from macrospin model. The colors red, blue and green correspond to anti-ferromagnetic, canted and forced - ferromagnetic regions respectively.

the applied field towards out-of-plane direction. All of the results are summarised in Fig. 5.24, 5.25 and 5.26. In order to study the effect of rotational symmetry breaking by tilting the field direction, we have to compare the coupling gap variation in canted regime. Because of experimental difficulties as described earlier, both modes could not be seen in the canted regime and so the theoretical model was used for detailed analysis of $g_c/2\pi$ and the gap variation with θ which is presented in next sections.

By using our macrospin model as detailed in previous section, the resonance frequency was obtained for the two modes and the results are plotted in Fig. 5.27, 5.28 and 5.29. The resonance position is plotted as a function of field obtained by the fittings of experimental data for $B_{||}$ configuration using Eq. 3.1. For these samples, the lower frequency mode in canted regime were hard to detect which can

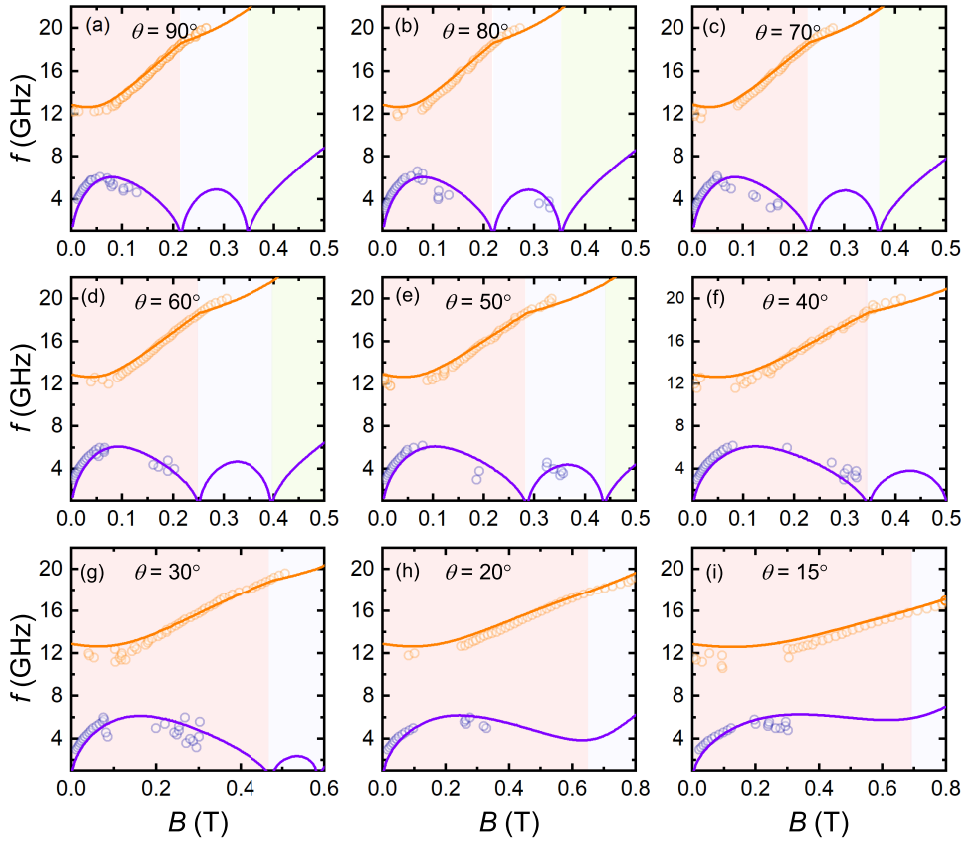

Figure 5.28: Fitting results for data of CoFeB(3)/Ru(0.5)/NiFe(1.5) sample shown in Fig. 5.25 for different θ values. The coupling gap varies as θ is decreased. The solid lines are fit curves obtained from macrospin model. The colors red, blue and green correspond to anti-ferromagnetic, canted and forced - ferromagnetic regions respectively.

be due to poor signal to noise ratio and broader linewidth at higher resonance field values and so only a few data points could be extracted. Our theoretical model matches well with the experimental results for all samples and enable to estimate the coupling gap efficiently in the canted regime. As the angle θ is decreased, the field required to cant the two moments increases. This is also shown in asymmetric NiFe/Ru/NiFe case where slightly larger field was required to cant the two moments as θ was changed. This shows that by choosing different Ru thickness and different FM we can tune the field strength for canting as well.

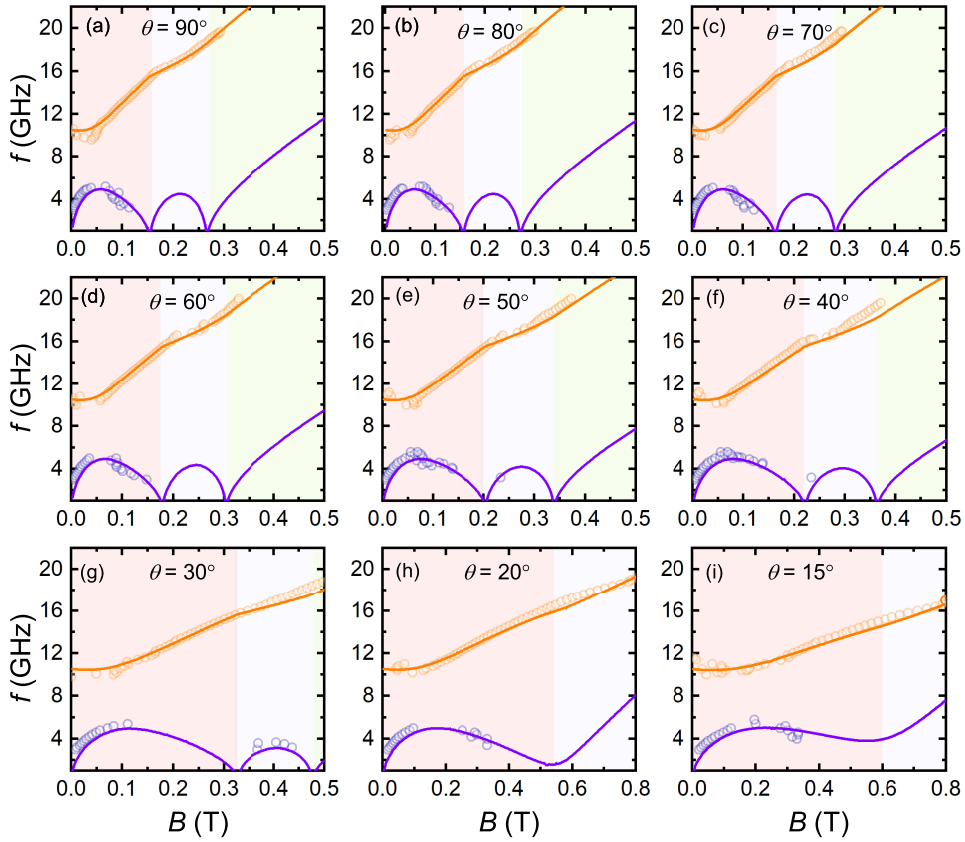

Figure 5.29: Fitting results for data of CoFeB(3)/Ru(0.55)/NiFe(1.5) sample shown in Fig. 5.26 for different θ values. The coupling gap varies as θ is decreased. The solid lines are fit curves obtained from macrospin model. The colors red, blue and green correspond to anti-ferromagnetic, canted and forced - ferromagnetic regions respectively.

5.13 Coupling Strength variation with θ

Fig. 5.30 (b) shows the variation of coupling strength, $g_c/2\pi$, for different samples as a function of θ. For the asymmetrical CoFeB/Ru/NiFe samples, the coupling gap is extracted in the canted regime from the theoretical model. It can be seen that for dissimilar NiFe/Ru/NiFe samples the maximum $g_c/2\pi$ achieved is about 2 GHz in the canted regime. This is twice that reported in Sud et. al [24] for CoFeB/Ru/CoFeB symmetrical SyAF sample. In comparison the samples with dissimilar FM as well as thickness show a larger $g_c/2\pi$ and the maximum value attained is 9 GHz for sample with Ru thickness 0.45 nm. The large values in samples with dissimilar FM and thickness show that larger coupling efficiency can be achieved by both variation in thickness as well as material of FM. Also we find that

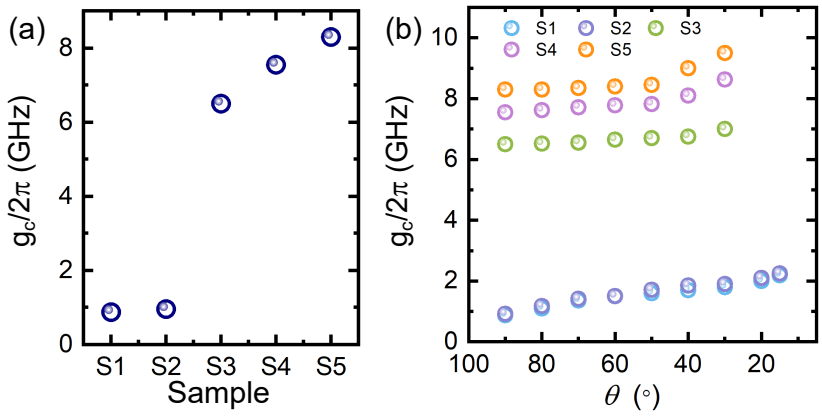

Figure 5.30: (a)The coupling strength $g_c/2\pi$ for $\theta = 90^{\circ}$ for five samples. Here, S1 = NiFe(3)/Ru(0.4)/NiFe(5), S2 = NiFe(5)/Ru(0.4)/NiFe(3), S3 = CoFeB(3)/Ru(0.55)/NiFe(1.5), S4 = CoFeB(3)/Ru(0.5)/NiFe(1.5) and S5 = CoFeB(3)/Ru(0.45)/NiFe(1.5). (b) $g_c/2\pi$ as a function of θ for different samples. The variation of $g_c/2\pi$ with θ is more profound for S1 and S2 samples. For the samples S3, S4, S5 the $g_c/2\pi$ is larger but the variation with angle is much small. Note - The error bars are smaller than the marker on the plots.

gap does not change much with θ for the asymmetrical CoFeB/Ru/NiFe samples as compared to asymmetrical NiFe/Ru/NiFe samples. These results thus show the ability of tuning the gap both intrinsically by varying the layer thickness/material as well extrinsically by tilting the field. Different thickness ratio and choice of FM materials can affect the coupling strength, $g_c/2\pi$. It is shown both experimentally and quantitatively through the model calculations.

Effect of Asymmetry on linewidth of magnon modes - The linewidth of the resonance for the two modes were compared and interpreted as a function of the applied field in different regimes for the two set of samples as shown in Fig. 5.31. The signal could be detected only in the canted regime for NiFe(3)/Ru/NiFe(5) sample. In the anti-ferromagnetic regime for CoFeB/Ru(0.55)/NiFe sample, the mode corresponding to low-frequency shown as lower mode has a significantly lower linewidth at low field values and increases gradually while approaching the canted regime. This is due to the change in precession type while going from antiferromagnetically coupled regime to canted regime. Moreover, the difference in linewidth is not constant and the linewidth for the higher frequency mode decreases with increase in field. In the canted regime the linewidth for upper mode increases as can be seen for both

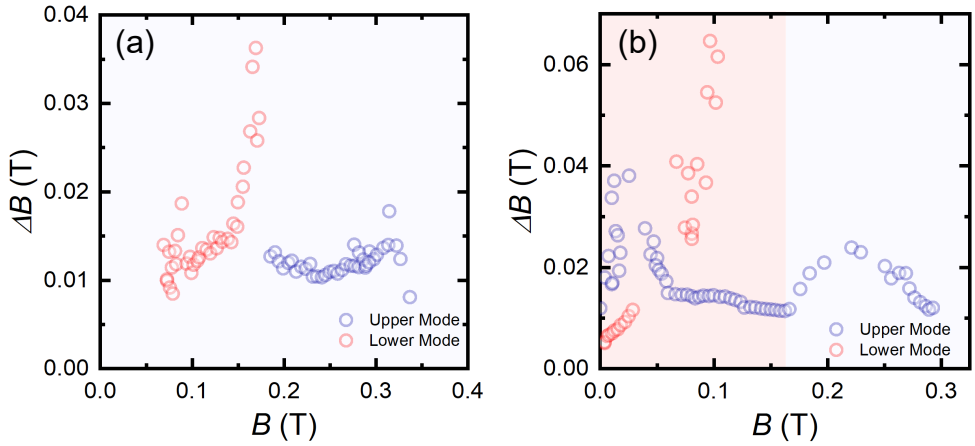

Figure 5.31: HWHM linewidth as a function of magnetic field for $\theta = 90^{\circ}$ for (a) NiFe(3)/Ru(0.4)/NiFe(5) and (b) CoFeB(3)/Ru(0.55)/NiFe(1.5). The coloured regions red and blue correspond to anti-ferromagnetic and canted regime respectively.

samples and finally saturates at high fields. This can be explained based on change in mutual spin pumping of two layers along with change in phase of precession in different regimes [237]. The results obtained are in agreement with previous studies which see similar behaviour of linewidth in different regimes [237].

In conclusion, we studied the dynamics of asymmetric synthetic ferrimagnetic structures and experimentally show the magnon-magnon coupling in SyFs with dissimlar material and thickness of two FM layers. This allows the control of coupling strength by intrinsic orthogonal symmetry breaking compared to symmetrical samples. The coupling strength far exceeds the losses, described by the frequency half-width at half maximum of the individual modes. By calculating the coupling gap as a function of external field tilt angle we can putatively claim that both intrinsic and extrinsic symmetry breaking (SB) can realise strong magnon-magnon coupling in SyAFs. Further, the strong coupling leads to an entanglement between even and odd parity modes, making it attractive for coherent information processing applications. A theoretical model was generalized in the macro spin limit by solving the two coupled equations to describe the microwave absorption spectroscopy for the SB induced coupling in SyFs. This study should shed light on the potential of SyFs for studying and controlling magnon-magnon coherent coupling at room temperature. Moreover large tunable coupling strengths in this system will provide a novel

platform for increased control of hybrid magnonic systems.

Chapter 6

Ferromagnetic resonance driven by current-induced torque in magnetic multi-layer thin films

Introduction

Static or alternating magnetic fields exert torque on a ferromagnet which induces magnetization switching or ferromagnetic resonance. This is the fundamental phenomena which is utilised in magneto-electronic applications. As outlined in previous Chapters 4 and 5, the ferromagnetic resonance (FMR) was induced by using external fields. However, for device applications a major aim in spintronics research is to replace the magnetic fields.

One such phenomena which utilises spin polarised electric current for manipulating the magnetization is spin transfer torque (STT). STT is a quantum phenomena in which the spins polarise on spatially varying magnetization via exchange interaction as described in Chapter 2. In thin film ferromagnetic-heavy metal (FM/HM) bilayers, two mechansims are responsible for generating STT which arise due to spin-orbit interaction. One is the spin Hall effect (SHE) [269, 270, 2] which generally has the damping-like (DL) form predicted by Slonczewski and Berger [28, 29] but it has been shown that a field-like (FL) term can also exist [271]. The other mechanism is the Rashba-Edelstein effect [272, 273] which can generate both FL

and DL torques. In this chapter current-induced torque (CIT) excitation of resonance is studied in two different magnetic multi-layer films. The CIT excitation of acoustic and optical modes in Ta/NiFe/Ru/NiFe/Ta synthetic antiferromagnet stacks grown on thermally oxidised Si substrates is first described. The two Ta layers serve as spin torque sources with the opposite polarisations both in spin currents and Oersted fields acting on their adjacent NiFe layers. This can create the odd symmetry of spatial spin torque distribution across the growth direction, allowing us to observe different spin-wave excitation efficiency from synthetic antiferromagnets excited by homogeneous torques. The torque symmetry is analysed by in-plane angular dependence of symmetric and anti-symmetric lineshape amplitudes for their resonance and this confirm that the parallel (perpendicular) pumping nature for the acoustic (optical) modes in our devices, which is in stark difference from the modes excited by spatially homogeneous torques. A macrospin model is presented for this particular spin-torque excitation geometry, which excellently supports our experimental observation. The results offer capability of controlling spin-wave excitations by local spin-torque sources and we can explore further spin-wave control schemes based on this concept.

The other half of this chapter is devoted to a study of CIT in Ni/Pt heterostructures. The effect of interfaces on FL and DL torque efficiencies is studied by systematic analysis in bilayer and multi-layer films grown on different substrates to control crystallinity by growth.

6.1 Current induced Spin wave excitation in Synthetic Antiferromagnets

Synthetic antiferromagnets (SyAFs) are an excellent platform to explore novel spintronic and magnonic concepts with coupled magnetic moments [215, 274]. Unlike a homogeneously magnetised single-layer ferromagnet, coupled magnetic layers are able to offer rich magnetic states where the competition between interlayer exchange coupling, external-field-induced Zeeman interaction as well as other magnetic anisotropy terms plays a role. This can expand into their dy-

namic regimes as the coupled moment nature inherently provides two eigenmodes, acoustic and optical modes [275, 223, 222], where time-dependent components of two coupled moments are oscillating in-phase (acoustic) and out-of-phase (optical) in a spin-flop (canted) regime (Also described in Chapter 5). These pure magnetic modes have been studied and discussed already around 1990s, e.g. by Grunberg et al. [224] and Zhang et al. [225], followed by a number of more recent reports to investigate magnetic dynamics in SyAFs for various topics [276, 226, 227, 277, 236, 229, 228, 237, 230, 278, 24]. SyAFs are also a subject of CIT excitations so far at (or close to) the dc limit [279, 280, 281, 282, 283, 284] and there has been little in the literature on the use of CITs for exciting SyAF spin-waves at GHz frequencies.

When we excite spin-waves by oscillating magnetic fields, the spatial symmetry/profile of microwave excitation determines which spin-wave modes are excited. In the simplest case, a uniform distribution of microwave excitation fields across a magnet can excite the uniform spin-wave mode (wavevetor $k = 0$) as well as higher-order spin-wave resonance modes ($k > 0$) with odd index numbers since the spatial profile of the microwave excitation and spin-wave mode amplitude (with phase) matches to each other in terms of symmetry. Higher-order spin-wave resonance modes with even index numbers are excluded because the mode overlapping between microwaves and the spin-waves becomes zero when it is integrated over the real space. This in turn suggests that it should be possible to control the selection rules of spin-wave excitations by designing the spatial profile of excitation fields. Accessing hidden spin-wave states as well as tailoring spin-wave excitation efficiency by this approach has not been much explored in the past.

The following sections describe the study of spin-wave excitation symmetry control by spatially anti-symmetric spin torques in our SyAF devices. By utilising local spin excitations due to SHE and Oersted fields from adjacent heavy-metal Ta layers, the spin-wave excitation nature is controlled in the SyAF devices. The torque symmetry of parallel (perpendicular) pumping configuration of acoustic (optical) modes is excited and measured in the devices, which is signature of the anti-

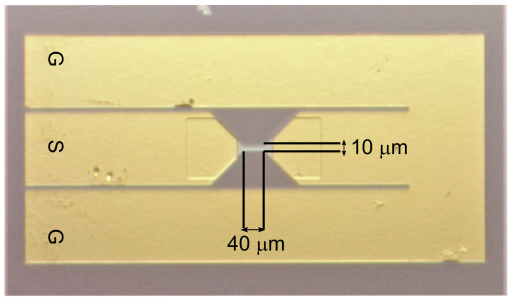

Figure 6.1: Optical micrograph of a 10×40 μm^2 rectangular bar patterned on Ta/NiFe/Ru/NiFe/Ta sample. Ti/Au bilayer GSG type waveguide is deposited on top which is connected to bias-tee via RF-Probe to measure the resonance.

symmetric spin torques for the two coupled moments. Analytical expressions for rectification voltages are calculated based on the Landau-Lifshitz-Gilbert (LLG) equation for coupled magnetic moments at the macrospin limit. The model equations fully support the torque symmetry observed in the experiments as well as allow to quantitatively analyse spin-orbit transport parameters such as the spin-Hall angle.

6.1.1 Sample growth and patterning

Preparation of SyAF films – The SyAF films used in this study were prepared by magnetron co-sputtering techniques at a base pressure of 3×10^{-7} Pa. The films were grown on thermally oxidized Si substrates with stacking patterns of Ta(5)/NiFe(5)/Ru(0.4 or 0.5)/NiFe(5)/Ta(5) where the number in the brackets represents the thickness in nm.

Sample Patterning – A micrograph of a 10×40 μm^2 bar with gold pads on SyAF sample is shown in Fig. 6.1. Standard Photolithography and Ar ion milling technique were used to pattern the sample into rectangular bars with width (length) of 10 (40) μm. The fabrication steps are described below:

Photolithography – The sample surface was first cleaned with acetone for 3 minutes and then with ethanol for 1 minute in a ultrasonic bath. After drying the sample surface with nitrogen spray gun, the samples were spin coated with Microposit S1818 at 6000 rpm for 50 seconds followed by baking on hot-plate at 115 $^\circ$ C for 1 minute. The samples were then exposed to ultraviolet light via a self-designed photomask for 5 seconds. Finally the samples were developed in Microposit MF319

for 1 minute and rinsed in de-ionized water for 1 minute followed by drying with nitrogen spray gun.

Ion Milling – The developed samples were etched using argon ion milling. The samples were placed in a chamber filled with argon gas. The hot filament at the top of the chamber emitted accelerating electrons to ionize the argon gas. The argon ions were then accelerated under a beam potential of 500 V and bombarded the sample surface, etching the area not protected by photoresist. The beam current was set at 25 mA for the whole milling process. The milling time of 20 minute was enough to remove the SyAF layer and penetrate into the Si substrate. The samples were then washed with acetone for 3 minutes and ethanol for 1 minute in ultrasonic bath to remove the resist.

Waveguide deposition – The Ti/Au bilayer were deposited for preparaing a microwave waveguide on top of each bar. The photolithography steps as above were followed to define the antenna. The antenna consisted of ground signal ground (GSG) configuration with width of 150 μm and and gap of 10 μm to ensure 50 Ω impedance matching. After developing, the samples were loaded into sputtering chamber. The chamber was evacuated to a 3×10^{-7} Pa or less. A Ti layer was sputtered for 5 minutes at rate of 0.6 Å/s followed by Au sputtering for 6 minutes at rate of 7.5 Å/s. The use of Ti provides improved adhesion. Finally, the lift-off process was carried out by washing the sample in acetone for 5 minutes in ultrasonic bath followed by 1 minute ethanol rinse to remove residual photoresist.

6.1.2 Vibrating sample magnetometer characterisation and inter-layer exchange interaction

Prior to device fabrication, the films were characterised by vibrating magnetometry techniques to quantify the interlayer exchange coupling strength and to confirm the presence of spin-flop regimes in the films. Figure 6.2 shows characterisation of two samples of Ru thickness 0.4 and 0.5 nm by a vibrating sample magnetometer. The red curves are obtained by minimising Eq. 5.1 iteratively to obtain $\phi(B)$ and thus obtain $M(B)$ given by $M(B) = M_s \cos\phi(B)$ [237, 222, 240]. Here, $\phi(B)$ is the angle between the applied magnetic field direction and equilibrium direction of individual

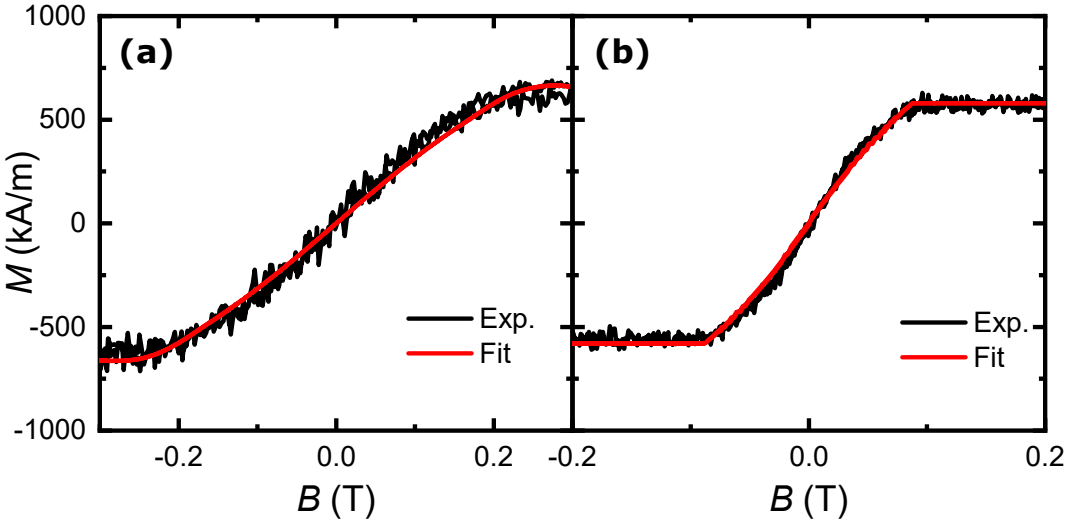

Figure 6.2: (a-b) Magnetization curve of the Ta (5 nm)/ NiFe (5 nm)/Ru (t nm)/NiFe (5 nm)/Ta (5 nm) measured by vibrating sample magnetometer for (a) t = 0.4 and (b) t = 0.5. The black (red) curve is the experimental (calculation) results.

moments. The values of the linear and quadratic exchange fields used to obtain the red curves are 120 (50) $\pm$ 1 (0.3) mT and 4 (2) $\pm$ 0.1 (0.02) mT for the 0.4 (0.5) nm Ru thickness sample, with M_s= 620 (600) kA/m for the 0.4 (0.5) nm Ru sample. The effective magnetic exchange field is obtained by differentiating the exchange coupling terms (F_{ex}) in Eq. 5.1 with respect to $\boldsymbol{m}_{1(2)}$ which is given by Eq. 5.2.

6.1.3 Microwave calibration

Due to impedance mismatch between microwave lines and the sample (with few hundreds Ω in resistance), it is expected that there is a large amount of power reflection from the devices. This results in the amount of power reaching to the sample is a fraction of power supplied from the source. In order to quantify the actual power propagating through the device, a bolometric technique [114, 178] was used. In this method, the resistance change caused by joule heating from either a known dc current I_{DC} or microwave power P_{input} is compared as current calibration. Figs. 6.3(a)-(d), show the resistance changes by two current excitations. By scaling two parameters (P_{input} and I_{DC}) by the sample resistance, the current flowing through the device is quantified at GHz frequency. The microwave power at sample (P_{sample}) is then calculated and plotted against microwave power at source (P_{input}) as shown in Figs. 6.3(e) and (f). From this slope, the ratio of 0.06 between P_{sample} and P_{input}

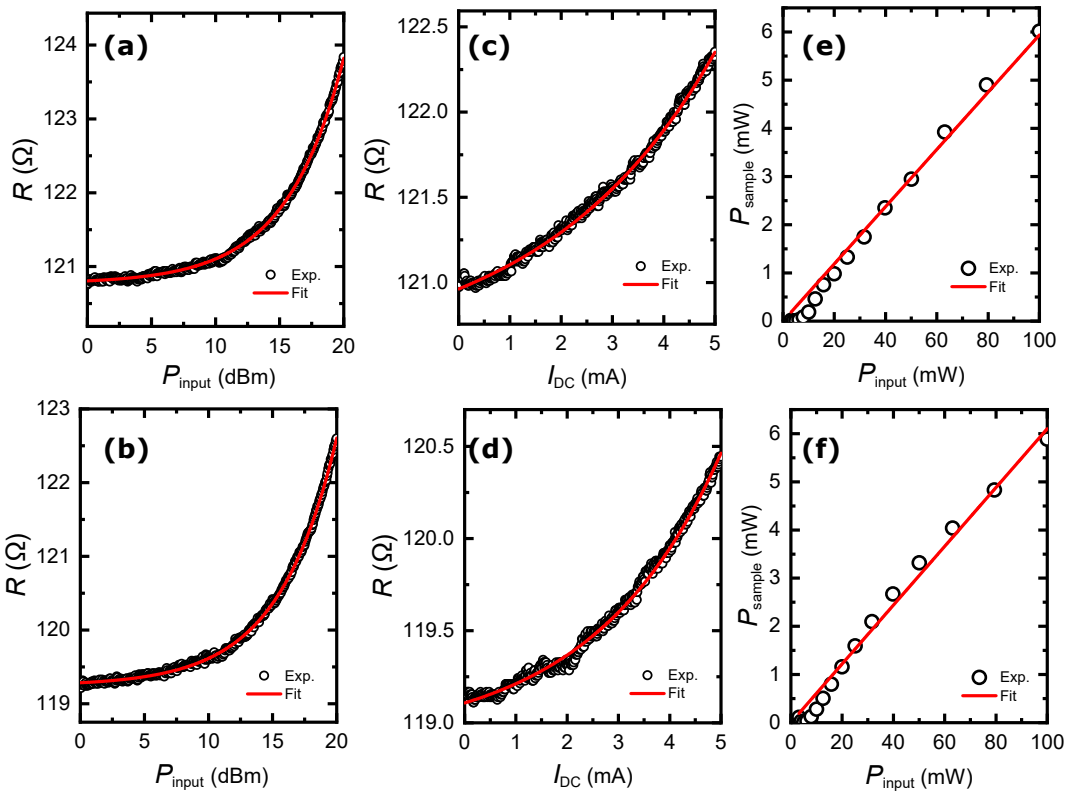

Figure 6.3: Resistance change as a function of microwave power for (a) 0.4 nm and (b) 0.5 nm. Resistance change as a function of dc current for (e) 0.4 nm and (f) 0.5 nm. Power from the source as a function of power in the sample for Ru thickness (e) 0.4 nm and (f) 0.5 nm.

was extracted, which would be a right value when we consider the refection from the device and microwave loss in lines and contacts in our microwave circuit.

6.1.4 Torque symmetry of optical and acoustic mode excitations (τ_{op} and τ_{ac})

In SyAFs for in-plane field canted conditions, optical and acoustic modes can be generated by adding two individual magnetic moments by using π rotation (C_2 operation) with respect to the applied magnetic field direction [266]. We can combine the excitation terms for each moment by following the same manner and produce the torque expressions for both modes as:

$$\boldsymbol{\tau}_{\mathrm{op}} = \boldsymbol{m}_1^0 \times (\boldsymbol{B}_1 + C_2\boldsymbol{B}_2) + \boldsymbol{m}_1^0 \times \{\boldsymbol{m}_1^0 \times (\boldsymbol{s}_1 + C_2\boldsymbol{s}_2)\}; \tag{6.1}$$

$$\boldsymbol{\tau}_{\mathrm{ac}} = \boldsymbol{m}_1^{\mathbf{0}} \times (\boldsymbol{B}_1 - C_2\boldsymbol{B}_2) + \boldsymbol{m}_1^{\mathbf{0}} \times \{\boldsymbol{m}_1^{\mathbf{0}} \times (\boldsymbol{s}_1 - C_2\boldsymbol{s}_2)\}. \tag{6.2}$$

Here, m_1^0, $\boldsymbol{B}_1$, $\boldsymbol{B}_2$, $\boldsymbol{s}_1$ and $\boldsymbol{s}_2$ are the time-independent component of magnetization for one of the coupled moments, field-like torque for first and second magnetic moments and spin polarisation causing spin-transfer torques for first and second magnetic moments respectively. Full derivations of these two torque expressions are available in the Appendix C. These expressions represent the torque symmetry of each mode excitation against the direction of external magnetic field ($\boldsymbol{B}$). When both moments are excited by uniform spin excitation, namely with the condition of $\boldsymbol{B}_1 = \boldsymbol{B}_2$ and $\boldsymbol{s}_1 = \boldsymbol{s}_2$, we can arrive at the following conclusions. (i) When $\boldsymbol{B}_1$ and $\boldsymbol{s}_1$ are symmetric for the C_2 rotation, $\boldsymbol{\tau}_{\mathrm{op}}$ is maximised ($\boldsymbol{B}_1 + C_2\boldsymbol{B}_2 = 2\boldsymbol{B}_1$) and $\boldsymbol{\tau}_{\mathrm{ac}} = 0$, and (ii) when $\boldsymbol{B}_1$ and $\boldsymbol{s}_1$ are anti-symmetric for the C_2 rotation, $\boldsymbol{\tau}_{\mathrm{op}} = 0$ and $\boldsymbol{\tau}_{\mathrm{ac}}$ is largest. Here the meaning of $\boldsymbol{B}_1$ and $\boldsymbol{s}_1$ being symmetric (anti-symmetric) for the C_2 rotation is the condition of $\boldsymbol{B}_1 \| \boldsymbol{B}$ ($\boldsymbol{B}_1 \perp \boldsymbol{B}$) which is in general termed as parallel (perpendicular) pumping configuration in magnetic dynamics. Altogether it can be summarised that under a uniform excitation condition, the optical (acoustic) mode can be excited by parallel (perpendicular) pumping configuration. In the present study, it was taken one step further to control the excitation symmetry by designing the local spin excitation configuration. When $\boldsymbol{m_1}$ and $\boldsymbol{m_2}$ experience non-uniform spin excitations, it is found from Eqs. 6.1 and 6.2 that the perpendicular/parallel pumping nature can be tuned in these experiments. On the extreme case where $\boldsymbol{B}_1 = -\boldsymbol{B}_2$ and $\boldsymbol{s}_1 = -\boldsymbol{s}_2$, it is predicted that the optical (acoustic) mode is excited by perpendicular (parallel) pumping configuration. This is because the odd-even parity of the spatial spin excitation is changed, leading to the parity change of excited spin-wave modes with this geometry.

6.1.5 Spin Transfer Torque driven resonance in SyAF

Spin-transfer-torque ferromagnetic resonance (STT-FMR) technique [285, 286] as described in Chapter 3 was used in order to excite spin-waves in the devices where the Ta layers are the source of spin torques acting on the adjacent NiFe layers individually. Crucially, the spin polarisation direction of spin torques in the Ta layers are

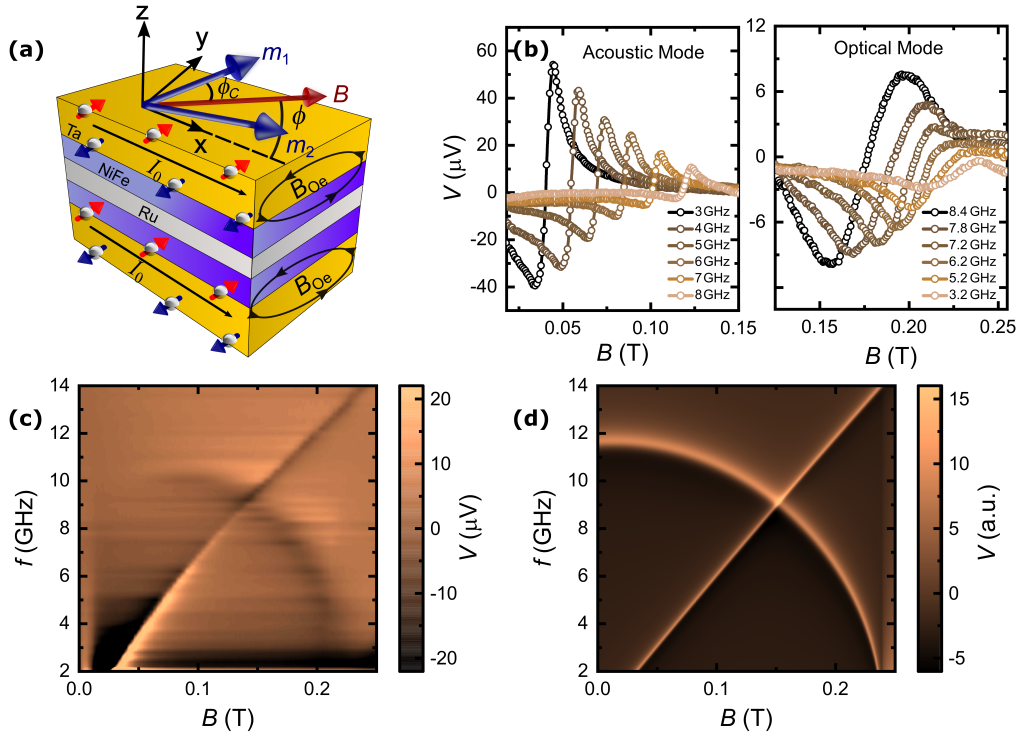

Figure 6.4: (a) A schematic of the sample geometry used for STT-FMR measurements in our study. (b) V obtained at different frequencies for acoustic and optical modes in our device for $\phi = 55^{\circ}$ (the values for some frequencies have been scaled to show them properly). (c) A 2D colorplot of V as a function of applied field and frequency, measured for $\phi = 55^{\circ}$. (d) Numerical results calculated for the experimental conditions as in (d).

opposite to each other due to the geometry, which achieves the anti-symmetric profile of these torques (e.g. $\boldsymbol{B}_1 = -\boldsymbol{B}_2$) that is utilised in this study. A schematic of the sample geometry is shown in Fig. 6.4 (a). Vector magnets are used to generate B at various in-plane angles ϕ with respect to current direction to map out the excitation symmetry in the devices. SHE [287] in the two Ta layers convert electric currents into spin-currents injected into both magnetic layers where spin torques are exerted via the STT mechanism, together with FL torques by Oersted fields. These cause a time-varying magnetization precession at resonance, producing the time-varying resistance change due to anisotropic magnetoresistance (AMR). The change of relative orientation between the magnetization, $\boldsymbol{M}$ and electrical current, $\boldsymbol{I}$ affects the electrical resistivity, ρ. This fundamental phenomena is known as AMR. To quantify the resistance change due to AMR, angle dependent measurements of resistance

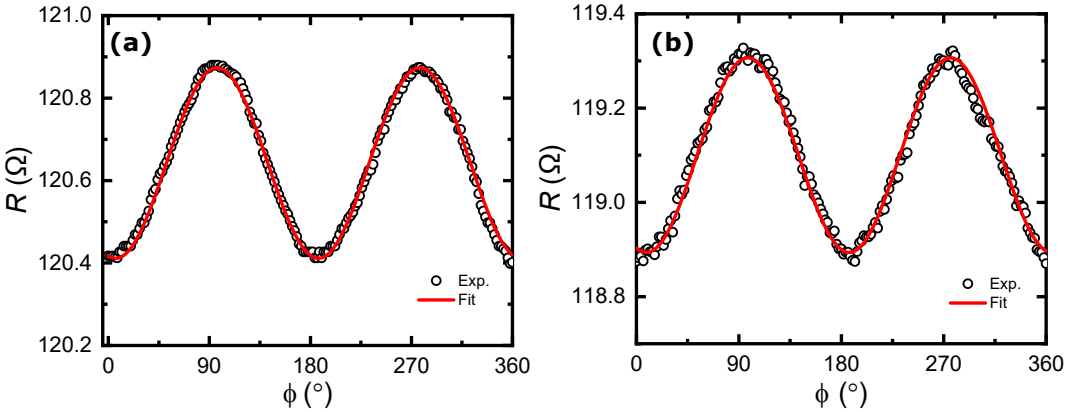

Figure 6.5: (a-b) Magnetoresistance measured as a function of static magnetization direction in the sample Ta (5 nm)/ NiFe (5 nm)/Ru (t nm)/NiFe (5 nm)/Ta (5 nm) for (a) t = 0.4 and (b) t = 0.5. The black (red) curve is the experimental (calculation) results.

as a function of magnetization direction were performed for an external magnetic field of 60 mT so that the magnetization lies in the canted regime. A DC current was applied to the sample bar and the resultant voltage was measured simultaneously using keithley K200 multimeter. The results are presented in Fig. 6.5 which shows a $\cos 2\phi$ dependence. By fitting the angular dependence using $R_0 + \Delta R_{\mathrm{AMR}} \cos 2\phi$, ΔR_{AMR}, the resistance change due to AMR was obtained as 0.5(0.4) Ω for the Ru thickness 0.4(0.5) nm. These values are used subsequently to quantify the spin Hall angle and symmetry of resultant voltages induced by STT-FMR.

As a result of AMR, the frequency mixing of two time-varying components (i.e. current and resistance) results in a time-independent voltage component which is experimentally measured. As discussed later, the experimental results were compared with analytical solutions obtained from a macrospin model with the LLG equation for coupled magnetic moments.

Both acoustic and optical modes have been clearly identified for different excitation frequencies as shown in Fig. 6.4 (b). The canted nature of synthetic antiferromagnets can be observed by the frequency dependence of resonance for both modes in our sample as shown in Fig. 6.4 (c), indicating the presence of anti-ferromagnetic inter-layer exchange coupling through the Ru layer. The optical (acoustic) mode frequency becomes lower (higher) as B is increased, as predicted by the fol-

lowing solutions of the LLG equation for coupled moments (see Appendix C), $f_{ac} = (\gamma/2\pi)B\sqrt{1+(\mu_0 M_s/2B_{ex})}$ and $f_{op} = (\gamma/2\pi)\sqrt{2B_{ex}\mu_0 M_s\left(1-(B/2B_{ex})^2\right)}$ where γ, M_s, μ_0 and B_{ex} are the gyromagnetic ratio, saturation magnetization, free space permeability and interlayer exchange field respectively. It is noticed that there is a very subtle non-linear component for the acoustic mode for low frequency region which cannot be accounted for by our macrospin model. Fig. 6.4 (d), displays the numerical solutions of our eigenvalue problem (see Appendix C) which shows good agreement between experimental observation in our device and model calculations. These demonstrations warrant that it is possible to excite and measure both acoustic and optical modes in our SyAF STT-FMR devices with dual spin excitation layers.

6.1.6 Analysis of Rectified Voltages

Individual resonance curves are further analysed by the following Lorentzian functions to decompose their symmetric (V_{sym}) and anti-symmetric (V_{asy}) components.

$$V_{dc} = V_{sym}\frac{\Delta B^2}{(B-B_{res})^2+\Delta B^2} + V_{asy}\frac{\Delta B(B-B_{res})}{(B-B_{res})^2+\Delta B^2} \tag{6.3}$$

Here, B_{res} and ΔB are resonance field and half width at half maximum linewidth of resonance respectively. Typical FMR curve fit results are shown in Fig. 6.6 (a) which represent excellent fit quality that is also the case for other curve fit analysis throughout this study.

Symmetry of Torques for acoustic mode – Fig. 6.6 (b) displays angular dependence of both V_{sym} and V_{asy} measured for acoustic modes while changing ϕ. Both components clearly show $\sin 2\phi \sin\phi$ angular dependence which can be explained by parallel pumping as follows. The angular dependence of observed rectification voltages can be interpreted by the product of the AMR angular dependence ($\sin 2\phi$) and torque symmetry [288, 289] (see Appendix C). Both V_{sym} and V_{asy} were divided by $\sin 2\phi$ to reveal the torque symmetry, which is shown as Fig. 6.6 (c) that strongly suggests the torque symmetry for the acoustic mode excitation being the form of $\sin\phi$. This is the case of parallel pumping, i.e. the torque is largest when

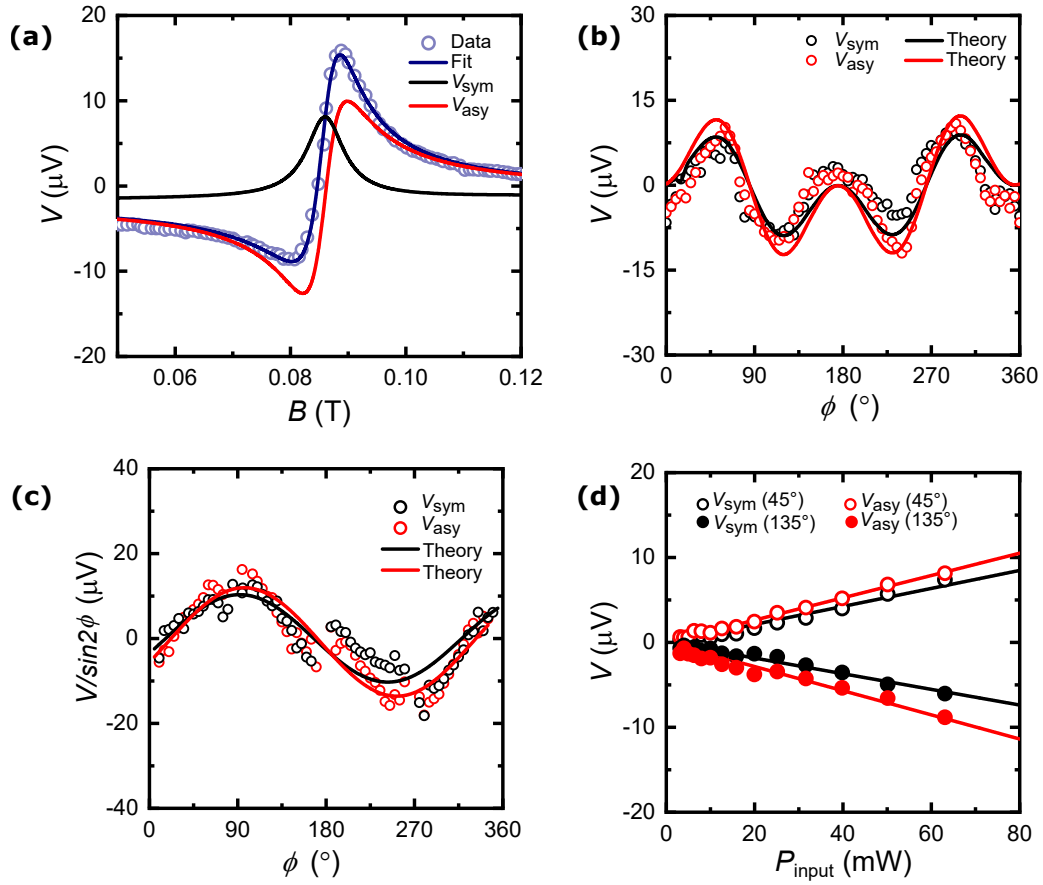

Figure 6.6: (a) FMR spectra measured for f = 6 GHz and $\phi = 45^{\circ}$, together with fitting curves produced by using Eq. 6.3. (b) Angular dependence of $V_{\rm sym}$ and $V_{\rm asy}$ for the acoustic mode measured at 8 GHz. We also add best fit solid curves using our model. (c) The symmetry of torques obtained by dividing the Voltage by $\sin 2\phi$. The dominant $\sin\phi$ dependence of torques confirms the parallel pumping configuration. (d) $V_{\rm sym}$ and $V_{\rm asy}$ as a function of P for $\phi = 45^{\circ}$ and 135° for 8 GHz. The solid lines are linear fit to the data.

applied magnetic field and oscillating excitation field are collinear ($\phi = 90^{\circ}$ in our case since both $\boldsymbol{B}_{1,2}$ and $\boldsymbol{s}_{1,2}$ are along this direction). This is remarkably different from the perpendicular pumping nature of acoustic modes in SyAFs which gives $\cos\phi$ dependence when they are homogeneously excited as discussed earlier. To determine the efficiency of spin-charge conversion in our devices, the spin-Hall angle ($\theta_{\rm SH}$) was quantified by using the following expression of $V_{\rm sym}$ for the acoustic modes; this is obtained by solving the LLG equation with coupled moments excited

by opposite spin torques at the macrospin limit as shown in Appendix C:

$$V_{\mathrm{sym}} = \frac{-\Delta R_{\mathrm{AMR}} C_0 B_{\mathrm{SHE}} \cos 2\phi_{\mathrm{c}} \sin \phi_{\mathrm{c}}}{8\Delta B \sqrt{1+(\mu_0 M_{\mathrm{s}}/2B_{\mathrm{ex}})} I_0 R_{\mathrm{sample}}} P_{\mathrm{input}} \sin 2\phi \sin \phi \tag{6.4}$$

where B_{SHE} is the field due to SHE and is defined as $\hbar\eta_{\mathrm{Ta}}\theta_{\mathrm{SH}} I_0/2eM_{\mathrm{s}} w d_{\mathrm{FM}} d_{\mathrm{Ta}}$. Here, $\hbar$, η_{Ta}, I_0, e, w, d_{FM}, d_{Ta}, ΔR_{AMR}, ϕ_{c}, P_{input}, R_{sample} and C_0 refer to the reduced Planck's constant, shunt ratio of current in Ta layer, current amplitude in the device, elementary charge, width of microbar, the thickness of the NiFe and Ta layers, AMR resistance change, cant angle, microwave power at the source, device resistance and the microwave calibration factor to convert the microwave power at the source to that in the device (see Sec. 6.1.3) respectively. This equation suggests linear relationship between V_{sym} and P_{input}, which can be observed in Fig. 6.6 (d). Using the slope fit by the V_{sym} plot and Eq. 6.4, the magnitude of θ_{SH} was extracted for the Ta layers to be 0.1, which is consistent with previous studies [290, 291]. This can strongly suggest that the source of generating V_{sym} in our measurements is due to SHE in the Ta layers and it is therefore concluded that the parallel pumping of SyAF acoustic modes can be achieved by dual spin sources with opposite spin polarisation. There can be another contribution to V_{sym} due to Rashba effect as explained in Sec. 2.8.1 but its effect is very small in our samples as mentioned above.

In order to support our claims same procedure as outlined above was followed for different frequencies. Fig. 6.7 shows the angular dependence of voltages for acoustic mode, the resultant torque symmetry plots and power dependence at different frequencies for the sample with Ru thickness of 0.4 nm. This supplements Fig. 6.6 and further supports our observation of the parallel pumping nature of acoustic mode.

Symmetry of Torques for optical mode – The analysis was expanded for the optical modes in our devices, which is summarised in Fig. 6.8. The rectification voltages generated by optical modes have the following forms (see full derivations

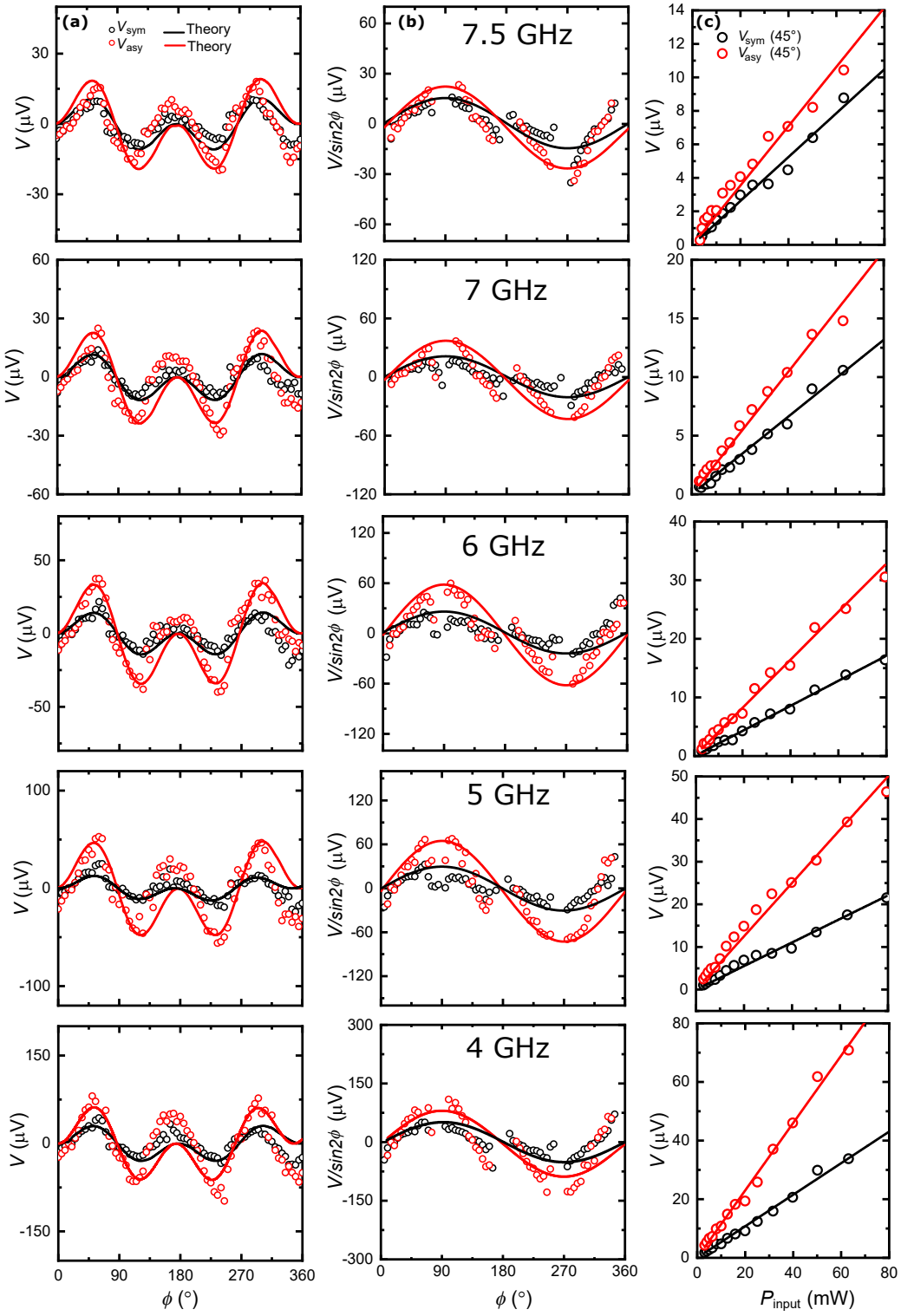

Figure 6.7: Angular dependence of V_{sym} and V_{asy} for the acoustic mode measured at different frequencies from 7.5 GHz (top) to 4 GHz (bottom) as labelled in Figs. (b). Solid curves are best fit curves using our model. (b) The symmetry of torques obtained by dividing the Voltage by $\sin 2\phi$. The dominant $\sin\phi$ dependence of torques confirms the parallel pumping configuration. (c) V_{sym} and V_{asy} as a function of P for $\phi = 45^{\circ}$. The solid lines are linear fit to the data.

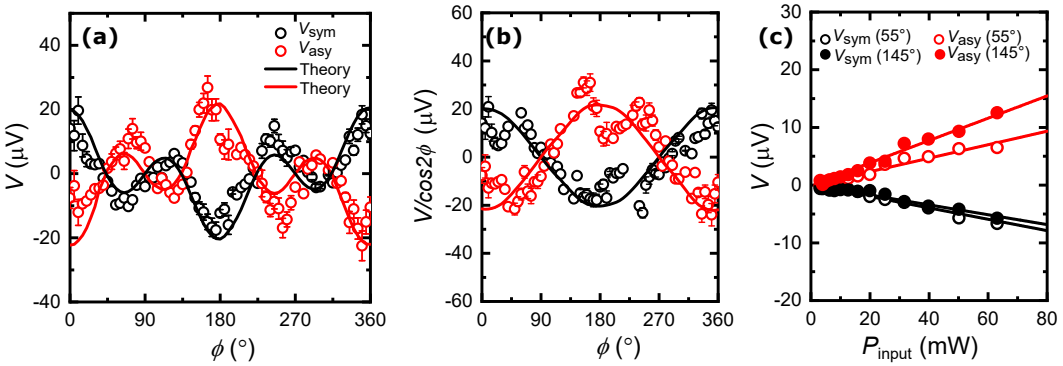

Figure 6.8: (a) Angular dependence of V_{sym} and V_{asy} for the optical mode measured at 8.5 GHz. The solid curves are obtained using Eq. 6.5. (b) The symmetry of torques obtained by dividing the Voltage by $\cos 2\phi$. The dominant $\cos\phi$ dependence of torques confirms the perpendicular pumping configuration. (c) The power dependence of V_{sym} and V_{asy} in the optical mode measured at $\phi = 55^{\circ}$and 145° for f = 8.5 GHz, together with linear fit results.

in Appendix C).

$$V_{sym} = -\frac{\Delta R_{AMR}}{8\Delta B}\sqrt{\frac{2B_{ex}}{\mu_0 M_s}} I_0 B_{SHE} \sin 2\phi_c \sin\phi_c \cos 2\phi \cos\phi;$$
$$V_{asy} = \frac{\Delta R_{AMR}}{8\Delta B} I_0 B_{Oe} \sin 2\phi_c \cos 2\phi \cos\phi \tag{6.5}$$

Here, $B_{Oe} = \mu_0 \eta_{asy} I_0/2w$ is the Oersted field due to current flowing in Ta layer with the parameter η_{asy} being the asymmetry factor of electric currents between the Ta and NiFe layers. AMR symmetry for the optical mode is given by $\cos 2\phi$ in these cases and therefore the experimentally-observed V_{sym} and V_{asy} were divided by this to reveal the excitation torque symmetry which is shown in Fig. 6.8 (b). Unlike the torque symmetry for the acoustic mode (Fig. 6.6 (c)), now this confirms the symmetry for the optical mode is mainly described by $\cos\phi$, which in our case indicates the perpendicular nature of spin-wave excitations, i.e. the torque (hence spin-wave excitation efficiency) is maximised when the oscillating fields and dc magnetic field are perpendicular to each other. It should be noted that there might be some higher-order terms in this angular dependence that our model cannot capture. However, it is emphasised that the main angular dependence in our experiments is clearly reproduced by our model, for both acoustic and optical mode excitations. The sign flip between V_{sym} and V_{asy} for the optical mode, which is predicted by

our macrospin model i.e. in Eq. 6.5, is also clearly demonstrated in our STT-FMR experiments. θ_{SH} extracted using the slope of our experimental data in Fig. 6.8 is 0.1, showing good agreement with one extracted by using the acoustic mode resonances.

Similarly results for the optical mode at different frequencies are presented in Fig. 6.9, which shows consistency of our claims across the frequency region measured and further supports our observation of the perpendicular pumping nature of optical mode.

6.1.7 STT-FMR results for sample with Ru thickness 0.5 nm

Similar set of experiments as described above were performed on the sample with Ru thickness of 0.5 nm where the interlayer exchange field is slightly weaker. Figures 6.10 summarises the results. Applying the same analysis procedure the resultant plots for experimental data along with theoretical derived curves are shown in Figure 6.11 and 6.12 for acoustic and optical mode respectively. Very similar results are observed as those from the sample with Ru thickness of 0.4 nm. This further supports the validity of our claims. Using the slope fit by the V_{sym} plot shown in Figure 6.13 and Eq. 6.4 and Eq. 6.5 for acoustic and optical mode respectively, the magnitude of θ_{SH} was extracted for the Ta layers to be about 0.1 which is in good agreement to the value obtained for sample with Ru thickness 0.4 nm. Figure 6.14 shows the magnitude of θ_{SH} of the Ta layer extracted from the measurements for both samples and different frequencies. As already discussed earlier, the size of these values is in good agreement with that measured in previous studies [290, 291] and suggests that V_{sym} is produced by SHE in the Ta layers in our study.

6.1.8 Frequency dependence of the torque symmetry

In order to quantitatively discuss the frequency dependence of the torque symmetry, the torque symmetry data (e.g. Fig. 6.6 (c)) was fitted by $A\sin\phi+B\cos\phi$ to capture both parallel and perpendicular natures of spin-wave excitations. Using the prefactors A and B, the angle $\Theta = \arctan(A/B)$ is defined which indicates the degree to which spin-waves are excited by parallel or perpendicular pumping configuration; Θ

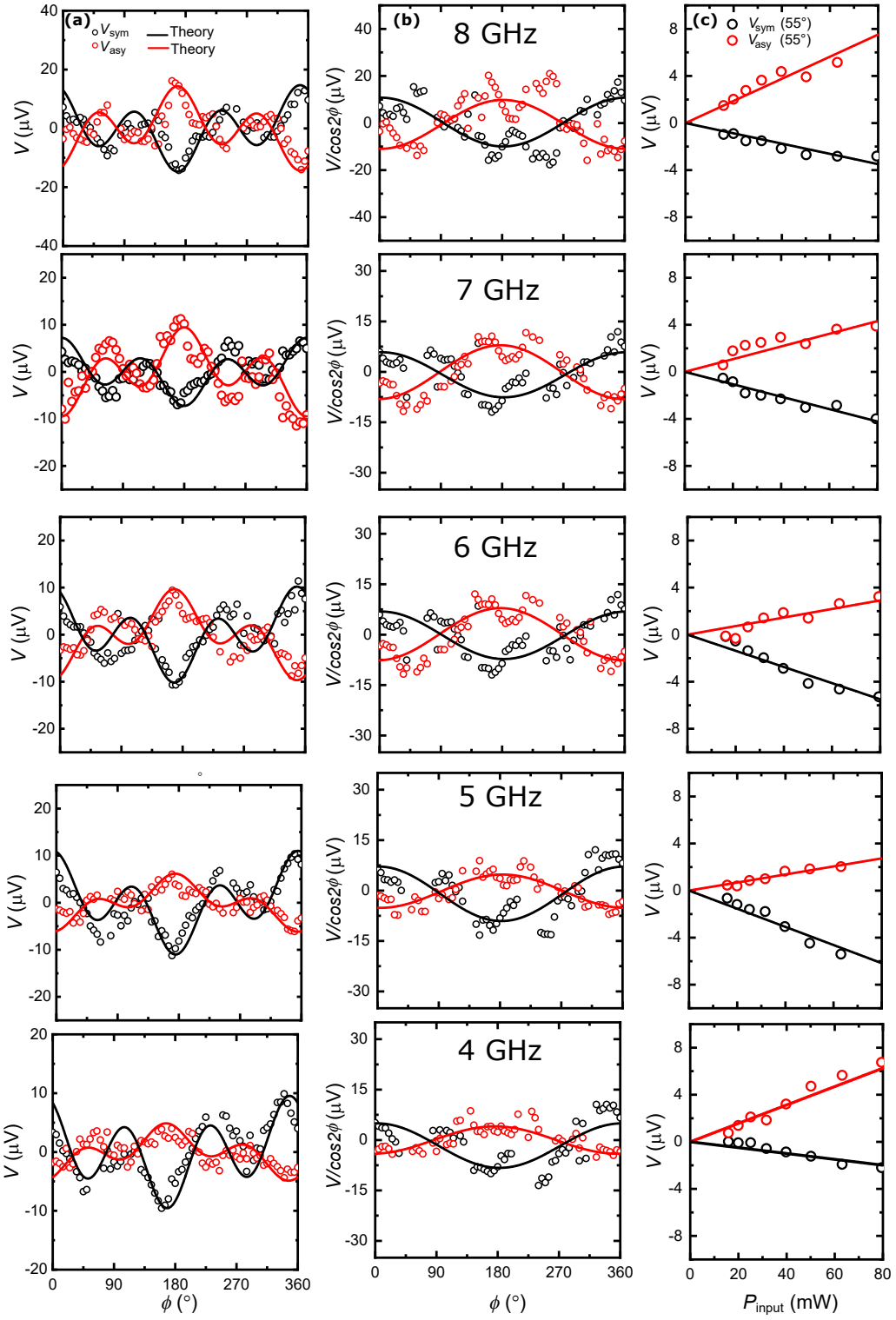

Figure 6.9: Angular dependence of V_{sym} and V_{asy} for the optical mode measured at different frequencies from 8 GHz (top) to 4 GHz (bottom) as labelled in Figs. (b). Solid curves are best fit curves using our model. (b) The symmetry of torques obtained by dividing the Voltage by $\cos 2\phi$. The dominant $\cos\phi$ dependence of torques confirms the perpendicular pumping configuration. (c) V_{sym} and V_{asy} as a function of P for $\phi = 55^{\circ}$. The solid lines are linear fit to the data.

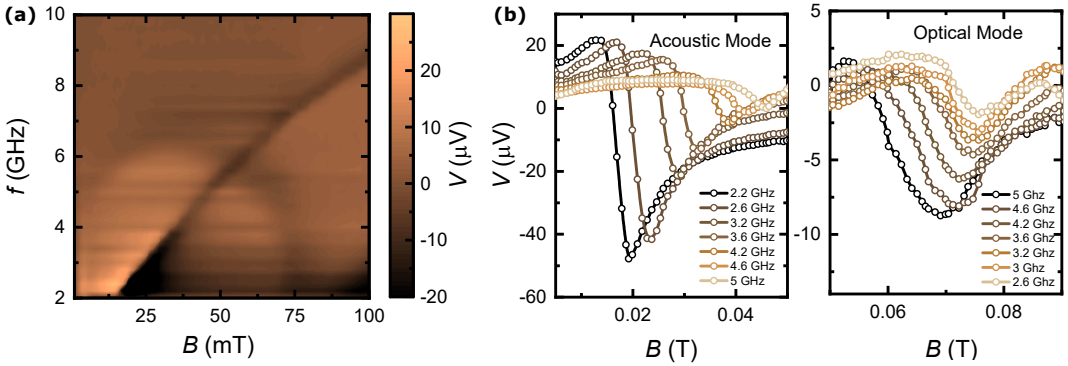

Figure 6.10: (a) A 2D colorplot of V as a function of applied field and frequency, measured for $\phi = 55^{\circ}$ for sample with Ru thickness 0.5 nm (b) V obtained at different frequencies for acoustic and optical modes in our device for $\phi = 145^{\circ}$ (the values for some frequencies have been scaled to show them properly).

close to $\pm 90^{\circ}$ (0°) suggests the parallel (perpendicular) pumping nature in this definition. Θ was extracted from the angular dependent measurements and results are shown in Fig. 6.15 (a) and (b) for the acoustic and optical modes respectively. Consistent behaviours of the torque symmetry is observed for both modes as a function

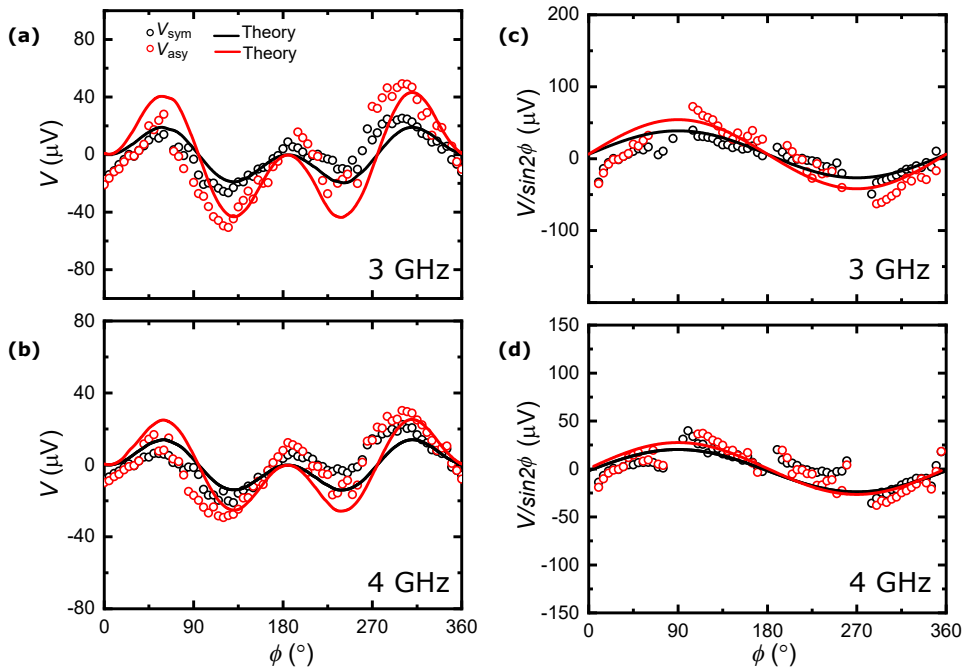

Figure 6.11: (a-b) Angular dependence of V_{sym} and V_{asy} for acoustic mode measured at a frequency of (a) 3 GHz and (b) 4 GHz for Ru thickness 0.5nm. Solid lines are the fitting curves using our model. (c-d) The symmetry of torques obtained by dividing the Voltages by $\sin 2\phi$ for different frequencies. The parallel pumping configuration is confirmed by the dominant $\sin\phi$ dependence of torques.

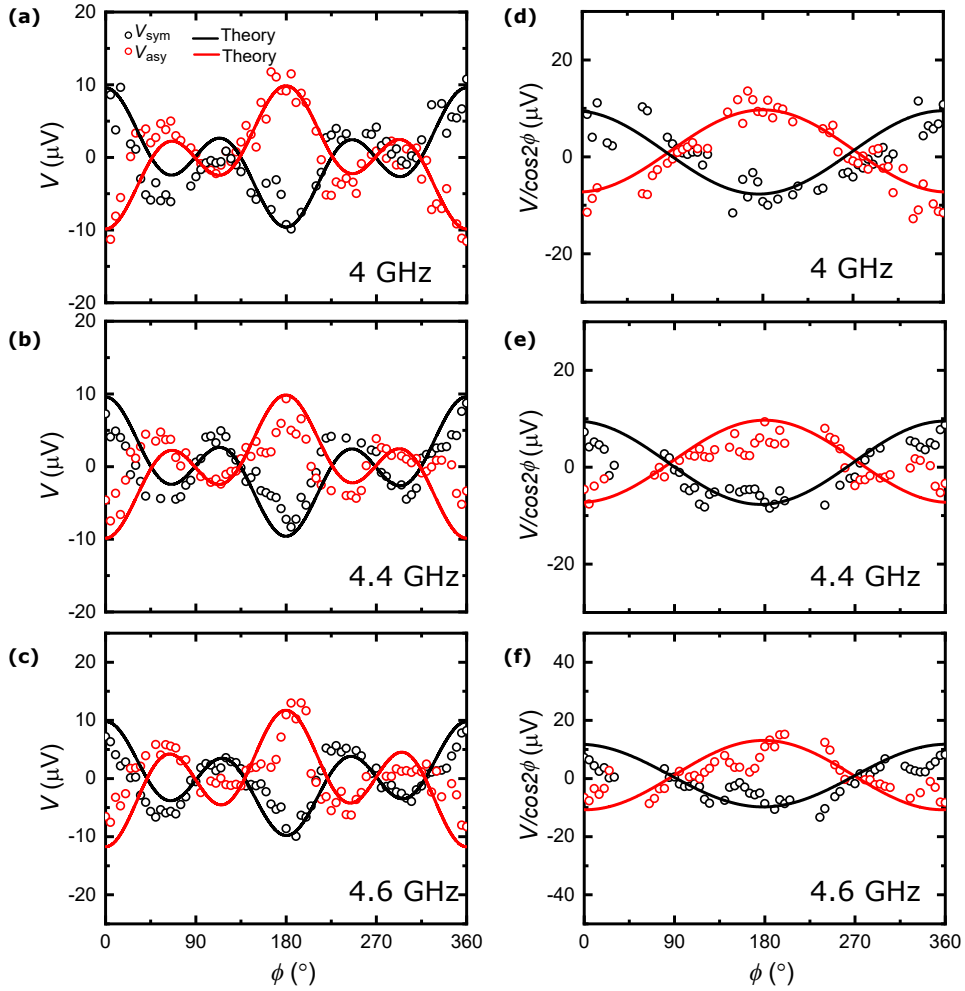

Figure 6.12: (a-c) Angular dependence of V_{sym} and V_{asy} for optical mode measured at a frequency of (a) 4 GHz (b) 4.4 GHz and (c) 4.6 GHz for Ru thickness 0.5nm. Solid lines are the fitting curves using our model. (d-f) The symmetry of torques obtained by dividing the Voltage by $\cos 2\phi$ for different frequencies. The perpendicular pumping configuration is confirmed by the dominant $\cos\phi$ dependence of torques.

of frequency. This confirms the robust parallel (perpendicular) pumping nature of acoustic (optical) modes excited in our SyAF devices with dual spin torque sources using our parity control.

In summary, it is demonstrated in this study that local spin torque excitations can convert mode excitation symmetry between perpendicular and parallel pumping configurations in SyAF STT-FMR devices. It is shown by using two spin-wave modes, acoustic and optical, both clearly exhibiting the torque symmetry change from the ones expected in spin-wave excitations with homogeneous fields. Full

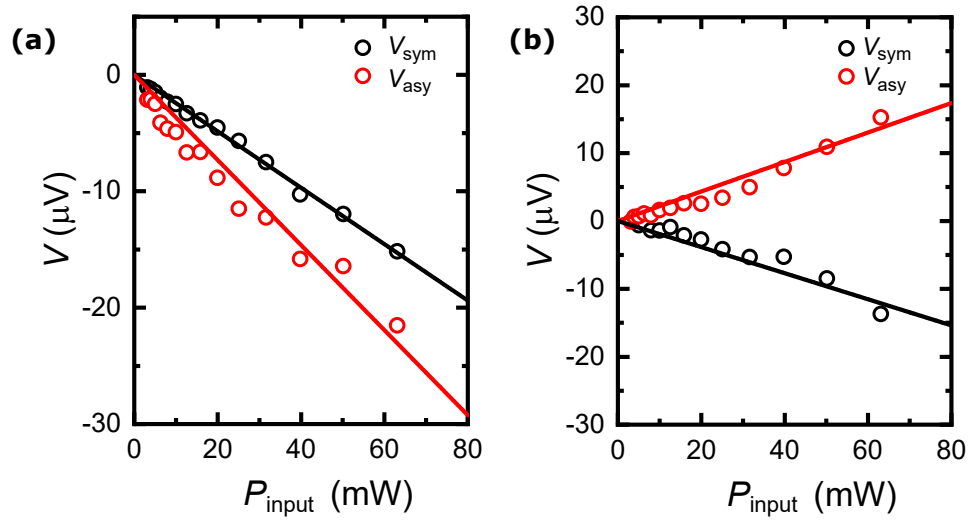

Figure 6.13: (a-b) V_{sym} and V_{asy} as a function of input P at a frequency of 4 GHz for (e) Acoustic mode at $\phi = 135^{\circ}$ and (f) Optical mode at $\phi = 180^{\circ}$.

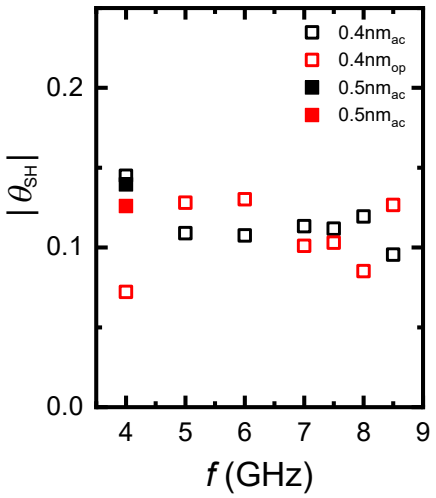

Figure 6.14: The magnitude of spin-Hall angle $|\theta_{SH}|$ in the Ta layer extracted for different frequencies with the two samples.

expressions of rectification voltages in SyAF STT-FMR devices with dual spin excitations are also presented, which supports our experimental observation as well as allows parameter extractions such as the spin-Hall angle using the rectification voltages. It is envisaged that the control of spin-wave excitations in STT nano-devices will be useful for future spintronic and magnonic nano-devices.

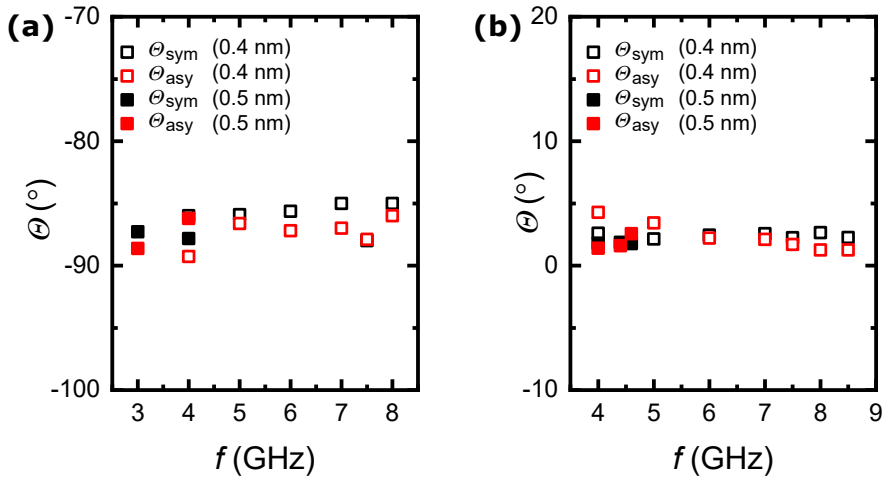

Figure 6.15: Θ extracted as a function of frequency for (a) acoustic and (b) optical modes for different frequencies, in two samples with different Ru thicknesses (0.5 or 0.4 nm). $\Theta_{\mathrm{sym(asy)}}$ represents the parameter extracted from the angular dependence of V_{sym} (V_{asy}) for each frequency. These figures confirm that the acoustic and optical modes are excited by the torque symmetry of parallel and perpendicular pumping configurations respectively.

6.2 Spin Orbit Torques and Spin-Transport in Ni/Pt multi-layer films

In FM/HM bilayer systems with large spin orbit coupling, an efficient way to manipulate the magnetization is provided by spin-orbit torques (SOTs) [2, 292, 293, 178, 294]. SOTs can originate both in the bulk as well as the interface of FM/HM bilayers due to the transfer of orbital angular momentum from the lattice to spin system [292]. The first mechanism originates in the bulk due to the SHE [269, 64, 270] and causes spin current to exert a torque expressed as, $\boldsymbol{\tau}_{\mathrm{DL}} = \tau_{\mathrm{DL}}(\mathbf{m} \times (\sigma \times \mathbf{m}))$ which manipulates the magnetization of ferromagnetic layer. Here, $\mathbf{m}$ is the unit vector of magnetization, σ is the spin polarization in direction of spin-current and τ_{DL} is the magnitude of torque. More details are given in Chapter 2. This torque is referred to as DL torque and follows the form predicted by Slonczewski[28] and Berger [29] however a FL non-adiabatic spin transfer torque can also occur [295, 271, 296].

The second mechanism of generation of SOTs occurs at the interface due to interfacial spin-orbit coupling in FM/HM bilayer. Due to structural inversion asymmetry, the spin orbit hamiltonian lifts the degeneracy and causes a spin momen-

tum locking, a charge current begins to flow parallel to the interface creating a non equilibrium spin accumulation. This process called Rashba-Edelstein (Inverse spin galvanic effect), exerts a torque due to exchange coupling at the interface and the resulting effective field causes rotation of spin accumulation [293]. This can result in both DL torques [293, 178] as given above and FL torque [272, 297] which is expressed as $\boldsymbol{\tau}_{\mathrm{FL}} = \tau_{\mathrm{FL}}(\sigma \times \mathbf{m})$ as already described in Chapter 2.

Since the origin of SOTs is in the bulk or interface, it is possible to manipulate them by interface engineering or electronic structure modification by growth [298, 299]. Earlier works have reported such manipulation in Pt-based structure [300, 301] however a clear picture about its origin is still missing for example there has been wide disparity in magnitude as well as sign of FL torques in the same system [299, 302, 303] thus implying the role of electronic structure in modifying the SOTs. Moreover, spin relaxation mechanisms are dependent on crystal morphology and structure. Both Elliot-Yafet (EY) [304, 305] relaxation(due to scattering in presence of impurities) and Dykanov-Perel (DP) relaxation [306] (due to spin precession around effective spin orbit field at interface) can be modulated by structural changes and thus produce different SHE. This implies the role of crystal structure as well as interfaces in SOTs generation.

In this work the SOTs and spin-transport is studied in $[\mathrm{Ni/Pt}]_{\times \mathrm{N}}$ multi-layer stacks (where, N is taken as 1 and 5) exhibiting either a polycrystalline grain structure (for films grown on SiO_2 substrate) or a epitaxial (111) oriented film. The dependence of CITs on the interface modification as well as crystal structure is investigated. This systematic study elucidates the importance of growth on SOT efficiency and also its effect on various magnetic parameters.

6.3 Sample Growth, Patterning and characterisation

The samples used for this study were grown by Dr. Takeshi Seki at Tohoku University, Japan. Four different types of samples were grown using the technique of magnetron co-sputtering in ultrahigh vacuum system with base pressure below 2×10^{-7} Pa. The Pt layer was first deposited on top of substrate followed by Ni

Table 6.1: Summary of the sample notation used, stacking pattern, deposition temperature and substrate. The RHEED and XRD measurements were done by Dr. Seki. The numbers in brackets represent thickness in nm and the blanks in the table indicate those measurements were not done for the samples.

Sample	Substrate	Deposition Temperature	Stack	RHEED, XRD	Easy Axis
K-01	Sapphire	$400^{\circ}C$	$[\text{Pt (1)/Ni(3)}]_{\times 5}\vert\text{Al}_2\text{O}_3(5)$	(111) epi.	In-Plane
K-02	SiO_2	Room Temp.	$[\text{Pt (1)/Ni(3)}]_{\times 5}\vert\text{Al}_2\text{O}_3(5)$	Poly.	In-Plane
K-03	Sapphire	$400^{\circ}C$	$[\text{Pt (1)/Ni(3)}]\vert\text{Al}_2\text{O}_3(5)$	-	In-Plane
K-04	SiO_2	Room Temp.	$[\text{Pt (1)/Ni(3)}]\vert\text{Al}_2\text{O}_3(5)$	-	In-Plane

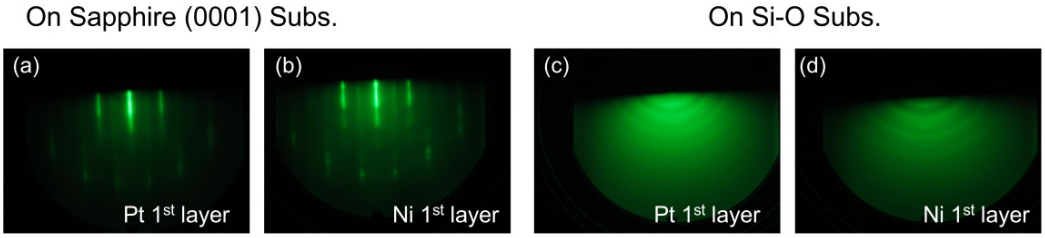

Figure 6.16: Reflection high-energy electron diffraction images for samples K-01 and K-02 grown on sapphire and SiO_2 respectively. The diffraction patterns were observed just after the growth of first Ni and Pt layer.

layer. The thickness of Ni and Pt layer was kept fixed as 3 and 1 nm respectively for all samples. The sample notation as defined in the Table. 6.1 is used throughout the thesis. The samples K-01, K-03 and K-02, K-04 were grown on Sapphire and SiO_2 substrate respectively. The stacking pattern for the samples $[\text{Ni/Pt}]_{\times \text{N}}$ is also defined in Table. 6.1. The total thickness of superlattice was approximately 20 nm for $N = 5$

To achieve the epitaxial growth on Sapphire, the deposition temperature was optimized to achieve successful formation of layered structure and also achieve the epitaxial growth. These conditions were met at temperature of 400° C which was maintained constant throughout the deposition process. Finally a 5 nm thick Al_2O_3 capping layer was deposited on top. The magnetic anisotropy induced at the interface of Ni/Al_2O_3 was negligible and was tested by using a reference sample of Ni single layer film with Al_2O_3 capping layer. Similar process was followed while K-02 and K-04 were grown on SiO_2 substrate.

In order to monitor the crystal orientation and morphology, $in-situ$ observa-

tion using reflection high-energy electron diffraction (RHEED)[1] was done as shown in Fig. 6.16. The rings in pattern show polycrystalline growth while sharp periodic streaks correspond to epitaxial growth on sapphire substrate. Structural characterisation was done using x-ray diffraction (XRD) with Cu- $K\alpha$ radiation [2]. As mentioned above from RHEED observation, the sample grown on SiO_2 substrate were non-epitaxial and similar is seen in XRD results showing no preferential orientation whereas the one grown on sapphire substrate show (111) preferential orientation. This can be explained as the Pt (111) diffraction peak was clearly observed for epitaxial samples. An important point is that in order to discuss the details of epitaxial growth, we need to consider the data of both XRD and RHEED. In case of polycrystalline Ni/Pt samples probably Pt (111) is the only peak observable because in the Pt bulk diffraction profile Pt (111) is the strongest peak. In order to quantitatively discuss the magnitude of Pt (111) peak, the intensities of other peaks are needed. However, this was difficult for the polycrystalline samples because those peaks were hidden by the noisy background. Although quantitative discussion is impossible, the fact that RHEED patterns show rings for epitaxial growth implies that the polycrystalline Ni/Pt do not exhibit remarkable preferential orientation. Thus from both RHEED and XRD data it is confirmed that the samples grown on sapphire substrate showed epitaxial growth. The XRD profiles for sample K-01 and K-02 are shown in Fig. 6.17.

Fig. 6.18 shows the magnetization curves for the four samples measured at room temperature [4]. The red curves are for the measurements with in-plane applied magnetic field. It can be seen that all samples have in-plane easy axis of magnetization. The saturation magnetization values obtained from the curves are summarised in Table. 6.3 below.

In order to study the spin transport and for SOT measurements the samples were patterned in shape of bars. The rectangular bars of width 5μm and length of 400 μm (K-01 and K-02) and 200 μm (K-03 and K-04) were defined by standard

[1]Measurements done by Dr. Seki
[2]Measurements done by Dr. Seki
[4]Measurements done by Dr. Seki

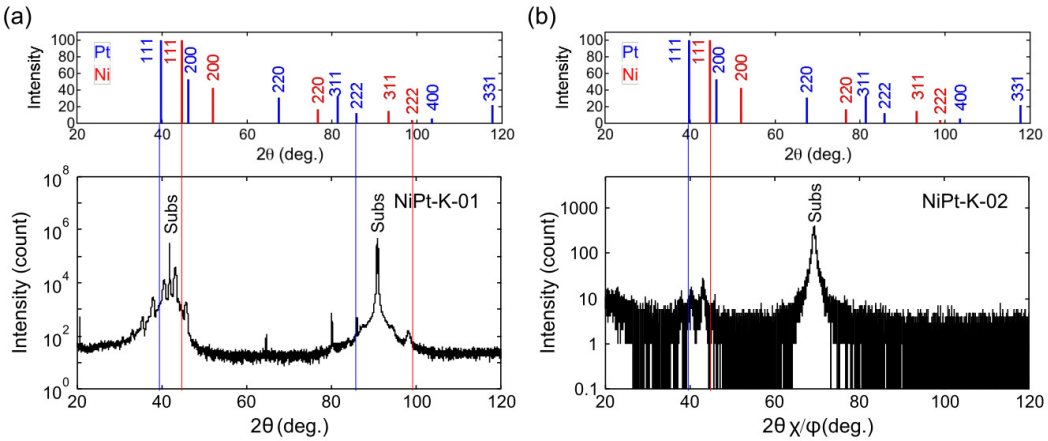

Figure 6.17: X-ray diffraction profiles for K-01 and K-02 samples grown at 400° C and room temperature respectively. The blue and red lines correspond to position of Pt and Ni peak respectively.

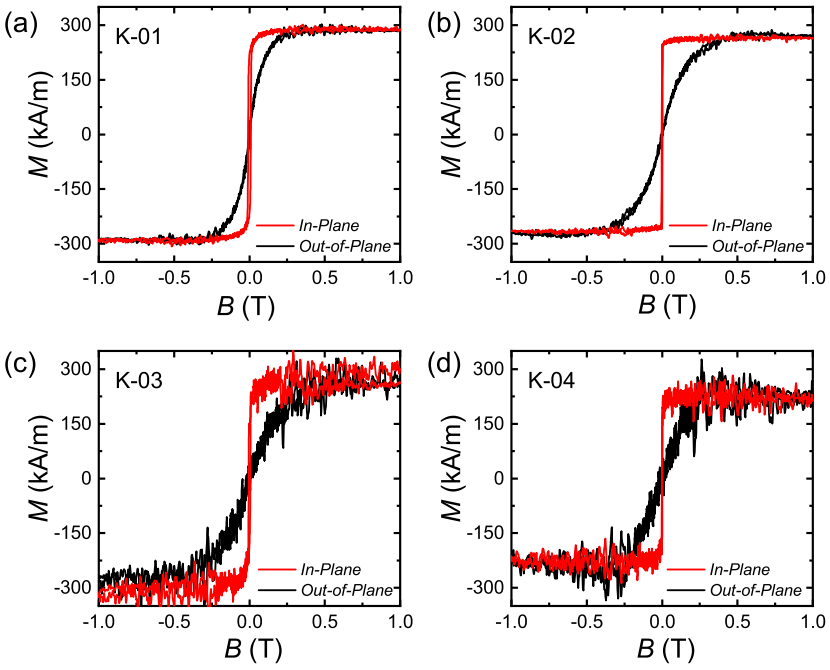

Figure 6.18: Magnetization curves for the samples measured using vibrating sample magnetometer (VSM). The red curves are measured with in-plane magnetic field (IP) while the black curves denote the measurements with out-of-plane magnetic field (OPP). The measurement was done at room temperature.[3]

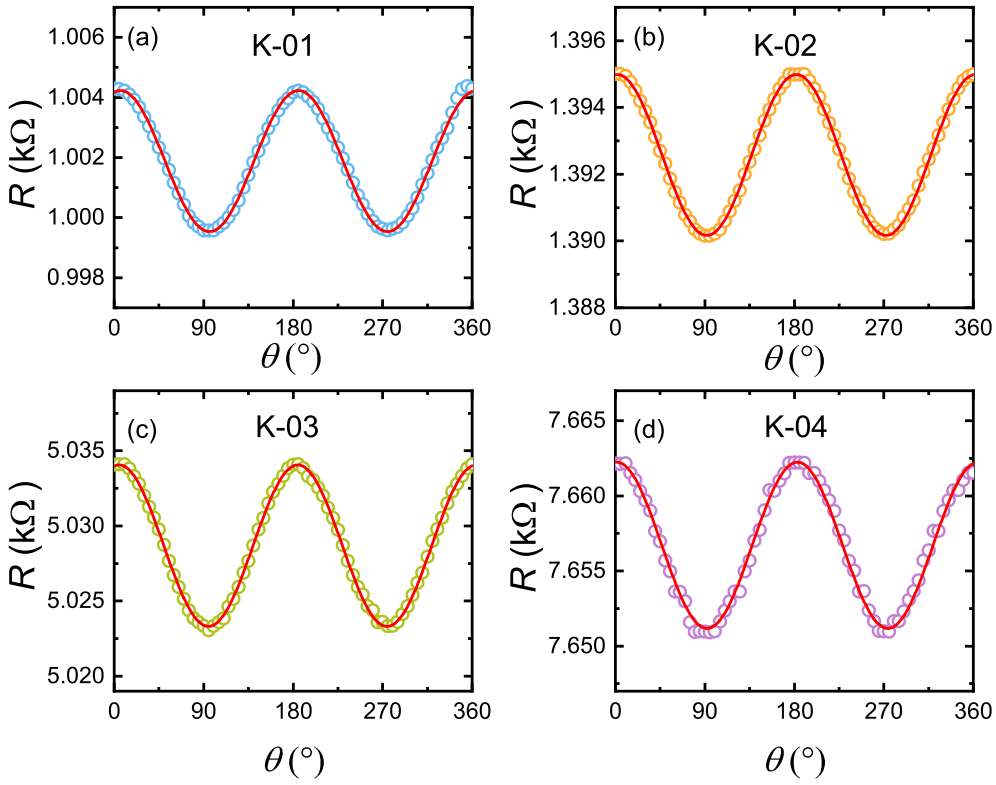

Figure 6.19: Angle dependent magnetoresistance measurements in the samples (a) K-01 (b) K-02 (c) K-03 and (d) K-04. The solid lines are the fitting results.

lithography techniques and Ar-ion milling. The device circuitry and bar pattern is shown in Fig. 6.21.

6.4 Magnetoresistance measurements

In order to calculate the current induced effective field in STT-FMR measurement (Eq. 3.8, 3.9) it is essential to quantify the resistance change ΔR which determines the anisotropy in resistance. Moreover, this helps to calibrate the angle θ (angle between applied external field and bar direction. see Fig. 6.21) and also identify mechanisms behind the anisotropy in resistance. The AMR measurement was carried by using an external field, $\mathbf{B}_{\text{ext}}$ of 0.1 T and rotating it in-plane direction. Fig. 6.19 shows the measurement in the four samples. Clearly the bars show anisotropy in resistance when $\mathbf{B}_{\text{ext}}$ is applied in-plane. The data is fitted using Eq. 3.3 and the value for ΔR is obtained from the fittings which are summarised in Table 6.2.

Table 6.2: Summary of the resistance change due to anisotropy obtained from angle dependent magnetoresistance measurements. Note - The uncertainty values reported here are the standard error of the fitting parameters obtained from curve fitting.

Sample	K-01	K-02	K-03	K-04
$\Delta R/R(\%)$	0.47 ± 0.01	0.35 ± 0.01	0.21 ± 0.02	0.14 ± 0.02

6.5 Microwave Calibration

Using similar procedure as outlined in Sec. 6.1.3, actual power reaching the device was quantified using the bolometric technique by comparing the resistance change caused by joule heating from a known dc current, I_{DC} with that caused by microwave power, P_{input}. Figs. 6.20, show the resistance change by two current excitations. The current flowing through the device is quantified at GHz frequency by scaling two parameters (P_{input} and I_{DC}) by the sample resistance. The microwave power at sample (P_{sample}) is then calculated and plotted against microwave power at source (P_{input}) as shown in Figs. 6.20 (c). It can be seen that that power input at the sample is fraction of the power from the microwave source. For samples K-03 and K-04 which had higher resistance, the current reaching the sample is smaller as compared to K-01 and K-02.

6.6 Characterisation by ferromagnetic resonance

STT-FMR technique was used to investigate the SOTs in Ni/Pt multi-layer films. The measurement setup is as shown in Fig. 6.21 (a). The RF current at a frequency f is applied to the sample and the external field is swept at different angles from the bar direction. The resultant DC voltage is measured using bias-tee. The RF current is converted into pure spin current in the Pt layer by SHE and also generates Oersted field (bulk) and interfacial Rashba-like field. Both of these fields and spin current act on the magnetization of the FM layer and exerts out-of plane and in-plane SOTs driving the magnetization into precession. The resultant magnetization change causes change in resistance of sample due to AMR and produces a DC voltage due to frequency mixing (see Chapter 3). Fig. 6.21 (b) shows the typical voltage signal obtained from SOT in the sample K-02 and K-04 on SiO_2 substrate. The current non-uniformity is negligible in our samples because the wavelength of

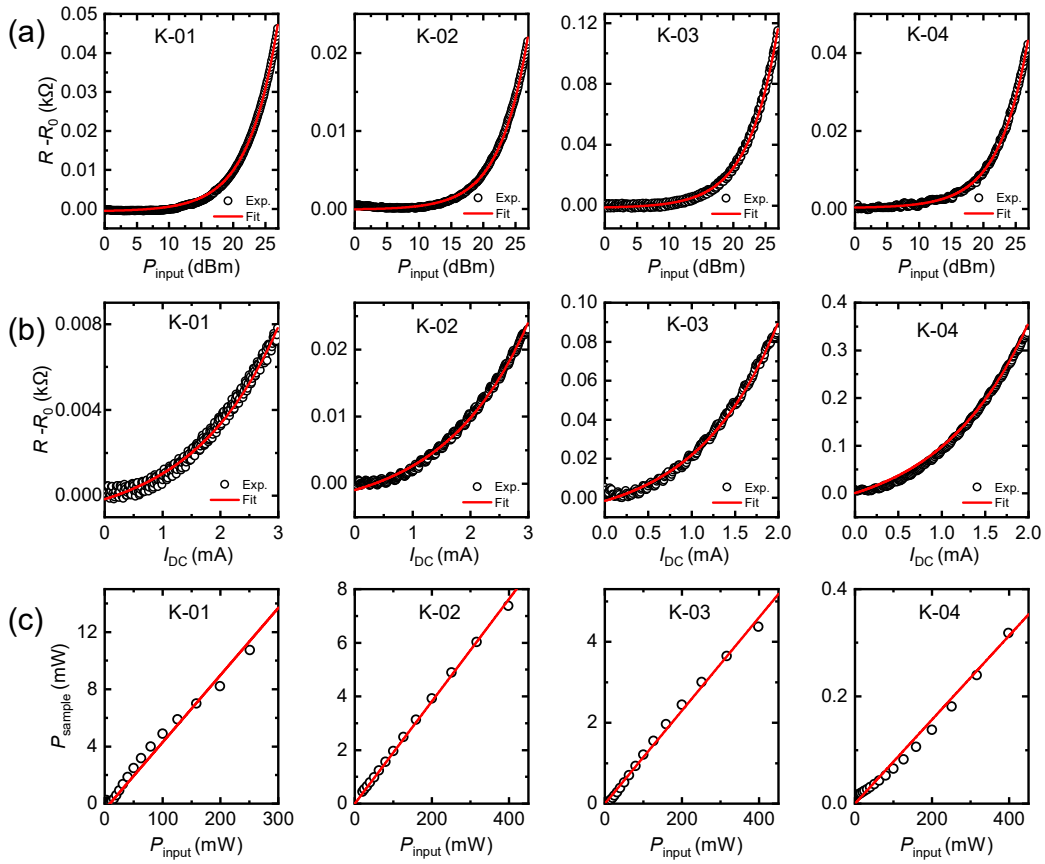

Figure 6.20: (a) Resistance change as a function of microwave power for four set of samples. (b) Resistance change as a function of dc current and (c) Power from source as a function of the power in the sample for different samples.

the RF current with frequency range 3-12 GHz is much larger than the length of device which is few hundreds of μm [307] and the phase is almost constant.

The voltage signal V is fitted using sum of symmetric and anti-symmetric Lorentzian given by Eq. F.12 (see Appendix F). Fig. 6.22 shows the spectra for the samples grown on sapphire substrate measured at 8 GHz microwave frequency. It can be seen that as compared to the samples grown on SiO_2 substrate the linewidth is much broader which can be due to inhomgeneities and so in order to quantify the damping constant and inhomogeneous broadening contribution, the frequency dependence of linewidth was performed at $\theta = 45^{\circ}$ for all the samples and is shown in Fig. 6.23.

By fitting the data using Eq. 6.6, the values of the inhomogeneous broadening,

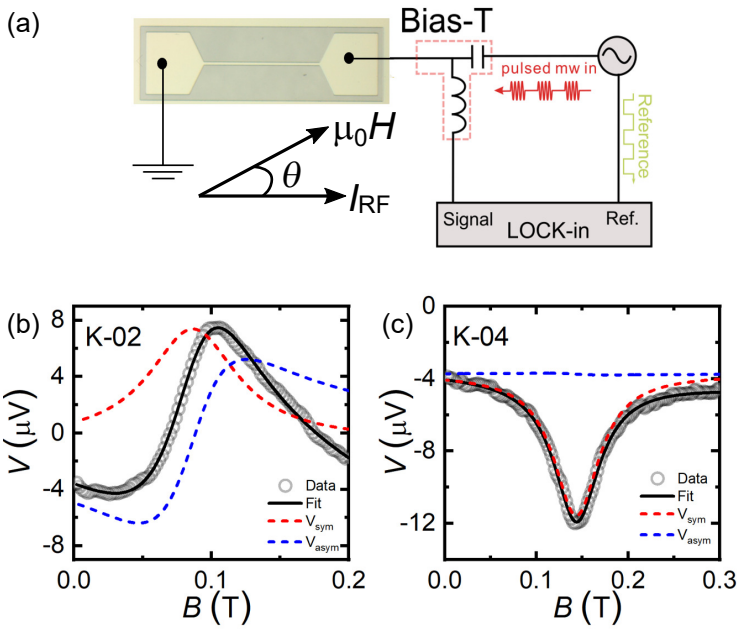

Figure 6.21: Schematic illustration of the experimental setup used for STT-FMR experiments. The microwave current, I_{RF} is injected into the bar with width 5μm through a bias-tee. θ denotes the in-plane angle between the external field B and the microstrip. (b) Magnetic field dependence of the DC voltage V for the samples K-02 and K-04 measured at 8 GHz and 7 GHz respectively. The data is fitted (solid black line) with a combination of symmetric (dashed red line) and anti-symmetric (dashed blue line). A clear anti-symmetric component is visible for multi-layer sample as compared to bilayer sample (K-04).

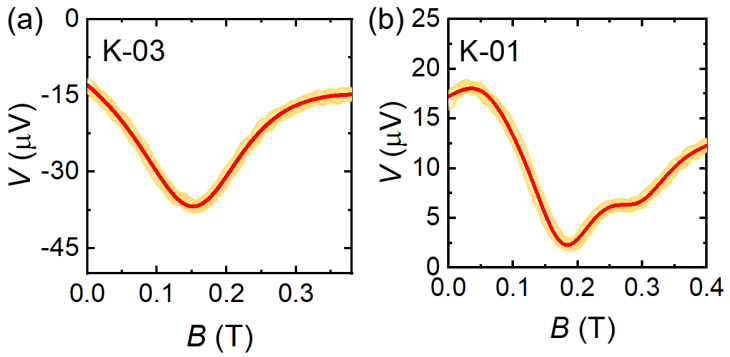

Figure 6.22: STT-FMR spectra for the samples K-03 and K-01 grown on sapphire substrates. The multi-layer sample K01 shows a antisymmetric peak shape compared to bilayer K-03 which has more dominant symmetric component. The additional small peak is observed for K-01 which is the spin-wave resonance mode.

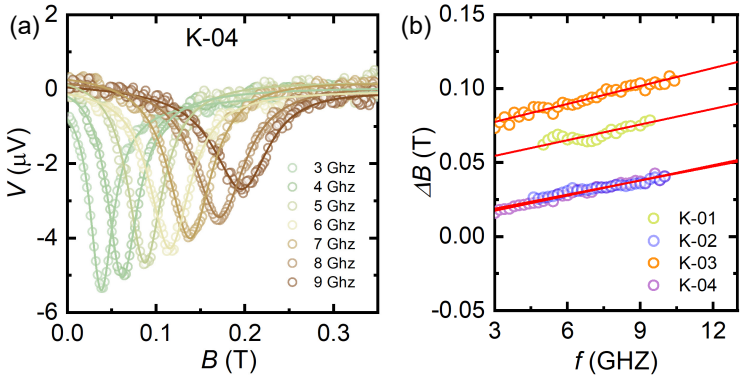

Figure 6.23: STT-FMR spectra measured at different frequencies from 3-9 GHz for K-04 sample at $\theta = 45^{\circ}$. (b) Frequency dependence of the HWHM linewidth at $\theta = 45^{\circ}$ for all samples. The inhomogeneous broadening is obtained from the intercept by fitting the data with linear-fit and the slope gives the Gilbert damping component,α.

ΔB_0 and intrinsic gilbert damping, α are obtained which is summarised in Table. 6.3

$$\Delta B = \Delta B_0 + \frac{2\pi\alpha}{\gamma} f \tag{6.6}$$

The value of α is fairly constant and very large ~ 0.1 for all the samples as can be seen from Table. 6.3. The reported values for α in Ni films is $\sim$ 0.02-0.05 [308]. The enhancement of the damping constant in the measured films can originate from several mechanism and one such mechanism can be due to spin pumping as given in Eq. G.7 (see Appendix G). This equation is valid when the non-magnet (NM) is a perfect sink and thickness is much smaller than the spin diffusion length of the material. Pt is known to act as a perfect spin sink. The spin-pumping term given by α_{sp} was calculated for obtaining the enhancement of damping due to spin-pumping. The value of $g_{\text{eff}}^{\uparrow\downarrow}$ was used as $3 \times 10^{18}\text{m}^{-2}$ [309] and the α_{sp} was obtained as $\sim$ 0.08 for the samples. This corresponds to intrinsic damping being about 0.02. Thus there is a sizable spin pumping component in all samples which leads to very large damping value being observed for these samples. From Fig. 6.23 (b) it can be seen that the inhomogeneous contribution for samples grown on sapphire is larger than that grown on SiO_2 substrate which shows strain induced magnetic inhomogeneity. Moreover similar damping value amongst all sample suggests that spin pumping

Table 6.3: Summary of the anisotropy constants obtained from fitting of frequency dependent resonance field and linewidth data. Note - The uncertainty values reported here are the standard error of the fitting parameters obtained from curve fitting.

Sample	$\mu_0 H_2$ (mT)	$\mu_0 H_4$ (μT)	$\mu_0 H_{2\perp}$ (T)	$\mu_0 M_{\text{eff}}$ (T)	$\mu_0 M_s$ (T)	α	ΔB_0 (T)
K-01	19.6 ± 0.1	650 ± 1	-0.261 ± 0.006	0.622 ± 0.006	0.362 ± 0.005	0.11 ± 0.01	0.0439 ± 0.0005
K-02	3.15 ± 0.01	1.11 ± 0.01	-0.504 ± 0.005	0.835 ± 0.005	0.331 ± 0.005	0.093 ± 0.005	0.0092 ± 0.0004
K-03	-13.8 ± 0.2	-19.8 ± 0.2	0.141 ± 0.002	0.237 ± 0.002	0.377 ± 0.002	0.115 ± 0.005	0.065 ± 0.001
K-04	-6.14 ± 0.04	-3.4 ± 0.4	-0.014 ± 0.004	0.317 ± 0.004	0.298 ± 0.004	0.096 ± 0.003	0.0093 ± 0.0007

Table 6.4: Summary of the anisotropy constants obtained from fitting of angular dependence of resonance field. Note - The uncertainty values reported here are the standard error of the fitting parameters obtained from curve fitting.

Sample	$\mu_0 H_2$ (mT)	$\mu_0 H_4$ (μT)	$\mu_0 H_{2\perp}$ (T)	$\mu_0 M_{\text{eff}}$ (T)	$\mu_0 M_s$ (T)
K-01	19.1 ± 0.1	650 ± 1	-0.35 ± 0.01	0.716 ± 0.006	0.362 ± 0.005
K-02	3.01 ± 0.01	1.35 ± 0.05	-0.43 ± 0.01	0.765 ± 0.005	0.331 ± 0.005
K-03	-8.1 ± 0.1	-20.1 ± 0.1	0.142 ± 0.002	0.241 ± 0.002	0.377 ± 0.002
K-04	-4.2 ± 0.1	-3.23 ± 0.06	-0.011 ± 0.004	0.314 ± 0.004	0.298 ± 0.004

contribution is fairly constant for all samples.

In a polycrystalline films there is no preferential orientation and in macroscopical sense it can be counted to be isotropic. However, in the presence of spatial orientation of crystalline lattices of separate constituents of a polycrystalline film can give rise to some presence of the allocated (preferred) directions. This is referred to as textures. The epitaxial growth occurs when new crystalline layers are formed with a well-defined orientations with respect to the seed layer. When the film grown on substrate is different then such growth is called hetroepitaxy and such growth can induce the strain component [195] due to the lattice mismatch. In our films there is a lattice mismatch between Pt (lattice constant a = 3.93Å) grown on sapphire (lattice constant a = 4.75Å [310]) which can cause strain induced anisotropy. The anisotropy components were calculated by fitting the frequency dependence of resonance field using Eq. 4.3 and the anisotropy constants obtained are summarised in the Table. 6.3. It can be seen that the uniaxial anisotropy (H_2) component is dominant in comparison to biaxial (H_4) for all the samples. For the epitaxial samples which are (111) oriented it is expected that the anisotropy should show 3-fold rotational in-plane symmetry. However, the dominant 2-fold component can be

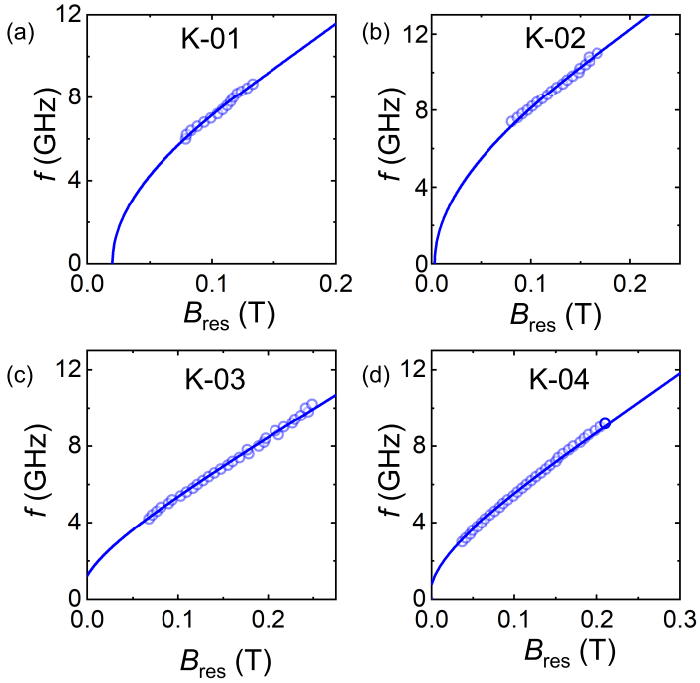

Figure 6.24: Resonance field, B_{res} as a function of frequency at an angle $\theta = 45^{\circ}$ for all samples. The solid lines are the fittings obtained using Eq. 4.3

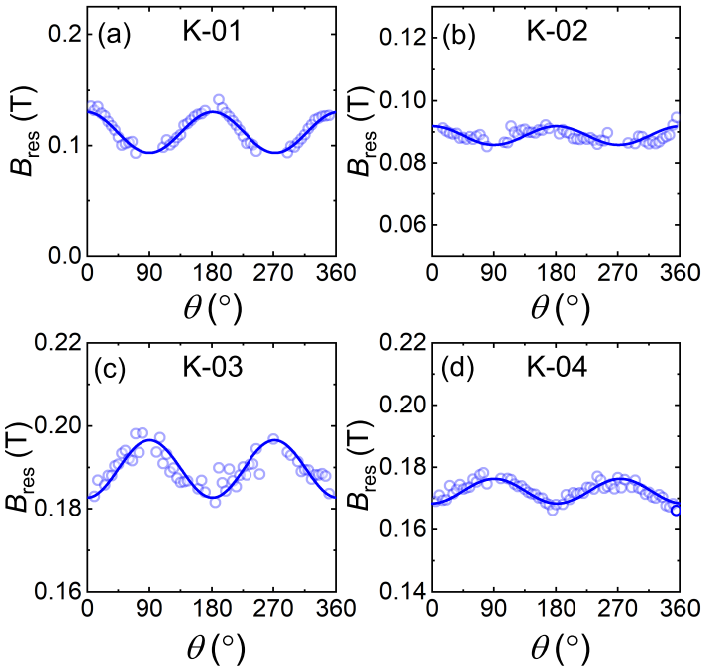

Figure 6.25: In plane angular dependence of resonance field, B_{res} obtained from fitting the FMR scans for different set of samples measured at 8 GHz.

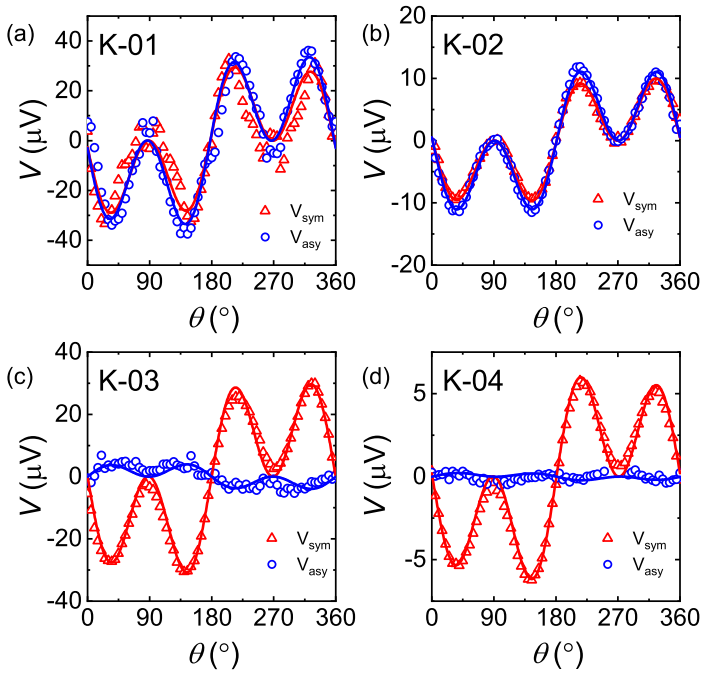

Figure 6.26: The symmetric and antisymmetric components of the STT-FMR spectra as a function of in-plane magnetic field angle θ for (a) K-01 (b) K-02 (c) K-03 and (d) K-04 films at $f = 8$ GHz. The bilayer samples show negligible anti-symmetric component while the anti-symmetric component is comparable to symmetric component for the multi-layer samples.

due to the symmetry lowering caused by lattice mismatch strain [172]. Also the polycrystalline samples show very little anisotropy compared to epitaxial grown samples which confirms growth induced strain in epitaxially grown samples. The multi-layer samples exhibit large perpendicular anisotropy ($H_{2\perp}$) which can come because of strain [311] and the negative sign shows that the magnetization lies in the sample plane. The value of anisotropy components was estimated by fitting the angular dependence of resonance field and the values are summarised in Table. 6.4. The values match fairly well with those calculated from frequency dependence.

6.7 Spin torque fields

The effective magnetic fields $(h_x, h_y, h_z)e^{j\omega t}$ are induced when the microwave current $I_0 e^{j\omega t}$ is injected into the bar. This drives the FMR precession and to quantify the values of the effective fields, complete angle dependent measurements were per-

formed. The values of symmetric and antisymmetric components of voltage were obtained by fittings of FMR lineshape at a given microwave injected power and frequency. Fig. 6.26 shows the magnetic field angular dependence of the symmetric, V_{sym} and antisymmetric, V_{asy} components of the voltage where the external field was applied in-plane at an angle θ with respect to the current direction where, V_{sym} and V_{asy} are given as:

$$V_{\text{sym}} = V_{\text{mix}} A_{\text{sym}} h_{\text{z}} \sin 2\theta, \tag{6.7}$$

$$V_{\text{asy}} = V_{\text{mix}} A_{\text{asy}} (h_{\text{y}} \cos\theta - h_{\text{x}} \sin\theta) \sin 2\theta, \tag{6.8}$$

Here, $V_{\text{mix}} = \frac{1}{2} I_0 \Delta R$, and $A_{\text{sym}}, A_{\text{asy}}$ are related to scalar amplitudes of the ac magnetic susceptibilities given by $A_{ij} = \chi_{ij}/M_{\text{s}}$. Their values are given as :

$$A_{\text{sym}} = \frac{\sqrt{H_{\text{res}}(H_{\text{res}} + M_{\text{eff}})}}{\Delta H (2H_{\text{res}} + M_{\text{eff}})}, \tag{6.9}$$

$$A_{\text{asy}} = \frac{(H_{\text{res}} + M_{\text{eff}})}{\Delta H (2H_{\text{res}} + M_{\text{eff}})} \tag{6.10}$$

In the Eq. 6.7 and 6.8 it is found that $V_{\text{sym}}, V_{\text{asy}} \propto I^2$ where $h_{\text{i}}, (i = x, y, z) \propto I$ and this can also be see from the linear dependence of rectified voltage V on microwave power as shown in Fig. 6.27 which is consistent with our model.

In all films the symmetric component is proportional to $\sin 2\theta \cos\theta$, consistent with other results [312]. A comparative study of angular dependence of SOT in the bilayer and multi-layer samples was done and it can be seen that the antisymmetric component is very small in the bilayer samples. This means DL torques are dominant in these samples. Moreover the sign of antisymmetric component (FL torque) is opposite compared to the multistacks. This indicates that the Oersted torque is opposing FL torque and its origin is thickness and material parameter dependent along with quality of interfaces [3] since the sign reversal is observed only in bilayers. The presence of DL torque in multi-layer samples indicates that there is no complete cancellation of spin current from opposite Pt layers. The large FL

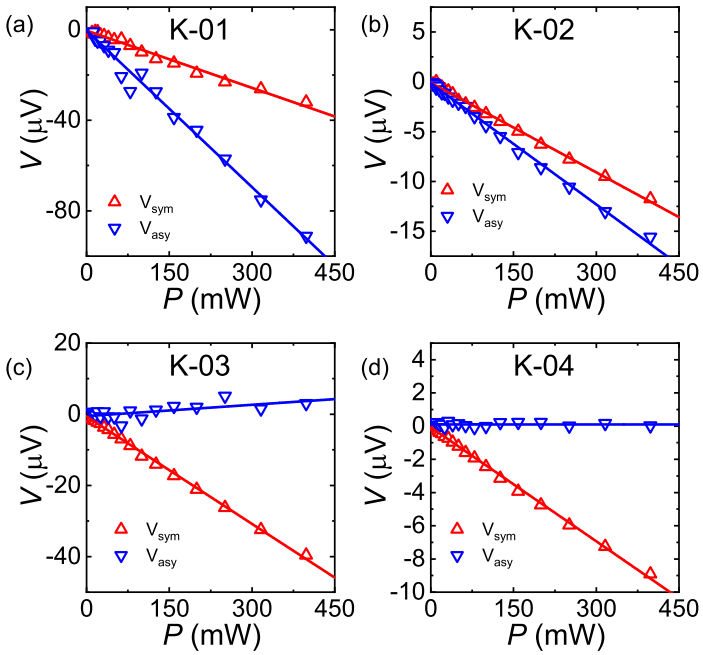

Figure 6.27: Plot of magnitude of the voltage for the symmetric and antisymmetric components as a function of injected microwave powers for different set of samples. All the samples show linear dependence for the given regime of injected power.

Table 6.5: SOT effective fields for different samples. All of them have been scaled by a current density of $j = 10^{10} A/m^2$. Note - The uncertainty values reported here are the standard error of the fitting parameters obtained from curve fitting.

Parameter	sample			
	K-01	K-02	K-03	K-04
h_y (mT)	-0.072 ± 0.002	-0.051 ± 0.004	(9.2 ± 0.1)×10^{-3}	(2.7 ± 0.5)× 10^{-3}
h_x (mT)	(-2.8 ± 0.2)× 10^{-3}	(-3.2 ± 0.4)× 10^{-5}	(-3.5 ± 0.1)× 10^{-4}	(-2.5 ± 0.5)× 10^{-4}
a (mT)	(0.91 ± 0.04)× 10^{-3}	(-1.9 ± 0.1)× 10^{-3}	(1.6 ± 0.1)× 10^{-3}	(5.6 ± 0.1)× 10^{-3}
b (mT)	-0.131 ± 0.001	-0.133 ± 0.002	-0.106 ± 0.002	-0.121 ± 0.002
c (mT)	(-4.14 ± 0.07)× 10^{-3}	(-4.2 ± 0.2)× 10^{-3}	(5.4 ± 0.2)× 10^{-3}	(2.7 ± 0.2)× 10^{-3}
I_0 (mA)	4.515 ± 0.001	2.162 ± 0.004	1.741 ± 0.003	0.429 ± 0.001
$\Delta R(\Omega)$	4.694 ± 0.001	4.821 ± 0.001	10.751 ± 0.002	11.062 ± 0.002

torque can be attributed to interfacial Rashba origin but we cannot rule out the non-adiabatic STT. By fitting the angular dependence of voltage using Eq. 6.7 and 6.8 (solid lines shown in Fig. 6.26) the values of h_x, h_y and, $h_z = a + b\cos\theta + c\sin\theta$ are extracted and summarised in Table. 6.5. The value of h_y and b is dominant which is consistent with $\sin 2\theta \cos\theta$ symmetry as observed in the angular dependence. As can be seen from the values, the DL components (b)are similar for the multi-layer

samples and the FL components (h_y) are negligible in bilayer films and also the magnitude of DL components is smaller in the bilayer films. This indicates that presence of interfaces in multi-layer stacks has caused the enhancement of the FL components but the DL torques are almost similar which is consistent with effect of Rashba field and also indicates the SHE origin of field-symmetric components of the FMR signals. The field-like components are about 7 times smaller in bilayer films and the DL-components are slighlty larger in polycrystalline films as compared to epitaxial films. These results highlight the importance of crystal orientation effects in bilayer structures. As the DL-SOT (damping like spin-orbit torque) is predominantly given by the SHE, which results from the spin-dependent scattering in the bulk of HM layer, we associate the difference in DL-SOT in polycrystalline and epitaxial bilayer samples to the difference in crystal orientation of Pt, which result in different scattering characteristics. Similar behaviour is not seen in multi-layer films which hints that bulk effects are less pronounced in them. This highlights the effect of crystal structure of the non magnetic Pt layer on SOTs. In case of bulk Pt the main relaxation mechanism is considered to be EY [313]. However, when Pt has single crystalline growth the DP mechanism also becomes significant. Since the spin relaxation mechanisms are induced by spin-orbit interactions (SOI) so the difference in SOT in case of epitaxial and polycrystalline growth indicates the effect of crystal growth of Pt on SOTs. Moreover, large FL torques in multi-layer stacks also hints at large DP relaxation in these samples which is induced due to Rashba SOI on the interface. Thus, due to different scattering properties of Pt originating from different growth induced crystal orientations can lead to difference in SOT.

It has also been shown by Ryu et. al. [313] that by modifying the thickness as well as crystal structure can lead to different spin relaxation rate. This occurs as a result of both EY and DP type of relaxation mechanism. This has also been seen in our study where the effect of crystal morphology was evident from difference in value of SOT. Thus, it suggests that it is important to consider the crystal orientation effects for engineering SOT-based devices for spintronic applications.

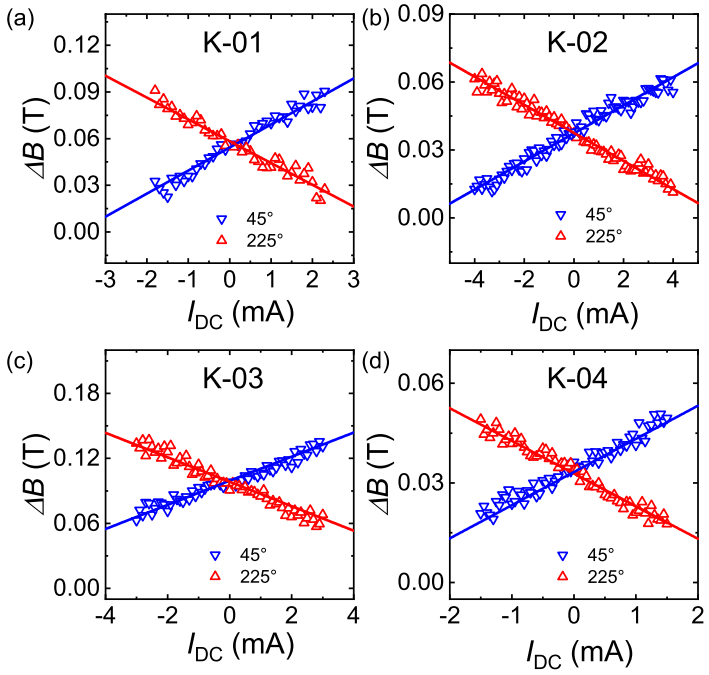

Figure 6.28: The change of the FMR linewidth as a function of injected current I_{DC} at frequency of 8 GHz for different set of samples.

6.8 Current induced linewidth modulation

To check the spin current density absorbed by the FM layer, the FMR linewidth ΔB was measured as a function of dc current, similar to technique used in [2] and the results are shown in Fig. 6.28. A clear linewidth broadening is seen for $\theta = 45°$ and vice versa for $\theta = 225°$ as the current, I_{DC} is ramped from negative to positive values. Eq. 3.12 is used to calculate the effective spin Hall angle given as $\theta_{SHA} = J_s/J_c$ where J_s is the spin current density in the platinum layer and J_c is the charge current density. The bulk resistivity of platinum layer is 10.6 μΩcm and that of nickel is 7μΩ cm and using these values the θ_{SHA} is calculated as given in Table. 6.6. These values are much larger than reported in the literature [313]. Such large values can be due to the bulk resistivity values used for calculating θ_{SHA}. Along with this another reason for such large values can be due to the interfacial contribution caused by spin-orbit fields and has been reported in earlier works [314, 315]. In general, the measurement of θ_{SHA} is correlated with another important material parameter, the spin diffusion length, λ_{sf}, which quantifies how the pure spin current decays

as well as its propagation. For a perfectly transparent FM/HM interface and for HM layer much thicker than λ_{sf}, the quantities J_s/J_c and θ_{SHA} should be equal. There has been a large difference in reported value of λ_{sf} of Pt in literature even for the same technique. The values reported showed variation from 1 nm [316] to 10 nm [317] likewise the values for θ_{SHA} show a variation from 0.01 to 0.20. It has been shown by Tao et. al [318] that interfacial spin loss caused at different FM/HM interfaces can lead to difference in values of λ_{sf}. More specifically, when a number of interfaces are present, the spin current can get depolarized at these multi-layer interfaces [319] and can thus effect the estimation of θ_{SHA} and λ_{sf}. The spin memory loss (SML) occurs due to interfacial dissipation of spin polarized current and so a careful consideration needs to be given regarding the correct method for estimation of θ_{SHA}. Tao et al. [318] considered the effect of SML and provided a self consistent method for estimating θ_{SHA}. This was based on the theory that at the interface the conduction electrons experience an abrupt change in scattering potential and the spin-orbit interaction (SOI) at the interface. Moreover, in materials with large SOC, a larger SML occurs and this can cause a variation in calculated values of θ_{SHA}. The disparity in calculated values of θ_{SHA} was also studied by Roy [320]. The theoretical approach followed in his paper accounts for a thickness dependent λ_{sf} to be required for correct estimation of θ_{SHA}. Two different spin relaxation mechanisms were considered in this study. They are EY which considers a thickness dependent λ_{sf} and DP mechanism in which λ_{sf} is considered constant. The conductivity of a sample varies depending on the growth, thickness as well as presence of interfaces. Thus in case of EY relaxation, a higher conductivity which is thickness dependent leads to larger λ_{sf} and thus explains a thickness dependent contribution to λ_{sf}. Moreover, interfacial θ_{SHA} can be different from bulk value which has been thought to be one of the reason of the overestimation of θ_{SHA} in our samples as explained earlier. Thus, his work highlights the sensitivity of the estimated parameters to the variation in interface conductances. Rojas-Sánchez et al. [319] proposes to use a trilayer spin current diffusion or relaxation model so as to account for the spin-depolarization at the interfaces. The larger values estimated

Table 6.6: θ_{SHA} for different samples calculated using Eq. 3.12.

Sample	K-01	K-02	K-03	K-04
θ_{SHA}	2.21 ± 0.02	0.92 ± 0.01	1.26 ± 0.02	0.91 ± 0.03

from our multi-layer samples can be due to neglect of various terms like SOC at the interface. The degree of spin momentum locking by SOC at the interface also determines the spin current density. When the electrons pass through an interface layer, the SOC at interface causes the electrons to be absorbed or rotated and even cause spin -flip. Thus, the interface affects the resultant current and can also create diffusive spin current. The presence of disorder as well as SOC at the interface need to taken into account for correct calculation of θ_{SHA} [321].

Moreover, because the Ni/Pt interface is likely not perfectly transparent and since Pt layer thickness is not $>> \lambda_{sf}$, our results might not give a good calculation for θ_{SHA}. For a transparent Ni/Pt interface there should be no spin accumulation transverse to the Ni moment at the interface but due to SML at interface and using the drift diffusion theory [322], the spin Hall current density in Pt should be reduced from the bulk value by $J_s(d)/J_s(\infty) = 1 - \mathrm{sech}(d/\lambda_{sf})$, where d corresponds to thickness of platinum. Using this expression and considering λ_{sf} as 1.5 nm [313], it is estimated that the value of J_s should be reduced by 0.2. This corresponds to the value of θ_{SHA} to be reduced to 0.18. Thus, this can account for reason of larger spin Hall angle quantified in our samples. In conclusion it can be said that interfacial SML effects as well as interfacial SOC need to be carefully addressed for calculating θ_{SHA}. Moreover, we need to separate the bulk and interfacial contribution to θ_{SHA} appropriately. Spin current generation mechanisms in FM/HM systems need to be properly explored to address the above issue.

In summary the effect of substrate induced growth morphology on the SOT is demonstrated. This allows to determine the effect of interfacial contribution on type of torques. θ_{SHA} was also estimated using the technique of linewidth modulation. The relatively large efficiency of spin current generation that is observed is promising for applications that utilize SHE to manipulate ferromagnetic dynamics however careful quantification of the value of θ_{SHA} needs further research to account for the

actual mechanism.

Chapter 7

Summary and Outlook

This thesis has presented the experimental studies of spin dynamics in non-centrosymmetric bulk ferromagnet (NiMnSb) and magnetic multilayer (synthetic antiferromagnet (SyAF), synthetic ferrimagnet (SyF), Ni/Pt) systems.

NiMnSb, a material with broken inversion symmetry and half metallic structure is known to have very high spin polarization, high Curie temperatue and low value of Gilbert damping. We investigated the intrinsic and extrinsic contributions to magnetization relaxation by performing broad band ferromagnetic resonance (FMR) experiments. The anisotropy of intrinsic Gilbert damping was realised and its dependence on ferromagnet (FM) thickness was studied. The symmetry of damping anisotropy changed from two-fold to four fold as thickness is reduced while thickest sample did not show any anisotropy. This characteristic is important for tuning the damping through growth.

In Chapter 5, the magnon-magnon coupling in SyAF and SyF systems was investigated. Hybridisation of acoustic and optical modes in symmetrical SyAF structures was clearly observed and the strength of coupling was tuned by breaking the orthogonality of two modes by tilting the magnetic moments. The effect of damping parameters on coupling strength was studied theoretically indicating that coupling is partially mediated by spin currents. The highest coupling strength, $g_c/2\pi$, achieved is 1.0 GHz and the system starts to enter strong coupling regime. This work is amongst one of the first works of experimental demonstration of tunability of magnon-magnon coupling at room temperature. We also show the tun-

ability of coupling due to the effect of inherent orthogonal symmetry breaking by using either two dissimilar FM or thickness variation in SyF samples. The largest coupling strength achieved in canted regime is 9.0 GHz which signifies greater efficiency in inducing magnon-magnon coupling in SyFs. Our theoretical model in macro spin limit obtained by solving two coupled equations provides numerical explanation and predictions of experimental data. The tunability of coupling strength in asymmetric SyF structures has not been shown experimentally till now and our work nicely demonstrates the coupling phenomena in both SyAF and SyF structures and their coherent manipulation and engineering for device applications.

In Chapter 6 we use the technique of spin transfer torque (STT) to study spin dynamics in two different multilayer structures, SyAF and Ni/Pt multistacks. By local spin torque excitations we can convert mode excitation symmetry between perpendicular and parallel pumping configurations in SyAF which has been demonstrated for the first time through our work. We see a change in torque symmetry in acoustic and optical modes compared to the spin-wave excitations through homogeneous fields. The theoretical model supports the experimental observations and different material parameters such as spin Hall angle are extracted. Finally, we show the manipulation of spin-orbit torques (SOTs) in Ni/Pt multi-layer structures by interface engineering and electronic structure modification by growth. By changing the growth from epitaxial to polycrystalline the inhomogeneous linewidth broadening was observed. The bilayer structures had dominant damping-like (DL) torque components indicating the spin Hall effect (SHE) as the main mechanism of torque injection. However the mulitlayer stacks show both DL and field-like (FL) torques and there was no complete cancellation of the spin currents also evident from large spin Hall angle. These large spin Hall angle values can have more interfacial contribution rather than bulk and need further work to find out the mechanism involved but it is beyond the scope of the work presented in Chapter 6.

In response to the experimental work carried out in this thesis, further future efforts are required to realise the full potential of the four magnetic systems, mentioned above, in the field of spintronics. The control of damping offers a strong

avenue for realization of efficient magnetization reversal in memory devices. There are several things that need to be investigated which can expand the understanding of anisotropy in damping. Investigating the effect of temperature on linewidth and damping anisotropy can provider deeper insight into mechanism behind the damping anisotropy. It is also important to understand the effect of stoichiometry i.e changing from Ni-rich to Mn-rich sample. Such changes can effect magnetodynamic properties and possibly their effect on relaxation is yet to be explored. Other materials from half-Heusler alloy family can potentially be studied like IrMnSb, CoTiSb which can offer more flexibility for future device buildup.

In terms of SyAF magnetic systems, potential improvement and control of coupling can be achieved in materials with low damping as suggested from our theoretical model. Further investigation need to be done in materials with larger exchange field B_{ex} and smaller demagnetisation field B_{s}. Our results suggested that an increased damping due to spin pumping can also lead to frequency crossing and loss rate splitting similar to cavity magnonics [323]. To fully confirm this we need more experiments to be done varying thickness of FM material since the damping term due to spin pumping is dependent on the thickness of the FM. For SyF samples we studied the effect of asymmetry in thickness as well as thickness along with dissimilar materials on mode coupling. However, the effect of only dissimilar material with same thickness still need to be explored which is the future work.

Another work which is yet to be explored is the Neél vector switching by DC current injection. Work has been started but not presented in this thesis. Switching by charge currents has been reported in SyAF structure earlier [324] however the study of dynamics with current injection has yet not been investigated. When dynamics are excited in the system in the presence of external current, it causes change in spin-orbit field (SOF) and acts as an effective field to cause rotation of the Neél vector which rotates oppositely for top and bottom layers and at certain current density it is enough to cause the two moments to switch thereby causing the change in sign of respective voltages detected as shown in Fig. 7.1. This can act as another way to probe the switching current density. To prove that switching is

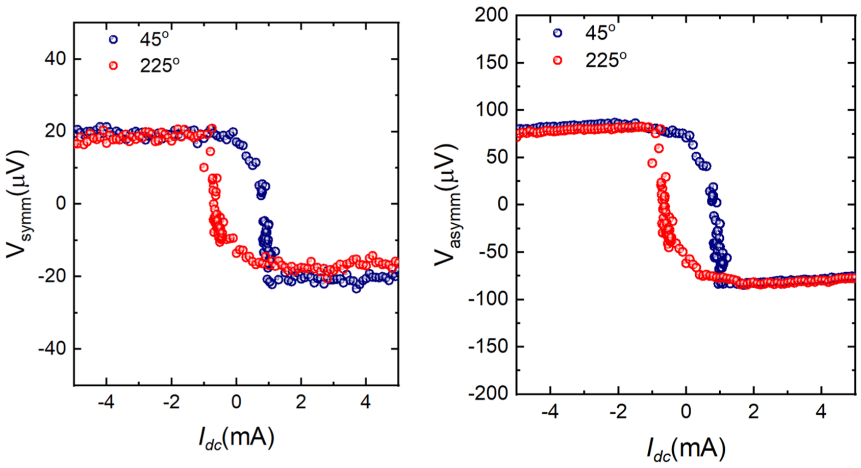

Figure 7.1: Symmetric and antisymmetric components of voltage as a function of applied DC current. The measurements is done for the sample in NiFe/Ru/NiFe sample as in Ch 6 using the technique in Sec 3.3

caused by SOT and not due to Oersted field or FL torques we will systematically do measurements for resistance applying current pulses and then reading them. The read write operation should cause opposite resistance change (high and low) for applied opposite direction of write current. We aim to show the spin torque switching seems to occur in a portion of the antiferromagnetic bit at a time, leading to the memresistive behavior which may be useful for the neuromorphic applications.

Another future work is the study of optical mode dynamics induced by spin orbit torque. By parametric pumping we can excite the optical mode dynamics. When the input threshold current is sufficiently large, at frequency where acoustic mode frequency is half the frequency of optical mode, it can create condition of three magnon confluence and an increase in amplitude of acoustic mode will occur. From our theoretical calculations we obtained this value as :

$$\theta_{\mathrm{SH}}\frac{\hbar}{e}\frac{\gamma}{M_{\mathrm{s}}d_{\mathrm{FM}}}\delta J_{\mathrm{e0}} > \frac{2(\frac{2}{\tau_{\mathrm{ac}}})(\frac{2}{\tau_{\mathrm{op}}})}{(1-p^{-2})\omega_{\mathrm{ac}}n_{\mathrm{y0}}} \tag{7.1}$$

where, $\delta J_{\mathrm{e0}}, M_{\mathrm{s}}, d_{\mathrm{FM}}, \tau_{\mathrm{ac}}, \tau_{\mathrm{op}}, \omega_{\mathrm{ac}}, p, n_{\mathrm{y0}}$ are the current density, saturation magnetization, thickness of two FM layers, relaxation time for acoustic and optical mode, resonance frequency for acoustic mode, ellipticity value and vector component respectively. This is the respective threshold value to obtain the condition

of parametric amplification. By using the SyAF parametric effect, spintronic and magnonic computing systems beyond von Neumann architectures can be fabricated at nanoscale. In case of SyAF, the inhomogeneous field excitation caused a change in torque symmetry. This concept can be extended where we can create the asymmetric excitation by using material with opposite spin Hall angle on two sides of a ferromagnet. Finally, the large spin Hall angle obtained in case of Ni/Pt multistacks implies that at certain current density the STT can become antidamping and exceed the intrinsic Gilbert damping, α_0, thus implying negative damping. This can lead to auto-oscillation of the magnetization precession and is another topic to be explored in these systems.

List of Publications from this Thesis

1. A. Sud, C. W. Zollitsch, A. Kamimaki, T. Dion, S. Khan, S. Iihama, S. Mizukami, and H. Kurebayashi. "Tunable magnon-magnon coupling in synthetic antiferromagnets." *Physical Review B* **102**, 100403 (2020).

2. A. Sud, Y. Koike, S. Iihama, C. Zollitsch, S. Mizukami, and H. Kurebayashi. "Parity-controlled spin-wave excitations in synthetic antiferromagnets." *Applied Physics Letters* **18**, 032403 (2021).

3. A. Sud, K. Yamamoto, C. W. Zollitsch, K. Suzuki, S. Mizukami, and H. Kurebayashi. "Control of magnon-magnon coupling strength in synthetic ferrimagnets." *(In-preparation).*

4. A. Sud, T. Seki, and H. Kurebayashi. "Spin-orbit torques and spin-transport in Ni/Pt multi-layers." *(In-preparation).*

5. A. Sud, K. Yamamoto, S. Khan, N. Zhao, and H. Kurebayashi. "Relaxation of magnetization dynamics in half-Heusler NiMnSb thin films." *(In-preparation).*

List of Presentations

1. A. Sud, C. W. Zollitsch, A. Kamimaki, S. Iihama, S. Mizukami, and H. Kurebayashi. *Mode coupling and spin-wave dissipaton in synthetic antiferromagnetic multi-layers (poster)*, 4th International Symposium for The Core Research Cluster for Spintronics, Japan, 2021.

2. A. Sud, Y. Koike, S. Iihama, C. Zollitsch, S. Mizukami, and H. Kurebayashi. *Parity Controlled spin-wave excitations in synthetic antiferromagnets (oral)*, IoP Magnetism Conference Online, 2021.

3. A. Sud, C. W. Zollitsch, A. Kamimaki, S. Iihama, S. Mizukami, and H. Kurebayashi. *Mode coupling and spin-wave dissipaton in synthetic antiferromagnetic multi-layers (poster)*, IoP Magnetism Conference, Online, 2021.

4. A. Sud, C. W. Zollitsch, M. Tam, A. Kamimaki, Y. Koike, S. Iihama, S. Mizukami, and H. Kurebayashi. *Modulation of magnon-magnon coupling by inherent symmetry breaking in synthetic antiferromagnets (oral)*, INTERMAG Online Conference, 2021.

5. A. Sud, Y. Koike, S. Iihama, C. Zollitsch, S. Mizukami, and H. Kurebayashi. *Parity Controlled spin-wave excitations in synthetic antiferromagnets (oral)*, INTERMAG Online Conference, 2021.

6. A. Sud, S. Khan, K. Yamamoto, S. Khan, N. Zhao, K. Yamanoi, H. Sukegawa and H. Kurebayashi. *Anisotropic Damping of Magnetisation Dynamics in Non-Centrosymmetric Ferromagnet (poster)*, IoP Magnetism Conference, Leeds, 2019.

Appendix A

Ferromagnetic Resonance in NiMnSb

In this appendix the resonance condition is derived. Using the Coordinate system as shown in Fig. A.1, the internal fields can be evaluated in terms of in-plane and out-of-plane angles as follows:

$$\alpha_x = \frac{M_x}{M_s}\cos\phi_M \sin\theta_M - \frac{M_y}{M_s}\sin\phi_M - \frac{M_z}{M_s}\cos\phi_M\cos\theta_M \tag{A.1}$$

$$\alpha_y = \frac{M_x}{M_s}\sin\phi_M \sin\theta_M + \frac{M_y}{M_s}\cos\phi_M - \frac{M_z}{M_s}\sin\phi_M\cos\theta_M \tag{A.2}$$

$$\alpha_z = \frac{M_x}{M_s}\cos\theta_M + \frac{M_z}{M_s}\sin\theta_M \tag{A.3}$$

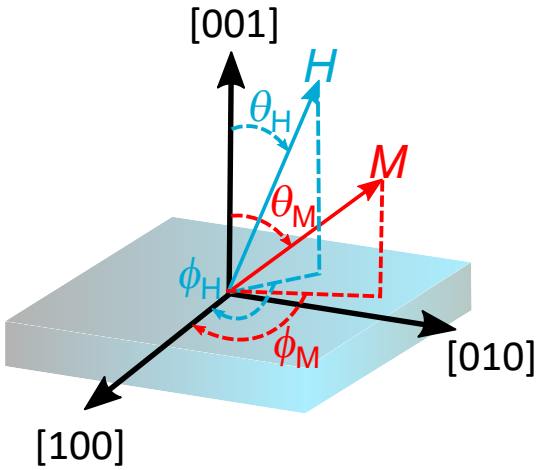

Figure A.1: Coordinate system used to describe motion of magnetization and Ferromagnetic resonance in NiMnSb.

A.1 In-plane configuration

For in-plane configuration the out-of-plane angles $\theta_{\mathrm{M}} = \theta_{\mathrm{H}} = 90^{\circ}$. Using this in Eq. (A.1) to Eq. (A.3) , the equations for in-plane configuration becomes:

$$\alpha_{\mathrm{x}}^{\mathrm{ip}} = \frac{M_{\mathrm{x}}}{M_{\mathrm{s}}}\cos\phi_{\mathrm{M}} - \frac{M_{\mathrm{y}}}{M_{\mathrm{s}}}\sin\phi_{\mathrm{M}} \tag{A.4}$$

$$\alpha_{\mathrm{y}}^{\mathrm{ip}} = \frac{M_{\mathrm{x}}}{M_{\mathrm{s}}}\sin\phi_{\mathrm{M}} + \frac{M_{\mathrm{y}}}{M_{\mathrm{s}}}\cos\phi_{\mathrm{M}} \tag{A.5}$$

$$\alpha_{\mathrm{z}}^{\mathrm{ip}} = \frac{M_{\mathrm{z}}}{M_{\mathrm{s}}} \tag{A.6}$$

A.1.1 Anisotropy in NiMnSb crystal

Due to the presence of spin-orbit coupling, the ferromagnets with crystalline structure exhibit energy minima and maxima. In NiMnSb both cubic and uniaxial anisotropies are present whose magnitude is dependent on the thickness [170]. The crystalline energy can be expresed as:

$$\varepsilon_{\mathrm{crystal}} = -\frac{K_1^{\parallel}}{2}\left(\alpha_{\mathrm{x}}^4 + \alpha_{\mathrm{y}}^4\right) - \frac{K_1^{\perp}}{2}\alpha_{\mathrm{z}}^4 - K_u^{\perp}\alpha_{\mathrm{z}}^2 \tag{A.7}$$

Here, α_{i} are the cosines of angle with respect to the crystal axis [100], [010], [001] for $i = x, y, z$ respectively and $K_1^{\parallel}$, $K_1^{\perp}$, $K_u^{\perp}$ refer to the biaxial in-plane, biaxial out-of-plane and uniaxial out-of-plane anisotropies. An additional in-plane uniaxial anisotropy is present in NiMnSb which can be described by another term, namely:

$$\text{uniaxial in-plane energy} = K_{\mathrm{u}}^{\parallel}\frac{\left(\hat{1}_{\mathrm{uni}}M\right)^2}{M_{\mathrm{s}}^2} \tag{A.8}$$

Here, $\hat{1}_{\mathrm{uni}}$ represents the unit-vector along the in-plane uniaxial axis. The effect of interfacial symmetry breaking induced anisotropy is accounted for by adding another term. The anisotropy constant for a film with thickness t and two interfaces can be represented as:

$$\kappa = K_{\mathrm{bulk}} + \frac{K_{\mathrm{I}}}{t} + \frac{K_{\mathrm{II}}}{t} \tag{A.9}$$

Here, κ stands for total anisotropy constant which is sum of bulk (K_{bulk}) and interfacial contributions ($K_{\text{I,II}}$).

A.1.2 Resonance condition for in-plane configuration

Using the Eq. (A.7) and Eq. (A.4) to Eq. (A.6), the anisotropy field can be obtained as:

$$\begin{aligned} H_{\text{x}}^{\text{aniso}} &= -\frac{\delta\varepsilon_{\text{aniso}}}{\delta M_{\text{x}}} = -\delta\left(-\frac{K_1^{\parallel}}{2}\left(\alpha_{\text{x}}^4+\alpha_{\text{y}}^4\right)-\frac{K_1^{\perp}}{2}\alpha_{\text{z}}^4-K_u^{\perp}\alpha_{\text{z}}^2\right)/\delta M_{\text{x}} \\ &= \frac{K_1^{\parallel}}{2M_{\text{s}}^4}\left(M_{\text{x}}^3\left(\cos 4\phi_{\text{M}}+3\right)-3M_{\text{x}}^2M_{\text{y}}\sin 4\phi_{\text{M}}+M_{\text{x}}M_{\text{y}}^2\left(3-3\cos 4\phi_{\text{M}}\right)\right. \\ &\quad \left.+M_{\text{y}}^3\sin 4\phi_{\text{M}}\right) \end{aligned} \tag{A.10}$$

$$\begin{aligned} H_{\text{y}}^{\text{aniso}} &= -\frac{\delta\varepsilon_{\text{aniso}}}{\delta M_{\text{y}}} = -\delta\left(-\frac{K_1^{\parallel}}{2}\left(\alpha_{\text{x}}^4+\alpha_{\text{y}}^4\right)-\frac{K_1^{\perp}}{2}\alpha_{\text{z}}^4-K_u^{\perp}\alpha_{\text{z}}^2\right)/\delta M_{\text{y}} \\ &= -\frac{K_1^{\parallel}}{2M_{\text{s}}^4}\left(M_{\text{x}}^3\sin 4\phi_{\text{M}}-M_{\text{x}}^2M_{\text{y}}\left(3-3\cos 4\phi_{\text{M}}\right)-3M_{\text{x}}M_{\text{y}}^2\sin 4\phi_{\text{M}}\right. \\ &\quad \left.-M_{\text{y}}^3\left(3+\cos 4\phi_{\text{M}}\right)\right) \end{aligned} \tag{A.11}$$

$$H_{\text{z}}^{\text{aniso}} = -4\pi DM_{\text{z}}+\frac{2K_{\text{u}}^{\perp}}{M_{\text{s}}^2}M_{\text{z}}+\frac{2K_1^{\perp}}{M_{\text{s}}^4}M_{\text{z}}^3 \tag{A.12}$$

Expressing the external field in terms of ϕ_{M} and ϕ_{H}.

$$\boldsymbol{H}_0 = H_0\left(\cos\left(\phi_{\text{M}}-\phi_{\text{H}}\right)\hat{x}-\sin\left(\phi_{\text{M}}-\phi_{\text{H}}\right)\hat{y}\right) \tag{A.13}$$

The effective field $\boldsymbol{H}_{\text{eff}}$ acting on the sample is the sum of RF-field, external and anisotropy fields. Considering a small RF-field $\boldsymbol{h}(t)$ which is in the film plane, $\boldsymbol{H}_{\text{eff}}$ can be expressed as:

$$\boldsymbol{H}_{\text{eff}} = \boldsymbol{H}_0+\boldsymbol{H}^{\text{aniso}}+\boldsymbol{h}\hat{y} \tag{A.14}$$

To calculate resonance condition we use the small angle approximation ($M_{\text{x}} >> M_{\text{y}}, M_{\text{z}}$) for the field applied along [100] direction.

$$\boldsymbol{M} = M_{\text{s}}\hat{x}+m_{\text{y}}^{\text{rf}}\hat{y}+m_{\text{z}}^{\text{rf}}\hat{z} \tag{A.15}$$

The dynamics of the damped magnetic motion is described phenomenologically by the Landau-Lifshitz-Gilbert (LLG) equation:

$$\frac{\delta \boldsymbol{M}}{\delta t} = -\gamma\mu_0 \boldsymbol{M} \times (\boldsymbol{H}_{\text{eff}}) + \frac{\alpha}{M_{\text{s}}}\left(\boldsymbol{M} \times \frac{\delta \boldsymbol{M}}{\delta t}\right) \tag{A.16}$$

Using Eq. (A.14) and Eq. (A.15) in the LLG equation we get the coupled equations for magnetization. Linearized solution of system of equation is obtained as below considering the components $m^{\text{rf}}_{\text{x,}y} << M_{\text{s}}$.

$$0 = i\frac{\omega}{\gamma} m^{\text{rf}}_{\text{y}} + \left(\mathcal{B}_{\text{eff}} + i\alpha\frac{\omega}{\gamma}\right) m^{\text{rf}}_{\text{z}} \tag{A.17}$$

$$hM_{\text{s}} = -i\frac{\omega}{\gamma} m^{\text{rf}}_{\text{z}} + \left(\mathcal{H}_{\text{eff}} + i\alpha\frac{\omega}{\gamma}\right) m^{\text{rf}}_{\text{y}} \tag{A.18}$$

Here, the effective fields $\mathcal{B}_{\text{eff}}$ and $\mathcal{H}_{\text{eff}}$ are defined as:

$$\begin{aligned}\mathcal{B}_{\text{eff}} = {} & H_0 \cos(\phi_{\text{M}} - \phi_{\text{H}}) + 4\pi D M_{\text{s}} - \frac{2K_u^{\perp}}{M_{\text{s}}} + \frac{K_1^{\parallel}}{2M_{\text{s}}}(\cos 4\phi_{\text{M}} + 3) \\ & + \frac{K_u^{\parallel}}{M_{\text{s}}}(1 + \cos 2(\phi_{\text{M}} - \phi_{\text{U}}))\end{aligned} \tag{A.19}$$

$$\mathcal{H}_{\text{eff}} = H_0 \cos(\phi_{\text{M}} - \phi_{\text{H}}) + \frac{2K_1^{\parallel}}{M_{\text{s}}}\cos 4\phi_{\text{M}} + \frac{2K_u^{\parallel}}{M_{\text{s}}}\cos 2(\phi_{\text{M}} - \phi_{\text{U}}) \tag{A.20}$$

The effective magnetization can be expressed as:

$$4\pi M_{\text{eff}} = 4\pi D M_{\text{s}} - \frac{2K_u^{\perp}}{M_{\text{s}}} \tag{A.21}$$

Here, D is the demagnetization factor. Using Eq. (A.17) and Eq. (A.18), the RF susceptibility can be calculated for a given frequency ω as:

$$\chi_{\text{y}} = \frac{m^{\text{rf}}_{\text{y}}}{h} = \frac{M_{\text{s}}\left(\mathcal{B}_{\text{eff}} + i\alpha\frac{\omega}{\gamma}\right)}{\left(\mathcal{B}_{\text{eff}} + i\alpha\frac{\omega}{\gamma}\right)\left(\mathcal{H}_{\text{eff}} + i\alpha\frac{\omega}{\gamma}\right) - \left(\frac{\omega}{\gamma}\right)^2} \tag{A.22}$$

Eq. (A.22) is valid for thin films with skin depth much larger than film thickness which gives a uniform RF field. The resonance condition is obtained by setting

denominator to zero. For the case of undamped motion this leads to the resonance condition as below:

$$\left(\frac{\omega}{\gamma}\right)^2 = \mathcal{B}_{\text{eff}}\mathcal{H}_{\text{eff}} \tag{A.23}$$

Due to component of field dragging as explained in Chapter 2 the external field is not aligned parallel to magnetization i.e $\phi_{\text{M}} \neq \phi_{\text{H}}.\phi_{\text{M}}$ can be found from static equilibrium condition assuming $\boldsymbol{M} = (M_{\text{s}}, 0, 0)$. Using Eq. (A.10) to Eq. (A.13) the expression for calculating ϕ_{M} is obtained as:

$$H_0 M_{\text{s}}\left(\phi_{\text{H}} - \phi_{\text{H}}\right) + K_u^{\parallel}\sin 2\left(\phi_{\text{U}} - \phi_{\text{M}}\right) + \frac{1}{2}K_1^{\parallel}\sin 4\phi_{\text{M}} \tag{A.24}$$

The lineshape of imaginary part of susceptibility $Im(\chi)$ is lorentzian in shape and can be described as:

$$Im[\chi_{\text{y}}] = M_{\text{s}}\frac{\mathcal{B}_{\text{eff}}}{\mathcal{B}_{\text{eff}} + \mathcal{H}_{\text{eff}}}\bigg|_{\text{H}_{\text{FMR}}} \frac{\Delta H}{\Delta H^2 + (H_0 - H_{\text{FMR}})^2} \tag{A.25}$$

Here, $\Delta H = \alpha\frac{\omega}{\gamma}$ is the half width at half maximum (HWHM) and H_{FMR} is the FMR peak position.

A.2 Resonance condition for Out-of-Plane Configuration

For out-of-plane configuration the out-of-plane angles $\theta_{\text{M}} = \theta_{\text{H}} = 0^{\circ}$ and $\phi_{\text{M}} = \phi_{\text{H}} = 0^{\circ}$. Using this in Eq. (A.1) to Eq. (A.3) , the equations for out-of-plane configuration becomes:

$$\alpha_{\text{x}}^{\text{op}} = -\frac{M_{\text{z}}}{M_{\text{s}}} \tag{A.26}$$

$$\alpha_{\text{y}}^{\text{op}} = \frac{M_{\text{y}}}{M_{\text{s}}} \tag{A.27}$$

$$\alpha_{\text{z}}^{\text{op}} = \frac{M_{\text{x}}}{M_{\text{s}}} \tag{A.28}$$

Using the Eq. (A.7) and Eq. (A.26) to Eq. (A.28), the anisotropy field can be obtained as:

$$H_{\mathrm{x}}^{\mathrm{aniso}} = -\frac{\delta\varepsilon_{\mathrm{aniso}}}{\delta M_{\mathrm{x}}} = -\delta\left(-\frac{K_1^{\parallel}}{2}\left(\alpha_{\mathrm{x}}^4+\alpha_{\mathrm{y}}^4\right)-\frac{K_1^{\perp}}{2}\alpha_{\mathrm{z}}^4-K_u^{\perp}\alpha_{\mathrm{z}}^2\right)/\delta M_{\mathrm{x}}$$
$$= 2K_1^{\perp}\frac{M_{\mathrm{x}}^3}{M_{\mathrm{s}}^4}+2K_u^{\perp}\frac{M_{\mathrm{x}}}{M_{\mathrm{s}}^2} \tag{A.29}$$
$$H_{\mathrm{y}}^{\mathrm{aniso}} = -\frac{\delta\varepsilon_{\mathrm{aniso}}}{\delta M_{\mathrm{y}}} = -\delta\left(-\frac{K_1^{\parallel}}{2}\left(\alpha_{\mathrm{x}}^4+\alpha_{\mathrm{y}}^4\right)-\frac{K_1^{\perp}}{2}\alpha_{\mathrm{z}}^4-K_u^{\perp}\alpha_{\mathrm{z}}^2\right)/\delta M_{\mathrm{y}}$$
$$= 2K_1^{\parallel}\frac{M_{\mathrm{y}}^3}{M_{\mathrm{s}}^4} \tag{A.30}$$
$$H_{\mathrm{z}}^{\mathrm{aniso}} = -\frac{\delta\varepsilon_{\mathrm{aniso}}}{\delta M_{\mathrm{y}}} = -\delta\left(-\frac{K_1^{\parallel}}{2}\left(\alpha_{\mathrm{x}}^4+\alpha_{\mathrm{y}}^4\right)-\frac{K_1^{\perp}}{2}\alpha_{\mathrm{z}}^4-K_u^{\perp}\alpha_{\mathrm{z}}^2\right)/\delta M_{\mathrm{z}}$$
$$= -4\pi D M_{\mathrm{z}}+2K_1^{\parallel}\frac{M_{\mathrm{z}}^3}{M_{\mathrm{s}}^4} \tag{A.31}$$

Expressing the external field and saturation magnetisation as:

$$\boldsymbol{H}_{\mathrm{eff}} = \boldsymbol{H}^{\mathrm{aniso}}+\boldsymbol{h}\hat{y}+\boldsymbol{H}_0\hat{z} \tag{A.32}$$
$$\boldsymbol{M} = m_{\mathrm{x}}^{\mathrm{rf}}\hat{x}+m_{\mathrm{y}}^{\mathrm{rf}}\hat{y}+M_{\mathrm{s}}\hat{z} \tag{A.33}$$

Using Eq. (A.32) and Eq. (A.33) in the LLG equation we get the coupled equations for magnetization for which linearized solution is obtained as below:

$$0 = -i\frac{\omega}{\gamma}m_{\mathrm{y}}^{\mathrm{rf}}+\left(\mathcal{H}_{\mathrm{eff}}^{\mathrm{op}}+i\alpha\frac{\omega}{\gamma}\right)m_{\mathrm{x}}^{\mathrm{rf}} \tag{A.34}$$
$$hM_{\mathrm{s}} = i\frac{\omega}{\gamma}m_{\mathrm{x}}^{\mathrm{rf}}+\left(\mathcal{H}_{\mathrm{eff}}^{\mathrm{op}}+i\alpha\frac{\omega}{\gamma}\right)m_{\mathrm{y}}^{\mathrm{rf}} \tag{A.35}$$

Here, the effective field $\mathcal{H}_{\mathrm{eff}}^{\mathrm{op}}$ is defined as:

$$\mathcal{H}_{\mathrm{eff}}^{\mathrm{op}} = H_0-4\pi M_{\mathrm{eff}}+\frac{2K_1^{\parallel}}{M_{\mathrm{s}}} \tag{A.36}$$

Using similar procedure as outlined in Eq. (A.22), the RF susceptibility can be calculated for a given frequency ω as:

$$\chi_{\mathrm{y}} = \frac{m_{\mathrm{y}}^{\mathrm{rf}}}{h} = \frac{M_{\mathrm{s}}\left(\mathcal{H}_{\mathrm{eff}}^{\mathrm{op}} + i\alpha\frac{\omega}{\gamma}\right)}{\left(\mathcal{H}_{\mathrm{eff}}^{\mathrm{op}} + i\alpha\frac{\omega}{\gamma}\right)^2 - \left(\frac{\omega}{\gamma}\right)^2} \tag{A.37}$$

Setting the denominator to zero in Eq. (A.37), the resonance condition for out-of-plane configuration is obtained as:

$$\frac{\omega}{\gamma} = \mathcal{H}_{\mathrm{eff}}^{\mathrm{op}} \tag{A.38}$$

Appendix B

Point group symmetries of NiMnSb

We consider NiMnSb thin films grown on the (001) surface of a GaAs substrate. Both NiMnSb and GaAs have bulk point group T_d and NiMnSb is expected to grow in the [001] direction. Due to the lattice mismatch, there will be a tetragonal strain (compression of the lattice in [100] and [010] directions) that removes the three-fold rotations and lowers the point group symmetry of NiMnSb to D_{2d}. The presence of the interface, however, further disqualifies the in-plane two-fold axes $C_{2x,y}$ as symmetry operations, reducing the group down to C_{2v}. For the rather intermediate values of the thickness used in the experiment, i.e.15, 20, 50 and 100 nm, it is not clear whether the tetragonal strain and/or the presence of the interface would lead to observable consequences. Note that symmetry analysis is incapable of predicting under what circumstances these symmetry breaking effects would be significant. Therefore, we here present symmetry constraints of relevant tensors for all the potentially relevant point groups, i.e. T_d, D_{2d} and C_{2v}.

B.1 Magnetic anisotropy tensors

The magneto-crystalline anisotropy energy can be phenomenologically written as a power series expansion with respect to the magnetic moment $\boldsymbol{M}$

$$W = \frac{1}{2}K_{ij}M^iM^j + \frac{1}{4}L_{ijkl}M^iM^jM^kM^l + \cdots \tag{B.1}$$

where the terms of higher than fourth order in the components of M are not

discussed here. We note that terms of odd powers in M are precluded because of the time-reversal symmetry. The task here is to constrain the tensors K_{ij} and L_{ijkl} by point group symmetries. Without any symmetry considerations, we can restrict ourselves to completely symmetric tensors, namely $K_{ji} = K_{ij}$ and $L_{ijkl} = L_{jikl} = L_{kjil} = \cdots$. For the second rank symmetric tensor K_{ij} that is even in inversion, the results are readily available and we just quote

$$K_{ij}\big|_{T_d} = a\begin{pmatrix} 1 & 0 & 0 \\ 0 & 1 & 0 \\ 0 & 0 & 1 \end{pmatrix}, \quad K_{ij}\big|_{D_{2d}} = \begin{pmatrix} a & 0 & 0 \\ 0 & a & 0 \\ 0 & 0 & b \end{pmatrix}, \quad K_{ij}\big|_{C_{2v}} = \begin{pmatrix} a & 0 & 0 \\ 0 & b & 0 \\ 0 & 0 & c \end{pmatrix} \tag{B.2}$$

where a, b, c are arbitrary real constants. In words, there is no quadratic anisotropy for T_d, and the anisotropy is uniaxial and biaxial for D_{2d} and C_{2v} respectively.

Some works are required for the fourth rank tensor L_{ijkl}. While not absolutely needed, we first place upper limits on the number of independent constants appearing in L_{ijkl} by the decomposition of product representations. Let D_1 be the axial vector representation of the full rotation group. Its decompositions in terms of the irreducible representations of T_d, D_{2d}, C_{2v} are given respectively by

$$D_1|_{T_d} = \Gamma_4, \quad D_1|_{D_{2d}} = \Gamma_2 + \Gamma_5, \quad D_1|_{C_{2v}} = \Gamma_2 + \Gamma_3 + \Gamma_4 \tag{B.3}$$

The tensor L_{ijkl} belongs to:

$$(D_1 \times D_1 \times D_1 \times D_1)_{\text{sym}} \subset \Big[(D_1 \times D_1)_{\text{sym}} \times (D_1 \times D_1)_{\text{sym}}\Big]_{\text{sym}} \tag{B.4}$$

Again from the standard tables, we note

$$(D_1 \times D_1)_{\text{sym}} \Big|_{T_d} = \Gamma_1 + \Gamma_3 + \Gamma_5 \tag{B.5}$$

$$(D_1 \times D_1)_{\text{sym}} \Big|_{D_{2d}} = 2\Gamma_1 + \Gamma_3 + \Gamma_4 + \Gamma_5 \tag{B.6}$$

$$(D_1 \times D_1)_{\text{sym}} \Big|_{C_{2v}} = 3\Gamma_1 + \Gamma_2 + \Gamma_3 + \Gamma_4, \tag{B.7}$$

so that

$$\begin{aligned}(D_1 \times D_1)_{\text{sym}} \times (D_1 \times D_1)_{\text{sym}} \Big|_{T_d} =& 3\Gamma_1 + [\Gamma_2] + 2\Gamma_3 + [\Gamma_4] + \Gamma_5 \\ &+ 2\Gamma_3 + 2\Gamma_5 + 2(\Gamma_4 + \Gamma_5),\end{aligned} \tag{B.8}$$

$$\begin{aligned}(D_1 \times D_1)_{\text{sym}} \times (D_1 \times D_1)_{\text{sym}} \Big|_{D_{2d}} =& 5\Gamma_1 + [\Gamma_2] + \Gamma_3 + \Gamma_4 \\ &+ 2(\Gamma_1 + 2\Gamma_3 + 2\Gamma_4 + 2\Gamma_5 + \Gamma_2 + 2\Gamma_5)\end{aligned} \tag{B.9}$$

$$\begin{aligned}(D_1 \times D_1)_{\text{sym}} \times (D_1 \times D_1)_{\text{sym}} \Big|_{C_{2v}} =& 6\Gamma_1 \\ &+ 2(3\Gamma_1 + 3\Gamma_2 + 3\Gamma_3 + 3\Gamma_4 + \Gamma_2 + \Gamma_3 + \Gamma_4),\end{aligned} \tag{B.10}$$

where the first lines arise from squaring representations while the second lines are cross terms. Symmetrisation between the two $(D_1 \times D_1)_{\text{sym}}$ factors eliminate $[X]$ and factor 2 in the second lines so that we have at most 3,6 and 9 constants for T_d, D_{2d} and C_{2v} respectively. Note that there is still one more symmetrisation left to be used which might further reduce the number of independent constants.

For T_d, the most efficient way to get the actual form of L_{ijkl} is by the method of invariants as presented in Sec. 4.7. in Lax [325]. Let $\boldsymbol{r} = (x, y, z)$ be components of a generic axial vector. The basis functions of $(D_1 \times D_1)_{\text{sym}}$ in the irreducible decomposition are given by

$$A = x^2+y^2+z^2, \quad E = \left[z^2 - \frac{x^2+y^2}{2}, \frac{\sqrt{3}}{2}\left(x^2-y^2\right)\right], \quad T = [iyz, zx, ixy]. \tag{B.11}$$

The three invariants are simply $A\cdot A, E\cdot E$ and $T\cdot T$. Note that unlike for the elasticity tensor exemplified in Lax [325], we here do not have to distinguish between the left and right factors. Therefore, the quartic anisotropy energy is directly obtained as

$$\begin{aligned} W_4 &= a\left\{\left(M_z^2 - \frac{M_x^2+M_y^2}{2}\right)^2 + \frac{3}{4}\left(M_x^2-M_y^2\right)^2\right\} + b\left(M_x^2M_z^2+M_y^2M_z^2+M_x^2M_y^2\right) \\ &\quad + c\left(M^2\right)^2 \\ &= a\left(M_x^4+M_y^4+M_z^4\right) + (b-a)\left(M_x^2M_y^2+M_y^2M_z^2+M_z^2M_x^2\right) \end{aligned} \tag{B.12}$$

where in the second equality, $M^2 = \text{const}$ has been used to reduce the number of independent constants. In fact, the a and b terms can also be combined together by the same constraint so that there is in fact only one independent constant which we take to be $a : W_4 = a\left(M_x^4+M_y^4+M_z^4\right)$. This is the well-known formula of the cubic anisotropy.

The method of invariants also works well with D_{2d}. In this case, we have five basis sets

$$A = x^2+y^2, \quad A' = z^2, \quad B_1 = x^2-y^2, \quad B_2 = ixy, \quad E = [zx, zy] \tag{B.13}$$

The six invariants are again obvious: $A\cdot A, A'\cdot A', A\cdot A', B_1\cdot B_1, B_2\cdot B_2, E\cdot E$. One obtains

$$\begin{aligned} W_4 &= a\left(M_x^2+M_y^2\right)^2 + bM_z^4 + cM_z^2\left(M_x^2+M_y^2\right) + d\left(M_x^2-M_y^2\right)^2 + eM_x^2M_y^2 \\ &\quad + fM_z^2\left(M_x^2+M_y^2\right) \\ &= (a+d)\left(M_x^4+M_y^4\right) + bM_z^4 + (c+f)M_z^2\left(M_x^2+M_y^2\right) + (2a-2d+e)M_x^2M_y^2 \end{aligned} \tag{B.14}$$

Note that we ended up with fewer than six terms, which is a consequence of the extra index symmetries. The third term can be eliminated by using $M^2 = \text{const}$ and the final form is

$$W_4 = a\left(M_x^4+M_y^4\right) + bM_z^4 + cM_x^2M_y^2 \tag{B.15}$$

For C_{2v}, the method of direct inspection is probably faster since the generating elements in D_1 are simply

$$C_{2z} = \begin{pmatrix} -1 & 0 & 0 \\ 0 & -1 & 0 \\ 0 & 0 & 1 \end{pmatrix}, \quad \sigma_x = \begin{pmatrix} 1 & 0 & 0 \\ 0 & -1 & 0 \\ 0 & 0 & -1 \end{pmatrix} \tag{B.16}$$

Denoting the number of times x, y, z appear in $ijkl$ by $n_{x,y,z}$ respectively, one obtains the constraints

$$C_{2z}\left(L_{ijkl}\right) = (-1)^{n_x+n_y}L_{jikl}, \quad \sigma_x\left(L_{ijkl}\right) = (-1)^{n_y+n_z}L_{ijkl}. \tag{B.17}$$

Noting $n_x + n_y + n_z = 4$, one can conclude that all the terms that contain odd numbers of x and z vanish. This automatically excludes terms odd in x too, and the order of the indices does not matter. Therefore, the possible combinations are $(ijkl) = (xxxx), (yyyy), (zzzz), (xxyy), (yyzz), (zzxx)$. One can eliminate the terms

quadratic in z by the constraint $M^2 = \text{const}$, yielding

$$W_4 = aM_x^4 + bM_y^4 + cM_z^4 + dM_x^2M_y^2 \tag{B.18}$$

Again the number of independent terms is a lot smaller than nine.

B.2 Gilbert damping tensors

Characterisation of Gilbert damping anisotropy by point group symmetries is far less frequently carried out in the literature. To fix the requirements for the tensors, we take the strategy explained below.

We regard the phenomenological Landau-Lifshitz-Gilbert equation to be a Lagrangian dynamical system extended to allow for dissipative forces by Rayleigh. This in practice means that the Gilbert damping is derived from the Rayleigh dissipation function expanded in powers of M and M :

$$R = \frac{1}{2}\alpha_{ij}\dot{M}_i\dot{M}_j + \frac{1}{4}\beta_{ijkl}\dot{M}_i\dot{M}_jM_kM_l + \cdots \tag{B.19}$$

Note that we ignore terms of higher than second order in $\dot{M}$ since they are irrelevant in the linearised dynamics. A major question is whether terms odd in M are allowed or not. The dissipation function R generically breaks the time reversal symmetry by its nature so that it is not clear whether the time-reversal constraint should be applied here or not. We do not consider the odd terms in the following. Another point to remark is that this definition precludes certain types of damping tensors, for example anti-symmetric part of α_{ij} cannot be included.

With these caveats in mind, the symmetry analysis can be carried out analogously to the magnetic anisotropy. The form of the quadratic tensor α_{ij} is constrained in exactly the same way as K_{ij}. Differences appear for the quartic tensor β_{ijkl} however since the indices ij and kl refer to different quantities. Individual pairs have the symmetries $\beta_{jikl} = \beta_{ijkl}, \beta_{ijlk} = \beta_{ijkl}$, which means we can use Eqs. B.8 to

B.10 to see the upper limits of the number of independent constants as before, which are 3,7 and 12 for T_d, D_{2d} and C_{2v} respectively. For T_d, the method of invariants can be applied without modification and yields

$$\begin{aligned}
R_4 =& a\left\{\left(M_z^2-\frac{M_x^2+M_y^2}{2}\right)\left(\dot{M}_z^2-\frac{\dot{M}_x^2+\dot{M}_y^2}{2}\right)+\frac{3}{4}\left(M_x^2-M_y^2\right)\left(\dot{M}_x^2-\dot{M}_y^2\right)\right\}\\
&+b\left(M_xM_y\dot{M}_x\dot{M}_y+M_yM_z\dot{M}_y\dot{M}_z+M_zM_x\dot{M}_z\dot{M}_x\right)+cM^2\left(\dot{M}_x^2+\dot{M}_y^2+\dot{M}_z^2\right)\\
=&\frac{3a}{2}\left(M_x^2\dot{M}_x^2+M_y^2\dot{M}_y^2+M_z^2\dot{M}_z^2\right)\\
&+b\left(M_xM_y\dot{M}_x\dot{M}_y+M_yM_z\dot{M}_y\dot{M}_z+M_zM_x\dot{M}_z\dot{M}_x\right)
\end{aligned}\tag{B.20}$$

where the terms reduced to quadratic by the constraint $M^2 = \text{const}$ have been dropped. Similarly for D_{2d}, but $A\cdot A'$ and $A'\cdot A$ must be distinguished now:

$$\begin{aligned}
R_4 =& a\left(M_x^2+M_y^2\right)\left(\dot{M}_x^2+\dot{M}_y^2\right)+bM_z^2\dot{M}_z^2+cM_z^2\left(\dot{M}_x^2+\dot{M}_y^2\right)+d\left(M_x^2+M_y^2\right)\dot{M}_z^2\\
&+e\left(M_x^2-M_y^2\right)\left(\dot{M}_x^2-\dot{M}_y^2\right)+fM_xM_y\dot{M}_x\dot{M}_y+gM_z\dot{M}_z\left(M_x\dot{M}_x+M_y\dot{M}_y\right)\\
=&(c-a)M_z^2\left(\dot{M}_x^2+\dot{M}_y^2\right)+(b-d)M_z^2\dot{M}_z^2+e\left(M_x^2-M_y^2\right)\\
&+fM_xM_y\dot{M}_x\dot{M}_y+gM_z\dot{M}_z\left(M_x\dot{M}_x+M_y\dot{M}_y\right)
\end{aligned}\tag{B.21}$$

Again those reducible to quadratic terms have been discarded. Finally, the index constraint for C_{2v} is the same; the number of times x,y,z appear in $ijkl$ in β_{ijkl} must be even. But the combinatorics generates more possibilities since ij and kl are not equivalent;

$$\begin{aligned}
(ijkl) =&(xxxx),(yyyy),(zzzz),(xxyy),(yyxx),(xyxy),\\
&(yyzz),(zzyy),(yzyz),(zzxx),(xxzz),(zxzx)
\end{aligned}\tag{B.22}$$

Therefore one obtains

$$
\begin{aligned}
R_4 =& aM_x^2\dot{M}_x^2 + bM_y^2\dot{M}_y^2 + cM_z^2\dot{M}_z^2 + \zeta_1 M_x^2\dot{M}_y^2 + \zeta_2 M_y^2\dot{M}_x^2 + \zeta_3 M_x M_y \dot{M}_x \dot{M}_y \\
&+ \xi_1 M_y^2\dot{M}_z^2 + \xi_2 M_z^2\dot{M}_y^2 + \xi_3 M_y M_z \dot{M}_y \dot{M}_z + \eta_1 M_z^2\dot{M}_x^2 + \eta_2 M_x^2\dot{M}_z^2 \\
&+ \eta_3 M_z M_x \dot{M}_z \dot{M}_x \\
=& \left(\beta_{yx}M_y^2 + \beta_{zx}M_z^2\right)\dot{M}_x^2 + \left(\beta_{zy}M_z^2 + \beta_{xy}M_x^2\right)\dot{M}_y^2 + \left(\beta_{xz}M_x^2 + \beta_{yz}M_y^2\right)\dot{M}_z^2 \\
&+ \gamma_x M_y M_z \dot{M}_y \dot{M}_z + \gamma_y M_z M_x \dot{M}_z \dot{M}_x + \gamma_z M_x M_y \dot{M}_x \dot{M}_y
\end{aligned} \tag{B.23}
$$

In summary, the quartic Gilbert damping tensor has 2,5 and 9 independent components for T_d, D_{2d} and C_{2v} respectively.

Appendix C

Spin wave Mode Analysis in Synthetic Antiferromagnets

C.1 Parity and symmetry analysis of spin-wave modes in synthetic antiferromagnets

To discuss the parity of spin-wave modes in synthetic antiferromagnets (SyAFs), we start with Landau-Lifshitz-Gilbert equations with coupled magnetic moments ($\boldsymbol{m_1}$ and $\boldsymbol{m_2}$) by the antiferromagnetic exchange interaction with the strength of B_{ex}:

$$\frac{d\boldsymbol{m_1}}{dt} = -\gamma \boldsymbol{m_1} \times (\boldsymbol{B} - B_{\mathrm{ex}}\boldsymbol{m_2} - M_{\mathrm{s}}(\boldsymbol{m_1}\cdot\boldsymbol{e}_{\mathrm{z}})\boldsymbol{e}_{\mathrm{z}}) + \boldsymbol{\tau_1} \tag{C.1}$$

$$\frac{d\boldsymbol{m_2}}{dt} = -\gamma \boldsymbol{m_1} \times (\boldsymbol{B} - B_{\mathrm{ex}}\boldsymbol{m_1} - M_{\mathrm{s}}(\boldsymbol{m_2}\cdot\boldsymbol{e}_{\mathrm{z}})\boldsymbol{e}_{\mathrm{z}}) + \boldsymbol{\tau_2}. \tag{C.2}$$

Here, t, γ, $\boldsymbol{B}$, M_{s}, $\boldsymbol{e}_{\mathrm{z}}$ and $\boldsymbol{\tau}_{1(2)}$ are time, the gyromagnetic ratio, the external magnetic field vector, the saturation magnetisation, the unit vector along the film growth direction and excitation torques for $\boldsymbol{m_1}(\boldsymbol{m_2})$ respectively. For the sake of simplicity, we ignore the damping term to discuss the symmetry and parity of spin-wave modes in this section. We now substitute the static and dynamic components of $\boldsymbol{m_1}$ and $\boldsymbol{m_2}$ as $\boldsymbol{m_1} = \boldsymbol{m_1^0} + \delta\boldsymbol{m_1}e^{i\omega t}$ and $\boldsymbol{m_2} = \boldsymbol{m_2^0} + \delta\boldsymbol{m_2}e^{i\omega t}$ respectively. Substituting these into Eqs. C.1 and C.2 and focusing on the first-order terms of $e^{i\omega t}$, we have:

$$i\omega\delta\boldsymbol{m_1} = -\gamma\boldsymbol{m_1^0} \times (\boldsymbol{B}_{\mathrm{eq}}\delta\boldsymbol{m_1} - B_{\mathrm{ex}}\delta\boldsymbol{m_2} - M_{\mathrm{s}}(\delta\boldsymbol{m_1}\cdot\boldsymbol{e}_{\mathrm{z}})\boldsymbol{e}_{\mathrm{z}}) + \boldsymbol{\tau_1} \tag{C.3}$$

$$i\omega\delta\boldsymbol{m_2} = -\gamma\boldsymbol{m_2^0}\times(\boldsymbol{B}_{\rm eq}\delta\boldsymbol{m_2} - B_{\rm ex}\delta\boldsymbol{m_1} - M_{\rm s}(\delta\boldsymbol{m_2}\cdot\boldsymbol{e}_{\rm z})\boldsymbol{e}_{\rm z}) + \boldsymbol{\tau_2} \tag{C.4}$$

Here, $\boldsymbol{B}_{\rm eq}$ for $\boldsymbol{m_1}(\boldsymbol{m_2})$ is represented by $\boldsymbol{B} - B_{\rm ex}\cdot\boldsymbol{m}^{\boldsymbol{0}}_{2(1)}$. Using the parity of optical and acoustic modes where the former (latter) is even for π rotation (i.e. C_2 operation) about $\boldsymbol{B}$, we can select $\delta\boldsymbol{m}_{\rm op} = \delta\boldsymbol{m_1} + C_2\delta\boldsymbol{m_2}$ and $\delta\boldsymbol{m}_{\rm ac} = \delta\boldsymbol{m_1} - C_2\delta\boldsymbol{m_2}$ as new bases of the above coupled LLG equations to describe the optical and acoustic modes, respectively[266]. These modes are excited by the corresponding torque terms which can be obtained also by the linear combination of original torques acting on $\boldsymbol{m_1}$ and $\boldsymbol{m_2}$. These linearly-combined torques are given by $\boldsymbol{\tau}_{\rm op} = \boldsymbol{\tau_1} + C_2\boldsymbol{\tau_2}$ and $\boldsymbol{\tau}_{\rm ac} = \boldsymbol{\tau_1} - C_2\boldsymbol{\tau_2}$ respectively. We now examine these torques to associate with our experimental observation. The individual torques can be written as $\boldsymbol{\tau}_{\rm i} = \boldsymbol{m}^{\boldsymbol{0}}_{\rm i}\times\boldsymbol{B}_{\rm i} + \boldsymbol{m}^{\boldsymbol{0}}_{\rm i}\times(\boldsymbol{m}^{\boldsymbol{0}}_{\rm i}\times\boldsymbol{s}_{\rm i})$ (i = 1, 2) where the first and second terms are field-like and damping-like torques acting on each moment with $\boldsymbol{B}_{\rm i}$ being the effective field and $\boldsymbol{s}_{\rm i}$ being the spin polarisation of the spin-transfer torque. Using these we write:

$$\boldsymbol{\tau}_{\rm op} = \boldsymbol{m}^{\boldsymbol{0}}_1\times\boldsymbol{B}_1 + \boldsymbol{m}^{\boldsymbol{0}}_1\times(\boldsymbol{m}^{\boldsymbol{0}}_1\times\boldsymbol{s}_1) + C_2\{\boldsymbol{m}^{\boldsymbol{0}}_2\times\boldsymbol{B}_2 + \boldsymbol{m}^{\boldsymbol{0}}_2\times(\boldsymbol{m}^{\boldsymbol{0}}_2\times\boldsymbol{s}_2)\}; \tag{C.5}$$

$$\boldsymbol{\tau}_{\rm ac} = \boldsymbol{m}^{\boldsymbol{0}}_1\times\boldsymbol{B}_1 + \boldsymbol{m}^{\boldsymbol{0}}_1\times(\boldsymbol{m}^{\boldsymbol{0}}_1\times\boldsymbol{s}_1) - C_2\{\boldsymbol{m}^{\boldsymbol{0}}_2\times\boldsymbol{B}_2 + \boldsymbol{m}^{\boldsymbol{0}}_2\times(\boldsymbol{m}^{\boldsymbol{0}}_2\times\boldsymbol{s}_2)\}. \tag{C.6}$$

Anti-ferromagnets with two identical moments has the even parity under C_2 operation for the static regime, i.e. $\boldsymbol{m}^{\boldsymbol{0}}_{\boldsymbol{1}} = C_2\boldsymbol{m}^{\boldsymbol{0}}_{\boldsymbol{2}}$. Using this property, Eq. C.5 can be re-written as:

$$\boldsymbol{\tau}_{\rm op} = \boldsymbol{m}^{\boldsymbol{0}}_1\times(\boldsymbol{B}_1 + C_2\boldsymbol{B}_2) + \boldsymbol{m}^{\boldsymbol{0}}_1\times\{\boldsymbol{m}^{\boldsymbol{0}}_1\times(\boldsymbol{s}_1 + C_2\boldsymbol{s}_2)\}. \tag{C.7}$$

Likewise, we can obtain the torque expression for exciting the acoustic mode as:

$$\boldsymbol{\tau}_{\rm ac} = \boldsymbol{m}^{\boldsymbol{0}}_1\times(\boldsymbol{B}_1 - C_2\boldsymbol{B}_2) + \boldsymbol{m}^{\boldsymbol{0}}_1\times\{\boldsymbol{m}^{\boldsymbol{0}}_1\times(\boldsymbol{s}_1 - C_2\boldsymbol{s}_2)\}. \tag{C.8}$$

These two expressions represent the torque symmetry of each mode excitation against the external magnetic field direction which is the axis of the C_2 rotation.

When both moments are excited by uniform spin excitation, namely with the condition of $\boldsymbol{B}_1 = \boldsymbol{B}_2$ and $\boldsymbol{s}_1 = \boldsymbol{s}_2$, we can arrive at the following conclusions. (i) When $\boldsymbol{B}_1$ and $\boldsymbol{s}_1$ are symmetric for the C_2 rotation, $\boldsymbol{\tau}_{\rm op}$ is maximised ($\boldsymbol{B}_1 + C_2\boldsymbol{B}_2 = 2\boldsymbol{B}_1$) and $\boldsymbol{\tau}_{\rm ac} = 0$, and (ii) when When $\boldsymbol{B}_1$ and $\boldsymbol{s}_1$ are anti-symmetric for the C_2 rotation, $\boldsymbol{\tau}_{\rm op} = 0$ and $\boldsymbol{\tau}_{\rm ac}$ is largest. Here the meaning of $\boldsymbol{B}_1$ and $\boldsymbol{s}_1$ being symmetric (anti-symmetric) for the C_2 rotation is the condition of $\boldsymbol{B}_1 \| \boldsymbol{B}$ ($\boldsymbol{B}_1 \perp \boldsymbol{B}$) which is in general termed as parallel (perpendicular) pumping configuration in magnetic dynamics. Altogether we can summarise that under a uniform excitation condition, the optical (acoustic) mode can be excited by parallel (perpendicular) pumping configuration. In the present study, we take one step further to control the excitation symmetry by designing the local spin excitation configuration. When $\boldsymbol{m_1}$ and $\boldsymbol{m_2}$ experience non-uniform spin excitations, here we show that the perpendicular/parallel pumping nature can be tuned in our experiments. On the extreme case where $\boldsymbol{B}_1 = -\boldsymbol{B}_2$ and $\boldsymbol{s}_1 = -\boldsymbol{s}_2$, we can predict that the optical (acoustic) mode is excited by perpendicular (parallel) pumping configuration. This is because the odd-even parity of the spin excitation is changed, leading to the parity change of excited modes by the spin torques with the spatial symmetry.

C.2 Rectification voltages arising from acoustic and optical modes

Using the Kittel and Neel vector definitions ($\mathbf{m} = (\mathbf{m}_1 + \mathbf{m}_2)/2$ and $\mathbf{n} = (\mathbf{m}_1 - \mathbf{m}_2)/2$), we rewrite the LLG equations as:

$$\frac{d\mathbf{m}}{dt} = -\Omega_{\rm L}\mathbf{m}\times\boldsymbol{u} + \Omega_{\rm B}\left\{[\mathbf{m}\times(\mathbf{m}\cdot\mathbf{e}_{\rm z})\mathbf{e}_{\rm z}] + [\mathbf{n}\times(\mathbf{n}\cdot\mathbf{e}_{\rm z})\mathbf{e}_{\rm z}]\right\} + \alpha\left[\mathbf{m}\times\frac{d\mathbf{m}}{dt} + \mathbf{n}\times\frac{d\mathbf{n}}{dt}\right], \tag{C.9}$$

$$\frac{d\mathbf{n}}{dt} = -\Omega_{\rm L}\mathbf{n}\times\boldsymbol{u} + \Omega_{\rm B}\left\{[\mathbf{n}\times(\mathbf{m}\cdot\mathbf{e}_{\rm z})\mathbf{e}_{\rm z}] + [\mathbf{m}\times(\mathbf{n}\cdot\mathbf{e}_{\rm z})\mathbf{e}_{\rm z}]\right\} + 2\Omega_{ex}(\mathbf{n}\times\mathbf{m}) + \alpha\left[\mathbf{n}\times\frac{d\mathbf{m}}{dt} + \mathbf{m}\times\frac{d\mathbf{n}}{dt}\right]. \tag{C.10}$$

Here, $\Omega_{\mathrm{L}} = \gamma B$, $\Omega_{\mathrm{B}} = \gamma B_{\mathrm{S}}$ (where $B_{\mathrm{S}} = \mu_0 M_{\mathrm{s}}$) and $\Omega_{ex} = \gamma B_{ex}$ respectively and $\boldsymbol{u}$ is the unit vector along the direction of $\boldsymbol{B}$ which in our case is applied along the in-plane x direction ($\boldsymbol{u} = \mathbf{e}_{\mathrm{x}}$) as shown in Fig. C.1 - $\mathbf{e}_{\mathrm{i}}$ is the unit vector expression for each axis i. Vector components of $\mathbf{m}$ and $\mathbf{n}$ can be linearized as the following equations:

$$
\begin{aligned}
m_{\mathrm{x}}(t) &= m_{\mathrm{x0}} + \delta m_{\mathrm{x}}(t) + \cdots \\
&= \cos\phi_{\mathrm{c}} + \delta m_{\mathrm{x}}(t), && \text{(C.11)} \\
m_{\mathrm{y}}(t) &= m_{\mathrm{y0}} + \delta m_{\mathrm{y}}(t) + \cdots \\
&= \delta m_{\mathrm{y}}(t), && \text{(C.12)} \\
m_{\mathrm{z}}(t) &= m_{\mathrm{z0}} + \delta m_{\mathrm{z}}(t) + \cdots \\
&= \delta m_{\mathrm{z}}(t), && \text{(C.13)} \\
n_{\mathrm{x}}(t) &= n_{\mathrm{x0}} + \delta n_{\mathrm{x}}(t) + \cdots \\
&= \delta n_{\mathrm{x}}(t), && \text{(C.14)} \\
n_{\mathrm{y}}(t) &= n_{\mathrm{y0}} + \delta n_{\mathrm{y}}(t) + \cdots
\end{aligned}
$$

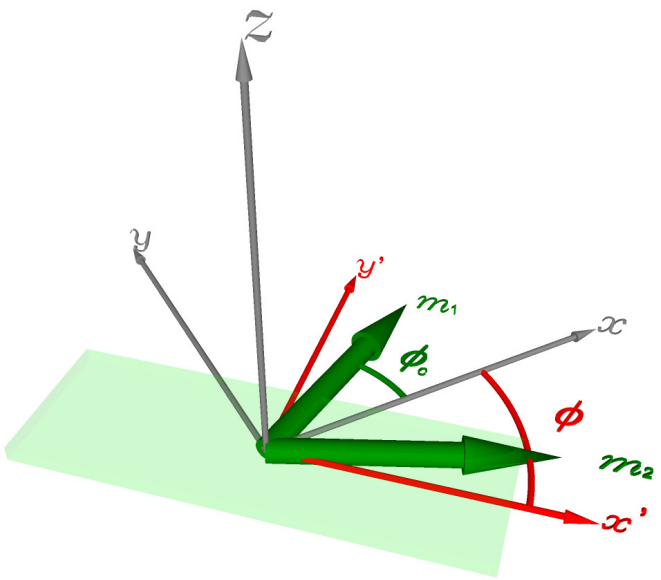

Figure C.1: A schematic of the coordinate system used in our macro-spin model. In this geometry, we have two Cartesian coordinate systems defined by the current flow (x') direction and the external magnetic field (x) direction. The angle between the two is defined by ϕ and the cant angle is defined by ϕ_{c}.

$$= \sin\phi_{\rm c} + \delta n_{\rm y}(t), \tag{C.15}$$

$$n_{\rm z}(t) = n_{\rm z0} + \delta n_{\rm z}(t) + \cdots$$

$$= \delta n_{\rm z}(t). \tag{C.16}$$

By using the linearization of Eqs. (C.9) and (C.10) and solving the first order term, where ($\delta m_{\rm y}$, $\delta m_{\rm z}$, $\delta n_{\rm x}$) and ($\delta m_{\rm x}$, $\delta n_{\rm y}$, $\delta n_{\rm z}$) are coupled and representing the motion of acoustic and optical modes respectively, we find the matrix form of two equations by using the Fourier transformation ($f(t) = \int_{-\infty}^{\infty} d\Omega f(\Omega)\exp(i\Omega t)/2\pi$) as:

$$\begin{pmatrix} i\Omega & i\alpha\Omega\cos\phi_{\rm c} + \Omega_{\rm B}\cos\phi_{\rm c} + \Omega_{\rm L} & 0 \\ -i\alpha\Omega\cos\phi_{\rm c} - \Omega_{\rm L} & i\Omega & i\alpha\Omega\sin\phi_{\rm c} \\ 0 & -i\alpha\Omega\sin\phi_{\rm c} - (2\Omega_{ex} + \Omega_B)\sin\phi_{\rm c} & i\Omega \end{pmatrix} \begin{pmatrix} \delta m_{\rm y} \\ \delta m_{\rm z} \\ \delta n_{\rm x} \end{pmatrix} = \boldsymbol{\tau}_{\rm m}, \tag{C.17}$$

$$\begin{pmatrix} i\Omega & 0 & -i\alpha\Omega\sin\phi_{\rm c} - \Omega_{\rm B}\sin\phi_{\rm c} \\ 0 & i\Omega & i\alpha\Omega\cos\phi_{\rm c} - (2\Omega_{ex} - \Omega_{\rm B})\cos\phi_{\rm c} + \Omega_{\rm L} \\ i\alpha\Omega\sin\phi_{\rm c} + 2\Omega_{ex}\sin\phi_{\rm c} & -i\alpha\Omega\cos\phi_{\rm c} - \Omega_{\rm L} + 2\Omega_{ex}\cos\phi_{\rm c} & i\Omega \end{pmatrix} \begin{pmatrix} \delta m_{\rm x} \\ \delta n_{\rm y} \\ \delta n_{\rm z} \end{pmatrix} = \boldsymbol{\tau}_{\rm n}. \tag{C.18}$$

The right hand side of the equations ($\boldsymbol{\tau}_{\rm m}, \boldsymbol{\tau}_{\rm n}$)are magnetic torques on each coupled moment to excite magnetisation dynamics. The complex resonance frequency for both modes ($\tilde{\Omega}_{\rm ac}$ and $\tilde{\Omega}_{\rm op}$) can be obtained by using the determinant of the 3×3 matrix in the left hand side as,

$$\tilde{\Omega}_{\rm ac} = \sqrt{\Omega_{\rm L}^2(1 + \frac{\Omega_{\rm B}}{2\Omega_{ex}})} + i\cdot\frac{1}{2}\alpha\left(\frac{\Omega_{\rm L}^2}{2\Omega_{ex}} + \Omega_{\rm B} + 2\Omega_{ex}\right), \tag{C.19}$$

$$\tilde{\Omega}_{\rm op} = \sqrt{\frac{\Omega_{\rm B}}{2\Omega_{ex}}\left(4\Omega_{ex}^2 - \Omega_{\rm L}^2\right)} + i\cdot\frac{1}{2}\alpha\left(\Omega_{\rm B} + \frac{1}{2\Omega_{ex}}(4\Omega_{ex}^2 - \Omega_{\rm L}^2)\right), \tag{C.20}$$

Here, the relation $\cos\phi_{\rm c} = \Omega_{\rm L}/2\Omega_{ex}$ is used. The real part of these equations represents the resonance field for each mode of SyAFs that we show in our main text. We

note that these equations are consistent with earlier work by Chiba *et al.* without considering the spin-pumping effect [277].

Now we consider current-induced torques and rectification voltages in the SyAF devices. We assume that an electric current $\boldsymbol{I}$ flows along the x' direction as defined in Fig. C.1. $\boldsymbol{B}$ is applied along the x direction from which we define ϕ with respect to the x' direction. In this coordinate, an Oersted field is generated along the y' direction, exerting torques ($\boldsymbol{\tau}_{\mathrm{Oe},1(2)}$) on $\boldsymbol{m_1}$ and $\boldsymbol{m_2}$ as

$$\begin{aligned}\boldsymbol{\tau}_{\mathrm{Oe},1(2)} &= \gamma B_{\mathrm{Oe},1(2)} \mathbf{m}_{1(2)} \times \mathbf{e}_{\mathrm{y}'} \\ &= \gamma B_{\mathrm{Oe},1(2)} \cos(\phi_{\mathrm{c}} + \phi) \mathbf{e}_{\mathrm{z}}. \end{aligned} \tag{C.21}$$

Here $B_{\mathrm{Oe},\,1(2)}$ can be approximated as $\mu_0 \eta_{\mathrm{asy}} I/2w$ with μ_0 and w being the permeability of free space and the width of the wire respectively. The parameter η_{asy} can be obtained by estimating currents flowing above and below the magnetic layers. When the stacking structure is symmetric, we have $B_{\mathrm{Oe},\,1} = -B_{\mathrm{Oe},\,2}$. Therefore, the torques acting on **m** and **n** in Eqs. (C.17) and (C.18) are obtained as:

$$\boldsymbol{\tau}_{\mathrm{m}} = \gamma \begin{pmatrix} 0 \\ -B_{\mathrm{Oe}} \sin\phi_{\mathrm{c}} \sin\phi \\ 0 \end{pmatrix}, \tag{C.22}$$

$$\boldsymbol{\tau}_{\mathrm{n}} = \gamma \begin{pmatrix} 0 \\ 0 \\ B_{\mathrm{Oe}} \cos\phi_{\mathrm{c}} \cos\phi \end{pmatrix}. \tag{C.23}$$

In addition to these torques, spin-transfer torques can be generated by the spin-Hall effect (SHE) from an adjacent nonmagnetic layer. Using our current direction which defines spin polarisation $\boldsymbol{\sigma}$ of the spin currents generated by the SHE as $\boldsymbol{\sigma} = \mathbf{e}_{\mathrm{y}'}$, we write the spin-transfer torques acting on two moments ($i = 1, 2$) as:

$$\boldsymbol{\tau}_{\mathrm{SHE,\,i}} = \gamma B_{\mathrm{SHE,\,i}} \left[\mathbf{m}_i \times (\mathbf{e}_{\mathrm{y}'} \times \mathbf{m}_i) \right], \tag{C.24}$$

where $B_{\mathrm{SHE,\,i}}$ is an effective magnetic field proportional to both I and the spin-Hall angle (θ_{SH}) with its magnitude B_{SHE} given as $B_{\mathrm{SHE}} = \hbar\eta_{\mathrm{Ta}}\theta_{\mathrm{SH}}I/2eM_{\mathrm{s}}wd_{\mathrm{FM}}d_{\mathrm{Ta}}$ where $\hbar$, η_{Ta}, e, M_{S}, d_{FM} and d_{Ta} refer to the reduced Planck's constant, shunt ratio of current in Ta layer(I_{Ta}/I), elementary charge, saturation magnetisation and thickness of the NiFe and Ta layers respectively.

In the symmetric sample stack case, the relationship of $B_{\mathrm{SHE},1} = -B_{\mathrm{SHE},2}$ is established, giving the torque expressions for both vectors as

$$\boldsymbol{\tau}_{\mathrm{SHE,\,m}} = \gamma \begin{pmatrix} -B_{\mathrm{SHE}} \sin\phi_{\mathrm{c}} \cos\phi_{\mathrm{c}} \sin\phi \\ 0 \\ B_{\mathrm{SHE}} \sin^2\phi_{\mathrm{c}} \sin\phi \end{pmatrix}, \tag{C.25}$$

$$\boldsymbol{\tau}_{\mathrm{SHE,\,n}} = \gamma \begin{pmatrix} -B_{\mathrm{SHE}} \sin\phi_{\mathrm{c}} \cos\phi_{\mathrm{c}} \cos\phi \\ B_{\mathrm{SHE}} \cos^2\phi_{\mathrm{c}} \cos\phi \\ 0 \end{pmatrix}. \tag{C.26}$$

By using Eqs. (C.17), (C.18), (C.22), (C.23), (C.25), (C.26) the expression for δm_y, δn_{x}, δm_x and δn_{y} can be written as:

$$\delta m_y = \frac{\gamma[(\Omega^2 B_{\mathrm{SHE}} \sin\phi_{\mathrm{c}} \cos\phi_{\mathrm{c}} \sin\phi) + i\cdot\Omega(\Omega_{\mathrm{L}} + \Omega_B \cos\phi_{\mathrm{c}})(B_{\mathrm{Oe}} \sin\phi_{\mathrm{c}} \sin\phi)]}{-i\Omega(-\Omega_{\mathrm{ac}} + i\cdot\delta_{\mathrm{ac}} - \Omega)(\Omega_{\mathrm{ac}} + i\cdot\delta_{\mathrm{ac}} - \Omega)} \tag{C.27}$$

$$\delta n_{\mathrm{x}} = \frac{\gamma[-\Omega_{\mathrm{L}}(\Omega_B + 2\Omega_{\mathrm{e}x})B_{\mathrm{SHE}} \sin^2\phi_{\mathrm{c}} \cos\phi_{\mathrm{c}} \sin\phi - i\Omega\cdot B_{\mathrm{Oe}}(\Omega_{\mathrm{B}} + 2\Omega_{\mathrm{e}x}) \sin^2\phi_{\mathrm{c}} \sin\phi]}{-i\Omega(-\Omega_{\mathrm{ac}} + i\cdot\delta_{\mathrm{ac}} - \Omega)(\Omega_{\mathrm{ac}} + i\cdot\delta_{\mathrm{ac}} - \Omega)} \tag{C.28}$$

$$\delta m_{\mathrm{x}} = \frac{\gamma[\Omega^2(B_{\mathrm{SHE}} \sin\phi_{\mathrm{c}} \cos\phi_{\mathrm{c}} \cos\phi + i\Omega\cdot B_{\mathrm{Oe}}\Omega_{\mathrm{B}} \sin\phi_{\mathrm{c}} \cos\phi_{\mathrm{c}} \cos\phi)]}{-i\Omega(-\Omega_{\mathrm{op}} + i\cdot\delta_{\mathrm{op}} - \Omega)(\Omega_{\mathrm{op}} + i\cdot\delta_{\mathrm{op}} - \Omega)} \tag{C.29}$$

$$\delta n_{\mathrm{y}} = \frac{\gamma[-\Omega^2 B_{\mathrm{SHE}} \cos^2\phi_{\mathrm{c}} \cos\phi - i\Omega\cdot B_{\mathrm{Oe}}\Omega_{\mathrm{B}} \cos^2\phi_{\mathrm{c}} \cos\phi]}{-i\Omega(-\Omega_{\mathrm{op}} + i\cdot\delta_{\mathrm{op}} - \Omega)(\Omega_{\mathrm{op}} + i\cdot\delta_{\mathrm{op}} - \Omega)} \tag{C.30}$$

Here, $\tilde{\Omega}_{\mathrm{ac}} = \pm\Omega_{\mathrm{ac}} + i\cdot\delta_{\mathrm{ac}}$, $\tilde{\Omega}_{\mathrm{op}} = \pm\Omega_{\mathrm{op}} + i\cdot\delta_{\mathrm{op}}$ are used. The above equations can be simplified by calculating residue at two poles $(-\Omega_{\mathrm{ac(op)}} + i\cdot\delta_{\mathrm{ac(op)}})$ and

$(\Omega_{\mathrm{ac(op)}} + i \cdot \delta_{\mathrm{ac(op)}})$ using the residue theorem given by:

$$Res(f,c) = \lim_{z \to +c} (z-c) f(c). \tag{C.31}$$

Thus, we obtain the simplified form which can be expressed as below:

$$\delta m_{\mathrm{y}}(\Omega) = \frac{\gamma}{\Omega_{\mathrm{ac}} + i \cdot \delta_{\mathrm{ac}} - \Omega} \cdot (a_{m_{\mathrm{y}}} + i \cdot b_{m_{\mathrm{y}}}) + \frac{\gamma}{-\Omega_{\mathrm{ac}} + i \cdot \delta_{\mathrm{ac}} - \Omega} \cdot (-a_{m_{\mathrm{y}}} + i \cdot b_{m_{\mathrm{y}}}),$$
$$\delta n_{\mathrm{x}}(\Omega) = \frac{\gamma}{\Omega_{\mathrm{ac}} + i \cdot \delta_{\mathrm{ac}} - \Omega} \cdot (a_{n_{\mathrm{x}}} + i \cdot b_{n_{\mathrm{x}}}) + \frac{\gamma}{-\Omega_{\mathrm{ac}} + i \cdot \delta_{\mathrm{ac}} - \Omega} \cdot (-a_{n_{\mathrm{x}}} + i \cdot b_{n_{\mathrm{x}}}),$$
$$\delta m_{\mathrm{x}}(\Omega) = \frac{\gamma}{\Omega_{\mathrm{op}} + i \cdot \delta_{\mathrm{op}} - \Omega} \cdot (a_{m_{\mathrm{x}}} + i \cdot b_{m_{\mathrm{x}}}) + \frac{\gamma}{-\Omega_{\mathrm{op}} + i \cdot \delta_{\mathrm{op}} - \Omega} \cdot (-a_{m_{\mathrm{x}}} + i \cdot b_{m_{\mathrm{x}}}),$$
$$\delta n_{\mathrm{y}}(\Omega) = \frac{\gamma}{\Omega_{\mathrm{ac}} + i \cdot \delta_{\mathrm{op}} - \Omega} \cdot (a_{n_{\mathrm{y}}} + i \cdot b_{n_{\mathrm{y}}}) + \frac{\gamma}{-\Omega_{\mathrm{ac}} + i \cdot \delta_{\mathrm{op}} - \Omega} \cdot (-a_{n_{\mathrm{y}}} + i \cdot b_{n_{\mathrm{y}}}).$$

The components a and b are given by,

$$a_{m_{\mathrm{y}}} = \frac{1}{2} B_{\mathrm{Oe}} \frac{\Omega_{\mathrm{ac}}}{\Omega_{\mathrm{L}}} \sin\phi_{\mathrm{c}} \sin\phi, \tag{C.32}$$
$$b_{m_{\mathrm{y}}} = -\frac{1}{2} B_{\mathrm{SHE}} \cos\phi_{\mathrm{c}} \sin\phi_{\mathrm{c}} \sin\phi, \tag{C.33}$$
$$a_{n_{\mathrm{x}}} = -\frac{1}{2\Omega_{\mathrm{ac}}} B_{\mathrm{Oe}} (\Omega_{\mathrm{B}} + 2\Omega_{\mathrm{e}x}) \sin^2\phi_{\mathrm{c}} \sin\phi, \tag{C.34}$$
$$b_{n_{\mathrm{x}}} = \frac{1}{2} B_{\mathrm{SHE}} \frac{\Omega_{\mathrm{L}} (\Omega_{\mathrm{B}} + 2\Omega_{\mathrm{e}x})}{\Omega_{\mathrm{ac}}^2} \sin^2\phi_{\mathrm{c}} \cos\phi_{\mathrm{c}} \sin\phi, \tag{C.35}$$
$$a_{m_{\mathrm{x}}} = \frac{1}{2} B_{\mathrm{Oe}} \frac{\Omega_{\mathrm{B}}}{\Omega_{\mathrm{op}}} \sin\phi_{\mathrm{c}} \cos\phi_{\mathrm{c}} \cos\phi, \tag{C.36}$$
$$b_{m_{\mathrm{x}}} = -\frac{1}{2} B_{\mathrm{SHE}} \sin\phi_{\mathrm{c}} \cos\phi_{\mathrm{c}} \cos\phi, \tag{C.37}$$
$$a_{n_{\mathrm{y}}} = -\frac{1}{2} B_{\mathrm{Oe}} \frac{\Omega_{\mathrm{B}}}{\Omega_{\mathrm{op}}} \cos^2\phi_{\mathrm{c}} \cos\phi, \tag{C.38}$$
$$b_{n_{\mathrm{y}}} = \frac{1}{2} B_{\mathrm{SHE}} \cos^2\phi_{\mathrm{c}} \cos\phi. \tag{C.39}$$

Eqs. (C.32) – (C.35) are the amplitude for acoustic mode, which are proportional to $\sin\phi$. Eqs. (C.36) – (C.39) are the amplitude for optical mode, which are proportional to $\cos\phi$. These essentially represent the torque symmetry we focus on our study.

The components B_{Oe} and B_{SHE} are both proportional to an injected current I into our

devices, which has the time-varying form of $I(t) = I_0 \cos(\omega t)$. This time-varying current in our device produces magnetisation dynamics which causes another time-varying component in resistance due to AMR. As a result, there is a time-averaging component $< \Delta R(t) \cdot I(t) >$ when these two are mixed, which we measure in our homodyne detection approach [285, 288, 114]. A resistance change due to AMR has the following general form and we expand these for finding first-order time-varying components in both **m** and **n**:

$$\begin{aligned}
\Delta R(t) &= \frac{1}{4}\Delta R_{\mathrm{A}MR}\left[(\mathbf{m}_1 \cdot \mathbf{e}_{\mathrm{x}'})^2 + (\mathbf{m}_2 \cdot \mathbf{e}_{\mathrm{x}'})^2\right] \\
&= \frac{1}{2}\Delta R_{\mathrm{A}MR}\left(\cos^2\phi\,(m_{\mathrm{x}}^2 + n_{\mathrm{x}}^2) + \sin^2\phi\,(m_{\mathrm{y}}^2 + n_{\mathrm{y}}^2)\right. \\
&\qquad \left. -2\sin\phi\cos\phi\,(m_{\mathrm{x}}m_{\mathrm{y}} + n_{\mathrm{x}}n_{\mathrm{y}})\right) \\
&= \Delta R_{\mathrm{A}MR}\left(\cos^2\phi\cos\phi_{\mathrm{c}}\delta m_{\mathrm{x}}(t)\right. \\
&\quad \left. + \sin^2\phi\sin\phi_{\mathrm{c}}\delta n_{\mathrm{y}}(t) - \sin\phi\cos\phi\,(\cos\phi_{\mathrm{c}}\delta m_{\mathrm{y}}(t) + \sin\phi_{\mathrm{c}}\delta n_{\mathrm{x}}(t))\right) + \cdots .
\end{aligned} \tag{C.40}$$

Equations (C.32) to (C.40) allow to find the analytical expression of rectification voltages we measure in our SyAF devices. The anti-symmetric amplitude for the acoustic mode ($V_{\mathrm{asy}}^{\mathrm{ac}}$) can be derived as,

$$\begin{aligned}
V_{\mathrm{asy}}^{\mathrm{ac}} &= \frac{\gamma\Delta R_{\mathrm{A}MR}}{2\delta_{\mathrm{ac}}} I_0^2 \cdot \frac{d}{dI}\left(a_{m_{\mathrm{y}}}\cos\phi_{\mathrm{c}}\sin\phi\cos\phi + a_{n_{\mathrm{x}}}\sin\phi_{\mathrm{c}}\sin\phi\cos\phi\right) \\
&= -\frac{\gamma\Delta R_{\mathrm{A}MR}}{4\Delta B_{\mathrm{ac}}(d\Omega_{\mathrm{ac}}/dB)} I_0^2 \cdot \frac{dB_{\mathrm{Oe}}}{dI}\sin^2\phi\cos\phi\left(-\frac{\Omega_{\mathrm{ac}}}{\Omega_{\mathrm{L}}}\sin\phi_{\mathrm{c}}\cos\phi_{\mathrm{c}}\right. \\
&\quad \left. + \frac{\Omega_{\mathrm{B}} + 2\Omega_{\mathrm{e}x}}{\Omega_{\mathrm{ac}}}\sin^3\phi_{\mathrm{c}}\right) \\
&= \frac{\Delta R_{\mathrm{A}MR}}{8\Delta B_{\mathrm{ac}}} I_0 B_{\mathrm{Oe}} \tan\phi_{\mathrm{c}}\cos 2\phi_{\mathrm{c}}\sin 2\phi\sin\phi .
\end{aligned} \tag{C.41}$$

Here, the linewidth δ_{ac} is converted to field-swept linewidth ΔB_{ac} using the relation $\delta_{\mathrm{ac}} = (d\Omega_{\mathrm{ac}}/dB)\Delta B_{\mathrm{ac}}$, where $d\Omega_{\mathrm{ac}}/dB$ is given by $\gamma\sqrt{1 + B_{\mathrm{S}}/(2B_{\mathrm{e}x})}$. The relations $\cos\phi_{\mathrm{c}} = \Omega_{\mathrm{L}}/(2\Omega_{\mathrm{e}x})$, $\Omega_{\mathrm{ac}} = \Omega_{\mathrm{L}}\sqrt{1 + \Omega_{\mathrm{B}}/(2\Omega_{\mathrm{e}x})}$ are used. Likewise, the symmetric

amplitude for the acoustic mode $V_{\rm sym}^{\rm ac}$ is given as:

$$\begin{aligned} V_{\rm sym}^{\rm ac} &= \frac{\gamma\Delta R_{AMR}}{2\delta_{\rm ac}} I_0^2 \cdot \frac{d}{dI}\left(b_{m_{\rm y}} \cos\phi_{\rm c} \sin\phi\cos\phi + b_{n_{\rm x}} \sin\phi_{\rm c} \sin\phi\cos\phi\right) \\ &= -\frac{\gamma\Delta R_{AMR}}{4\Delta B_{\rm ac}(d\Omega_{\rm ac}/dB)} I_0^2 \cdot \frac{dB_{\rm SHE}}{dI} \sin^2\phi\cos\phi\left(\sin\phi_{\rm c}\cos^2\phi_{\rm c} - \sin^3\phi_{\rm c}\right) \\ &= -\frac{\Delta R_{AMR}}{8\Delta B_{\rm ac}\sqrt{1+B_{\rm S}/(2B_{ex})}} I_0 B_{\rm SHE} \sin\phi_{\rm c}\cos 2\phi_{\rm c}\sin 2\phi\sin\phi. \end{aligned} \tag{C.42}$$

Using the relationships of $B_{\rm S} = \mu_0 M_{\rm s}$ and $P_{\rm input} = I_0^2 R_{\rm sample}/C_0$, we can find Eq. (4) in the main text. The symmetric and anti-symmetric amplitudes for the optical mode ($V_{\rm sym}^{\rm op}$ and $V_{\rm asy}^{\rm op}$) are:

$$\begin{aligned} V_{\rm sym}^{\rm op} &= \frac{\gamma\Delta R_{AMR}}{2\delta_{\rm op}} I_0^2 \cdot \frac{d}{dI}\left(b_{m_{\rm x}} \cos\phi_{\rm c}\cos^2\phi + b_{n_{\rm y}} \sin\phi_{\rm c}\sin^2\phi\right) \\ &= -\frac{\gamma\Delta R_{AMR}}{4\Delta B_{\rm op}(d\Omega_{\rm op}/dB)} I_0^2 \cdot \frac{dB_{\rm SHE}}{dI} \cos^2\phi_{\rm c}\sin\phi_{\rm c}\left(\cos^3\phi - \cos\phi\sin^2\phi\right) \\ &= -\frac{\Delta R_{AMR}}{8\Delta B_{\rm op}(\Omega_{\rm B}\cdot\cos\phi_{\rm c}/\Omega_{\rm op})} I_0^2 \frac{dB_{\rm SHE}}{dI} \sin 2\phi_{\rm c}\cos\phi_{\rm c}\cos 2\phi\cos\phi \\ &= -\frac{\Delta R_{AMR}}{8\Delta B_{\rm op}} \sqrt{\frac{2B_{ex}}{B_{\rm S}}} I_0 B_{\rm SHE} \sin 2\phi_{\rm c}\sin\phi_{\rm c}\cos 2\phi\cos\phi. \end{aligned} \tag{C.43}$$

.

$$\begin{aligned} V_{\rm asy}^{\rm op} &= \frac{\gamma\Delta R_{AMR}}{2\delta_{\rm op}} I_0^2 \cdot \frac{d}{dI}\left(a_{m_{\rm x}} \cos\phi_{\rm c}\cos^2\phi + a_{n_{\rm y}} \sin\phi_{\rm c}\sin^2\phi\right) \\ &= \frac{\gamma\Delta R_{AMR}}{4\Delta B_{\rm op}(d\Omega_{\rm op}/dB)} I_0^2 \cdot \frac{dB_{\rm Oe}}{dI} \cdot \frac{\Omega_{\rm B}}{\Omega_{\rm op}} \cos^2\phi_{\rm c}\sin\phi_{\rm c}\left(\cos^3\phi - \cos\phi\sin^2\phi\right) \\ &= \frac{\Delta R_{AMR}}{8\Delta B_{\rm op}(\Omega_{\rm B}\cdot\cos\phi_{\rm c}/\Omega_{\rm op})} I_0^2 \frac{dB_{\rm Oe}}{dI} \cdot \frac{\Omega_{\rm B}}{\Omega_{\rm op}} \sin 2\phi_{\rm c}\cos\phi_{\rm c}\cos 2\phi\cos\phi \\ &= \frac{\Delta R_{AMR}}{8\Delta B_{\rm op}} I_0 B_{\rm Oe} \sin 2\phi_{\rm c}\cos 2\phi\cos\phi. \end{aligned} \tag{C.44}$$

Here, we used the relation $\Omega_{\rm op} = \sqrt{\frac{\Omega_{\rm B}}{2\Omega_{ex}}(4\Omega_{ex}^2 - \Omega_{\rm L}^2)}$ to convert frequency swept linewidth $\delta_{\rm op}$ to field swept linewidth $\Delta B_{\rm op}$.

Appendix D

Solutions of the coupled LLG equation

D.1 The eigenvalue problem and analytical expressions

In this section, the two-coupled Landau-Lifshitz-Gilbert (LLG) equations at the macrospin limit are employed to model magnetic dynamics of optical and acoustic modes in SyAFs. We recognise that similar approaches have been taken by others previously [228, 233, 211] but not specifically for magnon-magnon coupling phenomena in SyAFs as we detail below. We consider a canted regime of two individual moments ($\boldsymbol{m}_1$ and $\boldsymbol{m}_2$) which are coupled antiferromagnetically by the exchange interaction with the strength of B_{ex}. These two moments reside in thin-film magnets subjected to a demagnetisation field B_{s} and we apply an external magnetic field $\boldsymbol{B}$ within the x-z plane with angle θ_{B} from the z axis which is the sample growth direction in our case. Following convention, we first define Kittel and Neel vectors as $\boldsymbol{m} = (\boldsymbol{m}_1 + \boldsymbol{m}_2)/2$ and $\boldsymbol{n} = (\boldsymbol{m}_1 - \boldsymbol{m}_2)/2$, respectively. Dynamics of these two coupled moments are given by [233]:

$$\frac{d\boldsymbol{m}}{dt} = -\Omega_{\mathrm{L}}\boldsymbol{m}\times\boldsymbol{u} + \Omega_{\mathrm{B}}\left[(\boldsymbol{m}\cdot\boldsymbol{z})\,\boldsymbol{m}\times\boldsymbol{z} + (\boldsymbol{n}\cdot\boldsymbol{z})\,\boldsymbol{n}\times\boldsymbol{z}\right] + \boldsymbol{\tau}_{\mathrm{m}}, \tag{D.1}$$

$$\frac{d\boldsymbol{n}}{dt} = -\Omega_{\mathrm{L}}\boldsymbol{n}\times\boldsymbol{u} + \Omega_{\mathrm{B}}\left[(\boldsymbol{m}\cdot\boldsymbol{z})\,\boldsymbol{n}\times\boldsymbol{z} + (\boldsymbol{n}\cdot\boldsymbol{z})\,\boldsymbol{m}\times\boldsymbol{z}\right] + 2\Omega_{\mathrm{ex}}\boldsymbol{n}\times\boldsymbol{m} + \boldsymbol{\tau}_{\mathrm{n}}. \tag{D.2}$$

Here, $\Omega_{\mathrm{L}} = \gamma B_0$, $\Omega_{\mathrm{B}} = \gamma B_{\mathrm{s}}$, and $\Omega_{\mathrm{ex}} = \gamma B_{\mathrm{ex}}$ where γ and B_0 are the gyromagnetic ratio and the resonance field, respectively; $\boldsymbol{u} = \sin\theta_{\mathrm{B}}\boldsymbol{x} + \cos\theta_{\mathrm{B}}\boldsymbol{z}$ represents the applied field direction in the x-z plane, given that $\boldsymbol{x}$ and $\boldsymbol{z}$ are unit vectors for the corresponding axes. The last terms in Eqs. D.1 and D.2 account for damping torques which are expressed as:

$$\boldsymbol{\tau}_{\mathrm{m}} = \alpha_0 \left(\boldsymbol{m} \times \frac{d\boldsymbol{m}}{dt} + \boldsymbol{n} \times \frac{d\boldsymbol{n}}{dt} \right), \tag{D.3}$$

$$\begin{aligned} \boldsymbol{\tau}_n = {} & \left(\alpha_0 + \alpha_{\mathrm{sp}}\right) \left(\boldsymbol{m} \times \frac{d\boldsymbol{n}}{dt} + \boldsymbol{n} \times \frac{d\boldsymbol{m}}{dt} \right) \\ & - \alpha_{\mathrm{sp}} \left[\boldsymbol{m} \cdot \left(\boldsymbol{n} \times \frac{d\boldsymbol{m}}{dt} \right) \frac{\boldsymbol{m}}{m^2} + \boldsymbol{n} \cdot \left(\boldsymbol{m} \times \frac{d\boldsymbol{n}}{dt} \right) \frac{\boldsymbol{n}}{n^2} \right], \end{aligned} \tag{D.4}$$

where α_0 and α_{sp} are the standard Gilbert damping constant and one arising from mutual spin pumping between the two magnetic layers. With approximation of small angle precession, we can separate the equilibrium ($\boldsymbol{m_0}$ and $\boldsymbol{n_0}$) and time-dependent ($\delta\boldsymbol{m}(t)$ and $\delta\boldsymbol{n}(t)$) terms as: $\boldsymbol{m}(t) = \boldsymbol{m_0} + \delta\boldsymbol{m}(t)$ and $\boldsymbol{n}(t) = \boldsymbol{n_0} + \delta\boldsymbol{n}(t)$ and here we define each vector component in a standard manner, *e.g.* $\boldsymbol{m_0} = (m_{0\mathrm{x}}, m_{0\mathrm{y}}, m_{0\mathrm{z}})$. Substituting $\boldsymbol{m}(t)$ and $\boldsymbol{n}(t)$ into Eqs. D.1 to D.4 and keeping the first order of the time-dependent and damping terms, we obtain the following six coupled equations:

$$\frac{1}{\Omega_{\mathrm{y}'}} \frac{d\delta m_{\mathrm{x}}}{dt} = n_{0\mathrm{y}}\delta n_{\mathrm{z}} - \alpha_0\eta \left(m_{0\mathrm{z}}^2 + n_{0\mathrm{y}}^2\right) \delta m_{\mathrm{x}} - \eta m_{0\mathrm{z}}\delta m_{\mathrm{y}} + \alpha_0(\eta+1) m_{0\mathrm{x}} m_{0\mathrm{z}} \delta m_{\mathrm{z}}, \tag{D.5}$$

$$\frac{1}{\Omega_B} \frac{d\delta m_{\mathrm{y}}}{dt} = \alpha_0 m_{0\mathrm{z}} n_{0\mathrm{y}} \delta n_{\mathrm{z}} + \eta m_{0\mathrm{z}} \delta m_x - \alpha_0 \eta m_0^2 \delta m_y - (\eta+1) m_{0\mathrm{x}} \delta m_{\mathrm{z}}, \tag{D.6}$$

$$\frac{1}{\Omega_B} \frac{d\delta m_{\mathrm{z}}}{dt} = \alpha_0 \eta m_{0\mathrm{x}} m_{0\mathrm{z}} \delta m_x + \eta m_{0\mathrm{x}} \delta m_y - \alpha_0(\eta+1) \left(m_{0x}^2 + n_{0\mathrm{y}}^2\right) \delta m_{\mathrm{z}}. \tag{D.7}$$

$$\begin{aligned} \frac{1}{\Omega_B} \frac{d\delta n_{\mathrm{x}}}{dt} = {} & (\alpha_0 + \alpha_{\mathrm{sp}}) m_{0\mathrm{x}} m_{0\mathrm{z}} \delta n_{\mathrm{z}} + \alpha_0 \eta n_{0\mathrm{y}} m_{0\mathrm{x}} \delta m_y + (\eta+1) n_{0\mathrm{y}} \delta m_{\mathrm{z}} \\ & + \alpha_{\mathrm{sp}} \frac{m_{0\mathrm{z}} m_{0\mathrm{x}} n_{0\mathrm{y}}^2}{m_0^2} \delta n_{\mathrm{z}}, \end{aligned} \tag{D.8}$$

$$\frac{1}{\Omega_B} \frac{d\delta n_{\mathrm{y}}}{dt} = -m_{0\mathrm{x}} \delta n_{\mathrm{z}} + \alpha_0 \eta m_{0\mathrm{x}} n_{0\mathrm{y}} \delta m_{\mathrm{x}} + \alpha_0(\eta+1) m_{0\mathrm{z}} n_{0\mathrm{y}} \delta m_{\mathrm{z}}, \tag{D.9}$$

$$\begin{aligned} \frac{1}{\Omega_B} \frac{d\delta n_{\mathrm{z}}}{dt} = {} & -\left(\alpha_0 + \alpha_{\mathrm{sp}}\right) \left(\left(m_{0x}^2 + n_{0\mathrm{y}}^2\right) \delta n_{\mathrm{z}} - \eta n_{0\mathrm{y}} \delta m_{\mathrm{x}} + \alpha_0 \eta m_{0\mathrm{z}} n_{0\mathrm{y}} \delta m_{\mathrm{y}} \right. \end{aligned}$$

$$+\alpha_{\rm sp}\frac{m_{0\rm z}^2 n_{0\rm y}^2}{m_0^2}\delta n_{\rm z}, \tag{D.10}$$

where the equilibrium conditions and a new parameter η are introduced: $\boldsymbol{m_0} = (m_{0\rm x}, 0, m_{0\rm z})$, $\boldsymbol{n_0} = (0, n_{0\rm y}, 0)$ and $\eta = 2\Omega_{ex}/\Omega_B$. Further simplification has been made by using additional parameter definitions as well as time derivative treatment:

$$\nu_{\rm o1} = (\alpha_0 + \alpha_{\rm sp})\left(m_{0\rm x}^2 + n_{0\rm y}^2\right) - \alpha_{\rm sp}\frac{m_{0\rm z}^2 n_{0\rm y}^2}{m_0^2} \tag{D.11}$$

$$\nu_{\rm o2} = \alpha_0\eta\left(m_{0\rm z}^2 + n_{0\rm y}^2\right), \tag{D.12}$$

$$\nu_{\rm a1} = \alpha_0\eta m_0^2, \tag{D.13}$$

$$\nu_{\rm a2} = \alpha_0(\eta+1)\left(m_{0\rm x}^2 + n_{0\rm y}^2\right), \tag{D.14}$$

$$\frac{1}{\Omega_{\rm y'}}\frac{d}{dt} \to -i\frac{\omega}{\Omega_{\rm y'}} \equiv -i\Omega. \tag{D.15}$$

These produce the following equations of motion for $\delta m_{\rm x}$, $\delta m_{\rm y}$, $\delta m_{\rm z}$ and $\delta n_{\rm z}$:

$$-i\Omega\delta m_{\rm x} = n_{0\rm y}\delta n_{\rm z} - \nu_{\rm o2}\delta m_{\rm x} - \eta m_{0\rm z}\delta m_{\rm y} + \alpha_0(\eta+1)m_{0\rm x}m_{0\rm z}\delta m_{\rm z}, \tag{D.16}$$

$$-i\Omega\delta m_{\rm y} = \alpha_0 m_{0\rm z}n_{0\rm y}\delta n_{\rm z} + \eta m_{0\rm z}\delta m_x - \nu_{\rm a1}\delta m_y - (\eta+1)m_{0\rm x}\delta m_{\rm z}, \tag{D.17}$$

$$-i\Omega\delta m_{\rm z} = \alpha_0\eta m_{0\rm x}m_{0\rm z}\delta m_x + \eta m_{0\rm x}\delta m_y - \nu_{\rm a2}\delta m_{\rm z}, \tag{D.18}$$

$$-i\Omega\delta n_{\rm z} = -\nu_{\rm o1}\delta n_{\rm z} - \eta n_{0\rm y}\delta m_{\rm x} + \alpha_0\eta m_{0\rm z}n_{0\rm y}\delta m_{\rm y}. \tag{D.19}$$

We write these as a matrix form as follows.

$$\Omega\begin{pmatrix}\delta n_{\rm z}\\ \delta m_{\rm x}\\ \delta m_{\rm y}\\ \delta m_{\rm z}\end{pmatrix} = i\begin{pmatrix} -\nu_{\rm o1} & -\eta n_{0\rm y} & \alpha_0\eta m_{0\rm z}n_{0\rm y} & 0\\ n_{0\rm y} & -\nu_{\rm o2} & -\eta m_{0\rm z} & \alpha_0(\eta+1)m_{0\rm x}m_{0\rm z}\\ \alpha_0 m_{0\rm z}n_{0\rm y} & \eta m_{0\rm z} & -\nu_{\rm a1} & -(\eta+1)m_{0\rm x}\\ 0 & \alpha_0\eta m_{0\rm x}m_{0\rm z} & \eta m_{0\rm x} & -\nu_{\rm a2}\end{pmatrix}\begin{pmatrix}\delta n_{\rm z}\\ \delta m_{\rm x}\\ \delta m_{\rm y}\\ \delta m_{\rm z}\end{pmatrix} \tag{D.20}$$

We can obtain the eigen mode frequency $\omega_{op/ac}$ and relaxation time $\tau_{op/ac}$ by solving the complex eigenvalue problem, which can be expressed as,

$$\Omega_{\rm op(ac)} = \frac{1}{\Omega_{\rm y'}}(\omega_{\rm op(ac)} - i\tau_{\rm op(ac)}^{-1}). \tag{D.21}$$

If we neglected damping terms in the off-diagonal components, we obtained the following relations:

$$\delta n_{\mathrm{z}} \sim -\frac{\eta n_{0\mathrm{y}}}{-i\Omega+\nu_{\mathrm{o1}}}\delta m_{\mathrm{x}}. \tag{D.22}$$

$$\delta m_{\mathrm{z}} \sim \frac{\eta m_{0\mathrm{x}}}{-i\Omega+\nu_{\mathrm{a2}}}\delta m_{\mathrm{y}}, \tag{D.23}$$

Using these relations, we reduced Eq. D.20 into an eigenvalue problem with a 2-by-2 matrix form given by:

$$\begin{pmatrix} \Omega^2-\Omega_{\mathrm{op}}^2+i(\nu_{\mathrm{o1}}+\nu_{\mathrm{o2}})\Omega & -(-i\Omega+\nu_{\mathrm{o1}})\,\eta m_{0\mathrm{z}} \\ (-i\Omega+\nu_{\mathrm{a2}})\,\eta m_{0\mathrm{z}} & \Omega^2-\Omega_{ac}^2+i(\nu_{\mathrm{a1}}+\nu_{\mathrm{a2}})\Omega \end{pmatrix} \begin{pmatrix} \delta m_{\mathrm{x}} \\ \delta m_{\mathrm{y}} \end{pmatrix} = 0 \tag{D.24}$$

During this process, we disregarded higher-order terms in the diagonal elements, such as $\nu_{\mathrm{o1}}\nu_{\mathrm{o2}}$. This is the matrix we show in the main text after converting Ω into ω using Eq. D.21. Here, Ω_{op} and Ω_{ac} are the eigen frequencies for optical mode and acoustic modes given by:

$$\Omega_{\mathrm{op}} = n_{0\mathrm{y}}\sqrt{\eta} - i\frac{1}{2}\left(\nu_{\mathrm{o1}}+\nu_{\mathrm{o2}}\right), \tag{D.25}$$

$$\Omega_{\mathrm{ac}} = \sqrt{\eta^2+\eta}\,m_{0\mathrm{x}} - i\frac{1}{2}\left(\nu_{\mathrm{a1}}+\nu_{\mathrm{a2}}\right). \tag{D.26}$$

Eqs. 5.3 and 5.4 in Chapter 5 can be obtained by the real part of these two equations by using the equilibrium conditions: $(m_{0\mathrm{x}}, m_{0\mathrm{y}}, m_{0\mathrm{z}}) = (B_0 \sin\theta_{\mathrm{B}}/2B_{\mathrm{ex}}, 0, B_0\cos\theta_{\mathrm{B}}/(B_{\mathrm{s}}+2B_{\mathrm{ex}}))$ and $(n_{0\mathrm{x}}, n_{0\mathrm{y}}, n_{0\mathrm{z}}) = (0, \sqrt{1-m_{0x}^2-m_{0z}^2}, 0)$ with $\theta_{\mathrm{B}} = \pi/2$. We note here that our numerical solutions of Eq. D.20 and D.24 are almost identical. In order to find the expression for coupling constant g_{c} , we further take out the damping terms and solved the following eigen problem.

$$\begin{pmatrix} \Omega^2-\Omega_{\mathrm{op}}^2 & i\Omega\eta m_{0\mathrm{z}} \\ -i\Omega\eta m_{0\mathrm{z}} & \Omega^2-\Omega_{\mathrm{ac}}^2 \end{pmatrix} \begin{pmatrix} \delta m_{\mathrm{x}} \\ \delta m_{\mathrm{y}} \end{pmatrix} = 0 \tag{D.27}$$

$$\left(\Omega^2-\Omega_{\mathrm{op}}^2\right)\left(\Omega^2-\Omega_{\mathrm{ac}}^2\right)-\Omega^2(\eta m_{0\mathrm{z}})^2=0 \tag{D.28}$$

By defining the crossing (dimensionless) frequency as $\Omega_{\mathrm{op}}=\Omega_{\mathrm{ac}}=\Omega_0$, we can find the energy gap ($\Delta\Omega_{\mathrm{gap}}$) using Eq. (S32).

$$\Delta\Omega_{\mathrm{gap}}{=}2(\Omega{-}\Omega_0)=\pm\frac{2\Omega}{\Omega+\Omega_0}\eta m_{0\mathrm{z}}\simeq\pm\eta m_{0\mathrm{z}}, \tag{D.29}$$

Therefore,

$$g_{\mathrm{c}}=\frac{1}{2}\Delta\Omega_{\mathrm{gap}}\gamma B_{\mathrm{s}}=\frac{\gamma B_{\mathrm{ex}}B_0}{2B_{\mathrm{s}}+4B_{\mathrm{ex}}}\cos\theta_{\mathrm{B}} \tag{D.30}$$

Note that this is only valid when $\Delta\Omega_{\mathrm{gap}}{\ll}\Omega_{_0}$.

Appendix E

Dynamics in Synthetic Ferrimagnets

In this appendix we investigate the classical dynamics of multilayer synthetic ferrimagnets (SyF). We consider two ferromagnetic layers coupled through a metallic spacer layer via RKKY exchange interactions. The two magnetic layers are allowed to have different thicknesses. In SyFs due to large intralayer nearest neighbour exchange the macrospin model is employed to study the dynamics. Let $\boldsymbol{M}_{\mathrm{A,B}}$ be the magnetizations for the respective layers, and normalised magnetization is given as $\boldsymbol{n}_{\mathrm{A,B}} = \boldsymbol{M}_{\mathrm{A,B}}/M_{\mathrm{A,B}} = |\boldsymbol{M}_{\mathrm{A,B}}|$.

E.1 Ground state

We consider the following total magnetic energy:

$$\begin{aligned} W = &\int_{v_{\mathrm{A}}} d^3r \left\{ -\mu_0 \boldsymbol{H}\cdot\boldsymbol{M}_{\mathrm{A}} + \frac{\mu_0}{2}(M_{\mathrm{A}}^{\mathrm{z}})^2 \right\} + \int_{v_{\mathrm{B}}} d^3r \left\{ -\mu_0 \boldsymbol{H}\cdot\boldsymbol{M}_{\mathrm{B}} + \frac{\mu_0}{2}(M_{\mathrm{B}}^{\mathrm{z}})^2 \right\} \\ &+ \int_{v_{\mathrm{A}}} d^3r_{\mathrm{A}} \int_{v_{\mathrm{B}}} d^3r_{\mathrm{B}} \Bigg[\lambda_{\mathrm{E}}(\boldsymbol{r}_{\mathrm{A}},\boldsymbol{r}_{\mathrm{B}}) \boldsymbol{n}_{\mathrm{A}}(\boldsymbol{r}_{\mathrm{A}})\cdot\boldsymbol{n}_{\mathrm{B}}(\boldsymbol{r}_{\mathrm{B}}) \\ &+ \int_{v_{\mathrm{A}}} d^3r'_{\mathrm{A}} \int_{v_{\mathrm{B}}} d^3r'_{\mathrm{B}} \lambda_{\mathrm{Q}}(\boldsymbol{r}_{\mathrm{A}},\boldsymbol{r}'_{\mathrm{A}},\boldsymbol{r}_{\mathrm{B}},\boldsymbol{r}'_{\mathrm{B}}) \left\{ \boldsymbol{n}_{\mathrm{A}}(\boldsymbol{r}_{\mathrm{A}})\cdot\boldsymbol{n}_{\mathrm{B}}(\boldsymbol{r}_{\mathrm{B}}) \right\} \left\{ \boldsymbol{n}_{\mathrm{A}}(\boldsymbol{r}'_{\mathrm{A}})\cdot\boldsymbol{n}_{\mathrm{B}}(\boldsymbol{r}'_{\mathrm{B}}) \right\} \Bigg]. \end{aligned} \tag{E.1}$$

Here $\boldsymbol{H}$ is an applied magnetic field, the film normal has been taken to be $\hat{\boldsymbol{z}}$, $v_{\mathrm{A,B}}$ denote the spatial volumes occupied by $\boldsymbol{M}_{\mathrm{A,B}}$ respectively, and $\lambda_{\mathrm{E,Q}}$ characterise the first and second order interlayer exchange interactions. Since we focus on spatially uniform dynamics, it is sufficient to approximate the dipole-dipole interactions by the effective easy-plane anisotropy. We have kept the variations of the exchange

terms in order to clarify the effect of having two different thicknesses. By assuming $\boldsymbol{n}_{\mathrm{A,B}}$ do not depend on $\boldsymbol{r}$, the total energy reads

$$W = v_{\mathrm{A}}\left\{-\mu_0 M_{\mathrm{A}}\boldsymbol{H}\cdot\boldsymbol{n}_{\mathrm{A}} + \frac{\mu_0 M_{\mathrm{A}}^2}{2}(n_{\mathrm{A}}^{\mathrm{z}})^2\right\} + v_{\mathrm{B}}\left\{-\mu_0 M_{\mathrm{B}}\boldsymbol{H}\cdot\boldsymbol{n}_{\mathrm{B}} + \frac{\mu_0 M_{\mathrm{B}}^2}{2}(n_{\mathrm{B}}^{\mathrm{z}})^2\right\} + \Lambda_{\mathrm{E}}\boldsymbol{n}_{\mathrm{A}}\cdot\boldsymbol{n}_{\mathrm{B}} + \Lambda_{\mathrm{Q}}\left(\boldsymbol{n}_{\mathrm{A}}\cdot\boldsymbol{n}_{\mathrm{B}}\right)^2, \tag{E.2}$$

where

$$\Lambda_{\mathrm{E}} = \int_{v_{\mathrm{A}}} d^3 r_{\mathrm{A}} \int_{v_{\mathrm{B}}} d^3 r_{\mathrm{B}} \lambda_{\mathrm{E}}(\boldsymbol{r}_{\mathrm{A}}, \boldsymbol{r}_{\mathrm{B}}) \tag{E.3}$$

$$\Lambda_{\mathrm{Q}} = \int_{v_{\mathrm{A}}} d^3 r_{\mathrm{A}} \int_{v_{\mathrm{B}}} \int_{v_{\mathrm{A}}} d^3 r'_{\mathrm{A}} \int_{v_{\mathrm{B}}} d^3 r'_{\mathrm{B}} \lambda_{\mathrm{Q}}(\boldsymbol{r}_{\mathrm{A}}, \boldsymbol{r}'_{\mathrm{A}}, \boldsymbol{r}_{\mathrm{B}}, \boldsymbol{r}'_{\mathrm{B}}). \tag{E.4}$$

Eq. E.2 can be expressed in terms of energy density by dividing with respect to reference volume v as:

$$\frac{W}{v} = \mu_{\mathrm{A}}\left\{-M_{\mathrm{A}}\boldsymbol{H}\cdot\boldsymbol{n}_{\mathrm{A}} + \frac{M_{\mathrm{A}}^2}{2}(n_{\mathrm{A}}^{\mathrm{z}})^2\right\} + \mu_{\mathrm{B}}\left\{-M_{\mathrm{B}}\boldsymbol{H}\cdot\boldsymbol{n}_{\mathrm{B}} + \frac{M_{\mathrm{B}}^2}{2}(n_{\mathrm{B}}^{\mathrm{z}})^2\right\} + \rho_{\mathrm{E}}\boldsymbol{n}_{\mathrm{A}}\cdot\boldsymbol{n}_{\mathrm{B}} + \rho_{\mathrm{Q}}\left(\boldsymbol{n}_{\mathrm{A}}\cdot\boldsymbol{n}_{\mathrm{B}}\right)^2, \tag{E.5}$$

where

$$\mu_{\mathrm{A}} = \mu_0\frac{v_{\mathrm{A}}}{v},\ \ \mu_{\mathrm{B}} = \mu_0\frac{v_{\mathrm{B}}}{v},\ \ \rho_{\mathrm{E}} = \frac{\Lambda_{\mathrm{E}}}{v},\ \ \rho_{\mathrm{Q}} = \frac{\Lambda_{\mathrm{Q}}}{v} \tag{E.6}$$

Here, v_{A} and v_{B} are the volume of two layers. Thus the net effect of thickness difference, (only in the present context), can be expressed as different permeabilities between the two layers. When the magnetic field is in the plane, $\boldsymbol{H} = H\hat{x}, H > 0$. Without loss of generality,$\mu_{\mathrm{A}}M_{\mathrm{A}} > \mu_{\mathrm{B}}M_{\mathrm{B}}$ is also assumed. The ground state occurs when both $\boldsymbol{n}_{\mathrm{A,B}}$ are also in the plane. Thus the energy density to be minimised using Eq. E.5 reads.

$$w = -\mu_{\mathrm{A}}M_{\mathrm{A}}H\cos\phi_{\mathrm{A}} - \mu_{\mathrm{B}}M_{\mathrm{B}}H\cos\phi_{\mathrm{B}} + \rho_{\mathrm{E}}\cos\left(\phi_{\mathrm{A}} - \phi_{\mathrm{B}}\right) + \rho_{\mathrm{Q}}\cos^2\left(\phi_{\mathrm{A}} - \phi_{\mathrm{B}}\right). \tag{E.7}$$

Using the Eq. E.7 we can define three regions:

Forced ferromagnetism This corresponds to the case $\phi_{\mathrm{A}} = \phi_{\mathrm{B}} = 0$, for which the

energy density is given by

$$w_{\rm ff} = -\mu_{\rm A} M_{\rm A} H - \mu_{\rm B} M_{\rm B} H + \rho_{\rm E} + \rho_{\rm Q}. \tag{E.8}$$

This state can be realised only under a sufficiently strong applied field.

Collinear antiferromagnetism In the low field limit, $\phi_{\rm A} = 0, \phi_{\rm B} = \pi$ is expected to be the ground state with the energy density

$$w_{\rm ff} = -\left(\mu_{\rm A} M_{\rm A} H - \mu_{\rm B} M_{\rm B}\right) H - \rho_{\rm E} + \rho_{\rm Q}. \tag{E.9}$$

It requires $\rho_{\rm E} > \rho_{\rm Q}$, but it should usually be satisfied considering the higher-order nature of $\rho_{\rm Q}$.

Spin-flop state In the intermediate field range, $\phi_{\rm A} \neq 0$ and one needs to solve the algebraic equations.

E.2 Resonance frequencies

We next consider the classical dynamics of $\boldsymbol{n}_{\rm A,B}$, dictated by the variational principle with respect to the following Lagrangian:

$$L = -\frac{v_{\rm A} M_{\rm A}}{\gamma_{\rm A}}(1-\cos\theta_{\rm A})\frac{d\phi_{\rm A}}{dt} - \frac{v_{\rm B} M_{\rm B}}{\gamma_{\rm B}}(1-\cos\theta_{\rm B})\frac{d\phi_{\rm B}}{dt} - W \tag{E.10}$$

The kinetic term depends on the choice of polar coordinates, but the difference is always a total derivative. We work with linear perturbation around the ground state $\boldsymbol{n}^0_{\rm A,B}$ determined by minimising w. In general, there is no simple relation between $\boldsymbol{H}$ and $\boldsymbol{n}^0_{\rm A,B}$, so we choose $\boldsymbol{H} = H(\hat{x}\sin\theta + \hat{z}\cos\theta)$. In this coordinate system, we parameterise $\boldsymbol{n}^0_{\rm A,B}$ as

$$\boldsymbol{n}^0_{\rm A,B} = \begin{pmatrix} \sin\theta_{\rm A,B}\cos\phi_{\rm A,B} \\ \sin\theta_{\rm A,B}\sin\phi_{\rm A,B} \\ \cos\theta_{\rm A,B} \end{pmatrix} \tag{E.11}$$

The lack of symmetry between A and B means there is no preferred coordinate system in general. Therefore it is sensible to introduce separate (right-handed) coordinate frames $\{\boldsymbol{n}_A^0, \boldsymbol{n}_A^\theta, \boldsymbol{n}_A^\phi\}$ and $\{\boldsymbol{n}_B^0, \boldsymbol{n}_B^\theta, \boldsymbol{n}_B^\phi\}$ for the two layers where

$$\boldsymbol{n}_{\mathrm{A,B}}^\theta = \begin{pmatrix} \sin\theta_{\mathrm{A,B}}\cos\phi_{\mathrm{A,B}} \\ \sin\theta_{\mathrm{A,B}}\sin\phi_{\mathrm{A,B}} \\ -\sin\theta_{\mathrm{A,B}} \end{pmatrix}, \quad \boldsymbol{n}_{\mathrm{A,B}}^\phi = \begin{pmatrix} -\sin\phi_{\mathrm{A,B}} \\ \cos\phi_{\mathrm{A,B}} \\ 0 \end{pmatrix} \tag{E.12}$$

With these bases, one can define the perturbation up to second order by

$$\boldsymbol{n}_{\mathrm{A}} \approx \left(1 - \frac{l_A^2 + m_A^2}{2}\right)\boldsymbol{n}_A^0 + l_A\boldsymbol{n}_A^\theta + m_A\boldsymbol{n}_A^\phi \tag{E.13}$$

$$\boldsymbol{n}_{\mathrm{B}} \approx \left(1 - \frac{l_B^2 + m_B^2}{2}\right)\boldsymbol{n}_B^0 + l_B\boldsymbol{n}_B^\theta + m_B\boldsymbol{n}_B^\phi \tag{E.14}$$

The rational behind the rotation is that in the polar coordinates

$$l_{\mathrm{A,B}} = \delta\theta_{\mathrm{A,B}}, \quad m_{\mathrm{A,B}} = \delta\phi_{\mathrm{A,B}}\sin\theta_{\mathrm{A,B}} \tag{E.15}$$

We shall substitute them into L and extract only the second order terms in the perturbation. Note

$$\begin{aligned} \boldsymbol{n}_A\cdot\boldsymbol{n}_B \approx{}& n^{00}\left(1 - \frac{l_A^2 + m_A^2 + l_B^2 + m_B^2}{2}\right) + l_A n^{\theta 0} + m_A n^{\phi 0} + l_B n^{0\theta} + m_B n^{0\phi} \\ &+ l_A l_B n^{\theta\theta} + m_A m_B n^{\phi\phi} + l_A m_B n^{\theta\phi} + l_B m_A n^{\phi\theta}, \\ \boldsymbol{n}_A\cdot\boldsymbol{n}_B \approx{}& 2n^{00}\boldsymbol{n}_A\cdot\boldsymbol{n}_B + \left(l_A n^{\theta 0} + m_A n^{\phi 0} + l_B n^{0\theta} + m_B n^{0\phi}\right)^2, \end{aligned} \tag{E.16}$$

where

$$n^{\alpha\beta} = \boldsymbol{n}_A^{alpha}\cdot\boldsymbol{n}_B^\beta, \quad \alpha,\beta = 0,\theta,\phi. \tag{E.17}$$

The second order Lagrangian reads

$$L^{(2)} = -\frac{v_A M_A}{\gamma_A} l_A \frac{dm_A}{dt} - \frac{v_A M_B}{\gamma_B} l_B \frac{dm_B}{dt}$$

$$
\begin{aligned}
&- v_A\mu_0 M_A H\left(\sin\theta\sin\theta_A\cos\phi_A+\cos\theta\cos\theta_A\right)\frac{l_A^2+m_A^2}{2}\\
&- v_B\mu_0 M_B H\left(\sin\theta\sin\theta_B\cos\phi_B+\cos\theta\cos\theta_B\right)\frac{l_B^2+m_B^2}{2}\\
&+\frac{v_A\mu_0 M_A^2}{2}\left(l_A^2\cos 2\theta_A+m_A^2\cos^2\theta_A\right)+\frac{v_B\mu_0 M_B^2}{2}\left(l_B^2\cos 2\theta_B+m_B^2\cos^2\theta_B\right)\\
&-\left(\Lambda_E+2n^{00}\Lambda_Q\right)\left(-n^{00}\frac{l_A^2+m_A^2+l_B^2+m_B^2}{2}+n^{\theta\theta}l_Al_B+n^{\phi\phi}m_Am_B\right.\\
&\left.+n^{\theta\phi}l_Am_B+n^{\phi\theta}l_Bm_A\right)-\Lambda_Q\left(l_An^{\theta 0}+m_An^{\phi 0}+l_Bn^{0\theta}+m_Bn^{0\phi}\right)^2.
\end{aligned}
\tag{E.18}
$$

At this point, it is helpful to note that $v_AM_A\gamma_A$ has the dimension of angular momentum and indeed represents the total angular momentum of the macrospin v_AM_A. This suggests that the correct normalisation for the Holstein-Primakoff variables should be (taking now into account $\gamma_{A,B}$<0)

$$
a=\sqrt{\frac{v_AM_A}{2\hbar\mod\gamma_A}}\left(l_A+im_A\right),\quad b=\sqrt{\frac{v_AM_B}{2\hbar|\gamma_B|}}\left(l_B+im_B\right)
\tag{E.19}
$$

In terms of a, b, after discarding total derivatives, one obtains the Lagrangian

$$
\begin{aligned}
\frac{L^{(2)}}{\hbar}=&-\frac{i}{2}\left(a^\dagger\frac{da}{dt}-\frac{da^\dagger}{dt}a+b^\dagger\frac{db}{dt}-\frac{db^\dagger}{dt}b\right)\\
&-|\gamma_A|\mu_0\left\{H\left(\sin\theta\sin\theta_A\cos\phi_A+\cos\theta\cos\theta_A\right)-M_A\frac{3cos^2\theta_A-1}{2}\right\}\frac{a^\dagger a+aa^\dagger}{2}\\
&-|\gamma_B|\mu_0\left\{H\left(\sin\theta\sin\theta_B\cos\phi_B+\cos\theta\cos\theta_B\right)-M_B\frac{3cos^2\theta_B-1}{2}\right\}\frac{b^\dagger b+bb^\dagger}{2}\\
&-|\gamma_A|\mu_0M_A\frac{\sin^2\theta_A}{2}\frac{aa+a^\dagger a^\dagger}{2}+\frac{|\gamma_A|}{v_AM_A}\left[n^{00}\left(\Lambda_E+2n^{00}\Lambda_Q\right)\frac{a^\dagger a+aa^\dagger}{2}\right.\\
&\left.-\Lambda_Q\left\{|\mathbf{e}_A\cdot\mathbf{n}_B^0|^2\frac{a^\dagger a+aa^\dagger}{2}+\frac{\left(\overline{\boldsymbol{e}_A}\cdot\boldsymbol{n}_B^0\right)^2aa+\left(\boldsymbol{e}_A\cdot n_B^0\right)^2a^\dagger a^\dagger}{2}\right\}\right]\\
&-|\gamma_B|\mu_0M_B\frac{\sin^2\theta_B}{2}\frac{bb+b^\dagger b^\dagger}{2}+\frac{|\gamma_B|}{v_BM_B}\left[n^{00}\left(\Lambda_E+2n^{00}\Lambda_Q\right)\frac{b^\dagger b+bb^\dagger}{2}\right.\\
&\left.-\Lambda_Q\left\{|\mathbf{n}_A^0\cdot\mathbf{e}_B|^2\frac{b^\dagger b+bb^\dagger}{2}+\frac{\left(\boldsymbol{n}_A^0\cdot\overline{\boldsymbol{e}_B}\right)^2bb+\left(\boldsymbol{n}_A^0\cdot e_B\right)^2b^\dagger b^\dagger}{2}\right\}\right]\\
&-\sqrt{\frac{\gamma_A\gamma_B}{v_Av_BM_AM_B}}\left[\Lambda_Q\left\{\left(\overline{\boldsymbol{e}_A}\cdot\boldsymbol{n}_B^0\right)a+\left(\overline{\boldsymbol{e}_A}\cdot\boldsymbol{n}_B^0\right)a^\dagger\right\}\left\{\left(\boldsymbol{n}_A^0\cdot\overline{\boldsymbol{e}_B}\right)b+\left(\boldsymbol{n}_A^0\cdot\overline{\boldsymbol{e}_B}\right)b^\dagger\right\}\right.
\end{aligned}
$$

$$+\left(\Lambda_E+2n^{00}\Lambda_Q\right)\frac{\left(\boldsymbol{e}_A\cdot\overline{\boldsymbol{e}_B}\right)a^\dagger b+\left(\overline{\boldsymbol{e}_A}\cdot\boldsymbol{e}_B\right)ab^\dagger+\left(\overline{\boldsymbol{e}_A\cdot\boldsymbol{e}_B}\right)ab+\left(\boldsymbol{e}_A\cdot\boldsymbol{e}_B\right)a^\dagger b^\dagger}{2}\Bigg], \tag{E.20}$$

where we have introduced chirality vectors

$$\boldsymbol{e}_{A,B}=\boldsymbol{e}^{\theta}_{A,B}+i\boldsymbol{e}^{\phi}_{A,B} \tag{E.21}$$

This form suggests that the reference volume should be taken $v=\sqrt{v_A v_B}$ if the priority is to maintain the symmetry of the expression in A and B. Thus we choose to introduce exchange energy densities $\rho_{E,Q}$, exchange fields $B_{E,Q}$ and exchange frequencies $\omega_{E,Q}$ by

$$\rho_{E,Q}=\frac{\Lambda_{E,Q}}{\sqrt{v_A v_B}},\quad B_{E,Q}=\frac{\lambda E,Q}{\sqrt{v_A v_B M_A M_B}},\quad \omega_{E,Q}=\sqrt{\frac{\gamma_A\gamma_B}{v_A v_B M_A M_B}}\Lambda_{E,Q} \tag{E.22}$$

The resulting equations of motion read in the original variables

$$\begin{aligned}\frac{v_A M_A}{\gamma_A}\frac{dl_A}{dt}&=v_A\mu_0 M_A\left\{H\left(\sin\theta\sin\theta_A\cos\phi_A+\cos\theta\cos\theta_A\right)-M_A\cos^2\theta_A\right\}m_A\\&+\left(\Lambda_E+2n^{00}\Lambda_Q\right)\left(-n^{00}m_A+n^{\phi\phi}m_B+n^{\phi\theta}l_B\right)\\&+2n^{\phi 0}\Lambda_Q\left(n^{\theta 0}l_A+n^{\phi 0}m_A+n^{0\theta}l_B+n^{0\phi}m_B\right),\end{aligned} \tag{E.23}$$

$$\begin{aligned}\frac{v_A M_A}{\gamma_A}\frac{dm_A}{dt}&=v_A\mu_0 M_A\left\{H\left(\sin\theta\sin\theta_A\cos\phi_A+\cos\theta\cos\theta_A\right)-M_A\cos 2\theta_A\right\}l_A\\&-\left(\Lambda_E+2n^{00}\Lambda_Q\right)\left(-n^{00}l_A+n^{\theta\theta}l_B+n^{\theta\phi}m_B\right)\\&+2n^{\theta 0}\Lambda_Q\left(l_A n^{\theta 0}+m_A n^{\phi 0}+l_B n^{0\theta}+m_B n^{0\phi}\right),\end{aligned} \tag{E.24}$$

$$\begin{aligned}\frac{v_B M_B}{\gamma_B}\frac{dl_B}{dt}&=v_B\mu_0 M_B\left\{H\left(\sin\theta\sin\theta_B\cos\phi_B+\cos\theta\cos\theta_B\right)-M_B\cos^2\theta_B\right\}m_B\\&+\left(\Lambda_E+2n^{00}\Lambda_Q\right)\left(-n^{00}m_B+n^{\phi\phi}m_A+n^{\theta\phi}l_A\right)\\&+2n^{0\phi}\Lambda_Q\left(l_A n^{\theta 0}+m_A n^{\phi 0}+l_B n^{0\theta}+m_B n^{0\phi}\right),\end{aligned} \tag{E.25}$$

$$\begin{aligned}\frac{v_B M_B}{\gamma_B}\frac{dm_B}{dt} &= v_B\mu_0 M_B\left\{H\left(\sin\theta\sin\theta_B\cos\phi_B+\cos\theta\cos\theta_B\right)-M_B\cos 2\theta_B\right\}l_B\\ &\quad-\left(\Lambda_E+2n^{00}\Lambda_Q\right)\left(-n^{00}l_B+n^{\theta\theta}l_A+n^{\phi\theta}m_A\right)\\ &\quad+2n^{0\theta}\Lambda_Q\left(l_A n^{\theta 0}+m_A n^{\phi 0}+l_B n^{0\theta}+m_B n^{0\phi}\right),\end{aligned}\tag{E.26}$$

They motivate the following notation

$$B^{\theta}_{A,B}=\mu_0 H\left(\sin\theta\sin\theta_{A,B}\cos\phi_{A,B}+\cos\theta\cos\theta_{A,B}\right)-\mu_0 M_{A,B}\cos 2\theta_{A,B},\tag{E.27}$$

$$B^{\phi}_{A,B}=\mu_0 H\left(\sin\theta\sin\theta_{A,B}\cos\phi_{A,B}+\cos\theta\cos\theta_{A,B}\right)-\mu_0 M_{A,B}\cos^2\theta_{A,B},\tag{E.28}$$

and $\omega^{\theta}_{A,B}=|\gamma_{A,B}|B^{\theta}_{A,B}, \omega^{\phi}_{A,B}=|\gamma_{A,B}|B^{\phi}_{A,B}$. This form will be used later, but for calculating eigenfrequencies, the following BdG form is more convenient:

$$\begin{aligned}i\frac{da}{dt} =& -\omega^{+}_{A}a-\omega^{-}_{A}a^{\dagger}+r^{-1}\left[\left(n^{00}\omega_E+\left\{2\left(n^{00}\right)^2-|\boldsymbol{e}_A\cdot\boldsymbol{n}^0_B|^2\right\}\omega_Q\right)a-\left(\boldsymbol{e}_A\cdot\boldsymbol{n}^0_B\right)^2\omega_Q a^{\dagger}\right]\\ &-\left\{\left(\omega_E+2n^{00}\omega_Q\right)\boldsymbol{e}_A+2\omega_Q\left(\boldsymbol{e}_A\cdot\boldsymbol{n}^0_B\right)\boldsymbol{n}^0_A\right\}\cdot\frac{\overline{\boldsymbol{e}_B}b+\boldsymbol{e}_B b^{\dagger}}{2},\end{aligned}\tag{E.29}$$

$$\begin{aligned}i\frac{db}{dt} =& -\omega^{+}_{B}b-\omega^{-}_{B}b^{\dagger}+r^{-1}\left[\left(n^{00}\omega_E+\left\{2\left(n^{00}\right)^2-|\boldsymbol{e}_B\cdot\boldsymbol{n}^0_A|^2\right\}\omega_Q\right)b-\left(\boldsymbol{e}_B\cdot\boldsymbol{n}^0_A\right)^2\omega_Q b^{\dagger}\right]\\ &-\left\{\left(\omega_E+2n^{00}\omega_Q\right)\boldsymbol{e}_B+2\omega_Q\left(\boldsymbol{e}_B\cdot\boldsymbol{n}^0_A\right)\boldsymbol{n}^0_B\right\}\cdot\frac{\overline{\boldsymbol{e}_A}a+\boldsymbol{e}_A a^{\dagger}}{2},\end{aligned}\tag{E.30}$$

where $\omega^{\pm}_{A,B}=\left(\omega^{\theta}_{A,B}\pm\omega^{\phi}_{A,B}\right)/2$ and the asymmetry parameter r is defined by

$$r=\sqrt{\frac{\gamma_B v_A M_A}{\gamma_A v_B M_B}}\tag{E.31}$$

We do not write the corresponding equations for $a^\dagger$, $b^\dagger$ since they are obtained by complex conjugation. In the matrix form, the eigenvalue problem is defined by

$$\begin{pmatrix} -\omega-\xi_A & -\eta_A & -\zeta_1 & -\zeta_2 \\ -\overline{\eta_A} & \omega-\xi_A & -\overline{\zeta_2} & -\overline{\zeta_1} \\ -\overline{\zeta_1} & -\zeta_2 & -\omega-\xi_B & -\eta_B \\ -\overline{\zeta_2} & -\zeta_1 & -\overline{\eta_B} & -\omega-\xi_B \end{pmatrix} \begin{pmatrix} a \\ a^\dagger \\ b \\ b^\dagger \end{pmatrix} = 0, \tag{E.32}$$

where

$$\xi_A = \omega_A^+ - r^{-1}\left(n^{00}\omega_E + \left\{2\left(n^{00}\right)^2 - |\boldsymbol{e}_A\cdot\boldsymbol{n}_B^0|^2\right\}\omega_Q\right), \tag{E.33}$$

$$\xi_B = \omega_B^+ - r\left(n^{00}\omega_E + \left\{2\left(n^{00}\right)^2 - |\boldsymbol{e}_B\cdot\boldsymbol{n}_A^0|^2\right\}\omega_Q\right), \tag{E.34}$$

$$\eta_A = \omega_A^- + r^{-1}\left(\boldsymbol{e}_A\cdot\boldsymbol{n}_B^0\right)^2\omega_Q, \tag{E.35}$$

$$\eta_B = \omega_B^- + r^{-1}\left(\boldsymbol{e}_B\cdot\boldsymbol{n}_A^0\right)^2\omega_Q, \tag{E.36}$$

$$\zeta_1 = \frac{\left(\omega_E + 2n^{00}\omega_Q\right)\boldsymbol{e}_A\cdot\overline{\boldsymbol{e}_B} + 2\omega_Q\left(\boldsymbol{e}_A\cdot\boldsymbol{n}_B^0\right)\left(\overline{\boldsymbol{e}_B}\cdot\boldsymbol{n}_A^0\right)}{2}, \tag{E.37}$$

$$\zeta_2 = \frac{\left(\omega_E + 2n^{00}\omega_Q\right)\boldsymbol{e}_A\cdot\boldsymbol{e}_B + 2\omega_Q\left(\boldsymbol{e}_A\cdot\boldsymbol{n}_B^0\right)\left(\boldsymbol{e}_B\cdot\boldsymbol{n}_A^0\right)}{2}, \tag{E.38}$$

Using the determinant formula

$$\det\begin{pmatrix} A & B \\ C & D \end{pmatrix} = \det(A)\det(D - CA^{-1}B), \tag{E.39}$$

one can derive the secular equation as

$$\begin{aligned} 0 &= \det\left[\left(\xi_A^2 - |\eta_A|^2 - \omega^2\right)\begin{pmatrix} -\omega-\xi_B & -\eta_B \\ -\overline{\eta_B} & \omega-\xi_B \end{pmatrix} - \begin{pmatrix} \overline{\zeta_1} & \zeta_2 \\ \overline{\zeta_2} & \zeta_1 \end{pmatrix}\begin{pmatrix} \omega-\xi_A & \eta_A \\ \overline{\eta_A} & -\omega-\xi_A \end{pmatrix}\begin{pmatrix} \zeta_1 & \zeta_2 \\ \overline{\zeta_2} & \overline{\zeta_1} \end{pmatrix}\right] \\ &\times\left(\xi_A^2 - |\eta_A|^2 - \omega^2\right)^{-1} \\ &= \omega^4 - \left(\xi_A^2 + \xi_B^2 - |\eta_A|^2 - |\eta_B|^2 + 2|\zeta_1|^2 - 2|\zeta_2|^2\right)\omega^2 + \left(\xi_A^2 - |\eta_A|^2\right)\left(\xi_B^2 - |\eta_B|^2\right) \\ &- 2\left(|\zeta_1|^2 + |\zeta_2|^2\right)\xi_A\xi_B + 2\xi_A\left(\eta_B\zeta_1\overline{\zeta_2} + \overline{\eta_B}\overline{\zeta_1}\zeta_2\right) + 2\xi_B\left(\eta_A\overline{\zeta_1\zeta_2} + \overline{\eta_A}\zeta_1\zeta_2\right) \\ &- \overline{\eta_A}\eta_B\zeta_1^2 - \eta_A\overline{\eta_B}\overline{\zeta_1}^2 - \eta_A\eta_B\overline{\zeta_2}^2 - \overline{\eta_A\eta_B}\zeta_2^2 + \left(|\zeta_1|^2 - |\zeta_2|^2\right)^2. \end{aligned} \tag{E.40}$$

The roots are given by

$$\begin{aligned}\omega^2 =& \frac{\xi_A^2 - |\eta_A|^2 + \xi_B^2 - |\eta_B|^2 + 2|\zeta_1|^2 - 2|\zeta_2|^2}{2} \pm \Bigg\{ \left(\frac{\xi_A^2 - \xi_B^2 - |\eta_A|^2 + |\eta_B|^2}{2} \right)^2 \\ & + |\zeta_1|^2 (\xi_A + \xi_B)^2 - |\zeta_2|^2 (\xi_A - \xi_B)^2 - 2\xi_A \left(\eta_B \zeta_1 \overline{\zeta_2} + \overline{\eta_B} \overline{\zeta_1} \zeta_2 \right) \\ & - 2\xi_B \left(\eta_A \overline{\zeta_1 \zeta_2} + \overline{\eta_A} \zeta_1 \zeta_2 \right) - |\eta_A \overline{\zeta_1} - \eta_B \zeta_1|^2 + |\eta_A \overline{\zeta_2} + \overline{\eta_B} \zeta_2|^2 \Bigg\}^{1/2} \\ =& \frac{\xi_A^2 - |\eta_A|^2 + \xi_B^2 - |\eta_B|^2 + 2|\zeta_1|^2 - 2|\zeta_2|^2}{2} \pm \Bigg\{ \left(\frac{\xi_A^2 - \xi_B^2 - |\eta_A|^2 + |\eta_B|^2}{2} \right)^2 \\ & + |(\xi_A + \xi_B)\zeta_1 - \eta_A \overline{\zeta_2} - \overline{\eta_B} \zeta_2|^2 - |(\xi_A - \xi_B)\zeta_2 - \eta_A \overline{\zeta_1} + \eta_B \zeta_1|^2 \Bigg\}^{1/2}\end{aligned} \tag{E.41}$$

Appendix F

Angle dependence of CI-FMR Lineshape

In this section the expression for angle dependence of FMR lineshape detected by spin rectification is derived using Landau-Lifshitz-Gilbert (LLG) equation:

$$\frac{\partial \mathbf{M}}{\partial t} = -\mu_0 \gamma \mathbf{M} \times (\mathbf{H}_{\text{tot}} + \mathbf{h}_{\text{eff}}) + \frac{\alpha}{M_{\text{s}}} \mathbf{M} \times \frac{\partial \mathbf{M}}{\partial t} \tag{F.1}$$

where the first term is the field torque and second is Gilbert damping term. $\mathbf{M}$, and $\mathbf{H}_{\text{tot}}$ are the vectors representing the magnetization and total static magnetic field including both the external field (H_{ext}), demagnetization field and anisotropy fields; $\mathbf{h}_{\text{eff}} = \left(h_{\text{x}}, h_{\text{y}}, h_{\text{z}}\right) \text{e}^{j\omega t}$ is the current-induced effective field at microwave frequency which drives the magnetic moments; γ, α and M_{s} are gyromagnetic ratio, Gilbert damping coefficient and the saturation magnetization. A new righthand coordinate system is defined as $(\text{x}' - \text{y}' - \text{z}')$ with respect to the $\mathbf{H}_{\text{tot}}$ as shown in Fig. F.1. In this new system, with small-precession angle approximation, we can assume that magnetization component along x'-axis is $m_{\text{x}'} \approx M_{\text{s}}$. Using this we can write it in the form as:

$$\mathbf{M} = \begin{pmatrix} M_{\text{s}} \\ m_{\text{y}'} \text{e}^{\text{j}\omega t} \\ \text{m}_{\text{z}'} \text{e}^{\text{j}\omega \text{t}} \end{pmatrix}, \mathbf{h}_{\text{eff}} = \begin{pmatrix} h_{\text{x}'} \\ h_{\text{y}'} \\ h_{\text{z}'} \end{pmatrix} = \begin{pmatrix} h_{\text{x}} \cos\theta + h_{\text{y}} \sin\theta \\ -h_{\text{x}} \sin\theta + h_{\text{y}} \cos\theta \\ h_z \end{pmatrix} \text{e}^{\text{j}\omega \text{t}} \tag{F.2}$$

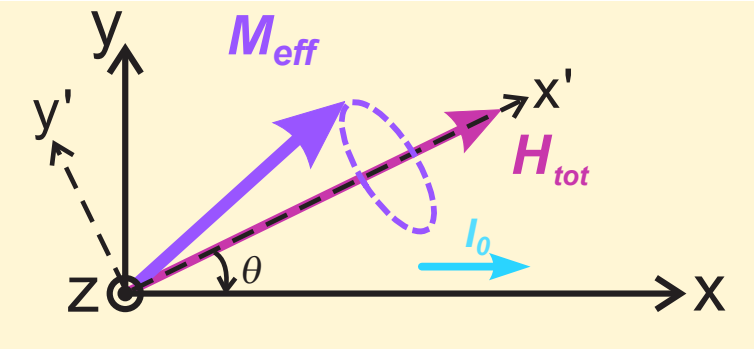

Figure F.1: The two coordinate systems defined with respect to the charge current direction (x-y-z system) and the total static magnetic field (x'-y'-z' system).

Solving the LLG equation to the first order [326], the following set of linearized equations are obtained:

$$\frac{i\omega}{\mu_0\gamma}m_{y'} + (i\Delta H + H_{ext} + H_1)\, m_{z'} = M_s h_z \tag{F.3}$$

$$(i\Delta H + H_{ext} + H_2)\, m_{y'} - \frac{i\omega}{\mu_0\gamma}m_{z'} = M_s\left(-h_x \sin\theta + h_y \cos\theta\right) \tag{F.4}$$

where $\mu_0\Delta H = \alpha\omega/\gamma$ is the resonance linewidth; H_1 and H_2 are the terms including the anisotropy which are defined as follows: [178, 114]:

$$\begin{aligned} H_1 = {} & M_s\left[-N_x\cos^2(\theta) - N_y\sin^2(\theta) + N_z\right] - H_{2\perp} \\ & + H_{2\parallel}\sin^2\left(\theta - \frac{\pi}{4}\right) + \frac{1}{4}H_{4\parallel}(3 + \cos 4\theta) \end{aligned} \tag{F.5}$$

$$H_2 = M_s\left(N_y - N_x\right)\cos 2(\theta + \phi) - H_{2\parallel}\sin 2\theta + H_{4\parallel}\cos 4\theta \tag{F.6}$$

Here, $H_{2\parallel}$ and $H_{4\parallel}$ are in-plane uniaxial and biaxial anisotropy fields respectively and $H_{2\perp}$ represents the out-of-plane anisotropy field. θ is defined as the angle between $\mathbf{H}_{tot}$ and the x direction; N_i is the demagnetization factors in i-axis.

By solving the Eq. F.3 and F.4 the expression for $m_{y'}$ and $m_{z'}$ is obtained as follows:

$$m_{y'} = \frac{\left[(H_{ext} + H_1 + i\Delta H)\left(-h_x\sin\theta + h_y\cos\theta\right) + \frac{i\omega}{\mu_0\gamma}h_z\right]M_s}{(H_{ext} + H_1 + i\Delta H)(H_{ext} + H_2 + i\Delta H) - \left(\frac{\omega}{\mu_0\gamma}\right)^2} \tag{F.7}$$

$$m_{z'} = \frac{\left[\left(H_{\text{ext}} + H_2 + i\Delta H\right) h_z - \left(-h_x \sin\theta + h_y \cos\theta\right) \frac{i\omega}{\mu_0 \gamma}\right] M_s}{\left(H_{\text{ext}} + H_1 + i\Delta H\right)\left(H_{\text{ext}} + H_2 + i\Delta H\right) - \left(\frac{\omega}{\mu_0 \gamma}\right)^2} \tag{F.8}$$

The DC voltage from spin rectification is given by:

$$\mathrm{V_{dc}} = -\frac{1}{2} I_0 \Delta R \theta_{\mathrm{c}} \sin(2\theta) = -\frac{1}{2} I_0 \Delta R \frac{m_{\mathrm{y}'}}{M_{\mathrm{s}}} \sin(2\theta) \tag{F.9}$$

where θ_{c} describes the deviation of $\mathbf{M}$ from its axis of rotation (referred to as the "cone angle" of the precession). To derive the lineshape near the resonance field H_{res} , we consider the profile of V_{dc} at a small perturbation $\delta H << H_{\text{res}}$, i.e

$$\delta H = \mid H_{\text{ext}} - H_{\text{res}} \mid \tag{F.10}$$

Substituting H_{ext} in Eq. F.7 as $H_{\text{res}} + \delta H$ and only keeping terms linear in δH and ΔH, the following simplified expression is obtained:

$$m_{\mathrm{y}'} = \frac{M_{\mathrm{s}}}{2H_{\text{res}} + H_1 + H_2} \frac{\left(H_{\text{res}} + H_1\right) \delta H \left(-h_{\mathrm{x}} \sin\theta + h_{\mathrm{y}} \cos\theta\right) + \frac{\omega}{\mu_0 \gamma} \Delta H h_{\mathrm{z}}}{\delta H^2 + \Delta H^2} \tag{F.11}$$

Finally the expression for DC signal from spin rectification is obtained by replacing δH with $H_{\text{ext}} - H_{\text{res}}$ and substituting Eq. F.11 in Eq. F.9 as:

$$\mathrm{V_{dc}} = V_{\text{sym}-\text{SR}} \frac{\Delta H^2}{\left(H_{\text{ext}} - H_{\text{res}}\right)^2 + \Delta H^2} + V_{\text{asy}-\text{SR}} \frac{\left(H_{\text{ext}} - H_{\text{res}}\right) \Delta H}{\left(H_{\text{ext}} - H_{\text{res}}\right)^2 + \Delta H^2} \tag{F.12}$$

where $V_{\text{sym-SR}}$ and $V_{\text{asy-SR}}$ are the Lorentzian components in symmetric and antisymmetric lineshape:

$$V_{\text{sym}-\text{SR}} = \frac{\mathrm{I_0 \Delta R}}{2} \frac{\omega}{\mu_0 \gamma \Delta H \left(2H_{\text{res}} + H_1 + H_2\right)} h_2 \sin 2\theta = \frac{\mathrm{I_0 \Delta R}}{2} \mathrm{A_{sym}} h_2 \sin 2\theta \tag{F.13}$$

$$\begin{aligned} V_{\text{asy}-\text{SR}} &= \frac{\mathrm{I_0 \Delta R}}{2} \frac{\left(H_{\text{res}} + H_1\right)}{\Delta H \left(2H_{\text{res}} + H_1 + H_2\right)} \left(-h_{\mathrm{x}} \sin\theta + h_{\mathrm{y}} \cos\theta\right) \sin 2\theta \\ &= \frac{\mathrm{I_0 \Delta R}}{2} \mathrm{A_{asy}} \left(-h_{\mathrm{x}} \sin\theta + h_{\mathrm{y}} \cos\theta\right) \end{aligned} \tag{F.14}$$

The terms A_{sym} and A_{asy} are the scalar amplitudes of the magnetic susceptibility ($A_{\mathrm{i}} = \chi_{\mathrm{i}}/M_{\mathrm{s}}$). These terms are also angle-dependent, as they depend on the magnetic anisotropy of the device.

Appendix G

Analysis of the DC voltage in Ferromagnet/heavy-metal bilayer system

In this appendix we discuss the dependence of DC resonance signal on θ_{SH}, t_{FM}, and α_{eff}. It has been shown in [1] that there are at least four components that contribute to the DC resonance signal, namely spin rectification and spin pumping at ferromagnetic resonance (FMR) condition induced by either Oersted field or spin transfer torque (STT). We denote these four components as $V_{\text{ST-SR}}$, $V_{\text{ST-SP}}$, $V_{\text{Oe-SR}}$ and $V_{\text{Oe-SP}}$ respectively. The FMR driving mechanism is described using the Landau-Lifshitz-Gilbert (LLG) equation. In the Ferromagnet (FM)/heavy-metal (HM) bilayer systems the spin pumping contribution leads to increase in effective damping. The resultant equation can be described as:

$$\frac{d\mathbf{M}}{dt} = -\mu_0\gamma_{\text{eff}}\left(\mathbf{H}_{\text{ext}} + \mathbf{h}_{\text{Oe}} + \mathbf{h}_{\text{ST}}\right) \times \mathbf{M} + \frac{\alpha_{\text{eff}}}{M_s}\mathbf{M} \times \frac{d\mathbf{M}}{dt} \tag{G.1}$$

where μ_0 is the vacuum permeability; M_s is the saturation magnetization; γ_{eff} and α_{eff} are the effective gyromagnetic ratio and the effective Gilbert damping factor respectively including the effect from spin pumping. The term $\mathbf{h}_{\text{Oe}}$ and $\mathbf{h}_{\text{ST}}$ are the

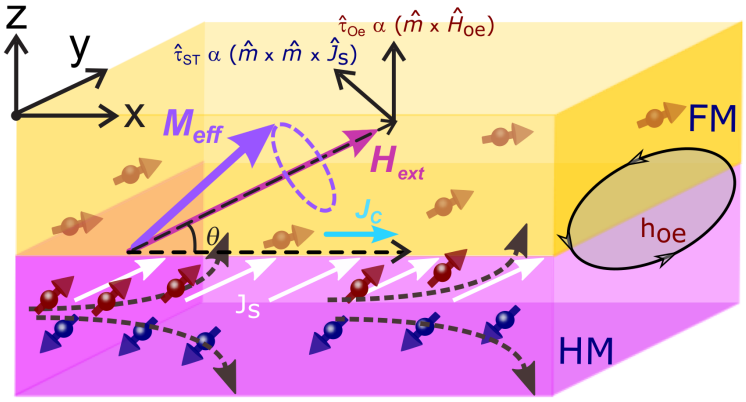

Figure G.1: The two coordinate systems defined with respect to the charge current direction (x-y-z system) and the total static magnetic field (x'-y'-z' system).

effective magnetic field created by Oersted field and STT respectively, given by:

$$\mathbf{h}_{\mathrm{Oe}} = \mathbf{y} \cdot J_c t_{\mathrm{HM}}/2 \tag{G.2}$$

$$\mathbf{h}_{\mathrm{ST}} = \frac{\hbar \xi \theta_{\mathrm{SH}} J_c}{2e\mu_0 M_s t_{\mathrm{FM}}} (\mathbf{M} \times \boldsymbol{\sigma}) \tag{G.3}$$

The mechanism for generation of these effective fields is explained in detail in Chapter 2. In the above Eqs. G.2 and G.3 $\mathbf{y}$ is the unit vector along the y -axis, as shown in Fig. G.1; $t_{\mathrm{HM}}, \theta_{\mathrm{SH}}$ and J_c are the thickness, spin Hall angle of heavy metal (HM), and the charge current density in it respectively. M_s and t_{FM} are the saturation magnetization and the thickness of ferromagnet, ξ is the spin absorption efficiency[1] ; e, μ_0 and $\hbar$ are the elementary charge, vacuum permeability and reduced Planck constant respectively; $\boldsymbol{\sigma}$ is the unit vector of the spin polarization created in HM due to flow of charge current by spin hall effect. From Eqs. G.2 and G.3 it can be seen that STT-induced effective field $\mathbf{h}_{\mathrm{ST}}$ is proportional to θ_{SH} and inversely proportional to t_{FM}, while the Oersted field is independent of both of them.

The magnetization dynamics causes a time varying change in bilayer resistance due to spin Hall magnetoresistance (SMR) [178]. Mixing of the applied microwave current and oscillating resistance produces a dc voltage that is referred to as spin

torque diode effect [115] given by[114]:

$$V(\mathrm{t}) = J_c w_{\mathrm{HM}} t_{\mathrm{HM}} \cos(2\pi \mathrm{ft}) \cdot \left\{ R_0 - \Delta R \cos^2 \left[\theta + \theta_{\mathrm{c}} \cos(2\pi f t + \phi) \right] \right\} \tag{G.4}$$

where w_{HM} is the width of HM layer; R_0 and ΔR are the bar resistance and the change in resistance due to SMR; θ_{c} is the cone angle of magnetization precession; f and t are the microwave frequency and time and ϕ is the phase difference between magnetization precession and current. In the case of small cone angle precession, the expression can be simplified by Taylor's series expansion up to first order[114]:

$$V_{\mathrm{SR}} = \frac{J_{\mathrm{c}} w_{\mathrm{HM}} t_{\mathrm{HM}} \cdot \Delta R \theta_{\mathrm{c}}}{2} \sin 2\theta \cos \phi \tag{G.5}$$

Assuming the inhomogeneous linewidth is very small, the maximum precession angle can be determined by the expression:

$$\theta_{\mathrm{c-max}} = \frac{h_{\mathrm{eff}}}{\Delta H} \approx \frac{\gamma_{\mathrm{eff}} \mu_0 h_{\mathrm{eff}}}{2\pi f \alpha_{\mathrm{eff}}} \tag{G.6}$$

where h_{eff} is the effective driving field that is either STT-induced effective field or Oersted field. As mentioned earlier due to the effect of spin pumping the damping factor includes additional term, α_{SP}, resulting in effective Gilbert damping factor given by [117]:

$$\alpha_{\mathrm{eff}}\ (t_{FM}) = \alpha_0 + \alpha_{\mathrm{SP}} = \alpha_0 + \frac{\gamma \hbar^2}{2e^2 M_{\mathrm{s}} t_{\mathrm{FM}}} g_{\mathrm{eff}}^{\uparrow\downarrow} \tag{G.7}$$

where $g_{\mathrm{eff}}^{\dagger\downarrow}$ is the effective interface spin-mixing conductance [117]. The dependence for ΔR on spin hall angle, θ_{SH} can be determined from the expression of SMR as given in [66]:

$$\Delta R \approx R_0 \theta_{\mathrm{SH}}^2 \frac{\frac{2\lambda_{\mathrm{HM}}^2}{\sigma_{\mathrm{HM}} t_{\mathrm{HM}}} g_{\mathrm{eff}}^{\uparrow\downarrow} \tanh^2 \frac{t_{\mathrm{HM}}}{2\lambda_{\mathrm{HM}}}}{1 + \frac{2\lambda_{\mathrm{HM}}}{\sigma_{\mathrm{HM}}} g_{\mathrm{eff}}^{\uparrow\downarrow} \coth \frac{t_{\mathrm{HM}}}{\lambda_{\mathrm{HM}}}} \tag{G.8}$$

where λ_{HM} and σ_{HM} is the spin diffusion length and conductivity of HM; This shows that $\Delta R \propto \theta_{SH}^2$ while it is independent from t_{FM}.. Putting Eqs. G.2,G.3,G.6 and G.8 in Eq. G.5 the expression for rectified dc voltage signal can be obtained as: $V_{ST-SR} \propto \theta_{SH}^3/(\alpha_{eff}\, t_{FM})$ and $V_{Oe\text{-}SR} \propto \theta_{SH}^2/\alpha_{eff}$.

The DC voltage created due to Inverse Spin Hall effect (ISHE) is described by symmetric Lorentzian component V_{sym-SP}, being independent of the phase between microwave current and the precessing magnetisation and is given by [117]:

$$V_{sym-SP} = R_0 w_{HM} \frac{2e}{\hbar} \theta_{SH} \lambda_{HM} \eta \tanh\left(\frac{t_{HM}}{2\lambda_{HM}}\right) j_s^0 \sin\theta \tag{G.9}$$

where, η is a correction factor for the ellipticity of the magnetization precession. j_s^0 is the spin-current density at the interface given by [63]:

$$j_s^0 = \frac{\hbar g_{eff}^{\uparrow\downarrow} \gamma^2 (\mu_0 h_{eff})^2 \left[\mu_0 M_{eff}\, \gamma + \sqrt{(\mu_0 M_{eff}\, \gamma)^2 + 16(\pi f)^2}\right]}{8\pi\alpha_{eff}^2 \left[(\mu_0 M_{eff}\, \gamma)^2 + 16(\pi f)^2\right]} \tag{G.10}$$

where M_{eff} is the effective magnetization. Putting Eq. G.2,G.3 and G.10 into G.9, it can be found that $V_{ST-SP} \propto \theta_{SH}^3/(\alpha_{eff} t_{FM})^2$ and $V_{Oe-SP} \propto \theta_{SH}/\alpha_{eff}^2$

A summary about the resonance DC signals and their dependence on θ_{SH}, t_{FM} and α_{eff} is given in Tab. G.1.

Table G.1: Summary of resonance DC signal components driven by h_{ST} and h_{Oe}

Driving field	Spin rectification	Lineshape (SR)	Spin pumping	Lineshape (SP)
h_{ST}	$C_1 \sin 2\theta \cos\theta$	Symmetric	$C_2 \sin 2\theta \cos\theta$	Symmetric
h_{Oe}	$C_3 \sin 2\theta \cos\theta$	Asymmetric	$C_4 \sin 2\theta \cos\theta$	Symmetric

where, $C_1 = -C_{ST\text{-}SR}[\theta_{SH}^3/(\alpha_{eff} t_{FM})]$, $C_2 = C_{ST\text{-}SP}[\theta_{SH}^3/(\alpha_{eff} t_{FM})^2]$, $C_3 = -C_{Oe\text{-}SR}(\theta_{SH}^2/\alpha_{eff})$ and $C_4 = C_{Oe\text{-}SP}(\theta_{SH}/\alpha_{eff}^2)$ are the constants.

Appendix H

FMR setups

In this appendix, pictures of the ferromagnetic resonance (FMR) setup used for the experiments are shown, along with the sample holding stage. Fig. H.1 shows the in plane and out-of-plane setups used in experiments and the sample holding stage used for out-of-plane measurements. The magnet used for out-of-plane measurements was GMW3473 which can provide high field upto 1.2 T. A motor at the bottom of electromagnet allows 180° rotation of the magnet. The sample holder is made from aluminium and is 22 cm in length and 3.6 cm in diameter. The sample holder is placed between the poles of the magnet such that the sample is always in the centre of the magnet that is in the region of uniform field.

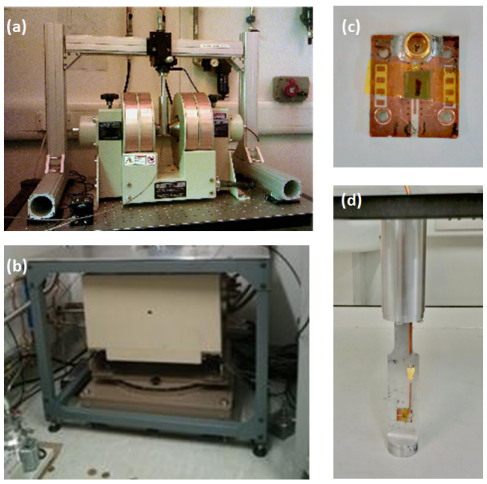

Figure H.1: (a-b) Magnet setups used for measuremens. A field upto 1.2 T can be reached and the motor assembly allows for the rotation of the magnet. (c) Coplanar waveguide with sample mounted on it. (d) Sample holder used for mounting the coplanar waveguide so that sample can be placed in region of uniform field.

Bibliography

[1] T. Chiba, G. E. W. Bauer, and S. Takahashi. Current-induced spin-torque resonance of magnetic insulators. *Physical Review Applied*, 2(3):034003, 2014.

[2] L. Liu, T. Moriyama, D. C. Ralph, and R. A. Buhrman. Spin-torque ferromagnetic resonance induced by the spin Hall effect. *Physical Review Letters*, 106(3):036601, 2011.

[3] T. D. Skinner, M. Wang, A. T. Hindmarch, A. W. Rushforth, A. C. Irvine, D. Heiss, H. Kurebayashi, and A. J. Ferguson. Spin-orbit torque opposing the Oersted torque in ultrathin Co/Pt bilayers. *Applied Physics Letters*, 104(6):062401, 2014.

[4] H. Adachi, K. Uchida, E. Saitoh, and S. Maekawa. Theory of the spin Seebeck effect. *Reports on Progress in Physics*, 76(3):036501, 2013.

[5] V. Kamberský. On the Landau–Lifshitz relaxation in ferromagnetic metals. *Canadian Journal of Physics*, 48(24):2906–2911, 1970.

[6] J. Pelzl, R. Meckenstock, D. Spoddig, F. Schreiber, J. Pflaum, and Z. Frait. Spin–orbit-coupling effects on g -value and damping factor of the ferromagnetic resonance in Co and Fe films. *Journal of Physics: Condensed Matter*, 15(5):S451, 2003.

[7] H. Kohno, G. Tatara, and J. Shibata. Microscopic calculation of spin torques in disordered ferromagnets. *Journal of the Physical Society of Japan*, 75(11):113706–113706, 2006.

[8] H. Ebert, S. Mankovsky, D. Ködderitzsch, and P. J. Kelly. Ab initio calculation of the Gilbert damping parameter via the linear response formalism. *Phys. Rev. Lett.*, 107:066603, Aug 2011.

[9] J. Seib and M. Fähnle. Calculation of the Gilbert damping matrix at low scattering rates in Gd. *Phys. Rev. B*, 82:064401, Aug 2010.

[10] Kh. Zakeri, J. Lindner, I. Barsukov, R. Meckenstock, M. Farle, U. von Hörsten, H. Wende, W. Keune, J. Rocker, S. S. Kalarickal, K. Lenz, W. Kuch, K. Baberschke, and Z. Frait. Spin dynamics in ferromagnets: Gilbert damping and two-magnon scattering. *Phys. Rev. B*, 76:104416, Sep 2007.

[11] S. Mizukami, D. Watanabe, M. Oogane, Y. Ando, Y. Miura, M. Shirai, and T. Miyazaki. Low damping constant for Co_2FeAl Heusler alloy films and its correlation with density of states. *Journal of Applied Physics*, 105(7):07D306, 2009.

[12] K. Gilmore, M. D. Stiles, J. Seib, D. Steiauf, and M. Fähnle. Anisotropic damping of the magnetization dynamics in Ni, Co, and Fe. *Phys. Rev. B*, 81:174414, May 2010.

[13] M. Dvornik, A. Vansteenkiste, and B. Van Waeyenberge. Micromagnetic modeling of anisotropic damping in magnetic nanoelements. *Phys. Rev. B*, 88:054427, Aug 2013.

[14] D. Thonig and J. Henk. Gilbert damping tensor within the breathing fermi surface model: anisotropy and non-locality. *New Journal of Physics*, 16(1):013032, 2014.

[15] A. Brataas, Y. Tserkovnyak, and G. E. W. Bauer. Scattering theory of Gilbert damping. *Phys. Rev. Lett.*, 101:037207, Jul 2008.

[16] S. Mankovsky, D. Ködderitzsch, G. Woltersdorf, and H. Ebert. First-principles calculation of the Gilbert damping parameter via the linear re-

sponse formalism with application to magnetic transition metals and alloys. *Phys. Rev. B*, 87:014430, Jan 2013.

[17] M. Oogane, T. Kubota, Y. Kota, S. Mizukami, H. Naganuma, A. Sakuma, and Y. Ando. Gilbert magnetic damping constant of epitaxially grown Co-based Heusler alloy thin films. *Applied Physics Letters*, 96(25):252501, 2010.

[18] P. Bruno. Tight-binding approach to the orbital magnetic moment and magnetocrystalline anisotropy of transition-metal monolayers. *Physical Review B*, 39(1):865, 1989.

[19] V. Kamberskỳ, B. Heinrich, and D. Fraitova. The influence of conduction electrons on the linewidth of FMR in metals. *Physics Letters*, 23(1):26–27, 1966.

[20] W. Platow, A. N. Anisimov, G. L. Dunifer, M. Farle, and K. Baberschke. Correlations between ferromagnetic-resonance linewidths and sample quality in the study of metallic ultrathin films. *Phys. Rev. B*, 58:5611–5621, Sep 1998.

[21] G. Kurizki, P. Bertet, Y. Kubo, K. Mølmer, D. Petrosyan, P. Rabl, and J. Schmiedmayer. Quantum technologies with hybrid systems. *Proceedings of the National Academy of Sciences*, 112(13):3866–3873, 2015.

[22] M. Harder, Y. Yang, B. M. Yao, C. H. Yu, J. W. Rao, Y. S. Gui, R. L. Stamps, and C.-M. Hu. Level attraction due to dissipative magnon-photon coupling. *Phys. Rev. Lett.*, 121:137203, 2018.

[23] M. Agrawal, V. I. Vasyuchka, A. A. Serga, A. D. Karenowska, G. A. Melkov, and B. Hillebrands. Direct measurement of magnon temperature: New insight into magnon-phonon coupling in magnetic insulators. *Physical Review Letters*, 111(10):107204, 2013.

[24] A. Sud, C. W. Zollitsch, A. Kamimaki, T. Dion, S. Khan, S. Iihama, S. Mizukami, and H. Kurebayashi. Tunable magnon-magnon coupling in synthetic antiferromagnets. *Physical Review B*, 102(10):100403, 2020.

[25] Y. Shiota, T. Taniguchi, M. Ishibashi, T. Moriyama, and T. Ono. Tunable magnon-magnon coupling mediated by dynamic dipolar interaction in synthetic antiferromagnets. *Physical Review Letters*, 125(1):017203, 2020.

[26] M. N. Baibich, J. M. Broto, A. Fert, F. N. Van Dau, F. Petroff, P. Etienne, G. Creuzet, A. Friederich, and J. Chazelas. Giant magnetoresistance of (001) Fe/(001) Cr magnetic superlattices. *Physical Review Letters*, 61(21):2472, 1988.

[27] G. Binasch, P. Grünberg, F. Saurenbach, and W. Zinn. Enhanced magnetoresistance in layered magnetic structures with antiferromagnetic interlayer exchange. *Physical Review B*, 39(7):4828, 1989.

[28] J. C. Slonczewski. Current-driven excitation of magnetic multilayers. *Journal of Magnetism and Magnetic Materials*, 159(1-2):L1–L7, 1996.

[29] L. Berger. Emission of spin waves by a magnetic multilayer traversed by a current. *Physical Review B*, 54(13):9353, 1996.

[30] D. Shum, D. Houssameddine, ST Woo, Y. S. You, J. Wong, K. W. Wong, C. C. Wang, K.H. Lee, K. Yamane, and V. B. Naik *et al.* CMOS-embedded STT-MRAM arrays in 2x nm nodes for GP-MCU applications. In *2017 Symposium on VLSI Technology*, pages T208–T209. IEEE, 2017.

[31] N. N. Mojumder, S. K. Gupta, S. H. Choday, D. E. Nikonov, and K. Roy. A three-terminal dual-pillar STT-MRAM for high-performance robust memory applications. *IEEE transactions on electron devices*, 58(5):1508–1516, 2011.

[32] J. G. Alzate, U. Arslan, P. Bai, J. Brockman, Y.-J. Chen, N. Das, K. Fischer, T. Ghani, P. Heil, and P. Hentges *et al.* 2 MB array-level demonstration of STT-MRAM process and performance towards L4 cache applications. In *2019 IEEE International Electron Devices Meeting (IEDM)*, pages 2–4. IEEE, 2019.

[33] C. Kittel. *Introduction to Solid State Physics*. Wiley, 8 edition, 2004.

[34] S. Blundell. *Magnetism in condensed matter*. Oxford Master Series in Condensed Matter Physics, OUP Oxford, 2001.

[35] A. I. M. Rae. *Quantum Physics: Illusion or Reality?* Canto. Cambridge University Press, 2 edition, 2004.

[36] V. Baltz, A. Manchon, M. Tsoi, T. Moriyama, T. Ono, and Y. Tserkovnyak. Antiferromagnetic spintronics. *Reviews of Modern Physics*, 90(1):015005, 2018.

[37] A. Aharoni et al. *Introduction to the Theory of Ferromagnetism*, volume 109. Clarendon Press, 2000.

[38] R. C. O'Handley. *Magnetism-From Fundamentals to Nanoscale Dynamics*. John Wiley and sons ,Inc., 2000.

[39] N.W. Ashcroft and N.D. Mermin. *Solid State Physics*. Saunders College, Philadelphia, 1976.

[40] N. W. Ashcroft, N. D. Mermin, et al. Solid state physics, 1976.

[41] M. A. Ruderman and C. Kittel. Indirect exchange coupling of nuclear magnetic moments by conduction electrons. *Phys. Rev.*, 96:99–102, Oct 1954.

[42] T. Kasuya. A Theory of Metallic Ferro- and Antiferromagnetism on Zener's Model. *Progress of Theoretical Physics*, 16(1):45–57, 07 1956.

[43] K. Yosida. Magnetic properties of Cu-Mn alloys. *Phys. Rev.*, 106:893–898, Jun 1957.

[44] I. Dzyaloshinsky. A thermodynamic theory of "weak" ferromagnetism of antiferromagnetics. *Journal of physics and chemistry of solids*, 4(4):241–255, 1958.

[45] T. Moriya. Anisotropic superexchange interaction and weak ferromagnetism. *Physical Review*, 120(1):91, 1960.

[46] A. Fert and P. M. Levy. Role of anisotropic exchange interactions in determining the properties of spin-glasses. *Physical Review Letters*, 44(23):1538, 1980.

[47] U. Larsen. The RKKY indirect exchange interaction in metals in arbitrary continuous dimension. *Physics Letters A*, 85(8-9):471–473, 1981.

[48] A. Fert, V. Cros, and J. Sampaio. Skyrmions on the track. *Nature nanotechnology*, 8(3):152–156, 2013.

[49] M. A. Gilleo. Superexchange interaction in ferrimagnetic garnets and spinels which contain randomly incomplete linkages. *Journal of Physics and Chemistry of Solids*, 13(1-2):33–39, 1960.

[50] J. D. Jackson. *Classical electrodynamics*. Wiley, 3rd ed. edition, 1999.

[51] J. A. Osborn. Demagnetizing factors of the general ellipsoid. *Physical Review*, 67(11-12):351, 1945.

[52] C. Tannoudji. *Quantum mechanics*. Wiley, 1978.

[53] J. StöhrHans and C. Siegmann. *Modern magnetic materials : principles and applications*. Heidelberg:Springer Verlag Berlin Heidelberg, 2006.

[54] A. Hubert and R. Schäfer. *Magnetic domains: the analysis of magnetic microstructures*. Springer Science & Business Media, 2008.

[55] M. Farle. Ferromagnetic resonance of ultrathin metallic layers. *Reports on Progress in Physics*, 61(7):755, 1998.

[56] S. Chikazumi and C. D. Graham. *Physics of Ferromagnetism 2e*, volume 94. Oxford University Press on Demand, 2009.

[57] A.Fert. *The Discovery of Giant Magnetoresistance*. The Royal Swedish Academy of Sciences, 2007.

[58] T. Jungwirth, J. Wunderlich, V. Novák, K. Olejník, B. L. Gallagher, R. P. Campion, K. W. Edmonds, A. W. Rushforth, A. J. Ferguson, and P. Němec. Spin-dependent phenomena and device concepts explored in (Ga, Mn) As. *Reviews of Modern Physics*, 86(3):855, 2014.

[59] U. Mizutani. *Introduction to the electron theory of metals*. Cambridge university press, 2001.

[60] M. Müller and R. Gross. Finite size effects of the anisotropic magnetoresistance. 2017.

[61] A. G. Ravlik. AMR and GMR layers and multilayers for magnetic field sensors. In *Nanostructured Magnetic Materials and Their Applications*, pages 22–42. Springer, 2002.

[62] J. Sinova, S. O. Valenzuela, J. Wunderlich, C. H. Back, and T. Jungwirth. Spin Hall effects. *Reviews of Modern Physics*, 87(4):1213, 2015.

[63] K. Ando, S. Takahashi, J. Ieda, Y. Kajiwara, H. Nakayama, T. Yoshino, K. Harii, Y. Fujikawa, M. Matsuo, S. Maekawa, and E. Saitoh. Inverse spin-Hall effect induced by spin pumping in metallic system. *Journal of applied physics*, 109(10):103913, 2011.

[64] J. Sinova, D. Culcer, Q. Niu, N. A. Sinitsyn, T. Jungwirth, and A. H. MacDonald. Universal intrinsic spin Hall effect. *Physical Review Letters*, 92(12):126603, 2004.

[65] F. P. Witek. *Spin Hall Magnetoresistive Noise*. PhD thesis, Master's thesis (Technische Universität München 2013), 2013.

[66] H. Nakayama, M. Althammer, Y. T. Chen, K. Uchida, Y. Kajiwara, D. Kikuchi, T. Ohtani, S. Geprägs, M. Opel, S. Takahashi, et al. Spin Hall magnetoresistance induced by a nonequilibrium proximity effect. *Physical Review Letters*, 110(20):206601, 2013.

[67] N. Vlietstra, J. Shan, V. Castel, B. J. Van Wees, and J. B. Youssef. Spin-Hall magnetoresistance in platinum on yttrium iron garnet: Dependence on platinum thickness and in-plane/out-of-plane magnetization. *Physical Review B*, 87(18):184421, 2013.

[68] N. Vlietstra, J. Shan, B. J. Van Wees, M. Isasa, F. Casanova, and J. B. Youssef. Simultaneous detection of the spin-Hall magnetoresistance and the spin-Seebeck effect in platinum and tantalum on yttrium iron garnet. *Physical Review B*, 90(17):174436, 2014.

[69] P. Kim, J.and Sheng, S. Takahashi, S. Mitani, and M. Hayashi. Spin Hall magnetoresistance in metallic bilayers. *Physical Review Letters*, 116(9):097201, 2016.

[70] S. Cho, S. C. Baek, K. Lee, Y. Jo, and B. Park. Large spin Hall magnetoresistance and its correlation to the spin-orbit torque in W/CoFeB/MgO structures. *Scientific reports*, 5(1):1–9, 2015.

[71] M. S. Schreier. *Spin transfer torque mediated magnetization dynamics*. PhD thesis, Technische Universität München, 2017.

[72] Y. T. Chen, S. Takahashi, H. Nakayama, M. Althammer, S. T. B. Goennenwein, E. Saitoh, and G. E. W. Bauer. Theory of spin Hall magnetoresistance. *Phys. Rev. B*, 87:144411, Apr 2013.

[73] T. L. Gilbert. A phenomenological theory of damping in ferromagnetic materials. *IEEE Transactions on Magnetics*, 40(6):3443–3449, 2004.

[74] L. Landau and E. Lifshitz. On the theory of the dispersion of magnetic permeability in ferromagnetic bodies. *Phys. Z. Sowjetunion*, 8(153):101–114, 1935.

[75] T. L. Gilbert. A lagrangian formulation of the gyromagnetic equation of the magnetization field. *Phys. Rev.*, 100:1243, 1955.

[76] S Azzawi, AT Hindmarch, and D Atkinson. Magnetic damping phenomena in ferromagnetic thin-films and multilayers. *Journal of Physics D: Applied Physics*, 50(47):473001, 2017.

[77] M. Grobis, I. G. Rau, R. M. Potok, and D. Goldhaber-Gordon. Handbook of magnetism and advanced magnetic materials. *H. Kronmüller et al., Wiley*, page 1, 2007.

[78] J. Smit and H. G. Beljers. Ferromagnetic resonance absorption in $BaFe_{12}O_{19}$, a highly anisotropic crystal. *Philips Res. Rep*, 10(113):31, 1955.

[79] H. Suhl. Ferromagnetic resonance in nickel ferrite between one and two kilomegacycles. *Physical Review*, 97(2):555, 1955.

[80] Y. Zhai, Y. X. Xu, J. G. Long, Y. B. Xu, M. Lu, Z. H. Lu, H. R. Zhai, and J. A. C. Bland. Ferromagnetic resonance study of Fe superparamagnetic nanoclusters on GaAs(100). *Journal of Applied Physics*, 89(11):7290–7292, 2001.

[81] K. Lenz, H. Wende, W. Kuch, K. Baberschke, K. Nagy, and A. Jánossy. Two-magnon scattering and viscous Gilbert damping in ultrathin ferromagnets. *Phys. Rev. B*, 73:144424, Apr 2006.

[82] N. Bloembergen. On the ferromagnetic resonance in nickel and supermalloy. *Phys. Rev.*, 78:572–580, Jun 1950.

[83] F. Bloch. Nuclear induction. *Phys. Rev.*, 70:460–474, Oct 1946.

[84] S. V. Vonsovskii. *Ferromagnetic resonance*. Pergamon Press, Oxford, London Edinburgh, 1966.

[85] B. Heinrich, D. Fraitová, and V. Kamberský. The influence of s-d exchange on relaxation of magnons in metals. *physica status solidi (b)*, 23(2):501–507.

[86] V. Kamberský. Spin-orbital Gilbert damping in common magnetic metals. *Phys. Rev. B*, 76:134416, Oct 2007.

[87] R. Arias and D. L. Mills. Extrinsic contributions to the ferromagnetic resonance response of ultrathin films. *Phys. Rev. B*, 60:7395–7409, Sep 1999.

[88] H. Kurebayashi, T. D. Skinner, K. Khazen, K. Olejník, D. Fang, C. Ciccarelli, R. P. Campion, B. L. Gallagher, L. Fleet, A. Hirohata, et al. Uniaxial anisotropy of two-magnon scattering in an ultrathin epitaxial Fe layer on GaAs. *Applied Physics Letters*, 102(6):062415, 2013.

[89] Kh. Zakeri, J. Lindner, I. Barsukov, R. Meckenstock, M. Farle, U. Von Hörsten, H. Wende, W. Keune, J. Rocker, S. S. Kalarickal, et al. Spin dynamics in ferromagnets: Gilbert damping and two-magnon scattering. *Physical Review B*, 76(10):104416, 2007.

[90] L. Chen, S. Mankovsky, S. Wimmer, M. A. W. Schoen, H. S. Körner, M. Kronseder, D. Schuh, D. Bougeard, H. Ebert, D. Weiss, and C. H. Back. Emergence of anisotropic Gilbert damping in ultrathin Fe layers on GaAs(001). *Nature Physics*, 14(5):490–494, 2018.

[91] C. Kittel. Excitation of spin waves in a ferromagnet by a uniform rf field. *Physical Review*, 110(6):1295, 1958.

[92] M. H. Seavey Jr and P. E. Tannenwald. Direct observation of spin-wave resonance. *Physical Review Letters*, 1(5):168, 1958.

[93] C. Etz, L. Bergqvist, A. Bergman, A. Taroni, and O. Eriksson. Atomistic spin dynamics and surface magnons. *Journal of Physics: Condensed Matter*, 27(24):243202, 2015.

[94] S. Manuilov. *Ferromagnetic resonance in films with growth induced anisotropy*. PhD thesis, KTH Royal Institute of Technology, 2011.

[95] R. L. White and I. H. Solt Jr. Multiple ferromagnetic resonance in ferrite spheres. *Physical Review*, 104(1):56, 1956.

[96] L. R. Walker. Resonant modes of ferromagnetic spheroids. *Journal of Applied Physics*, 29(3):318–323, 1958.

[97] R. W. Damon and J. R. Eshbach. Magnetostatic modes of a ferromagnet slab. *Journal of Physics and Chemistry of Solids*, 19(3-4):308–320, 1961.

[98] B. Lenk, G. Eilers, J. Hamrle, and M. Münzenberg. Spin-wave population in nickel after femtosecond laser pulse excitation. *Physical Review B*, 82(13):134443, 2010.

[99] A. Mahmoud, F. Ciubotaru, F. Vanderveken, A. V. Chumak, S. Hamdioui, C. Adelmann, and S. Cotofana. Introduction to spin wave computing. *Journal of Applied Physics*, 128(16):161101, 2020.

[100] D. D. Stancil and A. Prabhakar. *Spin waves*, volume 5. Springer, 2009.

[101] S. Klingler, A. V. Chumak, T. Mewes, B. Khodadadi, C. Mewes, C. Dubs, O. Surzhenko, B. Hillebrands, and A. Conca. Measurements of the exchange stiffness of YIG films using broadband ferromagnetic resonance techniques. *Journal of Physics D: Applied Physics*, 48(1):015001, 2014.

[102] P. Dürrenfeld, F. Gerhard, J. Chico, R. K. Dumas, M. Ranjbar, A. Bergman, L. Bergqvist, A. Delin, C. Gould, L. W. Molenkamp, and J. Åkerman. Tunable damping, saturation magnetization, and exchange stiffness of half-Heusler NiMnSb thin films. *Physical Review B*, 92(21):214424, 2015.

[103] C. Kittel. Excitation of spin waves in a ferromagnet by a uniform rf field. *Phys. Rev.*, 110:1295–1297, Jun 1958.

[104] Y. Zhou, H. Jiao, Y. Chen, G. E. W. Bauer, and J. Xiao. Current-induced spin-wave excitation in pt/yig bilayer. *Phys. Rev. B*, 88:184403, Nov 2013.

[105] A. M. Portis. Low-lying spin wave modes in ferromagnetic films. *Applied Physics Letters*, 2(4):69–71, 1963.

[106] S. Maekawa, S. O. Valenzuela, E. Saitoh, and T. Kimura. *Spin current*, volume 22. Oxford University Press, 2017.

[107] J. A. Katine, F. J. Albert, R. A. Buhrman, E. B. Myers, and D. C. Ralph. Current-driven magnetization reversal and spin-wave excitations in Co/Cu/Co pillars. *Physical Review Letters*, 84(14):3149, 2000.

[108] S. DuttaGupta, S. Fukami, C. Zhang, H. Sato, M. Yamanouchi, F. Matsukura, and H. Ohno. Adiabatic spin-transfer-torque-induced domain wall creep in a magnetic metal. *Nature Physics*, 12(4):333–336, 2016.

[109] M. Tsoi, A. G. M. Jansen, J. Bass, W.-C. Chiang, M. Seck, V. Tsoi, and P. Wyder. Excitation of a magnetic multilayer by an electric current. *Physical Review Letters*, 80(19):4281, 1998.

[110] A. Brataas, Y. V. Nazarov, and G. E. W. Bauer. Spin-transport in multi-terminal normal metal-ferromagnet systems with non-collinear magnetizations. *The European Physical Journal B-Condensed Matter and Complex Systems*, 22(1):99–110, 2001.

[111] Y. Tserkovnyak, A. Brataas, and G. E. W. Bauer. Enhanced Gilbert damping in thin ferromagnetic films. *Phys. Rev. Lett.*, 88(11):117601, 2002.

[112] Y. Tserkovnyak and M. Mecklenburg. Electron transport driven by nonequilibrium magnetic textures. *Physical Review B*, 77(13):134407, 2008.

[113] D. M. Pozar. *Microwave engineering*. John Wiley & Sons, 2009.

[114] D. Fang, H. Kurebayashi, J. Wunderlich, K. Vỳbornỳ, L. P. Zârbo, R. P. Campion, A. Casiraghi, B. L. Gallagher, T. Jungwirth, and A. J. Ferguson. Spin–orbit-driven ferromagnetic resonance. *Nature nanotechnology*, 6(7):413–417, 2011.

[115] A. A. Tulapurkar, Y. Suzuki, A. Fukushima, H. Kubota, H. Maehara, K. Tsunekawa, D. D. Djayaprawira, N. Watanabe, and S. Yuasa. Spin-torque diode effect in magnetic tunnel junctions. *Nature*, 438(7066):339–342, 2005.

[116] J. C. Sankey, P. M. Braganca, A. G. F. Garcia, I. N. Krivorotov, R. A. Buhrman, and D. C. Ralph. Spin-transfer-driven ferromagnetic resonance of individual nanomagnets. *Physical Review Letters*, 96(22):227601, 2006.

[117] M. B. Jungfleisch, A. V. Chumak, A. Kehlberger, V. Lauer, D. H. Kim, M. C. Onbasli, C. A. Ross, M. Kläui, and B. Hillebrands. Thickness and power dependence of the spin-pumping effect in $Y_3Fe_5O_{12}$/Pt heterostructures measured by the inverse spin Hall effect. *Physical Review B*, 91(13):134407, 2015.

[118] S. Petit, C. Baraduc, C. Thirion, U. Ebels, Y. Liu, M. Li, P. Wang, and B. Dieny. Spin-torque influence on the high-frequency magnetization fluctuations in magnetic tunnel junctions. *Physical Review Letters*, 98(7):077203, 2007.

[119] N. Bloembergen and R. W. Damon. Relaxation effects in ferromagnetic resonance. *Physical Review*, 85(4):699, 1952.

[120] R. W. Damon. Relaxation effects in the ferromagnetic resonance. *Reviews of Modern Physics*, 25(1):239, 1953.

[121] J. R. Macdonald. Ferromagnetic resonance and the internal field in ferromagnetic materials. *Proceedings of the Physical Society. Section A*, 64(11):968, 1951.

[122] B. Heinrich, D. Fraitová, and V. Kamberskỳ. The influence of s-d Exchange on Relaxation of Magnons in Metals. *physica status solidi (b)*, 23(2):501–507, 1967.

[123] V. Kambersky and C. E. Patton. Spin-wave relaxation and phenomenological damping in ferromagnetic resonance. *Physical Review B*, 11(7):2668, 1975.

[124] V. Kamberskỳ. On ferromagnetic resonance damping in metals. *Czechoslovak Journal of Physics B*, 26(12):1366–1383, 1976.

[125] V. Kamberskỳ. Spin-orbital Gilbert damping in common magnetic metals. *Physical Review B*, 76(13):134416, 2007.

[126] J. Kuneš and V. Kamberskỳ. First-principles investigation of the damping of fast magnetization precession in ferromagnetic 3 d metals. *Physical Review B*, 65(21):212411, 2002.

[127] V. Kamberskỳ. On the Landau–Lifshitz relaxation in ferromagnetic metals. *Canadian Journal of Physics*, 48(24):2906–2911, 1970.

[128] M. W. Covington, G. Ju, W. Scholz, and M. K. Minor. Recording heads including a magnetically damped write pole and recording systems including such heads, September 29 2009. US Patent 7,595,959.

[129] E. Schlömann. Spin-wave analysis of ferromagnetic resonance in polycrystalline ferrites. *Journal of Physics and chemistry of solids*, 6(2-3):242–256, 1958.

[130] S. Geschwind and A. M. Clogston. Narrowing effect of dipole forces on inhomogeneously broadened lines. *Physical Review*, 108(1):49, 1957.

[131] M. J. Hurben, D. R. Franklin, and C. E. Patton. Angle dependence of the ferromagnetic resonance linewidth in easy-axis and easy-plane single crystal hexagonal ferrite disks. *Journal of applied physics*, 81(11):7458–7467, 1997.

[132] C. E. Patton, C. H. Wilts, and F. B. Humphrey. Relaxation processes for ferromagnetic resonance in thin films. *Journal of Applied Physics*, 38(3):1358–1359, 1967.

[133] R. C. LeCraw, E. G. Spencer, and C. S. Porter. Ferromagnetic resonance line width in yttrium iron garnet single crystals. *Physical Review*, 110(6):1311, 1958.

[134] G. Woltersdorf and B. Heinrich. Two-magnon scattering in a self-assembled nanoscale network of misfit dislocations. *Physical Review B*, 69(18):184417, 2004.

[135] D. J. Twisselmann and R. D. McMichael. Intrinsic damping and intentional ferromagnetic resonance broadening in thin Permalloy films. *Journal of applied physics*, 93(10):6903–6905, 2003.

[136] R. D. McMichael, D. J. Twisselmann, and A. Kunz. Localized ferromagnetic resonance in inhomogeneous thin films. *Physical Review Letters*, 90(22):227601, 2003.

[137] C. Chappert, K. Le Dang, P. Beauvillain, H. Hurdequint, and D. Renard. Ferromagnetic resonance studies of very thin cobalt films on a gold substrate. *Physical Review B*, 34(5):3192, 1986.

[138] S. Mizukami, Y. Ando, and T. Miyazaki. The study on ferromagnetic resonance linewidth for NM/80NiFe/NM (NM= Cu, Ta, Pd and Pt) films. *Japanese journal of applied physics*, 40(2R):580, 2001.

[139] R. Arias and D. L. Mills. Extrinsic contributions to the ferromagnetic resonance response of ultrathin films. *Physical Review B*, 60(10):7395, 1999.

[140] J. Lindner, I. Barsukov, C. Raeder, C. Hassel, O. Posth, R. Meckenstock, P. Landeros, and D. L. Mills. Two-magnon damping in thin films in case of canted magnetization: Theory versus experiment. *Physical Review B*, 80(22):224421, 2009.

[141] J. Dubowik, K. Załęski, H. Głowiński, and I. Gościańska. Angular dependence of ferromagnetic resonance linewidth in thin films. *Physical Review B*, 84(18):184438, 2011.

[142] V. G. Bar'yakhtar. Crystal symmetry and the structure of the relaxation terms in the dynamic equations of motion for magnetization. *PhyB*, 159(1):20–25, 1989.

[143] V. G. Baryakhtar, BA Ivanov, AL Sukstanskii, and E Yu Melikhov. Soliton relaxation in magnets. *Physical Review B*, 56(2):619, 1997.

[144] V. G. Bar'yakhtar. Spontaneous ground-state degeneracy and relaxation processes in a ferromagnet. *Fizika Tverdogo Tela*, 29(5):1317–1322, 1987.

[145] T. Mewes, R. L. Stamps, H. Lee, E. Edwards, M. Bradford, C. K. A. Mewes, Z. Tadisina, and S. Gupta. Unidirectional magnetization relaxation in exchange-biased films. *IEEE Magnetics Letters*, 1:3500204–3500204, 2010.

[146] A. N. Anisimov, M. Farle, P. Poulopoulos, W. Platow, K. Baberschke, P. Isberg, R. Wäppling, A. M. N. Niklasson, and O. Eriksson. Orbital Magnetism and Magnetic Anisotropy Probed with Ferromagnetic Resonance. *Phys. Rev. Lett.*, 82:2390–2393, Mar 1999.

[147] R. Yilgin, Y. Sakuraba, M. Oogane, S. Mizukami, Y. Ando, and T. Miyazaki. Anisotropic intrinsic damping constant of Epitaxial Co_2MnSi Heusler Alloy Films. *Japanese Journal of Applied Physics*, 46, 2007.

[148] Y. Kasatani and Y. Nozaki. Crystallographic anisotropy of the intrinsic Gilbert damping for single-crystalline Fe film. *Journal of the Magnetics Society of Japan*, 39(6):221–226, 2015.

[149] A. Conca, S. Keller, M. R. Schweizer, E. Th. Papaioannou, and B. Hillebrands. Separation of the two-magnon scattering contribution to damping for the determination of the spin mixing conductance. *Phys. Rev. B*, 98:214439, Dec 2018.

[150] Q. Qin, S. He, H. Wu, P. Yang, L. Liu, W. Song, S. J. Pennycook, and J. Chen. arXiv:1804.00554, 04 2018.

[151] Y. Li, S. S. L. Zeng, F.and Zhang, H. Shin, H. Saglam, V. Karakas, O. Ozatay, J. E. Pearson, O. G. Heinonen, Y. Wu, A. Hoffmann, and W. Zhang. Giant Anisotropy of Gilbert Damping in Epitaxial CoFe Films. 122:117203, Mar 2019.

[152] J. Seib, D. Steiauf, and M. Fähnle. Linewidth of ferromagnetic resonance for systems with anisotropic damping. *Phys. Rev. B*, 79:092418, Mar 2009.

[153] K. Gilmore, Y. U. Idzerda, and M. D. Stiles. Spin-orbit precession damping in transition metal ferromagnets. *Journal of Applied Physics*, 103(7):07D303, 2008.

[154] K. Gilmore, Y. U. Idzerda, and M. D. Stiles. Identification of the Dominant Precession-Damping Mechanism in Fe, Co, and Ni by First-Principles Calculations. *Phys. Rev. Lett.*, 99:027204, Jul 2007.

[155] V. Kamberský. On ferromagnetic resonance damping in metals. *Czechoslovak Journal of Physics B*, 26(12):1366–1383, Dec 1976.

[156] A. Kumar, F. Pan, S. Husain, S. Akansel, R. Brucas, L. Bergqvist, S. Chaudhary, and P. Svedlindh. Temperature-dependent Gilbert damping of Co_2FeAl thin films with different degree of atomic order. *Phys. Rev. B*, 96:224425, Dec 2017.

[157] A. Manchon, H. C. Koo, J. Nitta, S. M. Frolov, and R. A. Duine. New perspectives for rashba spin-orbit coupling. *Nature Materials*, 14:871 EP –, Aug 2015. Review Article.

[158] F. Heusler and E. Take. The nature of the Heusler alloys. *Transactions of the Faraday Society*, 8(October):169–184, 1912.

[159] A. Hirohata, M. Kikuchi, N. Tezuka, K. Inomata, J. S. Claydon, Y. B. Xu, and G. Van der Laan. Heusler alloy/semiconductor hybrid structures. *Current Opinion in Solid State and Materials Science*, 10(2):93–107, 2006.

[160] R. A. de Groot, F. M. Mueller, P. G. van Engen, and K. H. J. Buschow. New class of materials: Half-metallic ferromagnets. *Phys. Rev. Lett.*, 50:2024–2027, Jun 1983.

[161] J.-S. Kang, J.H. Hong, S.W. Jung, Y.P. Lee, J.-G. Park, C.G. Olson, S.J. Youn, and B.I. Min. Electronic structures of the half-metallic Heusler alloys: NiMnSb and PtMnSb. *Solid State Communications*, 88(8):653 – 657, 1993.

[162] F. Gerhard, M. Baussenwein, L. Scheffler, J. Kleinlein, C. Gould, and L. W. Molenkamp. Engineering the magnetic anisotropy axes in epitaxial half-Heusler NiMnSb by Pt and Ta capping. *Applied Physics Letters*, 111(17):172402, 2017.

[163] M. J. Otto, R. A. M. van Woerden, P. J. van der Valk, J. Wijngaard, C. F. van Bruggen, C. Haas, and K. H. J. Buschow. Half-metallic ferromagnets. I. structure and magnetic properties of NiMnSb and related inter-metallic compounds. *Journal of Physics: Condensed Matter*, 1(13):2341–2350, apr 1989.

[164] I. Galanakis, E. Şaşıoğlu, and K. Özdoğan. Magnetic phase transition in half-metallic CoMnSb and NiMnSb semi-Heusler alloys upon Cu doping: First-principles calculations. *Phys. Rev. B*, 77:214417, Jun 2008.

[165] L. Ritchie, G. Xiao, Y. Ji, T. Y. Chen, C. L. Chien, M. Zhang, J. Chen, Z. Liu, G. Wu, and X. X. Zhang. Magnetic, structural, and transport properties of the Heusler alloys Co_2MnSi and NiMnSb. *Physical Review B*, 68(10):104430, 2003.

[166] Z. Wen, T. Kubota, T. Yamamoto, and K. Takanashi. Fully epitaxial $C1_b$-type NiMnSb half-Heusler alloy films for current-perpendicular-to-plane giant magnetoresistance devices with a Ag spacer. *Scientific Reports*, 5, Dec 2015.

[167] M. Jourdan, J. Minár, J. Braun, A. Kronenberg, S. Chadov, B. Balke, A. Gloskovskii, M. Kolbe, H.-J. Elmers, G. Schönhense, et al. Direct observation of half-metallicity in the Heusler compound Co_2MnSi. *Nature communications*, 5(1):1–5, 2014.

[168] Z. Bai, L. Shen, G. Han, and Y. P. Feng. Data storage: review of Heusler compounds. In *Spin*, volume 2, page 1230006. World Scientific, 2012.

[169] B. Heinrich, G. Woltersdorf, R. Urban, O. Mosendz, G. Schmidt, P. Bach, L. Molenkamp, and E. Rozenberg. Magnetic properties of NiMnSb (001)

films grown on InGaAs/InP (001). *Journal of applied physics*, 95(11):7462–7464, 2004.

[170] A. Koveshnikov, G. Woltersdorf, J. Q. Liu, B. Kardasz, O. Mosendz, B. Heinrich, K. L. Kavanagh, P. Bach, A. S. Bader, C. Schumacher, et al. Structural and magnetic properties of NiMnSb/InGaAs/InP (001). *Journal of Applied Physics*, 97(7):073906, 2005.

[171] Y. Kasatani, S. Yamada, H. Itoh, M. Miyao, K. Hamaya, and Y. Nozaki. Large anisotropy of Gilbert damping constant in $L2_1$-ordered Co_2FeSi film. *Applied Physics Express*, 7(12), 2014.

[172] C. Ciccarelli, L. Anderson, V. Tshitoyan, A. J. Ferguson, F. Gerhard, C. Gould, L. W. Molenkamp, J. Gayles, J. Zelezný, L. Smejkal, Z. Yuan, J. Sinova, F. Freimuth, and T. Jungwirth. Room-temperature spin-orbit torque in NiMnSb. *Nature Physics*, 12:855 EP –, May 2016. Article.

[173] F Gerhard, C Schumacher, C Gould, and LW Molenkamp. Control of the magnetic in-plane anisotropy in off-stoichiometric NiMnSb. *Journal of Applied Physics*, 115(9):094505, 2014.

[174] B. Botters, F. Giesen, J. Podbielski, P. Bach, G. Schmidt, L. W. Molenkamp, and D. Grundler. Stress dependence of ferromagnetic resonance and magnetic anisotropy in a thin NiMnSb film on InP (001). *Applied physics letters*, 89(24):242505, 2006.

[175] Z. Wen, T. Kubota, T. Yamamoto, and K. Takanashi. Fully epitaxial $C1_b$-type NiMnSb half-Heusler alloy films for current-perpendicular-to-plane giant magnetoresistance devices with a Ag spacer. *Scientific reports*, 5(1):1–10, 2015.

[176] C. Ciccarelli, L. Anderson, V. Tshitoyan, A. J. Ferguson, F. Gerhard, C. Gould, L. W. Molenkamp, J. Gayles, J. Železnỳ, L. Šmejkal, et al. Room-temperature spin-orbit torque in NiMnSb. *Nature Physics*, 12(9):855–860, 2016.

[177] A. Chernyshov, M. Overby, X. Liu, J. K. Furdyna, Y. Lyanda-Geller, and L. P. Rokhinson. Evidence for reversible control of magnetization in a ferromagnetic material by means of spin–orbit magnetic field. *Nature Physics*, 5(9):656–659, 2009.

[178] H. Kurebayashi, J. Sinova, D. Fang, A. C. Irvine, T. D. Skinner, J. Wunderlich, V. Novák, R. P. Campion, B. L. Gallagher, E. K. Vehstedt, et al. An antidamping spin–orbit torque originating from the berry curvature. *Nature nanotechnology*, 9(3):211–217, 2014.

[179] P. R. Pukite, S. Batra, and P. I. Cohen. Anisotropic Growth Processes on GaAs (100) And Ge (100). In *Growth of Compound Semiconductors*, volume 796, pages 22–26. International Society for Optics and Photonics, 1987.

[180] C.-Y. Fong, J. E. Pask, and L. H. Yang. *Half-metallic materials and their properties*, volume 2. World Scientific, 2013.

[181] M. E. Straumanis and C. D. Kim. Phase extent of gallium arsenide determined by the lattice constant and density method. *Acta Crystallographica*, 19(2):256–259, 1965.

[182] J. Narayan and B. C. Larson. Domain epitaxy: A unified paradigm for thin film growth. *Journal of Applied Physics*, 93(1):278–285, 2003.

[183] B. Kwon, Y. Sakuraba, H. Sukegawa, S. Li, G. Qu, T. Furubayashi, and K. Hono. Anisotropic magnetoresistance and current-perpendicular-to-plane giant magnetoresistance in epitaxial NiMnSb-based multilayers. *Journal of Applied Physics*, 119(2):023902, 2016.

[184] D. Orgassa, H. Fujiwara, T. C. Schulthess, and W. H. Butler. Disorder dependence of the magnetic moment of the half-metallic ferromagnet NiMnSb from first principles. *Journal of Applied Physics*, 87(9):5870–5871, 2000.

[185] M. Belmeguenai, H. Tuzcuoglu, M. S. Gabor, T. Petrisor Jr, C. Tiusan, F. Zighem, S. M. Chérif, and P. Moch. Co_2FeAl Heusler thin films grown

on Si and MgO substrates: Annealing temperature effect. *Journal of Applied Physics*, 115(4):043918, 2014.

[186] O. Thomas, Q. Shen, P. Schieffer, N. Tournerie, and B. Lépine. Interplay between anisotropic strain relaxation and uniaxial interface magnetic anisotropy in epitaxial Fe films on (001) GaAs. *Physical Review Letters*, 90(1):017205, 2003.

[187] Y. B. Xu, D. J. Freeland, M. Tselepi, and J. A. C. Bland. Anisotropic lattice relaxation and uniaxial magnetic anisotropy in Fe/InAs (100)- 4×2. *Physical Review B*, 62(2):1167, 2000.

[188] C. Ciccarelli, L. Anderson, V. Tshitoyan, A. J. Ferguson, F. Gerhard, C. Gould, L. W. Molenkamp, J. Gayles, J. Železnỳ, L. Šmejkal, et al. Room-temperature spin–orbit torque in NiMnSb. *Nature physics*, 12(9):855–860, 2016.

[189] A. Riegler. *Ferromagnetic resonance study of the Half-Heusler alloy NiMnSb:The benefit of using NiMnSb as a ferromagnetic layer in pseudo-spin-valve based spin-torque oscillators*. Südwestdeutscher Verlag für Hochschulschriften, 2012.

[190] R. D. McMichael and P. Krivosik. Classical model of extrinsic ferromagnetic resonance linewidth in ultrathin films. *IEEE transactions on magnetics*, 40(1):2–11, 2004.

[191] W. K. Peria, T. A. Peterson, A. P. McFadden, T. Qu, C. Liu, C. J. Palmstrøm, and P. A. Crowell. Interplay of large two-magnon ferromagnetic resonance linewidths and low Gilbert damping in Heusler thin films. *Physical Review B*, 101(13):134430, 2020.

[192] R. L. Hota, G. S. Tripathi, and J. N. Mohanty. Theory of effective g factors and effective masses in diluted magnetic semiconductors. *Phys. Rev. B*, 47:9319–9327, Apr 1993.

[193] M. A. W. Schoen, D. Thonig, M. L. Schneider, T. J. Silva, H. T. Nembach, O. Eriksson, O. Karis, and J. M. Shaw. Ultra-low magnetic damping of a metallic ferromagnet. *Nature Physics*, 12(9):839, 2016.

[194] R. F. Tinder. *Tensor properties of solids: phenomenological development of the tensor properties of crystals*, volume 4. Morgan & Claypool Publishers, 2008.

[195] N. Zhao, A. Sud, H. Sukegawa, S. Komori, K. Rogdakis, K. Yamanoi, J. Patchett, J. W. A. Robinson, C. Ciccarelli, and H. Kurebayashi. Growth, strain, and spin-orbit torques in epitaxial Ni-Mn-Sb films sputtered on GaAs. *Physical Review Materials*, 5(1):014413, 2021.

[196] H. K. Gweon, K.-J. Lee, and S. H. Lim. Influence of MgO sputtering power and post annealing on strength and angular dependence of spin-orbit torques in Pt/Co/MgO trilayers. *Phys. Rev. Applied*, 11:014034, Jan 2019.

[197] P. Dürrenfeld, F. Gerhard, J. Chico, R. K. Dumas, M. Ranjbar, A. Bergman, L. Bergqvist, A. Delin, C. Gould, L. W. Molenkamp, and J. Åkerman. Tunable damping, saturation magnetization, and exchange stiffness of half-Heusler NiMnSb thin films. *Phys. Rev. B*, 92:214424, Dec 2015.

[198] A. V. Chumak, V. I. Vasyuchka, A. A. Serga, and B. Hillebrands. Magnon spintronics. *Nature Physics*, 11:453–461, 2015.

[199] A. F. Kockum, A. Miranowicz, S. D. Liberato, S. Savasta, and Franco Nori. Ultrastrong coupling between light and matter. *Nat. Rev.Phys.*, 1:19, 2019.

[200] Z.-L. Xiang, S. Ashhab, J. Q. You, and Franco Nori. Hybrid quantum circuits: Superconducting circuits interacting with other quantum systems. *Rev. Mod. Phys.*, 85:623, 2013.

[201] A. A. Clerk, K. W. Lehnert, P. Bertet, J. R. Petta, and Y. Nakamura. Hybrid quantum systems with circuit quantum electrodynamics. *Nat. Phys.*, 16:257, 2020.

[202] L. Quirion, D. Tabuchi, A. Y., Gloppe, K. Usami, and Y. Nakamura. Hybrid quantum systems based on magnonics. *Appl. Phys. Express*, 12:070101, 2019.

[203] M. Harder and C.-M. Hu. *Cavity Spintronics: An Early Review of Recent Progress in the Study of MagnonPhoton Level Repulsion*. Academic Press, Cambridge, 2018.

[204] H. Huebl, C. W. Zollitsch, J. Lotze, F. Hocke, M. Greifenstein, A. Marx, R. Gross, and S. T. B. Goennenwein. High cooperativity in coupled microwave resonator ferrimagnetic insulator hybrids. *Phys. Rev. Lett.*, 111:127003, 2013.

[205] X. Zhang, C. L. Zou, L. Jiang, and H. X. Tang. Strongly coupled magnons and cavity microwave photons. *Phys. Rev. Lett.*, 113:156401, 2014.

[206] C. Eichler, A. J. Sigillito, S. A. Lyon, and J. R. Petta. Electron Spin Resonance at the Level of 10^4 Spins Using Low Impedance Superconducting Resonators. *Phys. Rev. Lett.*, 118:037701, 2017.

[207] G. Tosi, F. A. Mohiyaddin, H. Huebl, and A. Morello. Circuit-quantum electrodynamics with direct magnetic coupling to single-atom spin qubits in isotopically enriched ^{28}Si. *AIP Adv.*, 4:087122, 2014.

[208] B A Kalinikos and A N Slavin. Theory of dipole-exchange spin wave spectrum for ferromagnetic films with mixed exchange boundary conditions. *J. Phys. C: Solid State Phys.*, 19:7013, 1986.

[209] P. Grünberg. *Light scattering from spin waves in thin films and layered magnetic structures*, pages 303–335. Springer Berlin Heidelberg, Berlin, Heidelberg, 1989.

[210] L. Liensberger, A. Kamra, H. Maier-Flaig, S. Geprägs, A. Erb, S. T. B. Goennenwein, R. Gross, W. Belzig, H. Huebl, and M. Weiler. Exchange-enhanced

ultrastrong magnon-magnon coupling in a compensated ferrimagnet. *Phys. Rev. Lett.*, 123(11):117204, 2019.

[211] D. MacNeill, J. T. Hou, D. R. Klein, P. Zhang, P. Jarillo-Herrero, and L. Liu. Gigahertz Frequency Antiferromagnetic Resonance and Strong Magnon-Magnon Coupling in the Layered Crystal $CrCl_3$. *Phys. Rev. Lett.*, 123(4):047204, 2019.

[212] J. Chen, C. Liu, T. Liu, Y. Xiao, K. Xia, G. E. W. Bauer, M. Wu, and Haiming Yu. Strong interlayer magnon-magnon coupling in magnetic metal-insulator hybrid nanostructures. *Phys. Rev. Lett.*, 120:217202, 2018.

[213] S. Klingler, V. Amin, S. Geprags, K. Ganzhorn, H. Maier-Flaig, M. Althammer, H. Huebl, R. Gross, R. D. McMichael, M. D. Stiles, S. T. B. Goennenwein, and M. Weiler. Spin-Torque Excitation of Perpendicular Standing Spin Waves in Coupled YIG/Co Heterostructures. *Phys. Rev. Lett.*, 120:127201, 2018.

[214] Y. Li, W. Cao, V. P. Amin, Z. Zhang, J. Gibbons, J. Sklenar, J. Pearson, P. M. Haney, M. D. Stiles, W. E. Bailey, V. Novosad, A. Hoffmann, and W. Zhang. Unknown title. *Phys. Rev. Lett.*, 124:117202, 2020.

[215] R. A. Duine, K.-J. Lee, S. S. P. Parkin, and M. D. Stiles. Synthetic antiferromagnetic spintronics. *Nat. Phys.*, 14:217, 2018.

[216] Y. Li, W. Zhang, V. Tyberkevych, W.-K. Kwok, A. Hoffmann, and V. Novosad. Hybrid magnonics: Physics, circuits, and applications for coherent information processing. *Journal of Applied Physics*, 128(13):130902, 2020.

[217] A. Guedes, M. J. Mendes, P. P. Freitas, and J. L. Martins. Study of synthetic ferrimagnet-synthetic antiferromagnet structures for magnetic sensor application. *Journal of Applied Physics*, 99(8):08B703, 2006.

[218] P. Grünberg, R. Schreiber, Y. Pang, M. B. Brodsky, and H. Sowers. Layered magnetic structures: Evidence for antiferromagnetic coupling of Fe layers across Cr interlayers. *Physical Review Letters*, 57(19):2442, 1986.

[219] M. B. Salamon, S. Sinha, J. J. Rhyne, J. E. Cunningham, R. W. Erwin, J. Borchers, and C. P. Flynn. Long-range incommensurate magnetic order in a Dy-Y multilayer. *Physical Review Letters*, 56(3):259, 1986.

[220] C. F. Majkrzak, J. W. Cable, J. Kwo, M. Hong, D. B. McWhan, Y. Yafet, J. V. Waszczak, and C. Vettier. Observation of a magnetic antiphase domain structure with long-range order in a synthetic Gd-Y superlattice. *Physical Review Letters*, 56(25):2700, 1986.

[221] F. Keffer and C. Kittel. Theory of antiferromagnetic resonance. *Physical Review*, 85(2):329, 1952.

[222] S. M. Rezende, A. Azevedo, and R. L. Rodríguez-Suárez. Introduction to antiferromagnetic magnons. *J. Appl. Phys.*, 126:151101, 2019.

[223] J. J. Krebs, P. Lubitz, A. Chaiken, and G. A. Prinz. Observation of magnetic resonance modes of Fe layers coupled via intervening Cr. *J. Appl. Phys.*, 67:5920, 1990.

[224] P. Grunberg, R. Schreiber, Y. Pang, M. B. Brodsky, and H. Sowers. Layered magnetic structures: Evidence for antiferromagnetic coupling of Fe layers across Cr interlayers. *Phys. Rev. Lett.*, 57:2442, 1986.

[225] Z. Zhang, L. Zhou, P. E. Wigen, and K. Ounadjela. Angular dependence of ferromagnetic resonance in exchange-coupled Co/Ru/Co trilayer structures. *Phys. Rev. B*, 50:6094, 1994.

[226] A. Konovalenko, E. Lindgren, S. S. Cherepov, V. Korenivski, and D. C. Worledge. Spin dynamics of two-coupled nanomagnets in spin-flop tunnel junctions. *Phys. Rev. B*, 80:144425, 2009.

[227] T. Seki, H. Tomita, A. A. Tulapurkar, M. Shiraishi, T. Shinjo, and Y. Suzuk. Spin-transfer-torque-induced ferromagnetic resonance for Fe/Cr/Fe layers with an antiferromagnetic coupling field. *Appl. Phys. Lett.*, 94:212505, 2009.

[228] A. Kamimaki, S. Iihama, T. Taniguchi, and S. Mizukami. All-optical detection and evaluation of magnetic damping in synthetic antiferromagnet. *Appl. Phys. Lett.*, 115:132402, 2019.

[229] W. Wang, P. Li, C. Cao, F. Liu, R. Tang, G. Chai, and C. Jiang. Temperature dependence of interlayer exchange coupling and Gilbert damping in synthetic antiferromagnetic trilayers investigated using broadband ferromagnetic resonance. *Appl. Phys. Lett.*, 113:042401, 2018.

[230] M. Ishibashi, Yoichi Shiota, T. Li, S. Funada, T. Moriyama, and T. Ono. Switchable giant nonreciprocal frequency shift of propagating spin waves in synthetic antiferromagnets. *Sci. Adv.*, 6:eaaz6931, 2020.

[231] T. Taniguchi and H. Imamura. Enhancement of the Gilbert damping constant due to spin pumping in noncollinear ferromagnet/nonmagnet/ferromagnet trilayer systems. *Phys. Rev. B*, 76(9):092402, 2007.

[232] S. Takahashi. Giant enhancement of spin pumping in the out-of-phase precession mode. *Appl. Phys. Lett.*, 104:052407, 2014.

[233] T. Chiba, G. E. W. Bauer, and S. Takahashi. Magnetization damping in noncollinear spin valves with antiferromagnetic interlayer couplings. *Phys. Rev. B*, 92(5):054407, 2015.

[234] A. A. Timopheev, Yu. G. Pogorelov, S. Cardoso, P. P. Freitas, G. N. Kakazei, and N. A. Sobolev. Dynamic exchange via spin currents in acoustic and optical modes of ferromagnetic resonance in spin-valve structures. *Phys. Rev. B*, 89:144410, 2014.

[235] K. Tanaka, T. Moriyama, M. Nagata, T. Seki, K. Takanashi, S. Takahashi, and T. Ono. Linewidth broadening of optical precession mode in synthetic antiferromagnet. *Appl. Phys. Express*, 7:063010, 2014.

[236] H. Yang, Y. Li, and W. E. Bailey. Large spin pumping effect in antisymmetric precession of $Ni_{79}Fe_{21}$/Ru/$Ni_{79}Fe_{21}$. *Appl. Phys. Lett.*, 108:242404, 2016.

[237] S. Sorokin, R. A. Gallardo, C. Fowley, K. Lenz, A. Titova, G. Y. P Atcheson, G. Dennehy, K. Rode, J. Fassbender, J. Lindner, and A. M. Deac. Magnetization dynamics in synthetic antiferromagnets: Role of dynamical energy and mutual spin pumping. *Phys. Rev. B*, 101:144410, 2020.

[238] X. M. Liu, H. T. Nguyen, J. Ding, M. G. Cottam, and A. O. Adeyeye. Interlayer coupling in $Ni_{80}Fe_{20}$/Ru/$Ni_{80}Fe_{20}$ multilayer films: Ferromagnetic resonance experiments and theory. *Phys. Rev. B*, 90:064428, 2014.

[239] S. O. Demokritov. Biquadratic interlayer coupling in layered magnetic systems. *Journal of Physics D: Applied Physics*, 31(8):925, 1998.

[240] M. Belmeguenai, T. Martin, G. Woltersdorf, M. Maier, and G. Bayreuther. Frequency-and time-domain investigation of the dynamic properties of interlayer-exchange-coupled $Ni_{81}Fe_{19}$/ Ru/$Ni_{81}Fe_{19}$ thin films. *Physical Review B*, 76(10):104414, 2007.

[241] R. H. Koch, G. Grinstein, G. A. Keefe, Yu Lu, P. L. Trouilloud, W. J. Gallagher, and S. S. P. Parkin. Thermally assisted magnetization reversal in submicron-sized magnetic thin films. *Physical Review Letters*, 84(23):5419, 2000.

[242] R. Sbiaa, I. A. Al-Omari, Parashu R. Kharel, M. Ranjbar, D. J. Sellmyer, J. Åkerman, and S. N. Piramanayagam. Temperature effect on exchange coupling and magnetization reversal in antiferromagnetically coupled (Co/Pd) multilayers. *Journal of Applied Physics*, 118(6):063902, 2015.

[243] K. Rogdakis, A. Sud, M. Amado, C. M. Lee, L. McKenzie-Sell, K.-R. Jeon, M. Cubukcu, M. G. Blamire, J. W. A. Robinson, L. F. Cohen, and H. Kurebayashi. Spin transport parameters of NbN thin films characterised by spin pumping experiments. *Phys. Rev. Mater.*, 3:014406, 2019.

[244] P. K. Streit and G. E. Everett. Antiferromagnetic resonance in EuTe. *Phys. Rev. B*, 21(1):169, 1980.

[245] V. S. MANDEL, V. D. Voronkov, and D. E. Gromzin. Antiferromagnetic resonance in MnO. *SOVIET PHYSICS JETP*, 36:521, 1973.

[246] A. Kamimaki, S. Iihama, K. Z. Suzuki, N. Yoshinaga, and S. Mizukami. Parametric Amplication of Magnons in Synthetic Antiferromagnets. *Phys. Rev. Appl.*, 13:044036, 2020.

[247] A. F. Kockum, A. Miranowicz, S. De Liberato, S. Savasta, and F. Nori. Ultrastrong coupling between light and matter. *Nature Reviews Physics*, 1(1):19–40, 2019.

[248] D. S. Dovzhenko, S. V. Ryabchuk, Y. P. Rakovich, and I. R. Nabiev. Light–matter interaction in the strong coupling regime: configurations, conditions, and applications. *Nanoscale*, 10(8):3589–3605, 2018.

[249] B. Heinrich, Y. Tserkovnyak, G. Woltersdorf, A. Brataas, R. Urban, and G. E. W. Bauer. Dynamic exchange coupling in magnetic bilayers. *Phys. Rev.Lett.*, 90:187601, 2003.

[250] K. Eid, R. Fonck, M. AlHaj Darwish, W. P. Pratt Jr., and J. Bass. Current-perpendicular-to-plane-magnetoresistance properties of Ru and Co/Ru interfaces. *J. Appl. Phys.*, 91:8102, 2002.

[251] H. J. Carmichael, R. J. Brecha, M. G. Raizen, H. J. Kimble, and P. R. Rice. Subnatural linewidth averaging for coupled atomic and cavity-mode oscillators. *Phys. Rev. A*, 40:5516, 1989.

[252] M. Harder, L. Bai, P. Hyde, and C.-M. Hu. Topological properties of a coupled spin-photon system induced by damping. *Phys. Rev. B*, 95:214411, 2017.

[253] L. Bai, M. Harder, Y. P. Chen, X. Fan, J. Q. Xiao, and C.-M. Hu. Spin pumping in electrodynamically coupled magnon-photon systems. *Physical Review Letters*, 114(22):227201, 2015.

[254] N. J. Lambert, J. A. Haigh, and A. J. Ferguson. Identification of spin wave modes in yttrium iron garnet strongly coupled to a co-axial cavity. *Journal of Applied Physics*, 117(5):053910, 2015.

[255] S. Kosen, A. F. van Loo, D. A. Bozhko, L. Mihalceanu, and A. D. Karenowska. Microwave magnon damping in YIG films at millikelvin temperatures. *APL Materials*, 7(10):101120, 2019.

[256] Y. Kubo, F. R. Ong, P. Bertet, D. Vion, V. Jacques, D. Zheng, A. Dréau, J.-F. Roch, A. Auffèves, F. Jelezko, et al. Strong coupling of a spin ensemble to a superconducting resonator. *Physical Review Letters*, 105(14):140502, 2010.

[257] D. I. Schuster, A. P. Sears, E. Ginossar, L. DiCarlo, L. Frunzio, J. J. L. Morton, H. Wu, G. A. D. Briggs, B. B. Buckley, D. D. Awschalom, et al. High-cooperativity coupling of electron-spin ensembles to superconducting cavities. *Physical Review Letters*, 105(14):140501, 2010.

[258] D. Lachance-Quirion, Y. Tabuchi, A. Gloppe, K. Usami, and Y. Nakamura. Hybrid quantum systems based on magnonics. *Applied Physics Express*, 12(7):070101, 2019.

[259] Y. Li, T. Polakovic, Y.-L. Wang, J. Xu, S. Lendinez, Z. Zhang, J. Ding, T. Khaire, H. Saglam, R. Divan, et al. Strong coupling between magnons and microwave photons in on-chip ferromagnet-superconductor thin-film devices. *Physical Review Letters*, 123(10):107701, 2019.

[260] J. T. Hou and L. Liu. Strong coupling between microwave photons and nanomagnet magnons. *Physical Review Letters*, 123(10):107702, 2019.

[261] Robert H Dicke. Coherence in spontaneous radiation processes. *Physical Review*, 93(1):99, 1954.

[262] A. V. Chumak, V. I. Vasyuchka, A. A. Serga, and B. Hillebrands. Magnon spintronics. *Nature Physics*, 11(6):453–461, 2015.

[263] D. Grundler. Nanomagnonics around the corner. *Nature nanotechnology*, 11(5):407–408, 2016.

[264] T. Liu, H. Chang, V. Vlaminck, Y. Sun, M. Kabatek, A. Hoffmann, L. Deng, and M. Wu. Ferromagnetic resonance of sputtered yttrium iron garnet nanometer films. *Journal of Applied Physics*, 115(17):17A501, 2014.

[265] J. Chen, C. Liu, T. Liu, Y. Xiao, K. Xia, G. E. W. Bauer, Mi. Wu, and H. Yu. Strong interlayer magnon-magnon coupling in magnetic metal-insulator hybrid nanostructures. *Physical Review Letters*, 120(21):217202, 2018.

[266] D. MacNeill, J. T. Hou, D. R. Klein, P. Zhang, P. Jarillo-Herrero, and L. Liu. Gigahertz frequency antiferromagnetic resonance and strong magnon-magnon coupling in the layered crystal $CrCl_3$. *Physical Review Letters*, 123(4):047204, 2019.

[267] M. Li, J. Lu, and W. He. Symmetry breaking induced magnon-magnon coupling in synthetic antiferromagnets. *Physical Review B*, 103(6):064429, 2021.

[268] J. Sklenar and W. Zhang. Self-hybridization and tunable magnon-magnon coupling in van der waals synthetic magnets. *Physical Review Applied*, 15(4):044008, 2021.

[269] J. E. Hirsch. Spin Hall effect. *Physical Review Letters*, 83(9):1834, 1999.

[270] Y. K. Kato, R. C. Myers, A. C. Gossard, and D. D. Awschalom. Observation of the spin Hall effect in semiconductors. *science*, 306(5703):1910–1913, 2004.

[271] S. Zhang, P. M. Levy, and A. Fert. Mechanisms of spin-polarized current-driven magnetization switching. *Physical Review Letters*, 88(23):236601, 2002.

[272] A. Manchon and S. Zhang. Theory of nonequilibrium intrinsic spin torque in a single nanomagnet. *Physical Review B*, 78(21):212405, 2008.

[273] I. M. Miron, G. Gaudin, S. Auffret, B. Rodmacq, A. Schuhl, S. Pizzini, J. Vogel, and P. Gambardella. Current-driven spin torque induced by the Rashba effect in a ferromagnetic metal layer. *Nature materials*, 9(3):230–234, 2010.

[274] A. V. Chumak, V. I. Vasyuchka, A. A. Serga, and B. Hillebrands. Magnon spintronics. *Nature Physics*, 11(6):453–461, 2015.

[275] F. Keffer and C. Kittel. Theory of antiferromagnetic resonance. *Physical Review*, 85(2):329, 1952.

[276] T. Taniguchi and H. Imamura. Enhancement of the Gilbert damping constant due to spin pumping in noncollinear ferromagnet/nonmagnet/ferromagnet trilayer systems. *Physical Review B*, 76(9):092402, 2007.

[277] T. Chiba, G. E. W. Bauer, and S. Takahashi. Magnetization damping in noncollinear spin valves with antiferromagnetic interlayer couplings. *Physical Review B*, 92(5):054407, 2015.

[278] Y. Shiota, T. Taniguchi, M. Ishibashi, T. Moriyama, and T. Ono. Tunable Magnon-Magnon Coupling Mediated by Dynamic Dipolar Interaction in Synthetic Antiferromagnets. *Physical Review Letters*, 125(1):017203, 2020.

[279] C. Bi, H. Almasi, K. Price, T. Newhouse-Illige, M. Xu, S. R. Allen, X. Fan, and W. Wang. Anomalous spin-orbit torque switching in synthetic antiferromagnets. *Physical Review B*, 95(10):104434, 2017.

[280] W. J. Kong, C. H. Wan, X. Wang, B. S. Tao, L. Huang, C. Fang, C. Y. Guo, Y. Guang, M. Irfan, and X. F. Han. Spin–orbit torque switching in a t-type magnetic configuration with current orthogonal to easy axes. *Nature communications*, 10(1):1–7, 2019.

[281] P. X. Zhang, L. Y. Liao, G. Y. Shi, R. Q. Zhang, H. Q. Wu, Y. Y. Wang, F. Pan, and C. Song. Spin-orbit torque in a completely compensated synthetic antiferromagnet. *Physical Review B*, 97(21):214403, 2018.

[282] T. Moriyama, W. Zhou, T. Seki, K. Takanashi, and T. Ono. Spin-orbit-torque memory operation of synthetic antiferromagnets. *Physical Review Letters*, 121(16):167202, 2018.

[283] Y. Ishikuro, M. Kawaguchi, T. Taniguchi, and M. Hayashi. Highly efficient spin-orbit torque in Pt/Co/Ir multilayers with antiferromagnetic interlayer exchange coupling. *Physical Review B*, 101(1):014404, 2020.

[284] H. Masuda, T. Seki, Y.-C. Lau, T. Kubota, and K. Takanashi. Interlayer exchange coupling and spin Hall effect through an Ir-doped Cu nonmagnetic layer. *Physical Review B*, 101(22):224413, 2020.

[285] A. A. Tulapurkar, Y. Suzuki, A. Fukushima, H. Kubota, H. Maehara, K. Tsunekawa, D. D. Djayaprawira, N. Watanabe, and S. Yuasa. Spin-torque diode effect in magnetic tunnel junctions. *Nature*, 438(7066):339–342, 2005.

[286] L. Liu, T. Moriyama, D. C. Ralph, and R. A. Buhrman. Spin-torque ferromagnetic resonance induced by the spin Hall effect. *Physical Review Letters*, 106(3):036601, 2011.

[287] J. Sinova, S. O. Valenzuela, J. Wunderlich, C. H. Back, and T. Jungwirth. Spin Hall effects. *Reviews of Modern Physics*, 87(4):1213, 2015.

[288] N. Mecking, Y. S. Gui, and C.-M. Hu. Microwave photovoltage and photoresistance effects in ferromagnetic microstrips. *Physical Review B*, 76(22):224430, 2007.

[289] D. Fang, H. Kurebayashi, J. Wunderlich, K. Vỳbornỳ, L. P. Zârbo, R. P. Campion, A. Casiraghi, B. L. Gallagher, T. Jungwirth, and A. J. Ferguson. Spin–orbit-driven ferromagnetic resonance. *Nature nanotechnology*, 6(7):413–417, 2011.

[290] L. Liu, C.-F. Pai, Y. Li, H. W. Tseng, D. C. Ralph, and R. A. Buhrman. Spin-torque switching with the giant spin Hall effect of tantalum. *Science*, 336(6081):555–558, 2012.

[291] E. Sagasta, Y. Omori, S. Vélez, R. Llopis, C. Tollan, A. Chuvilin, L. E. Hueso, M. Gradhand, Y. Otani, and F. Casanova. Unveiling the mechanisms of the spin Hall effect in Ta. *Physical Review B*, 98(6):060410, 2018.

[292] A. Manchon, J. Železnỳ, I. M. Miron, T. Jungwirth, J. Sinova, A. Thiaville, K. Garello, and P. Gambardella. Current-induced spin-orbit torques in ferromagnetic and antiferromagnetic systems. *Reviews of Modern Physics*, 91(3):035004, 2019.

[293] I. M. Miron, K. Garello, G. Gaudin, P. Zermatten, M. V. Costache, S. Auffret, S. Bandiera, B. Rodmacq, A. Schuhl, and P. Gambardella. Perpendicular switching of a single ferromagnetic layer induced by in-plane current injection. *Nature*, 476(7359):189–193, 2011.

[294] H. Nakayama, Y. Kanno, H. An, T. Tashiro, S. Haku, A. Nomura, and K. Ando. Rashba-Edelstein magnetoresistance in metallic heterostructures. *Physical Review Letters*, 117(11):116602, 2016.

[295] M. A. Zimmler, B. Özyilmaz, W. Chen, A. D. Kent, J. Z. Sun, M. J. Rooks, and R. H. Koch. Current-induced effective magnetic fields in Co/ Cu/ Co nanopillars. *Physical Review B*, 70(18):184438, 2004.

[296] J. C. Sankey, Y.-T. Cui, J. Z. Sun, J. C. Slonczewski, R. A. Buhrman, and D. C. Ralph. Measurement of the spin-transfer-torque vector in magnetic tunnel junctions. *Nature Physics*, 4(1):67–71, 2008.

[297] K. Obata and G. Tatara. Current-induced domain wall motion in Rashba spin-orbit system. *Physical Review B*, 77(21):214429, 2008.

[298] L. Zhu, L. Zhu, M. Sui, D. C. Ralph, and R. A. Buhrman. Variation of the giant intrinsic spin Hall conductivity of Pt with carrier lifetime. *Science advances*, 5(7):eaav8025, 2019.

[299] T. Nan, S. Emori, C. T. Boone, X. Wang, T. M. Oxholm, J. G. Jones, B. M. Howe, G. J. Brown, and N. X. Sun. Comparison of spin-orbit torques and spin pumping across NiFe/Pt and NiFe/Cu/Pt interfaces. *Physical Review B*, 91(21):214416, 2015.

[300] R. Ramaswamy, Y. Wang, M. Elyasi, M. Motapothula, T. Venkatesan, X. Qiu, and H. Yang. Extrinsic spin Hall effect in $Cu_{1-x}Pt_x$. *Physical Review Applied*, 8(2):024034, 2017.

[301] H.-Y. Lee, S. Kim, J.-Y. Park, Y.-W. Oh, S.-Y. Park, W. Ham, Y. Kotani, T. Nakamura, M. Suzuki, T. Ono, et al. Enhanced spin–orbit torque via interface engineering in Pt/CoFeB/MgO heterostructures. *APL Materials*, 7(3):031110, 2019.

[302] A. J. Berger, E. R. J. Edwards, H. T. Nembach, M. Karis, O.and Weiler, and T. J. Silva. Determination of the spin Hall effect and the spin diffusion length of Pt from self-consistent fitting of damping enhancement and inverse spin-orbit torque measurements. *Physical Review B*, 98(2):024402, 2018.

[303] X. Fan, J. Wu, Y. Chen, M. J. Jerry, H. Zhang, and J. Q. Xiao. Observation of the nonlocal spin-orbital effective field. *Nature communications*, 4(1):1–7, 2013.

[304] R. J. Elliott. Theory of the effect of spin-orbit coupling on magnetic resonance in some semiconductors. *Physical Review*, 96(2):266, 1954.

[305] Y. Yafet. Calculation of the g factor of metallic sodium. *Physical Review*, 85(3):478, 1952.

[306] N. H. Long, P. Mavropoulos, David S. G. Bauer, B. Zimmermann, Y. Mokrousov, and S. Blügel. Strong spin-orbit fields and Dyakonov-Perel spin dephasing in supported metallic films. *Physical Review B*, 94(18):180406, 2016.

[307] Y. Li, H. Saglam, Z. Zhang, R. Bidthanapally, Y. Xiong, J. E. Pearson, V. Novosad, H. Qu, G. Srinivasan, A. Hoffmann, et al. Simultaneous optical and electrical spin-torque magnetometry with phase-sensitive detection of spin precession. *Physical Review Applied*, 11(3):034047, 2019.

[308] S. M. Bhagat, L. L. Hirst, and J. R. Anderson. Ferromagnetic resonance in nickel and iron. *Journal of Applied Physics*, 37(1):194–197, 1966.

[309] T. Yoshino, K. Ando, K. Harii, H. Nakayama, Y. Kajiwara, and E. Saitoh. Quantifying spin mixing conductance in F/Pt (F= Ni, Fe, and $Ni_{81}Fe_{19}$) bilayer film. In *Journal of Physics: Conference Series*, volume 266, page 012115. IOP Publishing, 2011.

[310] E. Dobrovinskaya, L. Lytvynov, and V. Pishchik. *Properties of Sapphire*, pages 55–176. 01 1970.

[311] T. Seki, M. Tsujikawa, K. Ito, K. Uchida, H. Kurebayashi, M. Shirai, and K. Takanashi. Perpendicularly magnetized Ni/Pt (001) epitaxial superlattice. *Physical Review Materials*, 4(6):064413, 2020.

[312] H. Hayashi, A. Musha, H. Sakimura, and K. Ando. Spin-orbit torques originating from the bulk and interface in Pt-based structures. *Physical Review Research*, 3(1):013042, 2021.

[313] J. Ryu, M. Kohda, and J. Nitta. Observation of the D'yakonov-Perel'spin relaxation in single-crystalline Pt thin films. *Physical Review Letters*, 116(25):256802, 2016.

[314] R. Wang, Z. Xiao, H. Liu, Z. Quan, X. Zhang, M. Wang, M. Wu, and X. Xu. Enhancement of perpendicular magnetic anisotropy and spin-orbit torque in

Ta/Pt/Co/Ta multi-layered heterostructures through interfacial diffusion. *Applied Physics Letters*, 114(4):042404, 2019.

[315] L. Wang, R. J. H. Wesselink, Y. Liu, Z. Yuan, K. Xia, and P. J. Kelly. Giant room temperature interface spin Hall and inverse spin Hall effects. *Physical Review Letters*, 116(19):196602, 2016.

[316] W. Zhang, W. Han, X. Jiang, S.-H. Yang, and S. S. P. Parkin. Role of transparency of platinum–ferromagnet interfaces in determining the intrinsic magnitude of the spin Hall effect. *Nature Physics*, 11(6):496–502, 2015.

[317] Z. Feng, J. Hu, L. Sun, B. You, D. Wu, J. Du, W. Zhang, A. Hu, Y. Yang, D. M. Tang, et al. Spin Hall angle quantification from spin pumping and microwave photoresistance. *Physical Review B*, 85(21):214423, 2012.

[318] X. Tao, Q. Liu, B. Miao, R. Yu, Z. Feng, L. Sun, B. You, J. Du, K. Chen, S. Zhang, et al. Self-consistent determination of spin Hall angle and spin diffusion length in Pt and Pd: The role of the interface spin loss. *Science advances*, 4(6):eaat1670, 2018.

[319] J.-C. Rojas-Sánchez, N. Reyren, P. Laczkowski, W. Savero, J.-P. Attané, C. Deranlot, M. Jamet, J.-M. George, L. Vila, and H. Jaffrès. Spin pumping and inverse spin Hall effect in platinum: the essential role of spin-memory loss at metallic interfaces. *Physical Review Letters*, 112(10):106602, 2014.

[320] K. Roy. Estimating the spin diffusion length and the spin Hall angle from spin pumping induced inverse spin Hall voltages. *Physical Review B*, 96(17):174432, 2017.

[321] K. Chen and S. Zhang. Spin pumping in the presence of spin-orbit coupling. *Physical Review Letters*, 114(12):126602, 2015.

[322] P. C. Van Son, H. Van Kempen, and P. Wyder. Boundary resistance of the ferromagnetic-nonferromagnetic metal interface. *Physical Review Letters*, 58(21):2271, 1987.

[323] Y.-P. Wang and C.-M. Hu. Dissipative couplings in cavity magnonics. *Journal of Applied Physics*, 127(13):130901, 2020.

[324] G. Y. Shi, C. H. Wan, Y. S. Chang, F. Li, X. J. Zhou, P. X. Zhang, J. W. Cai, X. F. Han, F. Pan, and C. Song. Spin-orbit torque in MgO/CoFeB/Ta/CoFeB/MgO symmetric structure with interlayer antiferromagnetic coupling. *Physical Review B*, 95(10):104435, 2017.

[325] M. Lax. *Symmetry principles in solid state and molecular physics*. Courier Corporation, 2001.

[326] B. Heinrich and J. F. Cochran. Ultrathin metallic magnetic films: magnetic anisotropies and exchange interactions. *Advances in Physics*, 42(5):523–639, 1993.